Crystallisation driven self-assembly study of polyester based triblock copolymers

Wei Yu

Submitted for the degree of Doctor of Philosophy

Department of Chemistry

April 2019

Table of contents

Acknowledgements VII

Declaration of Authorship VIII

Publication IX

Summary X

Abbreviations XI

List of Figures XV

List of Schemes XXIV

List of Tables XXV

Chapter 1. Introduction 1

1.1 Controlled/living radical polymerisation 2

1.2 RAFT polymerisation 4

1.3 Ring-opening Polymerisation (ROP) 9

1.4 Self-assembly of coil-coil block copolymers in solution 11

1.5 Self-assembly of crystalline-coil block copolymers in solution 14

1.6 Major factors affecting the CDSA process 16

1.6.1 Copolymer composition 17

1.6.2 Solvent condition 18

1.6.3 Presence of additives 19

1.7 Particle self-assembly methodology 21

1.8 Living CDSA 23

1.9 Applications of the nanostructures prepared by CDSA 27

1.9.1 Preparation of supermicelles 27

1.9.2 Biological applications 28

1.9.3 Organic electronics 29

1.10 Nanoparticles Characterisations 32

1.10.1 Transmission electron microscopy 32

1.10.2 Atomic force microscopy 34

1.10.3 Light scattering....36
1.11 Summary....37
1.12 References....38

Chapter 2. Understanding the CDSA of polylactide containing triblock copolymers....43
2.1 Abstract....44
2.2 Introduction....44
2.3 Results and Discussion....46
2.3.1 Ring-opening polymerisation of L-lactide....47
2.3.2 Synthesis of 2-(Dodecylthiocarbonothioylthio)-2-methylpropionic acid (DDMAT)....51
2.3.3 Coupling the RAFT agent to the polymer....52
2.3.4. Chain-extension of dual-functionalised macro-CTA....55
2.3.5 Crystallisation-Driven Self-Assembly of PDMA-*b*-PLLA-*b*-PDMA triblock copolymers....58
2.3.6 Tuning the size and morphology of the assemblies by changing the hydrophobic and hydrophilic block length....60
2.3.7 Comparison of the diblock to triblock system....67
2.4 Conclusion....74
2.5 Experimental Section....75
2.5.1 Materials....75
2.5.2 Instrument....75
2.5.3 Synthesis of PLLA homopolymers....78
2.5.4 Synthesis of dual functionalised macro-CTA....78
2.5.5 Synthesis of triblock copolymers poly(*N*,*N*-dimethylacrylamide)-*b*-poly(L-lactide)-*b*-poly(*N*,*N*-dimethylacrylamide)....79
2.5.6 Crystallisation-driven self-assembly of PDMA-*b*-PLLA-*b*-PDMA triblock copolymers and PDMA-*b*-PLLA diblock copolymers....80
2.6 References....81

Chapter 3. Monodisperse cylindrical micelles with controlled length and composition from polylactide based block copolymers *via* living crystallization driven self-assembly 82

3.1 Abstract 83

3.2 Introduction 84

3.3 Result and discussion 86

3.3.1 Synthesis of ABA type triblock copolymers 86

3.3.2 Preparation of cylindrical micelles from PXX-*b*-PLLA-*b*-PXX ABA triblock copolymers 90

3.3.3 Preparation of crystalline seeds from PLA-based block copolymers 91

3.3.4 Epitaxial growth of cylindrical micelles 95

3.3.4.1 The effect of common good solvent for both blocks 95

3.3.4.2 Epitaxial growth of unimer 4 on micelle seeds 4 97

3.3.4.3 Epitaxial growth of unimer 1, 2, 5 and 6 on micelle seeds 4 101

3.3.5 Epitaxial growth of PDMA-b-PLLA-b-PDMA 2D platelets 107

3.4 Conclusion 110

3.5 Experimental Section 111

3.5.1 Materials 111

3.5.2 Instruments 111

3.5.3 Synthesis of poly(4-vinylpyridine)-*block*-poly(L-lactide)-*block*-poly(4-vinylpyridine) (P4VP-*b*-PLLA-*b*-P4VP) 113

3.5.4 Synthesis of Poly(*N*-acryloylmorpholine)-*block*-poly(L-lactide)-*block*-Poly(*N*-acryloylmorpholine) (PNAM-*b*-PLLA-*b*-PNAM) 113

3.5.5 Synthesis of poly(*N*-Hydroxyethyl acrylate)-*block*-poly(L-lactide)-*block*-poly(*N*-Hydroxyethyl acrylate) (PHEA-*b*-PLLA-*b*-PHEA) 114

3.5.6 Typical crystallisation driven self-assembly method for PLLA based block copolymers 115

3.5.7 Sonication of $PDMA_{75}$-*b*-$PLLA_{50}$-*b*-$PDMA_{75}$ cylindrical micelles 115

3.5.8 Typical crystallinzation driven self-assembly method for the epitaxial growth of PLLA block copolymers 115

3.6 References 116

Chapter 4. Structural reorganization of cylindrical nanoparticles triggered by polylactide stereocomplexation in aqueous solution 118

4.1 Abstract 119

4.2 Introduction 120

4.3 Results and Discussion 122

4.3.1 Selection of the polymer model for the stereocomplex-triggered morphological transition study 122

4.3.1.1 Polymer architecture 122

4.3.1.2 Corona chemistry optimisation 123

4.3.2 Synthesis of ABA type triblock copolymers PHEAAmy-b-PL(D)LAx-b-PHEAAmy 124

4.3.3 Crystallisation-Driven Self-Assembly of PHEAAm$_y$-*b*-PL(D)LA$_x$-*b*-PHEAAm$_y$ triblock copolymers 129

4.3.4 Stereocomplexation-triggered morphological transition in methanol: from homochiral cylinders to aggregates 131

4.3.5 Elucidating the mechanism of stereocomplexation 135

4.3.6 Study of the parameters affecting the morphological transition 138

4.3.6.1 The effect of core length 138

4.3.6.2 The effect of corona length 140

4.3.6.3 The effect of aging temperature 141

4.3.6.4 The effect of corona chemistry 143

4.3.7 Stabilising the assemblies in aqueous solution 144

4.3.7.1 Preparation of pentablock copolymers 145

4.3.7.2 Removal of the RAFT end group 151

4.3.8 Morphological transition under physiological conditions 154

4.4 Conclusions 162

4.5 Experimental Section 163

4.5.1 Materials 163

4.5.2 Characterisation techniques 163

4.5.3 Synthesis of poly(*N*-hydroxyethyl acrylamide)-*block*-poly(L(D)-lactide)-*block*-poly(*N*-hydroxyethyl acrylamide); (PHEAAm$_y$-*b*-PL(D)LA$_x$-*b*-PHEAAm$_y$) 164

4.5.4 Synthesis of poly(n-butyl acrylate)-*block*-poly(L-lactide)-*block*-poly(n-butyl acrylate); ($PBuA_y$-*b*-$PLLA_x$-*b*-$PBuA_y$) 165

4.5.5 Synthesis of poly(*N*-hydroxyethyl acrylamide)-*block*-poly(n-butyl acrylate)-*block*-poly(L-lactide)-*block*-poly(n-butyl acrylate)-*block*-poly(*N*-hydroxyethyl acrylamide); ($PHEAAm_z$-*b*-$PBuA_y$-*b*-$PLLA_x$-*b*-$PBuA_y$-*b*-$PHEAAm_z$) 166

4.5.6 Removal of the RAFT end group 167

4.5.7 Synthesis of the amine-terminated $PHEAAm_{42}$-*b*-$PLLA_{32}$-*b*-$PHEAAm_{42}$ copolymer 167

4.5.8 Crystallisation-driven self-assembly method for $PHEAAm_y$-*b*-$PL(D)LA_x$-*b*-$PHEAAm_y$ block copolymers 168

4.5.9 Sonication of $PHEAAm_y$-*b*-$PL(D)LA_x$-*b*-$PHEAAm_y$ cylindrical micelles 168

4.6 References 170

Chapter 5. Understanding the CDSA of poly(ε-caprolactone) containing triblock copolymers 171

5.1 Abstract 172

5.2 Introduction 173

5.3 Result and discussion 175

5.3.1 Ring-opening polymerisation of ε-caprolactone 175

5.3.2 Conjugation of RAFT agent DDMAT to PCL homopolymers 180

5.3.3 Chain-extension of dual-functionalised Macro-CTA 182

5.3.4 Optimisation of the self-assembly methodology 184

5.3.4.1 The selection of a proper assembly solution 184

5.3.4.2 Optimisation of assembly concentration 188

5.3.5 Kinetic study of the self-assembly process 188

5.3.6 Study of the effect of block length on the resultant assembly morphology 194

5.3.7 Self-seeding process of PCL based triblock copolymers 198

5.4 Conclusion 202

5.5 Experimental section 203

5.5.1 Materials 203

5.5.2 Instrument 203

5.5.3 Typical procedure for the homopolymerisation of ε-caprolactone (PCL_{30}, PCL_{40} and PCL_{60}) 206

5.5.4 Typical procedure for Coupling RAFT agent to homopolymer PCL_x (PCL_{30}, PCL_{40} and PCL_{60}) 206

5.5.5 Typical procedure for the chain-extension of the macro-CTA ($PDMA_{150}$-*b*-PCL_{30}-*b*-$PDMA_{150}$) 206

5.5.6 Typical crystallisation-driven self-assembly method for PCL based block copolymers 207

5.6 References 208

Acknowledgements

My sincere thanks goes to my supervisors, Professor Andrew Dove and Professor Rachel O'Reilly, not only for their invaluable guidance and advice during my PhD study but also for their support and encouragement. Though quite challenging sometimes, their high expectation kept pushing me for which I am grateful. I really appreciate the outstanding academic atmosphere they create, not only for the world-class facilities and international cooperation, but also for the experienced senior researchers' guidance. I feel very lucky to work with them in both well-organized research groups.

I would like to thank all of the group members for their help during the last three and half years, especially to Dr Annette Christie and Dr Marianne Rolph for their selfless supports at the beginning of my PhD. My genuine thanks also goes to Dr Zan Hua, Dr Maria Chiara Arno, Dr Maria Inam, Dr Craig Bell, Dr Lewis Blackman, Dr Victor Quan, Dr Anaïs Pitto-Barry, Dr Tom Wilks, and Dr Turgay Yildirim for fielding many a question over the years. A special thanks to Gordon Herwig for being a great friend sorting out all kinds of life problems for me, you surely made my life better here. Last but not the least, a big thank you to Dr Maria Perez-Madrigal, Dr Josh Worch and Dr Joe Jones for their great patience to answer tons of stupid questions from me.

Finally and most importantly, thanks to my family, my parents "Jianming Yu" and "Wenqin Luo" for their unconditional support and encouragement throughout this often difficult journey. I would like to devote my deepest thanks to my girlfriend Yujie Xie, you make my PhD life and life in the future colourful.

Declaration of Authorship

This thesis is submitted to the University of Warwick in support for the degree of Doctor of Philosophy. It has been composed by myself and has not been submitted in any previous application for any degree.

The work presented (including data generated and data analysis) was carried out by the author other than the author were clearly stated in each chapter.

Parts of this thesis have been published by the author.

Publication

1. Yu, W.; Inam, M.; Jones, J. R.; Dove, A. P.; O'Reilly, R. K., Understanding the CDSA of poly (lactide) containing triblock copolymers. Polymer Chemistry 2017, 8 (36), 5504-5512. (Chapter 2)

Summary

Chapter 1 gives the introduction of the main concepts and techniques throughout this thesis.

Chapter 2 describes the control over the morphology of various poly(*N*,*N*-dimethylacrylamide)-poly(L-lactide)-*b*-poly(*N*,*N*-dimethylacrylamide) micelles based on crystallisation driven self-assembly. Such change of the shapes was realized by tuning the composition of the triblock copolymers, when solubility-based shape selectivity mechanism was proposed to explain.

Chapter 3 expands the scope of the crystallization-driven self-assembly of PLLA-based ABA type copolymers using different hydrophilic corona-forming blocks. Besides, by taking advantage of crystalline properties of the PLLA segments, monodisperse 1D cylinders with varying length were prepared.

Chapter 4 intend to trigger the morphological transition of the PLLA based terpolymers cylindrical micelles under physiological condition with the addition of enantiomer assemblies. According to the "unimer-assembly exchanging" theory, it was proved the block composition and polymer solubility played a vital role in the transition process.

Chapter 5 employs the use of poly(ε-caprolactone) crystallisable core-forming block for the preparation of 1D cylindrical structures of controlled length and dispersity. The effect of the polymer composition on the assembly morphology and size was also studied in detail.

Abbreviations

1D	One-dimensional
2D	Two-dimensional
δ	Chemical shift
δ_h	Hildebrand solubility parameter
µg	Microgram(s)
µL	Microlitre(s)
µmol	Micromole(s)
Å	Angstrom(s)
AFM	Atomic force microscopy
AIBN	2,2-Azobis(2-methylpropionitrile)
ATRP	Atom transfer radical polymerisation
br	Broad
BCP	Block copolymer
c	Concentration
ca.	Circa
CDSA	Crystallisation-driven self-assembly
CTA	Chain transfer agent
d	Doublet
D	Diffusion co-efficient
DCM	Dichloromethane
DCTB	Trans-2-[3-(4-*tert*-butylphenyl)-2-methyl-2-propylidene] malonitrile
DDMAT	2-(Dodecylthiocarbonothioylthio)-2-methylpropionic acid
DLS	Dynamic light scattering

$Đ_M$	Molar-mass dispersity
DMA	*N*,*N*-Dimethlyacrylamide
DMF	Dimethylformamide
DMSO	Dimethylsulfoxide
DP	Number average degree of polymerisation
DOSY	Diffusion-Ordered NMR Spectroscopy
DPP	Diphenyl phosphate
DMAEA	2-(dimethylamino)ethyl acrylate
EtOH	Ethanol
EPHP	1-Ethylpiperidine hypophosphite
FTIR	Fourier transform infrared
GO	Graphene oxide
kDa	Kilodaltons
L_n	Number-average length
L_w	Weight-average length
LogP_{oct}	Octanol-water partition co-efficient
m	Multiplet
m/z	Mass to charge ratio
MALDI-ToF	Matrix-assisted laser desorption ionisation – time of flight
MeOH	Methanol
mg	Milligram(s)
mL	Millilitre(s)
mmol	Millimole(s)
M_n	Number average molecular weight

mol	Mole(s)
M_w	Weight average molecular weight
NMR	Nuclear magnetic resonance
NMP	Nitroxide-mediated polymerisation
PNAM	Poly(4-acryloyl morpholine)
PCL	Poly(ε-caprolactone)
PDLA	Poly(D-lactide)
PDMA	Poly(*N*,*N*-dimethlyacrylamide)
PDMS	Poly(dimethylsiloxane)
PE	Poly(ethylene)
PHEA	Poly(*N*-hydroxyethyl acrylate)
P4VP	Poly(4-vinyl pyridine)
P2VP	Poly(2-vinylpyridine)
PS	Polystyrene
PFDMS	Poly(ferrocenyldimethylsilane)
P3HT	Poly(3-hexylthiophene)
PIP	Poly(isoprene)
PAA	Poly(acrylic acid)
PGMA	Poly(glycerol monomethacrylate)
PHPMA	Poly(2-hydroxypropyl methacrylate)
PISA	Polymerisation-induced self-assembly
PMMA	Poly(methyl methacrylate)
PHEAAm	Poly(*N*-hydroxyethyl acrylamide)
ppm	Parts per million

q	Quartet
RAFT	Reversible addition-fragmentation chain transfer
RI	Refractive index
ROP	Ring-opening polymerisation
SAXS	Small-angle X-ray scattering
SEC	Size exclusion chromatography
SLS	Static light scattering
TEM	Transmission electron microscopy
THF	Tetrahydrofuran
Thiourea	1-[3,5-bis(trifluoromethyl)phenyl]-3-cyclohexylthiourea
UA	Uranyl acetate
UV	Ultraviolet
WAXS	Wide angle X-ray scattering
wt. %	Weight percent

List of Figures

Figure 1.1 Schematic representation of the four main types of RAFT agent. 6
Figure 1.2 Guidelines for the selection of the RAFT agent for various monomer classes. For the Z group, addition rates decrease and fragmentation rates increase from left to right. For the R group, fragmentation rates decrease from left to right. A dashed line indicates partial control.[12] 8
Figure 1.3 Various processes for the end group removal of RAFT derived polymers.[15] 9
Figure 1.4 Different self-assembled structures obtained by targeting different packing parameter values, p.[34] 13
Figure 1.5 Transmission electron microscopy (TEM) image on the left showing the polymer vesicles and a scheme on the right which represents their structure.[42] 14
Figure 1.6 Transmission electron micrographs of the cylindrical micelles formed from $PFDMS_{50}$-b-$PDMS_{300}$ diblock copolymer.[45] 15
Figure 1.7 Chain-folding model of crystalline-coil diblock copolymers with low and high folding number. 16
Figure 1.8 Transmission electron micrographs of the aggregates formed by A) PIP_{320}-*b*-$PFDMS_{53}$, and B) PIP_{30}-*b*-$PFDMS_{60}$ in a mixed solvent (Tetrahydrofuran and hexane v/v 2:8).[52] 17
Figure 1.9 Transmission electron micrographs of the aggregates formed by A) $PDMA_{600}$-*b*-$PLLA_{48}$ and B) $PDMA_{150}$-b-$PLLA_{48}$. Samples were self-assembled in ethanol at 90 ℃ for 8 h and cooled to room temperature. Scale bar = 1 μm.[56] 18
Figure 1.10 Morphological transformations of PEO_{45}-*b*-PCL_{24} diblock copolymers induced by incorporation of a PCL_{10} homopolymer with different varying homopolymer content. Scale bar = 2μm.[63] 20
Figure 1.11 PI-CDSA (at 10% w/w solids) of PIP-b-PFDMS diblock copolymers at 10% v/v THF/n-hexanes with varying block ratios. Lenticular platelet micelles were formed for PIP-b-PFDMS BCPs with a targeted block ratio of approximately 1:1 (a) and cylindrical micelles were formed for block ratios of approximately 5:1 (b) and 10:1 (c). Small seeds micelles (d) were blended into the self-assembly solution when the block ratio is fixed at 5:1, whilst when the PIP-to-seed ratio was varied from 6:1 (f) to 18:1 (e), the cylinder length elongated accordingly. Scale bars = 1 μm.[82] 23
Figure 1.12 Homogeneous nucleation followed by epitaxial growth producing cylindrical micelles with a semicrystalline core and a relatively narrow distribution of lengths. The rod ends remain active to further growth if additional polymer containing a PFDMS block is added to the system.[84] 24
Figure 1.13 (A) Cylindrical micelles were obtained through a CDSA approach. Addition of different crystalline-coil block copolymer unimers leading to the elongation of the micelles. (B) The ends of BAB co-micelles were interfered by crosslinking of the corona, preventing the CDSA at both ends. Then the middle micelles were selectively dissolved forming daughter micelles to initiate non-centrosymmetric living CDSA growth.[87] 25
Figure 1.14 (a) Schematic representation for the formation of uniform concentric 2D lenticular platelets; (b) TEM image and (c and d) laser scanning confocal microscopy (LSCM) images of

lenticular platelet micelles showing their concentric structure. Scale bars are 500 nm (b and c) and 2 mm (d).[89] 26
Figure 1.15 (a) LSCM image of a multi-layer lenticular platelet by sequential addition of different block copolymer; (b) atomic force microscopy (AFM) images and (c) TEM images of perforated rectangular platelet micelles and corresponding rectangular ring platelet micelle after crosslinking and subsequent dissolution of the non-crosslinked segment.[67] 26
Figure 1.16 Multidimensional superstructures through end-to-end stacking of P-H-P triblock co-micelles characterised by TEM. (**A**) Self-assembly of triblock co-micelles $P_{145\ nm}$-$H_{110\ nm}$-$P_{145\ nm}$ in hexane/iPrOH (H = PFS_{49}-b-$PDMS_{504}$, P =PFS_{48}-b-$P2VP_{414}$); (**B**) An immobilised chain formed by intermicellar cross-linking of P2VP coronas of stacked terminal segments; and (**C**) Self-assembly of triblock co-micelles $P_{50\ nm}$-$H_{190\ nm}$-$P_{50\ nm}$ by adding decane to hexane/iPrOH.[91] 28
Figure 1.17 A) Scheme of B-A-B type triblock co-micelles prepared by a living CDSA approach B) Laser scanning confocal microscopy of the uniform and segmented nanofibres, blue represents the $PDHF_{14}$-b-PEG_{227} block, and yellow corresponds to the $PDHF_{14}$-b-QPT_{22} block. C) Photoluminescence spectra of segmented PDHF nanofibres with different block lengths.[100] 31
Figure 1.18 Diagram of AFM convolution effect, the size and shape of the tip affects the measured profile whereby a square was depicted as trapezoid (a), and spheres were larger (b).[107] 35

Figure 2.1 ^{1}H NMR spectra (400 MHz, $CDCl_3$) of various PLLA homopolymers $PLLA_{25}$, $PLLA_{32}$, $PLLA_{50}$ and $PLLA_{68}$. 48
Figure 2.2 An overlay of SEC traces of homopolymers $PLLA_{25}$, $PLLA_{32}$, $PLLA_{50}$, $PLLA_{68}$ (DMF with 5 mM NH_4BF_4). 48
Figure 2.3 MALDI-ToF mass spectra of (a) $PLLA_{25}$, (b) $PLLA_{32}$, (c) $PLLA_{50}$ and (d) $PLLA_{68}$. 50
Figure 2.4 ^{1}H NMR spectrum of the RAFT agent DDMAT (400 MHz, $CDCl_3$). 51
Figure 2.5 ^{1}H NMR spectra (400 MHz, $CDCl_3$) of $PLLA_{32}$(a), $PLLA_{32}$-CTA(b) and macro-initiator (c) $PLLA_{25}$-CTA, $PLLA_{50}$-CTA and $PLLA_{68}$-CTA 53
Figure 2.6 a) An overlay of SEC RI traces of homopolymers $PLLA_{32}$ and macro-CTA CTA-$PLLA_{32}$-CTA (DMF with 5 mM NH_4BF_4). b) An overlay of SEC RI and UV traces of b) CTA-$PLLA_{32}$-CTA, c) CTA-$PLLA_{25}$-CTA d) CTA-$PLLA_{50}$-CTA and e) CTA-$PLLA_{68}$-CTA macro-initiator. 54
Figure 2.7 MALDI-ToF mass spectra of $PLLA_{32}$ and CTA-$PLLA_{32}$-CTA. 55
Figure 2.8 ^{1}H NMR spectrum of PDMA-b-PLLA-b-PDMA triblock copolymer **T7** (400 MHz, $CDCl_3$). 57
Figure 2.9 SEC curves of polymers (DMF with 5 mM NH_4BF_4). a) Macro-initiator **$PLLA_{25}$** and triblock copolymers **T1-T4**. b) Macro-initiator **$PLLA_{32}$** and triblock copolymers **T5-T8**. c) Macro-initiator **$PLLA_{50}$** and triblock copolymers **T9-T11**. d) Macro-initiator **$PLLA_{68}$** and triblock copolymers **T12, T13**. 57
Figure 2.10 ^{1}H-DOSY NMR spectra (500 MHz, $CDCl_3$) of homopolymer $PLLA_{32}$, macro-initiator CTA-$PLLA_{32}$-CTA and triblock copolymer PDMA-*b*-PLLA-*b*-PDMA **T7**. 58
Figure 2.11 The dispersity trace of micelles achieved from polymer **T5** (a), **T7** (b), **T9** (c), **T10** (d), **T12** (e) and **T13** (f) by DLS analysis. 60

Figure 2.12 TEM images of micelles obtained from CDSA of the series of PDMA-b-PLLA-b-PDMA triblock copolymers **T4** (A), **T11** (B), **T12** (C). Samples were negatively stained using uranyl acetate. Scale bar = 1 µm. 61
Figure 2.13 Phase diagram constructed for PDMA-b-PLLA-b-PDMA triblock terpolymers, **T1** (D), **T2** (C), **T3** (B), **T4** (A), **T5** (H), **T6** (G), **T7** (F), **T8** (E), **T9** (K), **T10** (J), **T11** (I), **T12** (L), **T13** (M). TEM characterisation of **T11** (I) is shown in **Figure 4** (B). As the target PLLA DP and the hydrophobic weight were systematically varied, the achieved morphology changed from lamellae (red) to wide cylinders (blue) and pure cylinders (green). Samples were negatively stained using uranyl acetate for TEM characterisation. Scale bar = 1 µm.....62
Figure 2.14 AFM and height profile of triblock copolymer **T9** cylinders (a, b) and **T8** diamond platelets (c, d). Samples were self-assembled in methanol at room temperature and aged for one day. TEM images of micelles obtained from the CDSA of triblock copolymers **T4** (e) and **T12** (f) prepared by a slow drying method on GO grids.....63
Figure 2.15 TEM images of micelles obtained from the CDSA of triblock copolymers **T8** (a), **T7** (b), **T6** (c), **T5** (d) after aging for one day. TEM images of the same assembled samples after one month (**T8** (e), **T7** (f), **T6** (g), **T5** (h)). Samples were negatively stained using uranyl acetate for TEM characterisation. Scale bar = 1 µm. 64
Figure 2.16 WAXS diffractogram of $PDMA_{188}$-b-$PLLA_{32}$-b-$PDMA_{188}$ (**T8**) diamond platelets and $PDMA_{66}$-b-$PLLA_{32}$-b-$PDMA_{66}$ (**T6**) cylinders showing the 2θ peak at ca. 16 ° characteristic of crystalline PLLA.....65
Figure 2.17 TEM images of micelles obtained from the CDSA of triblock copolymers **T4** (A), **T8** (B), **T11** (C). Scale bar = 1 µm. 66
Figure 2.18 Assemblies achieved from PDMA-*b*-PLLA diblock copolymers **D6** (A)**, D5** (B), **D4** (C), **D3** (D), **D2** (E), **D1** (F) in methanol at room temperature. Samples were prepared by slow drying on carbon grids and were negatively stained using uranyl acetate for TEM characterisation. Scale bar = 1 µm.....67
Figure 2.19 Triblock copolymer **T3** and diblock copolymer **D2** (with similar block lengths) were dissolved in different alcoholic solvents, i.e. methanol, ethanol, *n*-propanol, *n*-butanol, at a concentration of 5 mg mL^{-1}. The assembly solution was heated to 90 °C before cooling to room temperature and aged for one day. A laser pen was used to monitor the Tyndall effect of the triblock copolymer (A) and the diblock copolymer (B). TEM characterisation of the assemblies of polymers **T3** (C) and **D2** (D) in methanol and polymers **T3** (E) and **D2** (F) in ethanol. Samples were negatively stained using uranyl acetate for TEM characterisation. 69
Figure 2.20 PLLA based triblock copolymer **T3** was assembled in methanol and ethanol (5 mg mL^{-1}). Tyndall phenomenon was observed.....70
Figure 2.21 ^{1}H NMR spectra of PLLA based triblock copolymer **T3** assembled in d_4-methanol before aging (a) and after aging for two days (b). The corresponding TEM results showed intact diamonds (c). 70
Figure 2.22 ^{1}H NMR spectra of PLLA based triblock copolymer **T3** assembled in d_6-ethanol before aging (a) and after aging for two days (b). The corresponding TEM results showed a blending of spheres, cylinders and incomplete platelet (c, d).....71

Figure 2.23 Phase diagram constructed for PDMA-*b*-P*L*LA diblock copolymers D6 (A), D5 (B), D4 (C), D3 (D), D2 (E), D1 (F). As target PLLA DP and the hydrophobic weight were systematically varied, the achieved morphology changed from lamella (red hollow square) to mixed phase (blue) and to cylinder (green). Scale bar = 1 μm. 72
Figure 2.24 A combined phase diagram of PDMA-*b*-PLLA-*b*-PDMA triblock and PDMA-*b*-PLLA diblock copolymers. Triblock copolymers were assembled in methanol at room temperature, whereas diblock copolymers were assembled in ethanol after elevating the temperature to 90 °C for 8 hours. The solid circles represent the triblock copolymers, while the hollow squares represent the diblock copolymers. As the target PLLA DP and the hydrophobic weight were systematically varied, the achieved morphology ranged from 2D lamellae (red) to 'transition state' wide cylinders (blue) and pure cylinders (green). 73

Figure 3.1 Characterisation data for ^{1}H NMR spectra (400 MHz) of (a) $PHEA_{75}$-b-$PLLA_{50}$-b-$PHEA_{75}$ (d_6-DMSO) (b) $P4VP_{70}$-b-$PLLA_{50}$-b-$P4VP_{70}$ ($CDCl_3$) (c) $PNAM_{80}$-b-$PLLA_{50}$-b-$PNAM_{80}$ ($CDCl_3$). 88
Figure 3.2 SEC chromatograms of (a) $PHEA_{75}$-b-$PLLA_{50}$-b-$PHEA_{75}$, (b) $P4VP_{70}$-b-$PLLA_{50}$-b-$P4VP_{70}$ and (c) $PNAM_{80}$-b-$PLLA_{50}$-b-$PNAM_{80}$, DMF (5 mM NH_4BF_4) was used as the eluent. 89
Figure 3.3 TEM micrographs of micelles obtained from the CDSA of triblock copolymers (a) polymer **1**, (b) polymer **2**. Samples were negatively stained using uranyl acetate (0.5 wt %). Scale bar = 1 μm. 91
Figure 3.4 TEM micrographs of polymer **4** cylinders assembled in methanol after sonication at 0 ℃ using a sonic probe (a) 0, (b) 4, (c) 10 and (d) 20 min. (e) Seeds aged for one month in solution. Samples were negatively stained using uranyl acetate (0.5 wt %). Scale bar = 0.5 μm. 92
Figure 3.5 Histogram showing the length distribution of sonicated cylinders after 4, 10 and 20 min of sonication at 0 °C using a sonic probe. 93
Figure 3.6 Overlaid RI SEC chromatography of polymer **4** before self-assembly (solid, red line) and after sonication of the assembled cylinders for 20 min at 0 ℃ using a sonic probe (dashed, blue line). DMF (5 mM NH_4BF_4) was used as the eluent. 94
Figure 3.7 TEM images of cylindrical micelles of $PDMA_{75}$-b-$PLLA_{50}$-b-$PDMA_{75}$ obtained by adding equivalent mass of unimers (5 mg mL^{-1}) in (b) chloroform, (c) DMF and (d) THF to the (a) seeds micelles in methanol (1 mL, 0.01 mg mL^{-1}) at room temperature (25 ℃). Scale bar = 0.5 μm. Samples were negatively stained using uranyl acetate (0.5 wt %). 95
Figure 3.8 TEM micrograph obtained from mixing 200 μL of unimer solution in THF (5 mg mL^{-1}) and 1 mL seed solution (methanol, 0.01 mg mL^{-1}) and aging for 2 days. Scale bar = 0.5 μm. Samples were negatively stained using uranyl acetate (0.5 wt %). 96
Figure 3.9 TEM micrographs of polymer **4** fibres grown from polymer **4** seed micelles with m_{unimer}/m_{seed} of (a) 40/1 and (b) 100/1. Scale bar = 0.5 μm. Samples were negatively stained using uranyl acetate (0.5 wt %). 97

Figure 3.10 (a) TEM and AFM micrographs of seed micelles of polymer **4** prepared by sonication for 20 min at 0 ℃ (L_n = 65 nm, L_w/L_n = 1.06) and near monodisperse cylindrical micelles drop-cast from methanol prepared by living CDSA by the addition of 3 equiv, 6 equiv, 12 equiv, 18 equiv, and 30 equiv of unimer (polymer **4**); (b) Graph showing the linear dependence of micelle length on the unimer-to-seed ratio of polymer **4**. Scale bar = 1 μm. Samples were negatively stained using uranyl acetate (0.5 wt %). (c) Schematic representation of the preparation of near monodisperse fibres.....99
Figure 3.11 TEM images of assemblies obtained when 36 μL of unimer solution (polymer **4** at 5 mg mL^{-1}) was added to 1 mL methanol. Scale bar = 1 μm. Samples were negatively stained using uranyl acetate (0.5 wt %).....101
Figure 3.12 TEM micrographs of polymer **5** fibres grown from polymer **4** seed micelles with m_{unimer}/m_{seed} of (a) 6/1, (b) 12/1, and (c) 25/1. (d) unimers of polymer **6** were added in the seeds (polymer **4**) and aged for 7 days showing no growth over the time period. Scale bar = 0.5 μm. Samples were negatively stained using uranyl acetate (0.5 wt %). (e) Plot showing experimentally obtained fibre length (L_n) is consistent with theoretical lengths (red line) based on different m_{unimer}/m_{seed} mass ratios. (f) Length dispersity of cylinders formed upon epitaxial growth of polymer **5** cylindrical micelles. 102
Figure 3.13 (a) Schematic representation of the preparation of near monodisperse fibres. TEM micrographs of polymer **1** fibres grown from polymer **4** seed micelles with m_{unimer}/m_{seed} of (b) 3:1, (c) 6:1 and (d) 18:1. Scale bar = 0.5 μm. Samples were negatively stained using uranyl acetate (0.5 wt %). (e) Plot showing experimentally obtained fibre length (L_n) is consistent with theoretical lengths (red line) based on different m_{unimer}/m_{seed} mass ratios. (f) Length dispersity of cylinders formed upon epitaxial growth of polymer **4** cylindrical micelles.....104
Figure 3.14 (a) Schematic representation of the formation of ABA block co-micelles. TEM micrographs of representative triblock co-micelles prepared from monodisperse seed micelles when drop-casted from methanol: (b) the long seed micelles composed of polymer **4** and (c) a triblock co-micelle with a central seed segment composed of polymer **4**, with outer blocks derived from unimers of polymer **2**. Scale bar = 1 μm. Samples were negatively stained using uranyl acetate (0.5 wt %) for sample (b). (d) Length dispersity of cylinders of ABA block co-micelles.....106
Figure 3.15 TEM micrographs of polymer **6** platelets assembled in methanol after sonication at 0 ℃ using a sonic probe at (a) 0, (b) 4, (c) 10, (d) 20 min. (e) Seeds aged for one month. Scale bar = 1 μm. Samples were negatively stained using uranyl acetate (0.5 wt %).....107
Figure 3.16 (a) Schematic representation of the preparation of uniform platelets. TEM micrographs of polymer **6** 2D platelets grown from polymer **6** seed micelles with m_{unimer}/m_{seed} of (b) 5/1, (c) 10/1, and (d) 25/1. (e) TEM images of final structures obtained when 50 μL of unimer solution was added to methanol solution without seeds. Scale bar = 0.5 μm. Samples were negatively stained using uranyl acetate (0.5 wt %). (f) Plot showing linear dependence between micelle area and the m_{unimer}/m_{seed} ratio with error bars and standard deviation.....109

Figure 4.1 Plots of normalized transmittance versus temperature obtained for polymers $PDMA_{60}$-b-$PLLA_{25}$-b-$PDMA_{60}$ and $PLLA_{25}$-b-$PDMA_{120}$ (5 mg mL^{-1}) in (a) methanol and (b) ethanol.....123
Figure 4.2 Normalized octanol-water partition coefficients ($LogP_{oct}$/SA) for oligomeric models based on hexamers (orange bars) and decamers (red bars).....124
Figure 4.3 Homonuclear decoupled ^{1}H spectra of the methine region of (a) $PLLA_{32}$ and (b) $PDLA_{32}$ (500 MHz, $CDCl_3$). Quantitative ^{13}C NMR of (c) $PLLA_{32}$ and (d) $PDLA_{32}$.....125
Figure 4.4 (a) ^{1}H NMR spectrum of CTA-$PDLA_{32}$-CTA (400 MHz, $CDCl_3$). (b) SEC analysis of CTA-$PDLA_{32}$-CTA (DMF with 5 mM NH_4BF_4).....126
Figure 4.5 ^{1}H NMR spectrum (400 MHz, d_6-DMSO) of $PHEAAm_{92}$-b-$PDLA_{32}$-b-$PHEAAm_{92}$.....127
Figure 4.6 SEC traces of copolymers (a) **L1-L4** and (b) **D1-D4** from refractive index signals (DMF with 5 mM NH_4BF_4). 128
Figure 4.7 TEM micrographs of copolymers assembled in methanol 5 mg mL^{-1} at room temperature (25 ℃) for two days: (a) **SA-L1,** (b) **SA-L2**, (c) **SA-L3**, (d) **SA-L4**, (e) **SA-D1**, (f) **SA-D2**, (g) **SA-D3** and (h) **SA-D4**. Samples were negatively stained using uranyl acetate (0.5 wt %). Scale bar = 1 μm. 130
Figure 4.8 TEM micrographs of assemblies **SA-L1** and **SA-L2** after aging for one month. Samples were negatively stained using uranyl acetate (0.5 wt %). Scale bar = 1 μm. 131
Figure 4.9 TEM micrographs of the cylindrical assemblies (a) **SA-L1** and (b) **SA-L2**. (c) Image showing the resulting morphology after mixing the enantiomer pure cylinders for one day at body temperature. Samples were negatively stained using uranyl acetate (0.5 wt %). Scale bar = 1 μm. 132
Figure 4.10 TEM micrographs of the mixed assembly solution **SA-L1** and **SA-D1** after aging at 37 ℃ for (a) 0 h, (b) 2 h, (c) 5 h, (d) 8 h and (e) 24 h. (f) Homo-chiral micelles **SA-L1** aged at body temperature (37 ℃) for 24 h. Samples were negatively stained using uranyl acetate (0.5 wt %). 133
Figure 4.11 The mixed assembly solution **SA-L1** and **SA-D1** after sonication was aged at body temperature (37 ℃) and monitored at different time interval: (a) FTIR spectra revealed that the wavenumber of the carbonyl group vibration of PLA shifted from 1758 to 1750 cm^{-1} over time during the morphological transition process. (b) Quantification of the transformation process by FTIR. 134
Figure 4.12 The mixed assembly solution **SA-L1** and **SA-D1** after sonication was aged at body temperature (37 ℃). WAXD diffractograms evidenced the appearance of stereocomplex Bragg peak at a 2θ value of 12° and 23.8° and the disappearance of homochiral Bragg peak at a 2θ value of 16.6° after aging for 24 hours. 135
Figure 4.13 (a) TEM micrographs of aggregated worm-like structures obtained after mixing polymers **L1** and **D1** at body temperature (37 ℃) in methanol. (b) TEM images of aggregated worm-like structures obtained after mixing micelles **SA-L1** and **SA-D1** at 37 ℃ in methanol. Samples were negatively stained using uranyl acetate (0.5 wt %). (c) Schematic representation of the formation of the new morphology triggered by sterecomplexation. 137

Figure 4.14 TEM micrographs of the mixed assembly solution **SA-L3** and **SA-D3** after aging at 37 ℃ in methanol for (a) 0 h, (b) 3 d, and (c) 7 d. Samples were negatively stained using uranyl acetate (0.5 wt %). (d) FTIR spectra revealed that the wavenumber of the carbonyl group vibration of PLA shifted from 1758 to 1750 cm^{-1} over time during the morphological transition process. 139
Figure 4.15 TEM micrographs of the mixed assembly solution **SA-L2** and **SA-D2** after aging at 37 ℃ in methanol for (a) 0 h, (b) 2 h, and (c) 1 d. Samples were negatively stained using uranyl acetate (0.5 wt %). (d) FTIR spectra revealed that the wavenumber of the carbonyl group vibration of PLA shifted from 1758 to 1750 cm^{-1} over time during the morphological transition process. 141
Figure 4.16 TEM micrographs of the mixed assembly solution **SA-L1** and **SA-D1** after aging at room temperature (25 ℃) in methanol for (a) 4 d, (b) 9 d, and (c) 20 d. Samples were negatively stained using uranyl acetate (0.5 wt %). Samples were negatively stained using uranyl acetate (0.5 wt %). (d) FTIR spectra revealed that the wavenumber of the carbonyl group vibration of PLA shifted from 1758 to 1750 cm^{-1} over time during the morphological transition process. 142
Figure 4.17 TEM micrographs of cylindrical micelles from polymer (a) $PDMA_{45}$-b-$PLLA_{32}$-b-$PDMA_{45}$ and (b) $PDMA_{50}$-b-$PDLA_{32}$-b-$PDMA_{50}$ as prepared. They were mixed at body temperature (37 ℃) in methanol and aged for 7 days before another analysis (c). Samples were negatively stained using uranyl acetate (0.5 wt %). (d) FTIR spectra of the mixture assembly solution (37 ℃, MeOH) after 7 d. 144
Figure 4.18 TEM micrographs of the assemblies **SA-L1** in methanol (a) and after being transferred to water, which resulted in an aggregated morphology (b). Samples were negatively stained using uranyl acetate (0.5 wt %). 145
Figure 4.19 ^1H NMR spectra (400 MHz, $CDCl_3$) of (a) $PMMA_4$-b-$PLLA_{32}$-b-$PMMA_4$, (b) $PMMA_{10}$-b-$PLLA_{32}$-b-$PMMA_{10}$, (c) $PMMA_3$-b-$PDLA_{32}$-b-$PMMA_3$ and (d) $PMMA_9$-b-$PDLA_{32}$-b-$PMMA_9$. 146
Figure 4.20 SEC analysis (DMF with 5 mM NH_4BF_4) of copolymers (a) $PMMA_4$-b-$PLLA_{32}$-b-$PMMA_4$, (b) $PMMA_{10}$-b-$PLLA_{32}$-b-$PMMA_{10}$, (c) $PMMA_3$-b-$PDLA_{32}$-b-$PMMA_3$ and (d) $PMMA_9$-b-$PDLA_{32}$-b-$PMMA_9$. 147
Figure 4.21 ^1H NMR spectra (400 MHz, $CDCl_3$) of (a) $PBuA_{14}$-b-$PLLA_{32}$-b-$PBuA_{14}$, (b) $PBuA_4$-b-$PLLA_{32}$-b-$PBuA_4$, (c) $PBuA_{13}$-b-$PDLA_{32}$-b-$PBuA_{13}$ and (d) $PBuA_6$-b-$PDLA_{32}$-b- $PBuA_6$. 148
Figure 4.22 SEC analysis (DMF with 5 mM NH_4BF_4) of copolymers (a) $PBuA_{14}$-b-$PLLA_{32}$-b-$PBuA_{14}$, (b) $PBuA_4$-b-$PLLA_{32}$-b-$PBuA_4$, (c) $PBuA_{13}$-b-$PDLA_{32}$-b-$PBuA_{13}$ and (d) $PBuA_6$-b-$PDLA_{32}$-b- $PBuA_6$. 148
Figure 4.23 ^1H NMR spectra (400 MHz, d_6-DMSO) of (a) $PHEAAm_{100}$-b-$PBuA_{14}$-b-$PLLA_{32}$-b-$PBuA_{14}$-b-$PHEAAm_{100}$ and (b) $PHEAAm_{93}$-b-$PBuA_{13}$-b-$PDLA_{32}$-b-$PBuA_{13}$-b-$PHEAAm_{93}$. 149
Figure 4.24 SEC analysis (DMF with 5 mM NH_4BF_4) of copolymers (a) $PHEAAm_{100}$-b-$PBuA_{14}$-b-$PLLA_{32}$-b-$PBuA_{14}$-b-$PHEAAm_{100}$ and (b) $PHEAAm_{93}$-b-$PBuA_{13}$-b-$PDLA_{32}$-b-$PBuA_{13}$-b-$PHEAAm_{93}$. 150
Figure 4.25 Removal of the trithiocarbonate group using EPHP and AIBN. UV-vis (309 nm) and RI SEC traces of a) polymer **L5** and b) polymer **D5**. TEM micrographs of the micelles c) **SA-L5** and d) **SA-D5**. Samples were negatively stained using uranyl acetate (0.5 wt %). 152

Figure 4.26 Assemblies **SA-L5** in methanol were transferred to an aqueous solution and characterised by DLS: (a) Correlation coefficient function of the nanoparticles in methanol and water. (b) Size distribution by intensity of the assemblies in methanol and water. 153
Figure 4.27 Schematic representation showing the corona conformation of the assemblies derived from $PHEAAm_y$-b-$PL(D)LA_x$-b-$PHEAAm_y$ in methanol and water. 154
Figure 4.28 TEM micrographs of the mixed assembly solution **SA-L5** and **SA-D5** after aging at 37 ℃ in methanol for (a) 0 d, (b) 1 d, and (c) 4 d. Samples were negatively stained using uranyl acetate (0.5 wt %). (d) FTIR spectra of the mixture assemblies over time. 155
Figure 4.29 Cylindrical micelles **SA-L5** and **SA-D5** were mixed together and aged under different conditions (**Test 1-6, Table 4.3**). TEM micrographs of the assemblies after four days of aging: (a) **Test 1**, (b) **Test 2**, (c) **Test 3**, (d) **Test 4**, (e) **Test 5**, and (f) **Test 6**. Samples were negatively stained using uranyl acetate (0.5 wt %). (g) FTIR spectra of mixture assemblies **Test 1-6** after aging for 4 days. 157
Figure 4.30 (a) ^{1}H NMR ($CDCl_3$, 400 MHz) spectrum of polymer **L6**. (b) SEC analysis of polymer **L6** (DMF with 5 mM NH_4BF_4). 159
Figure 4.31 TEM micrographs of assemblies **SA-L6** in methanol (a) and water (c). Assemblies **SA-D6** in methanol (b) and water (d). Samples were negatively stained using uranyl acetate (0.5 wt %). 160
Figure 4.32 Micelles **SA-L6** and **SA-D6** were mixed at body temperature (37 ℃) in water for 4 days before analysis. (a) TEM image of the micelles. Samples were negatively stained using uranyl acetate (0.5 wt %). (b) FTIR spectra of the mixture assembly solution. 161

Figure 5.1 ^{1}H NMR spectrum (400MHz, $CDCl_3$) of the reaction mixture of PCL polymerisation initiated by 1, 3-propanediol and catalysed by DPP. 176
Figure 5.2 Ring-opening polymerisation of ε-caprolactone with initiator 1, 3-propanediol. First order kinetics of ε-CL consumption with linear fit. 176
Figure 5.3 SEC chromatogram (DMF with 5 mM NH_4BF_4) of PCL polymerised in different solvents (benzene and chloroform). 177
Figure 5.4 ^{1}H NMR spectra (400MHz, $CDCl_3$) of PCL_{60} (a), PCL_{40} (b) and PCL_{30} (c). 178
Figure 5.5 SEC chromatograms (DMF with 5 mM NH_4BF_4) of PCL_{30}, PCL_{40} and PCL_{60}. Signals were collected from RI detectors. 178
Figure 5.6 MALDI-ToF MS spectrum of homopolymer PCL_{40} showing minimal no transesterification. 179
Figure 5.7 ^{1}H NMR spectra (400 MHz, $CDCl_3$) of PCL_{30}-CTA (a), PCL_{40}-CTA (b), and PCL_{60}-CTA (c). 181
Figure 5.8 SEC chromatograms (DMF with 5 mM NH_4BF_4) of PCL_{30}-CTA (a), PCL_{40}-CTA (b) and PCL_{60}-CTA (c). 181
Figure 5.9 ^{1}H NMR spectrum (400 MHz, $CDCl_3$) of $PDMA_{150}$-b-PCL_{30}-b-$PDMA_{150}$. 182
Figure 5.10 Overlaid SEC chromatograms (DMF with 5 mM NH_4BF_4) of different PCL homopolymers and copolymers. a) Macro-CTA PCL_{30} and triblock copolymers

T1-T3. b) Macro-initiator PCL_{40} and triblock copolymers **T4-T6**. c) Macro-initiator PCL_{60} and triblock copolymers **T7-T9**. 183
Figure 5.11 ^{1}H-DOSY NMR spectrum (500 MHz, $CDCl_3$) of triblock copolymer $PDMA_{150}$-b-PCL_{30}-b-$PDMA_{150}$ in $CDCl_3$ at 298 K. 184
Figure 5.12 TEM micrographs of the micelles achieved from polymer **T5** in (a) methanol, (b) ethanol, (c) 1-propanol and (d) 1-butanol at room temperature aging for 2 d. Samples were negatively stained using uranyl acetate (0.5 wt %). 186
Figure 5.13 TEM micrographs of the micelles achieved from polymer **T5** in (a) 100 vol % methanol, (b) 80 vol % methanol and 20% water, (c) 70 vol % methanol and 30% water and (d) 60 vol % methanol and 40% water at room temperature. Samples were negatively stained using uranyl acetate (0.5 wt %). 187
Figure 5.14 TEM micrographs of the micelles achieved from polymer **T5** in methanol at different polymer concentration: (a) 0.5 mg mL^{-1} (b) 5 mg mL^{-1}, (c) 20 mg mL^{-1} at room temperature. Samples were negatively stained using uranyl acetate (0.5 wt %). 188
Figure 5.15 TEM micrographs of the micelles achieved from polymer **T5** in methanol at room temperature: (a) 10 min (b) 30 min (c) 3 h. Samples were negatively stained using uranyl acetate (0.5 wt %). 189
Figure 5.16 TEM micrographs of the micelles achieved from polymer **T4** and **T6** in methanol at room temperature: (a) polymer **T4,** 3 h (b) polymer **T4,** 3 h (c) polymer **T6,** 1 d. (d) polymer **T6,** 1 d. Samples were negatively stained using uranyl acetate (0.5 wt %). 190
Figure 5.17 Schematic representation of the preparation of crystalline micelles by PDMA-*b*-PCL-*b*-PDMA triblock copolymer. 191
Figure 5.18 a) Correlation coefficient function of polymer **T5** assemblies in situ with a measurement interval of 5 min. b) Size distribution by intensity with the same time period. 193
Figure 5.19 TEM micrographs of the micelles obtained from polymers PDMA-*b*-PCL-*b*-PDMA: (a) **T9**, (b) **T8**, (c) **T7**, (d) **T6**, (e) **T5**, (f) **T4**, (g) **T3**, (h) **T2** and (i) **T1**. Samples were negatively stained using uranyl acetate (0.5 wt %). Scale bar = 0.5 µm. (j) Phase diagram constructed for PDMA-*b*-PCL-*b*-PDMA triblock terpolymers. 195
Figure 5.20 Histograms of the lengths of PDMA-*b*-PCL-*b*-PDMA cylindrical micelles, a) **T1**, b) **T2**, c) **T3**, d) **T4** and e) **T5** as determined by TEM analysis. 198
Figure 5.21 TEM analysis of $PDMA_{302}$-b-PCL_{60}-b-$PDMA_{302}$ self-assembled in methanol at 5 mg mL^{-1} following heating at (a) 25 ℃ (b) 30 ℃ (c) 35 ℃ and (d) 70 ℃ for 4 hours before cooling down in 25 ℃ and aging for two days. Samples were negatively stained using uranyl acetate (0.5 wt %). Histograms of the lengths of the samples aging at (e) 30 ℃ and (f) 35 ℃. 199
Figure 5.22 TEM analysis of $PDMA_{302}$-b-PCL_{60}-b-$PDMA_{302}$ self-assembled in a) 100% methanol b) 96% methanol + 4% THF c) 90% methanol + 10% THF 5 mg mL^{-1} at room temperature and for 2 d. Samples were negatively stained using uranyl acetate (0.5 wt %). Histograms of the lengths of the samples aging in (d) 4% THF and (e) 10% THF. 200
Figure 5.23 Schematic representation of the preparation of near monodisperse fibres by self-seeding method. 201

List of Schemes

Scheme 1.1 Schematic representation for the NMP activation/deactivation equilibrium.[3] 3
Scheme 1.2 Schematic representation for the ATRP equilibrium.[3].....4
Scheme 1.3 The mechanism of RAFT polymerisation.....5
Scheme 1.4 Coordination-insertion mechanism for the synthesis of a polyester via metal-catalysed ROP.[22] 10
Scheme 1.5 Schematic representation for the mechanism of ROP using a metal-free organocatalyst.[26].....11
Scheme 1.6 Schematic representation for the mechanism for the ROP of lactone using a DPP catalyst.[28] 11

Scheme 2.1 Ring-opening polymerisation of L-lactide.....47
Scheme 2.2 Synthesis of RAFT agent DDMAT. 51
Scheme 2.3 Coupling of the RAFT agent DDMAT to PLLA.....52

Scheme 3.1 Synthetic route for the preparation of PHEA-b-PLLA-b-PHEA, P4VP-b-PLLA-b-P4VP and PNAM-b-PLLA-b-PNAM triblock copolymers. 87
Scheme 3.2 Schematic representation of the process of epitaxial growth of unimer on seeds with different block lengths.....103

Scheme 4.1 Modification of the RAFT end group of polymers **L1** and **D1** with 1-Ethylpiperidine hypophosphite (EPHP).....151
Scheme 4.2 Modification of the RAFT end group of **L1** and **D1** block copolymers with a tertiary amine group. 158

Scheme 5.1 Ring-opening polymerisation of ε-caprolactone.....175
Scheme 5.2 Coupling reaction of the RAFT DDMAT to PCL homopolymer.....180

List of Tables

Table 2.1 Characterisation data of PLLA. The M_n determined by SEC is on the basis of polymer hydrodynamic volume of the polymer, the deviation mainly caused by the difference of the polymer PLLA from the standard calibration polymer PMMA. 49
Table 2.2 Characterisation data of PDMA-b-PLLA-b-PDMA triblock copolymers and PLLA-b-PDMA diblock copolymers [§]. 56
Table 2.3 DLS analysis of micelles from triblock copolymers PDMA-b-PLLA-b-PDMA. 59

Table 3.1 Characterisation data of PXX-b-PLLA-b-PXX ABA type triblock copolymers. 89
Table 3.2 Length distribution for cylinders formed upon sonication of cylindrical micelles (polymer **4**) at 0 ℃ using a sonic probe.....93
Table 3.3 Length dispersity of cylinders formed upon epitaxial growth of $PDMA_{75}$-b-$PLLA_{50}$-b-$PDMA_{75}$ (polymer **4**) cylindrical micelles.....100

Table 4.1 $PHEAAm_y$-b-$PL(D)LA_x$-b-$PHEAAm_y$ triblock copolymers prepared with varying core and corona lengths. 128
Table 4.2 The RAFT end group of polymers **L1** and **D1** was modified into different functionalities to yield new polymers. 152
Table 4.3 Morphological transition tests performed with assemblies **SA-L5** and **SA-D5** applying different experimental conditions.....156

Table 5.1 Properties of the triblock copolymer $PDMA_x$-b-PCL_y-b-$PDMA_x$ with varying core and corona lengths. 183
Table 5.2 Characterisation data of cylinder dimensions 197

Chapter 1. Introduction

1.1 Controlled/living radical polymerisation

Synthetic polymers play an essential and ubiquitous role in everyday life and possess many variables that must be considered in order to fabricate robust and useful materials. Apart from the general characteristics such as monomer type and molecular weight, polymer architecture is also of importance with regards to determining the polymer's properties. Precise control over polymer composition can be realised by reversible-deactivation radical polymerisation and living polymerisation methodologies. The discovery of living anionic polymerisation by Szwarc *et al.* represented a significant development for synthetic polymer chemistry,[1] as it enabled the production of well-defined polymers on an industrial scale and allowed the synthesis of complex architectures, e.g. multi-block copolymers. Inspired by the success of living anionic polymerisation, controlled radical polymerisation (CRP) methods have been extensively investigated owing to their potential to overcome the limitations of conventional free radical polymerisation, for instance the short average lifetime of a propagating chain and the large dispersity of the resultant polymers.[2] To successfully impart control over a radical polymerisation, a dynamic equilibrium between propagating radicals and various dormant species is introduced. Radicals can be either reversibly trapped in a deactivation/activation process which relies upon the persistent radical effect, as observed in nitroxide-mediated polymerisation (NMP) and atom-transfer radical polymerisation (ATRP), or an alternative strategy in which a degenerative transfer mechanism is used, as utilised in reversible addition fragmentation chain transfer (RAFT) polymerisation.[3]

NMP, first reported by Georges *et al.*, is centred upon an equilibrium between an activated propagating radical and a deactivated alkoxyamine species (**Scheme 1.1**).[4] Georges reported the use of a 2,2,6,6-tetramethyl-1-piperidynyl-*N*-oxy (TEMPO)-

based system, which employed TEMPO as a persistent stable radical. The persistent stable radical which acts as a control agent by ensuring low levels of free polymeric radicals allows for the synthesis of well-defined polymers. Further research into NMP has been demonstrated by the Hawker group, who have reported the polymerisation of a vast range of monomers using different TEMPO derivatives.[5] Nevertheless, NMP still has limitations; for instance relatively high temperatures are required for the decomposition of the thermally unstable C-O bond,[6] polymer end-group functionality is hard to determine, and the polymerisation of some monomers, e.g. disubstituted alkenes, is hard to control using this technique.[3]

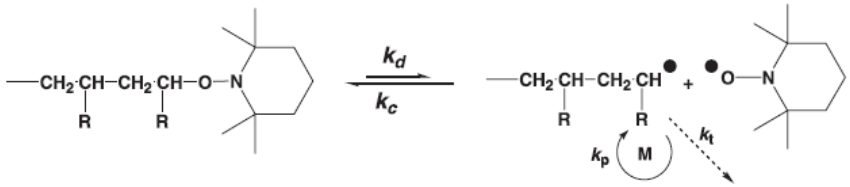

Scheme 1.1 Schematic representation for the NMP activation/deactivation equilibrium.[3]

Proceeding *via* a similar activation/deactivation equilibrium, ATRP is currently one of the most widely investigated CRP techniques.[7] The polymerisation proceeds *via* a reversible-reduction-oxidation reaction between an organic halide (halide-capped dormant polymer chain, P_n-X) and a transition metal complex ($Mt^{n+1}X/L$) (**Scheme 1.2**).[8] ATRP has several advantages, including good retention and facile functionalisation of polymer chain ends, which allows for the formation of copolymers with complex and precise monomer sequences.[9] However, ATRP is not without its disadvantages: the transition metal complex has to be removed from the product polymer which can lead to complex purification procedures, and the metal complex is incompatible with certain monomers which limit their application.[3]

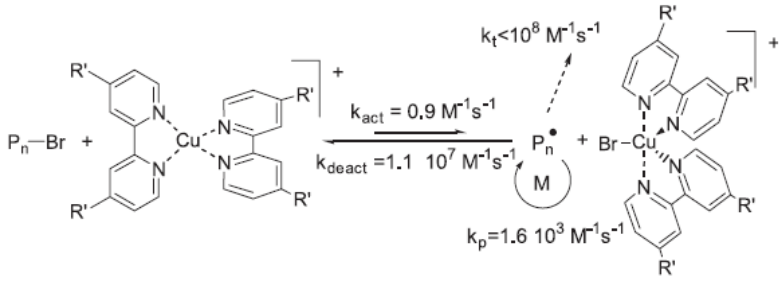

Scheme 1.2 Schematic representation for the ATRP equilibrium.[3]

1.2 RAFT polymerisation

In contrast to ATRP and NMP, RAFT polymerisation is based upon a degenerative transfer mechanism, whereby the presence of a RAFT agent results in the establishment of the RAFT equilibria. The equilibria neither produce nor consume radicals and thus the presence of the RAFT agent ideally has no effect upon the polymerisation kinetics.[10] There are several steps in a RAFT polymerisation: initiation, reversible chain-transfer, reinitiation, chain-equilibration and termination (**Scheme 1.3**).

Initiation: Radicals are produced by thermal decomposition or photolysis, which then proceeds to react with a monomer species to yield a propagating polymeric radical species.

RAFT pre-equilibrium: Polymeric radical reacts with the RAFT agent to form a RAFT intermediate radical, which can undergo further fragmentation to either yield the starting materials or a polymeric RAFT agent, specifically a growing macro chain transfer agent (macroCTA), and a CTA-derived radical (R•).

Reinitiation: CTA-derived radical then reacts with further monomers producing more polymeric radicals.

RAFT main equilibration: Polymeric radicals rapidly undergo chain transfer reactions *via* the formation of an intermediate RAFT agent derived radical species and thus the active propagating radical concentration is kept low. Therefore, bimolecular termination events are minimised and the symmetrical nature of the RAFT agent derived intermediate species allows for propagating polymeric chains equal chance to propagate resulting in a narrow molecular weight distribution.

Termination: Two polymer radicals react with each other leading to "dead" polymer chains by disproportionation or recombination which are not able to propagate any further.

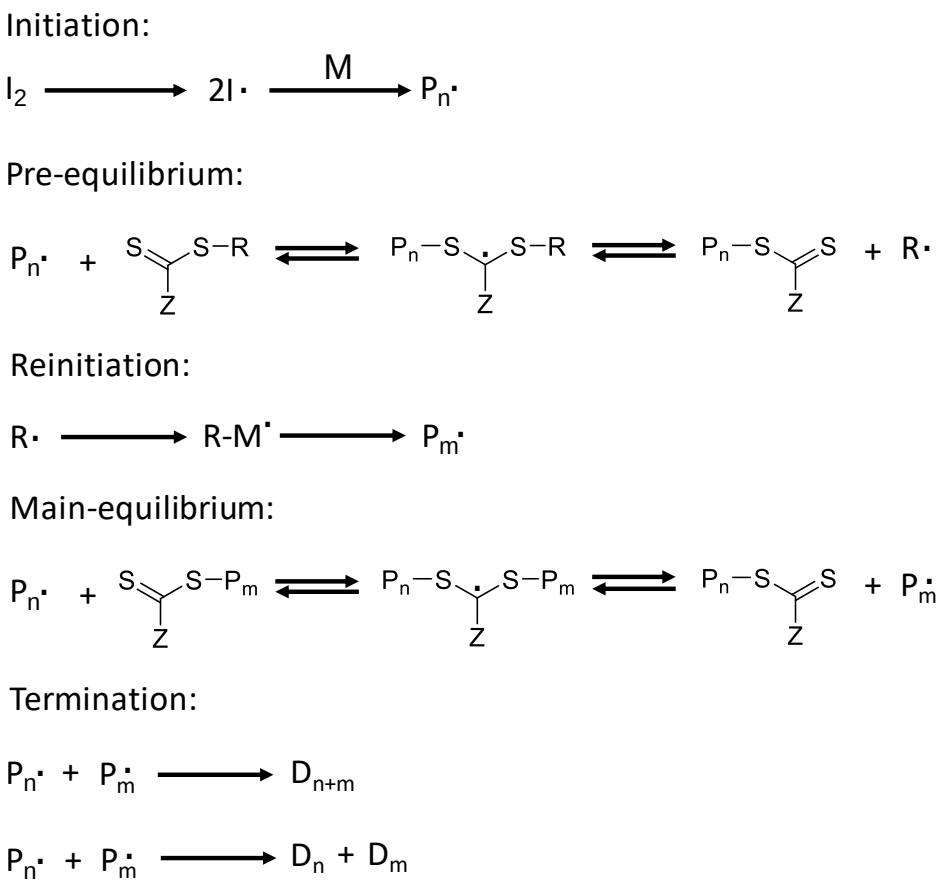

Scheme 1.3 The mechanism of RAFT polymerisation.

Selection of the Z and R groups of the thiocarbonylthio compound has a strong effect upon the RAFT agent by controlling the addition and fragmentation rates of the polymerisation. The choice of Z group has a great impact upon the electron density of the thiocarbonylthio group and thus its reactivity toward propagating radicals. Electron donating groups such as Z = -$N(Et)_2$ tend to reduce the reactivity of the thiocarbonyl bond towards radical addition whereas electron withdrawing, or more weakly electron donating groups, e.g. Z = -Ph accelerate the rate of addition for the propagating radicals.[11] Four main types of RAFT agent have been reported based on the nature of the Z group (**Figure 1.1**), trithiocarbonates, xanthates, dithioesters, dithiocarbamates.[10, 12]

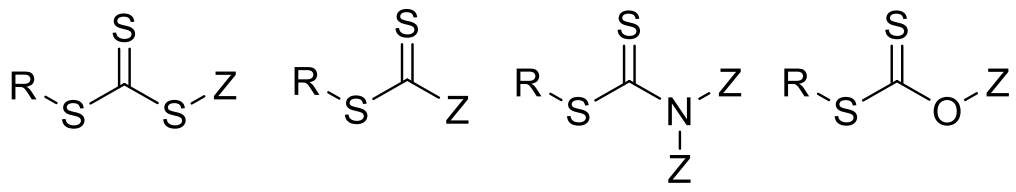

Figure 1.1 Schematic representation of the four main types of RAFT agent.

More activated monomers such as acrylamides and acrylates require more active RAFT agents e.g. trithiocarbonates to ensure a sufficient addition rate towards the propagating radicals, which helps to control the concentration of active radicals and *vice versa* for less activated monomers. The mismatch of the monomer reactivity and RAFT agent would either lead to polymerisation retardation or leads to a loss of control. The nature of the R group is also of great importance in the RAFT polymerisation process, as the R group is required to be a good leaving group whilst also effective at reinitiating the polymerisation. Guidelines for the selection of the RAFT agent with the correct R and Z group with regards to the monomer class are

summarised in **Figure 1.2**.[12] Proper selection of the RAFT agent enables the successful controlled polymerisation of a myriad of monomers which makes RAFT polymerisation a versatile and applicable methodology.

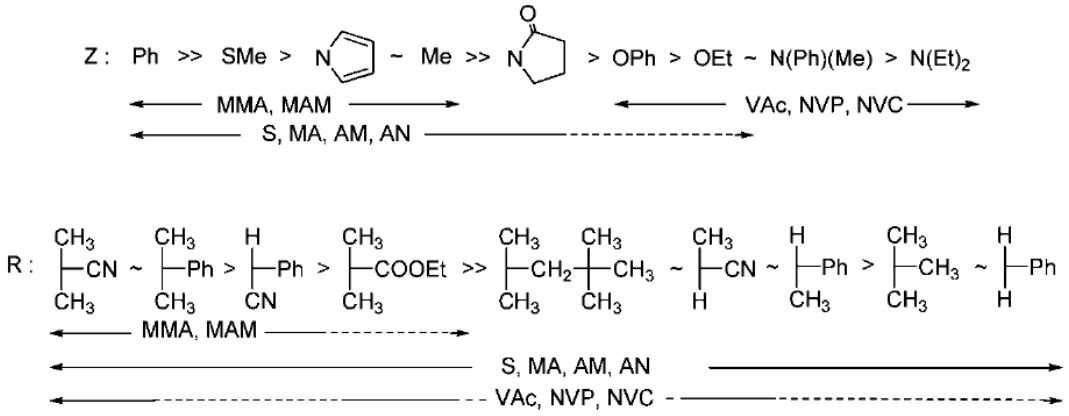

Figure 1.2 Guidelines for the selection of the RAFT agent for various monomer classes. For the Z group, addition rates decrease and fragmentation rates increase from left to right. For the R group, fragmentation rates decrease from left to right. A dashed line indicates partial control.[12]

The thiocarbonylthio functional group located at the ω-chain end of RAFT polymers can easily decompose into malodorous sulphur-containing materials as a consequence of the labile C-S bond. A number of methods such as thermolysis,[13] and radical induced reactions,[14] (reduction and termination) were developed to cleave the RAFT end group providing complete desulphurisation (**Figure 1.3**). One of the most common approaches of end-group modification is to react RAFT-derived polymers with nucleophilic reducing agents e.g. amines, hydroxides, which transforms the thiocarbonylthio group into a free thiol. Subsequently, through thiol-ene click reactions, different functionalities such as acrylate and maleimide derivatives can be conjugated to the polymer backbone under mild conditions which ultimately expands the usage of RAFT-derived polymers for a wide range of applications.[15, 16]

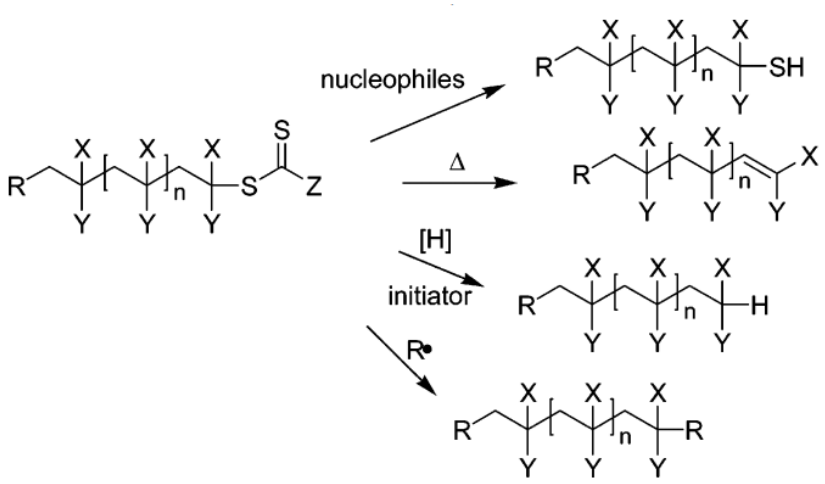

Figure 1.3 Various processes for the end group removal of RAFT derived polymers.[15]

1.3 Ring-opening Polymerisation (ROP)

Aliphatic polyesters, in particular poly(lactide) (PLA) and poly(ε-caprolactone) (PCL), have received significant attention on account of their good biocompatibility and biodegradability. A large amount of research has been conducted to explore their potential applications in tissue engineering,[17, 18] and drug delivery.[19, 20] In order to be used in nanomedicine, it is crucial to design well-defined polyesters with predictable molecular weights, narrow molecular weight distributions and high end-group fidelity. Compared to conventional polycondensations, ROP affords greater polymerisation control and therefore provides a suitable route to achieve this purpose.[21]

Organometallic catalysts such as bis-2-ethylhexanoate (stannous octanoate) have been widely used to control the ROP of cyclic lactone and carbonate monomers by a coordination-insertion mechanism. Specifically, the metal centre coordinates to the carbonyl oxygen first and then the alkoxide undergoes nucleophilic attack of the carbonyl group. After the insertion of the catalyst, the metal alkoxide chain end can

propagate the monomer repeatedly (**Scheme 1.4**).[22] As a consequence of the specific mechanism of organometallic catalysts, the coordination-insertion process can result in inter- and intramolecular transesterification which results in increasing the dispersity of the polymer. Furthermore, the removal of the toxic metal end group is time consuming and expensive which results in adverse effects for biological applications.[23]

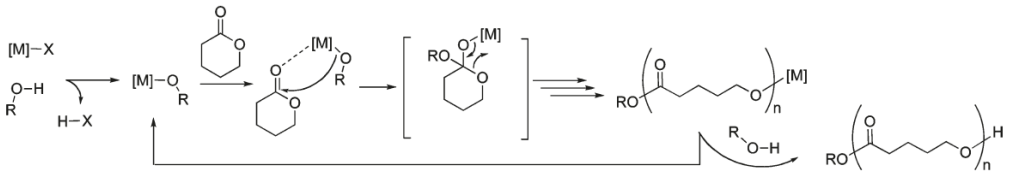

Scheme 1.4 Coordination-insertion mechanism for the synthesis of a polyester *via* metal-catalysed ROP.[22]

In the last two decades, organocatalysts have emerged as an alternative strategy to catalyse the ROP of cyclic lactone and carbonate monomers and offer significant advantages such as simpler preparation methods and reduced sensitivity to water and air in comparison to their metal counterparts.[24, 25] One of the most widely investigated organocatalysts for the ROP of cyclic monomers are bases with the substructure amidine or guanidine, e.g. 1,8-diazabicyclo(5.4.0)undec-7-ene (DBU). In order to minimise the potential transesterification side reactions and avoid the racemisation in the ROP process, a catalytic system with lower activity, thiourea-based bifunctional organocatalysts, was designed by Dove *et.al*. The carbonyl group in lactide could be activated by a thiourea compound through hydrogen bonding between the urea and lactide carbonyl when the initiating alcohol was activated by tertiary amines (**Scheme 1.5**).[26] In a subsequent study, it was reported that the tertiary amine structure linked to

the thiourea could be replaced by other bases such as DBU or (-)-sparteine, whilst still maintaining control over the ROP process.[27]

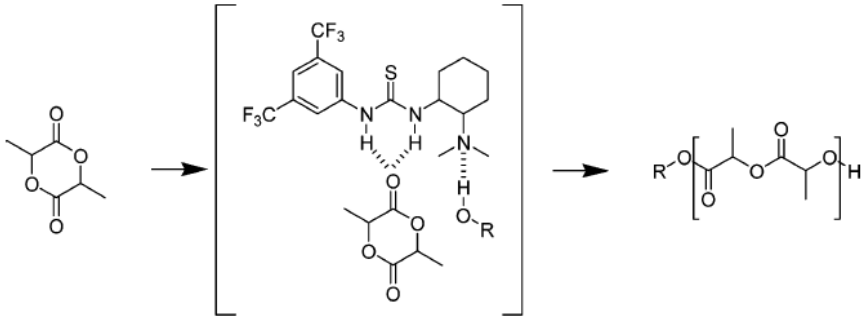

Scheme 1.5 Schematic representation for the mechanism of ROP using a metal-free organocatalyst.[26]

Brønsted acids were also shown to catalyse the ROP of cyclic esters, for instance Kakuchi *et al.* used diphenyl phosphate (DPP) as an efficient cationic organocatalyst for the controlled ring-opening polymerisation of δ-valerolactone and ε-caprolactone (**Scheme 1.6**).[28] DPP is not only commercially available, but also demonstrates low toxicity and high chemical stability which in general simplifies the reaction conditions.

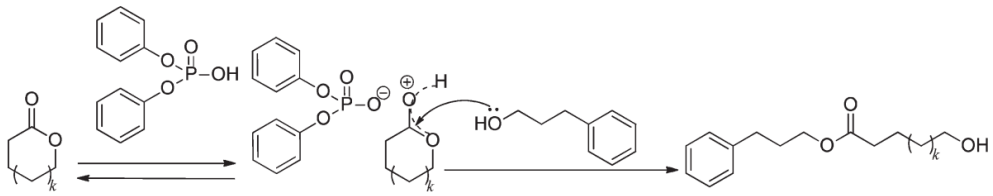

Scheme 1.6 Schematic representation for the mechanism for the ROP of lactone using a DPP catalyst.[28]

1.4 Self-assembly of coil-coil block copolymers in solution

Block copolymers are defined as macromolecules consisting of two or more chemically different polymer segments connected by a covalent linkage. In solution, amphiphilic block copolymers can self-assemble to minimise unfavourable

interactions between the solvophobic block and the solvent.[29] In a typical coil-coil block copolymer system, the resultant morphology is mainly controlled by the degree of repulsion amongst the coronal block, chain stretching of the core block segments and the interfacial tension between the core and the solvent.[30] Any contribution that influence these three main factors such as the polymer composition,[31] and self-assembly conditions such as solvent, [32, 33] temperature,[32] and salt concentration can affect the resultant assembly morphology.[29, 33] A dimensionless 'packing parameter', *p*, is defined in Equation (1), to predict the potential structure of self-assemblies:

$$p = \frac{v}{a_o l_c} \quad \text{(Equation 1)}$$

Where v is the volume of the hydrophobic chain, a_o is the optimal area of the head group and l_c is the length of the hydrophobic block. As a general rule, spherical micelles are formed if $p < ⅓$, if $⅓ < p \leq ½$ cylindrical micelles are observed, and if $½ < p \leq 1$ vesicles are formed (**Figure 1.4**).

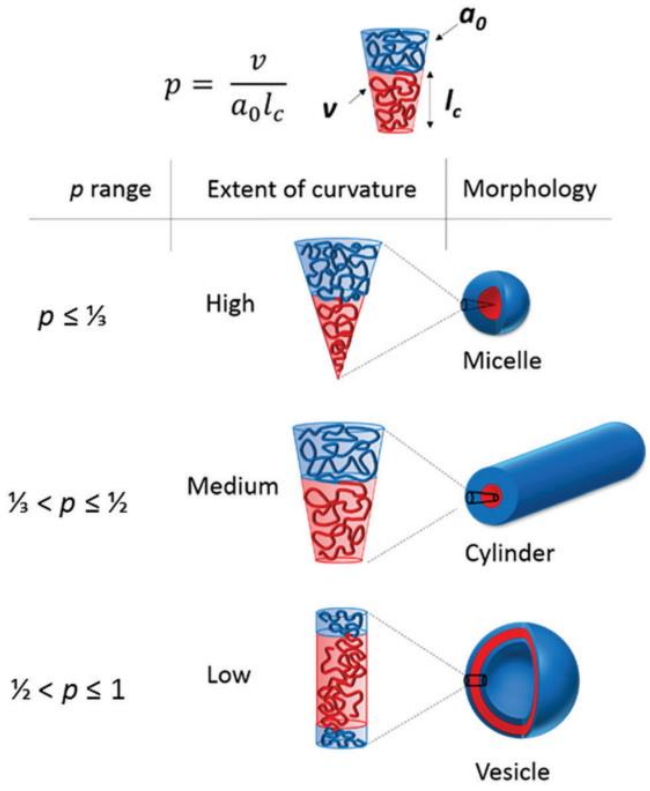

Figure 1.4 Different self-assembled structures obtained by targeting different packing parameter values, *p*.[34]

Similar to surfactant molecules in solution spherical micelles, obtained in the smallest packing parameter area, are the most widely investigated self-assembled morphology and thus are the most commonly studied nanostructures.[35, 36] To form spherical micelles, the weight fraction of the solvophilic block is normally larger than the solvophobic block.

Access to cylindrical micelles can be difficult in theory, as the packing parameter is constrained to a narrow ($⅓ < p \leq ½$) region. The resultant self-assemblies are often contaminated with mixed morphologies such as spherical micelles and vesicles. Despite the difficulty in preparing pure cylinders, a few examples from the literature have demonstrated their potential in biomedical applications. For instance, anisotropic

cylinders have exhibited altered cell internalisation pathways and longer *in vivo* circulation times in comparison to their spherical counterparts.[37, 38]

The vesicular morphology which has the largest packing parameter exhibits bilayer structures whereby the solvophobic block resides between solvophilic membranes forming hollow polymersomes (**Figure 1.5**). Compared to lipid-based vesicles, block copolymer vesicles demonstrate superior mechanical and physical properties which attract considerable attention in the bio-relevant area. As a well-developed nanoplatform, polymer vesicles have shown a high loading of hydrophilic molecules, a rapid and smart response to various stimuli and diverse functionalities.[39-41]

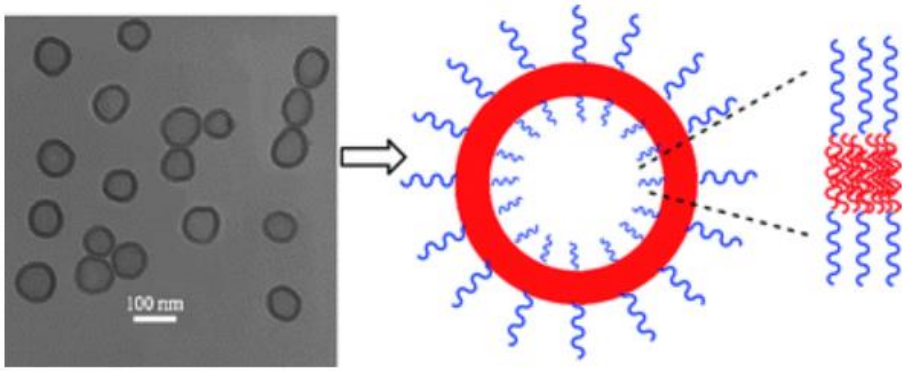

Figure 1.5 Transmission electron microscopy (TEM) image on the left showing the polymer vesicles and a scheme on the right which represents their structure.[42]

1.5 Self-assembly of crystalline-coil block copolymers in solution

Although the majority of research regarding block copolymer self-assembly has been focussed upon coil-coil structures the first reported example of self-assemblies with crystalline cores dates back to the 1960s whereby platelets micelles were formed from poly(ethylene oxide)-*block*-polystyrene (PEO-*b*-PS) diblock copolymers in ethyl benzene.[43] In 1991, Vilgis and Halperin used a chain-folding model to describe the self-assembly of block copolymers into crystalline micelles which provided the theoretical analysis.[44]

In the late 1990s, Winnik and Manners first used an organometallic-inorganic diblock copolymer, poly(ferrocenyldimethylsilane)-*block*-poly(dimethylsiloxane) (PFDMS-*b*-PDMS) to form long rod-like micelles (**Figure 1.6**) in hexane.[45] In a later study by the same group, it was demonstrated that the crystalline nature of the PFDMS block played a pivotal role in the unexpected formation of cylindrical micelles and such self-assembly was defined as cystallisation driven self-assembly (CDSA).[46]

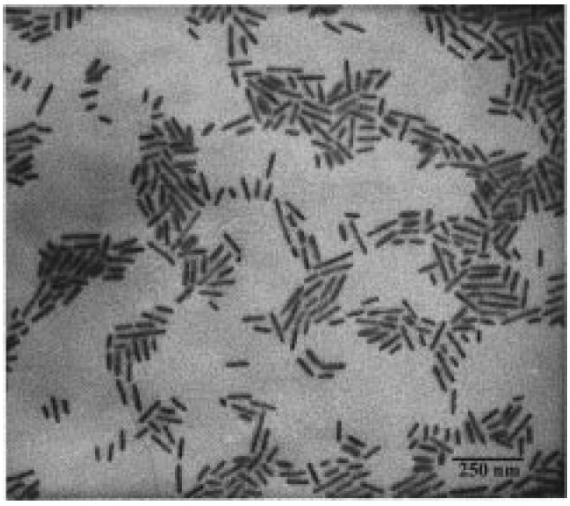

Figure 1.6 Transmission electron micrographs of the cylindrical micelles formed from $PFDMS_{50}$-*b*-$PDMS_{300}$ diblock copolymer.[45]

In contrast to coil-coil block copolymers, it is relatively easy to access cylindrical and lamellar micelles with crystalline-coil compositions *via* a CDSA approach. Apart from the success of PFDMS based block copolymers, more recent examples include block copolymers with PCL,[47] PLA,[48] poly(acrylonitrile),[49] poly(peptoids),[52, 53] and poly(3-hexylthiophene) (P3HT)[50] as core-forming blocks which have been reported to perform CDSA leading to well-defined 1D and 2D micelles.

1.6 Major factors affecting the CDSA process

During the self-assembly process of such crystalline-coil block copolymers, three factors are mainly considered that determine the resultant morphology; the folding of the crystalline core, the repulsion of the soluble corona, and the exposed area of the crystal surface. Reducing the folding amount of the core block is advantageous from an entropic standpoint but this could lead to an increase in entropically unfavourable stretching of the corona block (**Figure 1.7**). Apart from that, the active crystal area prefers to be minimised to lower the free energy of the system. The nanostructures eventually obtained are a result of a balance in terms of these interactions.[51] A range of parameters are reported to affect the core crystallinity and the resultant self-assembly morphologies such as core/coronal block ratio, solvent properties, temperature, etc.

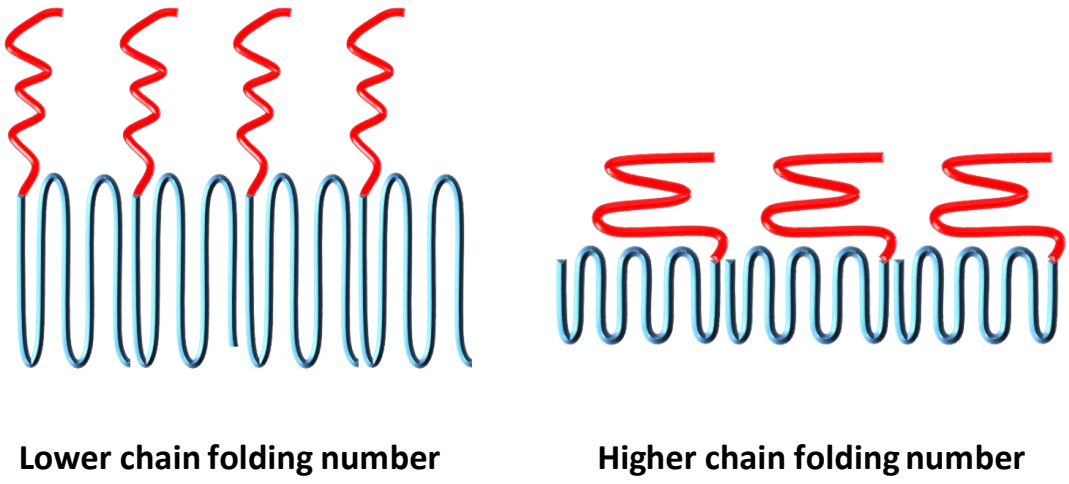

Figure 1.7 Chain-folding model of crystalline-coil diblock copolymers with low and high folding number.

1.6.1 Copolymer composition

Cao *et al.* prepared a series of poly(isoprene)-*block*-PFDMS (PIP-*b*-PFDMS) crystalline-coil block copolymers with various block ratios. They found that block copolymers with larger corona/core ratios favoured the formation of cylindrical morphologies whereas the shorter counterparts resulted in the formation of lamellae (**Figure 1.8**). The soluble corona is stretched to a greater degree in a lamellar structure than in the cylinders and thus polymers with long corona chains prefer to assemble into cylindrical micelles to reduce the energy cost for the corona stretching.[52]

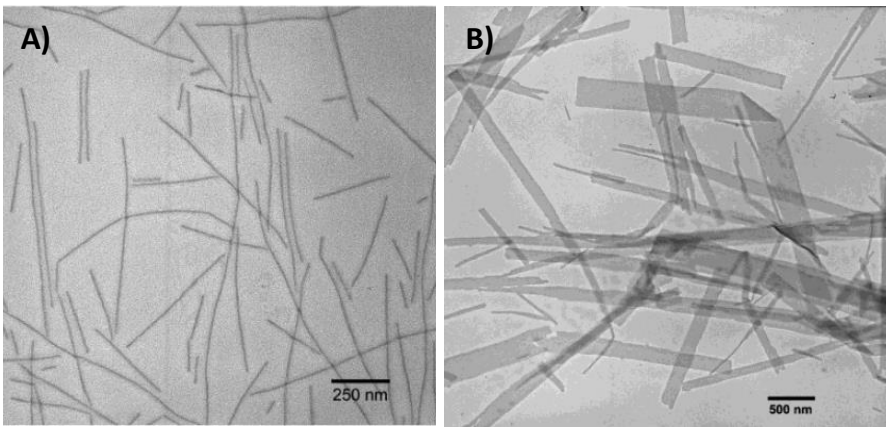

Figure 1.8 Transmission electron micrographs of the aggregates formed by A) PIP_{320}-*b*-$PFDMS_{53}$, and B) PIP_{30}-*b*-$PFDMS_{60}$ in a mixed solvent (Tetrahydrofuran and hexane v/v 2:8).[52]

Although there are many examples that support this trend,[53-55] Inam *et al.* remove the contradictory results in their PLLA-*b*-poly(*N*,*N*-dimethylacryamide) (PLLA-*b*-PDMA) block copolymer system in which diamond-shaped platelets were formed for large corona–core ratios, whilst more elongated and ill-defined structures were formed for smaller block ratios (**Figure 1.9**). This was rationalised by the polymer solubility i.e. polymers with short corona lengths become less soluble which prevent the PLLA chain from adopting a preferred crystal conformation (kinetically trapped) leading to ill-defined crystal structures (cylinders instead of platelets).[56] The overall relationship

between the block ratio and resultant self-assembly morphology appears to be complex, and thus further studies and insight are required to understand these systems.

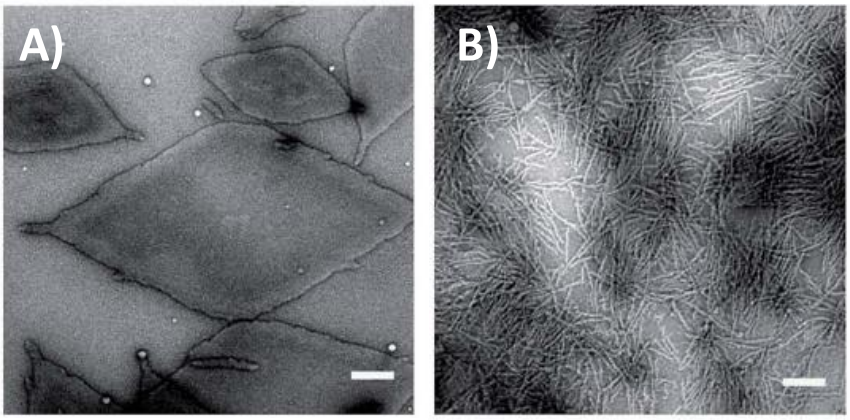

Figure 1.9 Transmission electron micrographs of the aggregates formed by A) $PDMA_{600}$-*b*-$PLLA_{48}$ and B) $PDMA_{150}$-b-$PLLA_{48}$. Samples were self-assembled in ethanol at 90 °C for 8 h and cooled to room temperature. Scale bar = 1 μm.[56]

1.6.2 Solvent condition

Similar to the process of culturing a single crystal, the self-assembly conditions for crystalline-coil block copolymers is chosen to be neither too soluble, in which case the polymer could stabilise as a single polymer chain, nor insoluble to prevent polymer precipitation. The intermediate solubility not only triggers aggregation of the crystalline core-forming block but also enables the polymer chain to pack into a favourable crystal lattice. Therefore, the solvent properties have a significant impact upon the CDSA process. Shen *et al.* assembled PFDMS-*b*-poly(2-vinylpyridine) (PFDMS-*b*-P2VP) diblock copolymers in different alcoholic solvents (methanol, ethanol, 2-propanol). The best solvent according to solubility parameter arguments was 2-propanol which triggered the nucleation and growth of the polymers within a day, whereas the worst solvent methanol showed no evidence of nucleation after aging for one week.[57] Following this work, Hsiao *et.al* reported the use of a mixed solvent system, tetrahydrofuran (THF) and isopropanol (i-PrOH), to self-assemble polymers

PFDMS-*b*-P2VP diblock copolymers. By increasing the solvent ratio of the non-selective good solvent (THF) over the selective solvent (i-PrOH), the self-assembly morphology transformed from amorphous spheres into crystalline cylinders and eventually to lenticular platelets. It was proposed that the non-selective good solvent THF acted as a "plasticiser" to increase the solubility of the crystallisable core block (PFDMS) and therefore facilitate crystallisation.[58] These results were further supported by Schmalz *et al.* for their polyethylene (PE) based triblock copolymers system.[59] It was found that the polymers favoured self-assembling into spherical micelles in a poor solvent (toluene) whereas in THF, a good solvent for molten PE, worm-like morphologies were formed.

1.6.3 Presence of additives

Xu *et al.* carried out a series of investigations to explore the morphological transformation of crystalline micelles by adding additives to the self-assembly solution. For example, PCL-*b*-poly((2-dimethylamino)ethyl methacrylate) (PCL-*b*-PDMAEMA) diblock copolymers were reported to form platelet micelles *via* a CDSA approach and by adding a small amount of organic solvent (0.74% v/v *n*-hexanol) to the self-assembly solution (water), the lamellar structure disassembled into cylinders. It was proposed that *n*-hexanol was able to interrupt the PCL crystal lattice by introducing H-bonding interactions to the crystalline units.[60] Meanwhile, by adding a phenol to PCL-*b*-PEO,[65] or monoamine to PE-*block*-poly(acrylic acid) (PE-*b*-PAA) diblock copolymers,[61] the coronal repulsion in the cylindrical micelles could be reversibly tuned which consequently facilitated the morphological transformation.

Other than that, semicrystalline homopolymers have been found to play a significant role in the CDSA process. Compared to block copolymer chains, which experience restrictions as a consequence of their covalent attachment to an incompatible polymer block, homopolymers crystallise more effectively which normally result in single-crystalline platelets.[62] Therefore, blending homopolymers into the CDSA of block copolymers provides an effective tool for developing the original 1D structure into 2D micelles. For instance, it was found that for a PEO-b-PCL diblock copolymer system in water, co-assembly with a PCL homopolymer can induce a series of morphological changes which mainly evolve the micelles from rods to lamellae by increasing the amount of homopolymer blended into the solution (**Figure 1.10**).[63] Based upon the same concept, there are several studies in which mixed unimers of homopolymer and block copolymers were utilised to transform crystal nuclei into 2D aggregates.[64-67] Interestingly, the added homopolymer can even act as a glue to connect already formed crystalline cylinders to form a micelle network.[68]

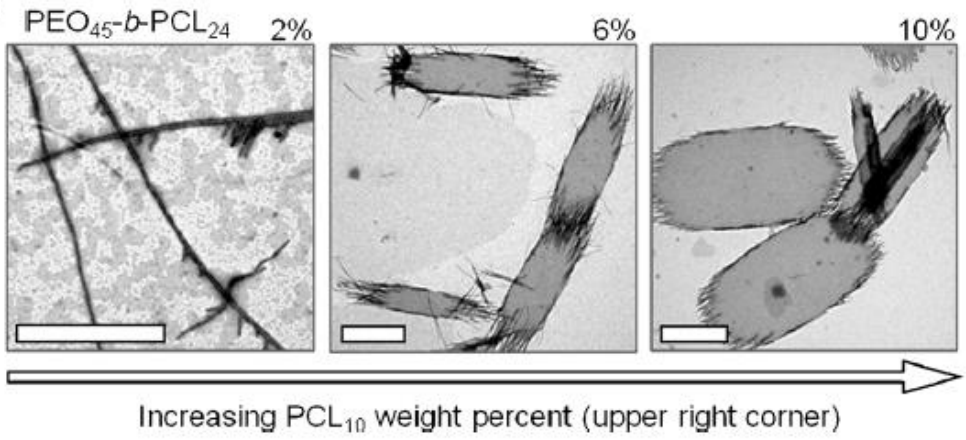

Figure 1.10 Morphological transformations of PEO_{45}-*b*-PCL_{24} diblock copolymers induced by incorporation of a PCL_{10} homopolymer with different varying homopolymer content. Scale bar = 2μm.[63]

1.7 Particle self-assembly methodology

Generally, for amphiphilic coil-coil block copolymers, the solvent switch method is frequently used to prepare self-assemblies.[69, 70] Typically, the block copolymers are initially dissolved in a good solvent e.g. THF or dimethylformamide (DMF) and then a selective solvent, such as water, is slowly added into the self-assembly solution leading to micellisation. This approach is also applicable to a CDSA system whereby semicrystalline cores such as PFDMS,[46] and PCL[71] were reported to fabricate cylinders and lamellae. Apart from that, another self-assembly approach called "spontaneous nucleation" was more commonly used in the field of CDSA.[72] Generally, unimers using an intermediate solvent (in which the solubility of the polymer is between soluble and insoluble) at elevated temperatures and then the solution is cooled down until a nucleus is formed and crystallisation is initiated. An appropriate solvent system is a prerequisite for the success of CDSA. When a solvent cannot meet the specific solubility, a mixed solvent system is required. For instance, P3HT-*b*-PDMS diblock copolymers were assembled in 85% (v/v) Et_2O/toluene,[50] whilst poly(spiro[fluorene-9,5′-[1,3]-dioxan]-2′-one)-*b*-PEO (PFTMC-*b*-PEO) diblock copolymers were assembled in 80% (v/v) MeOH/DMSO to provide well-defined crystalline micelles *via* a CDSA approach.[53]

Although polymer self-assembly exhibits great potential in many fields such as biomedicine,[73] and catalysis,[74] the lengthy polymer preparation process (synthesis, isolation and purification) and low concentration assembly conditions greatly restrict its commercial viability.[75] Charleux and Armes performed pioneering work to combine polymer synthesis and solution self-assembly in a one-pot approach termed polymerisation-induced self-assembly (PISA).[76-79] Take the poly(glycerol

monomethacrylate)-*block*-poly(2-hydroxypropyl methacrylate) (PGMA-*b*-PHPMA) system for example, the water-soluble macro-initiator (PGMA) was used to polymerise the water-soluble monomer HPMA which formed a water-insoluble block at a critical degree of polymerisation and subsequently formed a variety of morphologies *in situ* which were highly concentrated.[80] In this way, polymeric nanoparticles can be produced at much higher solids content without the need for purification of preformed amphiphilic block copolymers.

Borrowing the concept from PISA, the ferrocenyldimethylsilane monomer was reported to be polymerised by a PIP macro-initiator forming an insoluble and semicrystalline PFDMS block which triggered the *in situ* CDSA at the same time. This process was defined as polymerisation-induced (PI)-CDSA by Boote *et al*.[81] By altering the designated block ratio, different self-assembly morphologies (lamellae and cylinders) could be obtained at concentrations up to 25% w/w solids. Significantly, by blending in a small amount of crystalline seeds the sizes of resultant cylinders could be controlled up to 3 μm after the PISA process (**Figure 1.11**).[82] Although a PFDMS functionalised block copolymer is thus far the only reported example of PI-CDSA, the great potential in scalable formation of low disperse samples of cylindrical micelles of controlled length is highly significant and increasing the range of semicrystalline polymer chemistry will no doubt be explored in the near future.

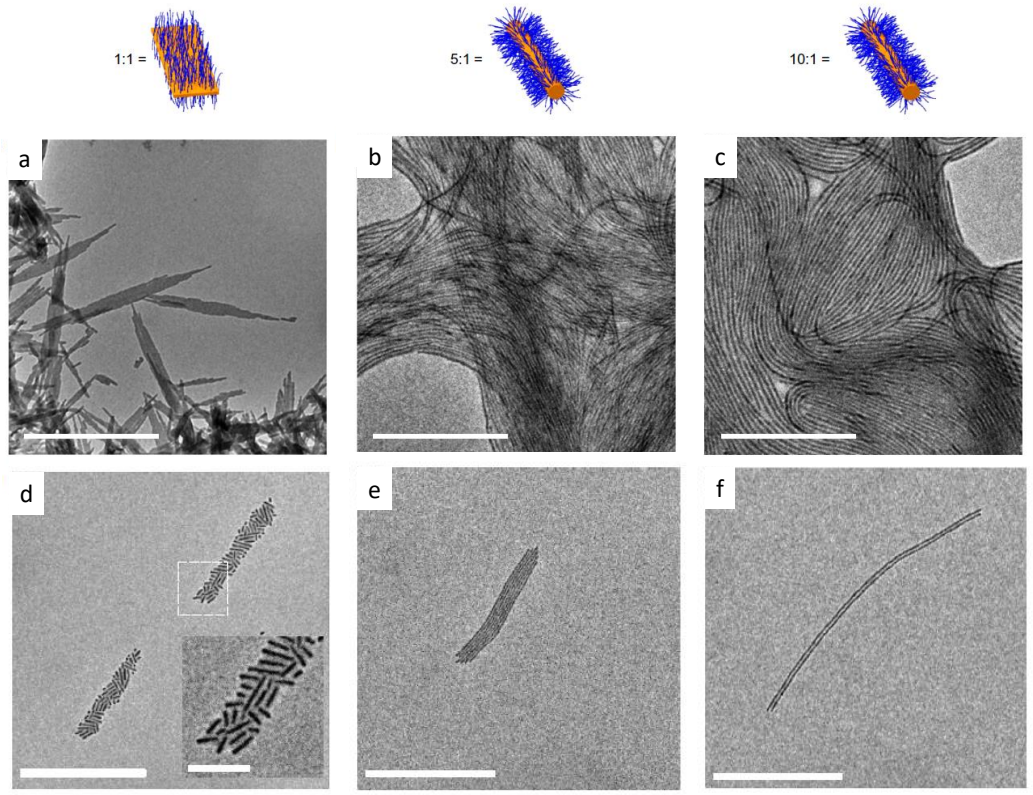

Figure 1.11 PI-CDSA (at 10% w/w solids) of PIP-b-PFDMS diblock copolymers at 10% v/v THF/n-hexanes with varying block ratios. Lenticular platelet micelles were formed for PIP-b-PFDMS BCPs with a targeted block ratio of approximately 1:1 (a) and cylindrical micelles were formed for block ratios of approximately 5:1 (b) and 10:1 (c). Small seeds micelles (d) were blended into the self-assembly solution when the block ratio is fixed at 5:1, whilst when the PIP-to-seed ratio was varied from 6:1 (f) to 18:1 (e), the cylinder length elongated accordingly. Scale bars = 1 μm.[82]

1.8 Living CDSA

Living CDSA was initially defined by Manners and Winnik when their groups discovered that pre-formed crystalline seeds were able to grow epitaxially through the addition of solubilised polymers i.e. unimers.[83] The first example of living CDSA was demonstrated by Wang *et al.* which was based on the classic crystalline-coil PFDMS-*b*-PIP diblock copolymers.[84] The cylinders achieved *via* CDSA were sonicated into truncated crystalline seeds which were later shown to remain active at the ends.[85, 86] By varying the unimer to seeds ratio, the length of the nano-cylinders could be

precisely controlled. Interestingly, the addition of a block copolymer with the same crystalline core but different corona chemistry i.e. PFDMS-*block*-polymethylvinylsiloxane (PFDMS-*b*-PMVS) resulted in BAB type co-micelles with a segmented corona phase on the cylinder surface (**Figure 1.12**). The living CDSA process was analogous to the growth of a living polymerisation and was demonstrated as an efficient tool to construct complex morphologies.

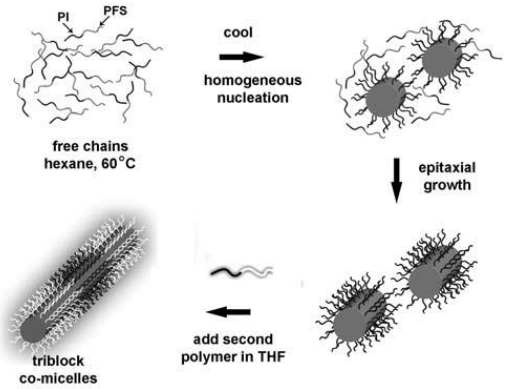

Figure 1.12 Homogeneous nucleation followed by epitaxial growth producing cylindrical micelles with a semicrystalline core and a relatively narrow distribution of lengths. The rod ends remain active to further growth if additional polymer containing a PFDMS block is added to the system.[84]

Except for the BAB co-micelles, non-centrosymmetric cylindrical micelles (ABC type) were also achieved by a unidirectional living CDSA approach. Rupar *et al*. used crystalline seeds (PFS_{60}-*b*-$PDMS_{660}$) to fabricate BAB triblock co-micelles with PIP_{1424}-*b*-$PFDMS_{63}$ unimers by a living CDSA method.[87] The PIP corona was subsequently cross-linked by Karstedt's catalyst which blocked the living crystal facet on the ends of the co-micelles. Next, the co-micelles were solubilised in a good solvent resulting in asymmetrical seeds (PIP_{1424}-*b*-PFS_{63}, with one living end) which were utilised to initiate non-centrosymmetric living CDSA growth which produced ABC triblock co-micelles (**Figure 1.13**).

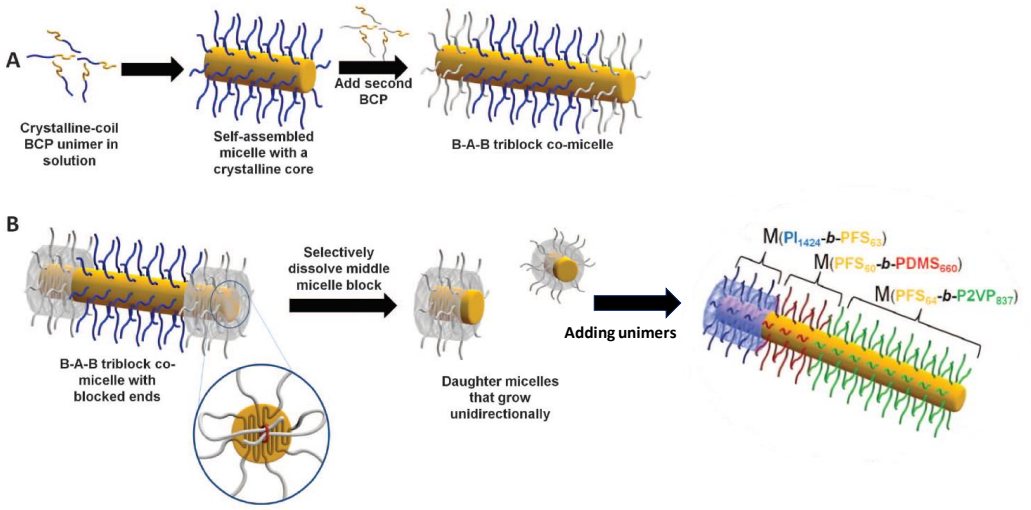

Figure 1.13 (A) Cylindrical micelles were obtained through a CDSA approach. Addition of different crystalline-coil block copolymer unimers leading to the elongation of the micelles. (B) The ends of BAB co-micelles were interfered by crosslinking of the corona, preventing the CDSA at both ends. Then the middle micelles were selectively dissolved forming daughter micelles to initiate non-centrosymmetric living CDSA growth.[87]

Hudson *et al.* demonstrated that living CDSA was not only suitable for well-defined 1D epitaxial growth but also applicable for delicate 2D morphology design.[88] In order to produce the 2D morphologies, Hudson *et al*. performed experiments involving the addition of a series of platelet-forming PFDMS-based block copolymers (BCPs) to short cylindrical crystalline seed micelles. Using a fluorescently-tagged corona block, the concentric 2D structures could be easily visualised (**Figure 1.14**).

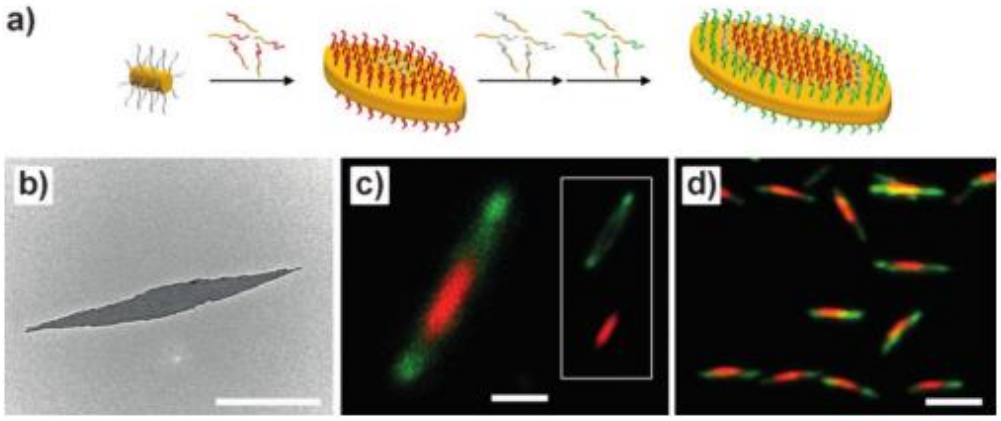

Figure 1.14 (a) Schematic representation for the formation of uniform concentric 2D lenticular platelets; (b) TEM image and (c and d) laser scanning confocal microscopy (LSCM) images of lenticular platelet micelles showing their concentric structure. Scale bars are 500 nm (b and c) and 2 mm (d).[89]

Furthermore, Qiu *et al.* investigated 2D growth methods to fabricate rectangular platelet micelles with controllable size. The sequential addition of different blends to the short seed micelles led to concentric rectangular patches with varied coronal chemistry. Moreover, the selective crosslinking of the corona with subsequent disassembly of the platelet yielded a hollow rectangular morphology (**Figure 1.15**).[67] Therefore, employment of a living CDSA technique demonstrated its outstanding capability to prepare block copolymer micelles with unprecedented complexity.

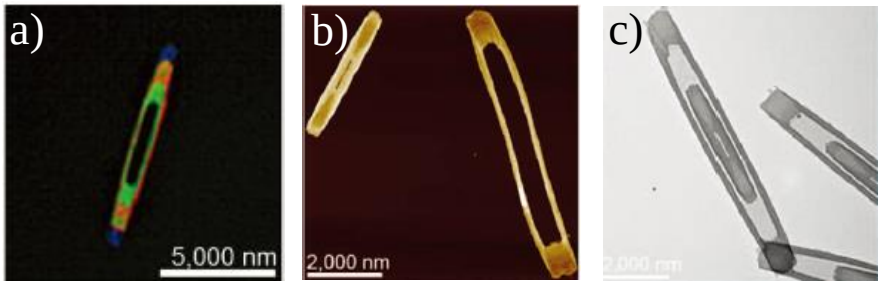

Figure 1.15 (a) LSCM image of a multi-layer lenticular platelet by sequential addition of different block copolymer; (b) atomic force microscopy (AFM) images and (c) TEM images of perforated rectangular platelet micelles and corresponding rectangular ring platelet micelle after crosslinking and subsequent dissolution of the non-crosslinked segment.[67]

Apart from PFDMS-functionalised block copolymers, semicrystalline blocks such as PCL,[90] PLLA,[66] P3HT,[50] and polycarbonate,[53] were also reported to undergo a living CDSA approach resulting in uniform cylindrical or lamellar aggregates.

1.9 Applications of the nanostructures prepared by CDSA

1.9.1 Preparation of supermicelles

By virtue of the living CDSA technique, Qiu *et al.* fabricated amphiphilic P-H-P and H-P-H cylindrical triblock co-micelles with nonpolar (H) or polar (P) segments, in which P represents PFDMS-*b*-P2VP, and H represents PFDMS-*b*-PDMS. These triblock co-micelles acted as a building unit to construct a variety of complex superstructures. With the addition of nonpolar solvent (hexane) to the micelle solution (1:3 (v/v) hexane/iPrOH), building units (co-micelles $P_{145\ nm}$-$H_{110\ nm}$-$P_{145\ nm}$) gradually assembled into single-stranded chains (**Figure 1.16 A**) whereby the end-to-end stacking model was preferred to minimise the interactions between the polar segment (P) and nonpolar solution. The properties of the co-micelle unit could be precisely tuned by altering the length or order of each block segment which in turn could effectively influence the morphology of the resultant supermicelles. For instance, when decane was added into a $P_{50\ nm}$-$H_{190\ nm}$-$P_{50\ nm}$ micelle solution which were shorter terminal segments, an irregular network was formed (**Figure 1.16 C**) whereby the end-to-end interactions were random in direction. These self-assemblies possess multiple levels of structural hierarchy in combination with the fact that they exist on a multi-micrometre length scale.[91] Apart from the amphiphilic interactions, hydrogen bonding interactions were also utilised to fabricate supermicellar structures in a subsequent report.[92]

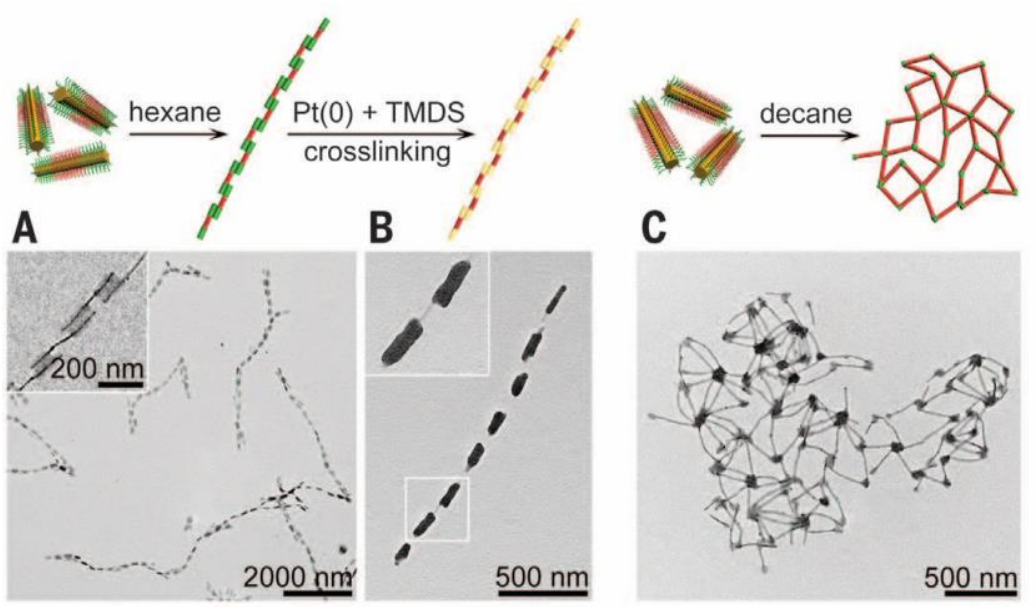

Figure 1.16 Multidimensional superstructures through end-to-end stacking of P-H-P triblock co-micelles characterised by TEM. (**A**) Self-assembly of triblock co-micelles $P_{145\ nm}$-$H_{110\ nm}$-$P_{145\ nm}$ in hexane/iPrOH (H = PFS_{49}-*b*-$PDMS_{504}$, P =PFS_{48}-*b*-$P2VP_{414}$); (**B**) An immobilised chain formed by intermicellar cross-linking of P2VP coronas of stacked terminal segments; and (**C**) Self-assembly of triblock co-micelles $P_{50\ nm}$-$H_{190\ nm}$-$P_{50\ nm}$ by adding decane to hexane/iPrOH**.**[91]

1.9.2 Biological applications

As mentioned in Section 1.4, cylindrical nanoparticles often demonstrate unique behaviour *in vivo* compared to their spherical counterparts. However, in certain cases drug-delivery vectors with cylindrical morphologies were not well understood because of the challenges with respect to their formation and, in particular, the lack of precise control over their dimensions.[93] The CDSA technique facilitates access to cylindrical micelles with a variety of functionality and with precise control. Moreover, there are examples of cylindrical micelles produced from biocompatible semicrystalline polymers such as PCL or PLLA *via* CDSA which have demonstrated their viability as a potential drug-delivery vehicles.[53, 94] For instance, Li *et al.* studied the effect of the shape of glyco-nanoparticles on macrophage cellular uptake and immune response.

The nanostructures were prepared by PLA-*b*-PAA block copolymers whereby PDLLA-*b*-PAA result in the formation of spheres and PLLA-*b*-PAA produced cylinders with crystalline cores. Three different morphologies of nanostructures (spheres, long cylinders and short cylinders) were functionalised with mannose before further interaction with the macrophage. Compared to spheres, cylindrical micelles were uptaken by cells to a lesser degree which was ascribed to the difference in the internalisation pathway. Spheres could access the cell by clathrin- and caveolin-mediated endocytosis whilst cylinders mostly relied on the clathrin-mediated pathway. With regards to the inflammatory response, long cylindrical nanoparticles demonstrated outstanding efficiency in comparison to the other two which provided support for further immunological therapeutic study.[95]

1.9.3 Organic electronics

On account of the low density and solution processability, π-conjugated semiconducting polymers receive extensive attention in the realm of photovoltaics, [96] sensors,[97] etc. The control over the self-assembly morphology is of great importance with respect to their electric performance since grain boundaries and defects would impede efficient charge transport.[98] With the help of living CDSA techniques, fibre-like micelles with good colloidal stability and controlled length dispersity were fabricated to explore their potential in organic electronic applications. Li *et al.* prepared cylindrical micelles with controllable length from crystalline (regioregular poly(3-hexylthiophene))-coil (regiosymmetric poly(3-hexylthiophene)) block copolymers. A monolayer film prepared from the self-assemblies was shown to be electroactive using tunnelling atomic force microscopy. Organic field-effect

transistors were fabricated and shown to be highly functionalised with full channel saturation and negligible leakage.[99] Other than that, Xu *et al.* prepared organic semiconducting nanofibres with crystalline poly(di-*n*-hexylfluorene) (PDHF) cores and segmented coronas comprising of PEO in the middle and polythiophene at the ends, whilst the block length of these B-A-B type triblock co-micelles could be precisely tuned. Upon analysis using photoluminescence spectroscopy, a Förster resonance energy transfer phenomenon was observed for these nanofibres when the length of centre segment was restricted below 775 nm (**Figure 1.17**). It was proposed that the exciton produced in the middle block transferred along the π-π stacking crystal core to low energy polythiophene coronas. The diffusion length was unprecedentedly high (> 200 nm) coupled with large diffusion coefficients which offers a new avenue to optimise organic photovoltaic materials.[100]

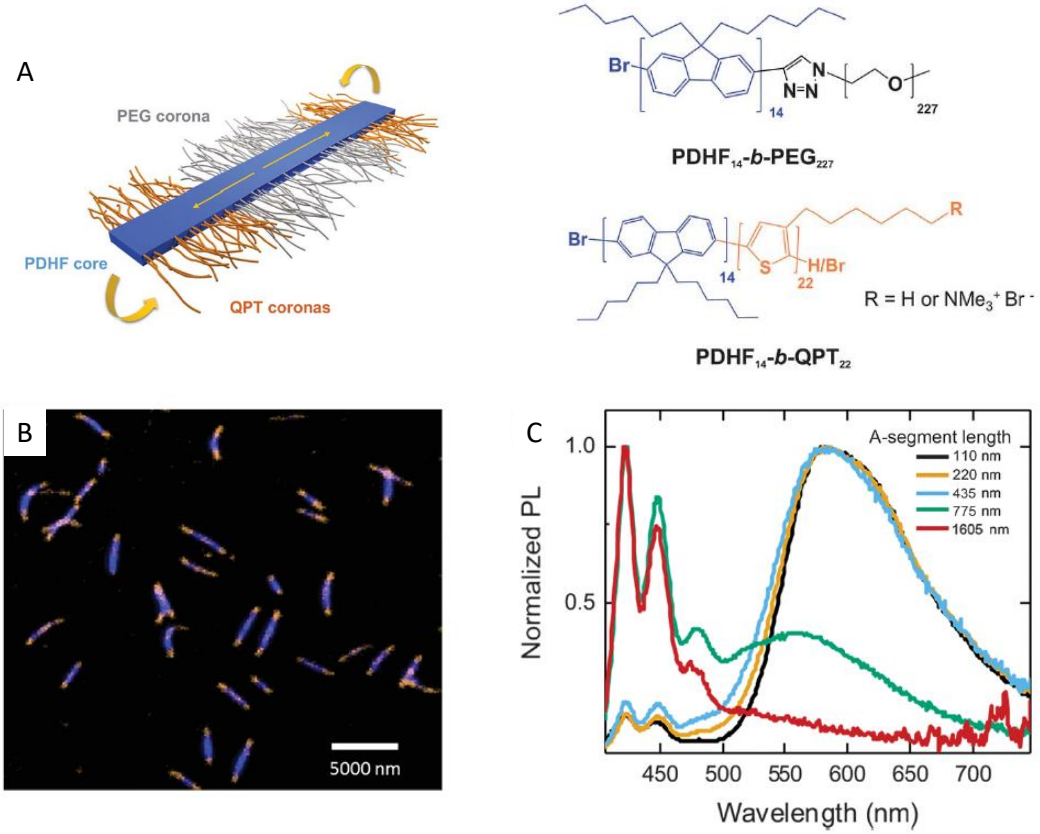

Figure 1.17 A) Scheme of B-A-B type triblock co-micelles prepared by a living CDSA approach B) Laser scanning confocal microscopy of the uniform and segmented nanofibres, blue represents the $PDHF_{14}$-*b*-PEG_{227} block, and yellow corresponds to the $PDHF_{14}$-*b*-QPT_{22} block. C) Photoluminescence spectra of segmented PDHF nanofibres with different block lengths.[100]

1.10 Nanoparticles Characterisations

The solution self-assembly of amphiphilic block copolymers provides access to a myriad of nanoparticles with all types of morphologies. Characterising the shapes and dimensions of nanoscale materials is of great importance before in depth understanding and further application. The most widely applied technique to determine the properties of polymer nanostructures are microscopies and light scattering. Light scattering experiments normally provide a statistical analysis of the nanostructures, however, considering the unconventional morphologies reported herein (e.g. platelets), microscopy was selected as the principal method for analysing the self-assembled nanostructures in this thesis.

1.10.1 Transmission electron microscopy

Transmission electron microscopy (TEM) is one of the most important techniques for visualising nanoparticles whereby a beam of electron is utilised to transmit through a specimen and ultimately generate images. Unlike in optical microscopy, the short wavelength of the electron beam helps to image a specimen at a significantly higher resolution. A complex set of lenses is incorporated in the device to adjust the beam path and a high vacuum is applied to minimise the interaction of air with the electrons.

The characterisation of self-assemblies in solutions *in situ* by TEM has been shown to be possible but it is still at an early stage whereby bespoke equipment and chamber were needed.[101, 102] The general approach to prepare the sample is to dry the self-assembly solution on the grid thoroughly before imaging, which is referred to as "dry-state TEM". However, the drying process could have potential effects upon the resultant morphology observed. For instance, it was discovered that in dry-state the

collapse of the solvated corona reduced the size of the original nanostructures as well as lead to the aggregation of smaller morphologies as a consequence of solvent evaporation which might result in misleading hierarchical morphologies.[103] These shortcomings can be overcome by using cryogenic TEM in which nanostructures are frozen in ice using liquefied ethane immediately after deposition onto the grid. The images obtained by this technique often reveal the original state of the nanostructures which avoids potential changes incurred by drying, but the unavoidable ice crystal formation can make imaging difficult.[104] Other than that, the preparation of a proper sample is demanding and to get an optimised image is time consuming and relatively expensive.

Image contrast is a necessity to visualise the nanoparticles effectively whereby the sample is supposed to scatter more electrons compared to the background support. The substrate utilised is normally covered with a carbon film, but particles obtained from block copolymers are often mainly composed of the element carbon which make it difficult to differentiate from the background scattering. Therefore, a common method has been developed which utilises high atomic number stains such as uranyl acetate or phosphotungstic acid to selectively bind to the background (negative staining), or the nanostructures themselves (positive staining), to increase the contrast. Although staining has been shown to be very useful, the optimisation of the staining conditions such as concentration or choice of stains is troublesome. Besides, stains have been known to cause some unexpected artefacts as well as show poor and unstable staining which limit the usage and obscure the original morphology. To avoid the use of stain, an alternative method is to use a thinner substrate, for example graphene oxide, to minimise the scattering of the substrate and thus provide enough contrast for particle imaging. [105]

1.10.2 Atomic force microscopy

Atomic force microscopy (AFM) is a type of scanning probe microscopy which is used to measure the surface information of a specimen. It can be mainly divided into two parts: a cantilever with a tip positioned at the very end and an optical system whereby a laser is used to detect the tip's deflection. When the tip is in contact with the sample and moving along the sample, the laser's deviation depicts the outline of the sample's surface.

One of the most widely used modes in AFM is called "tapping mode" whereby the tips oscillates up and down along the surface of the sample but does not contact the sample so as to avoid damaging the specimen. With the help of a feedback loop, the cantilever oscillates at a constant frequency and as the tip approaches the sample, the change in the oscillation amplitude at each intermittent point results in an image profile of the sample.[106]

Compared to TEM, AFM demonstrates many advantages in the following aspects. Firstly, facile sample preparation and easy to handle equipment, for instance AFM samples are prepared by dropping solution on a mica or a silica slice and the characterisation can be performed on a bench without vacuum preparation or complex optical alignments. Secondly, AFM obtains additional information such as height and force. However, the resolution of the lateral direction of AFM is highly restricted by the size of the tips on account of convolution effects (**Figure 1.18**).[107] In general, TEM and AFM techniques are complementary which work together to reveal the original solution state of the nanoparticles.

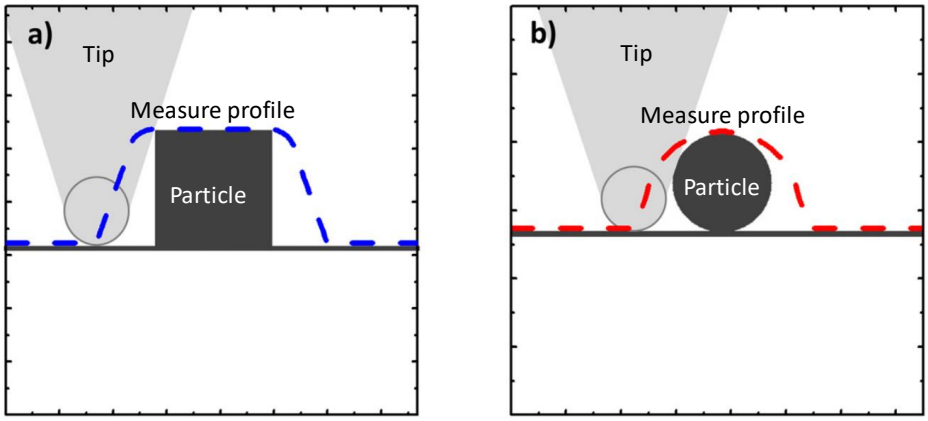

Figure 1.18 Diagram of AFM convolution effect, the size and shape of the tip affects the measured profile whereby a square was depicted as trapezoid (a), and spheres were larger (b).[107]

1.10.3 Light scattering

Scattering characterisation gives complementary information of nanoparticles in a non-destructive way. The most common scattering techniques used for soft nanomaterials are dynamic light scattering (DLS), static light scattering (SLS), small-angle X-ray (SAXS) and small angle neutron scattering (SANS). The fundamental principles of these characterisations methods are to illuminate the self-assembly solution with a radiation source of known wavelength and collect the signal scattered by the sample at a range of angles.

If the scattered intensity of light is monitored as a function of time, it is known as DLS measurement. In contrast, SANS, SLS and SAXS collect averaged scattered signal over time on a greater scale than DLS and thus help to determine the shape, size and molecular weight of the particles. The length scale measured is inversely proportional to the scattering wave vector *q* which is defined in Equation (2), where λ represent the wavelength of the radiation beam, *n* is the refractive index of the solution and θ stands for the scattering angle. Therefore, when X-ray or neutrons are applied as the incident beam (low wavelength), the value of *q* becomes larger and thus the scattering information from a smaller length scale can be obtained. Since light scattering is not the main characterisation method used herein, a detailed discussion is omitted.

$$q = \frac{4\pi n}{\lambda} \sin\left(\frac{\theta}{2}\right) \qquad \text{(Equation 2)}$$

1.11 Summary

This introductory chapter outlined many of the themes discussed within this thesis. Advanced living polymerisation techniques i.e. reversible deactivation radical polymerisation and ring-opening polymerisation were described in detail with a specific focus on RAFT polymerisation. Block copolymer self-assembly was introduced including conventional solution self-assembly and crystallisation-driven self-assembly which were the main topics in this chapter. The development of the CDSA technique and the self-assembly methodologies used to prepare crystalline micelles was summarised. An emphasis was placed on advanced living CDSA techniques which could be utilised to prepare a diverse range of nanostructures with complex morphologies and with great control. Meanwhile, an overview of the potential applications for these crystalline micelles was discussed with select examples. Finally, the characterisation techniques used to determine the size and morphology of nanostructures throughout this thesis was briefly discussed.

1.12 References

1. Hadjichristidis, N.; Pitsikalis, M.; Pispas, S.; Iatrou, H. *Chemical Reviews* **2001,** 101 (12), 3747-3792.

2. Chiefari, J.; Chong, Y.; Ercole, F.; Krstina, J.; Jeffery, J.; Le, T. P.; Mayadunne, R. T.; Meijs, G. F.; Moad, C. L.; Moad, G. *Macromolecules* **1998,** 31 (16), 5559-5562.
3. Braunecker, W. A.; Matyjaszewski, K. *Progress in Polymer Science* **2007,** 32 (1), 93-146.
4. Georges, M. K.; Veregin, R. P.; Kazmaier, P. M.; Hamer, G. K. *Macromolecules* **1993,** 26 (11), 2987-2988.
5. Benoit, D.; Chaplinski, V.; Braslau, R.; Hawker, C. J. *Journal of the American Chemical Society* **1999,** 121 (16), 3904-3920.
6. Hawker, C. J.; Bosman, A. W.; Harth, E. *Chemical Reviews* **2001,** 101 (12), 3661-3688.
7. Matyjaszewski, K. *Macromolecules* **2012,** 45 (10), 4015-4039.
8. Wang, J.-S.; Matyjaszewski, K. *Journal of the American Chemical Society* **1995,** 117 (20), 5614-5615.
9. Ramakrishnan, A.; Dhamodharan, R. *Macromolecules* **2003,** 36 (4), 1039-1046.
10. Moad, G.; Rizzardo, E.; Thang, S. H. *Australian journal of chemistry* **2005,** 58 (6), 379-410.
11. Chiefari, J.; Mayadunne, R. T.; Moad, C. L.; Moad, G.; Rizzardo, E.; Postma, A.; Skidmore, M. A.; Thang, S. H. *Macromolecules* **2003,** 36 (7), 2273-2283.
12. Skey, J.; O'Reilly, R. K. *Chemical Communications* **2008,** 6 (35), 4183-4185.
13. Postma, A.; Davis, T. P.; Moad, G.; O'Shea, M. S. *Macromolecules* **2005,** 38 (13), 5371-5374.
14. Perrier, S.; Takolpuckdee, P.; Mars, C. A. *Macromolecules* **2005,** 38 (6), 2033-2036.
15. Willcock, H.; O'Reilly, R. K. *Polymer Chemistry* **2010,** 1 (2), 149-157.
16. Heredia, K. L.; Grover, G. N.; Tao, L.; Maynard, H. D. *Macromolecules* **2009,** 42 (7), 2360-2367.
17. Ma, Z.; Gao, C.; Gong, Y.; Shen, J. *Biomaterials* **2005,** 26 (11), 1253-1259.
18. Yoshimoto, H.; Shin, Y.; Terai, H.; Vacanti, J. *Biomaterials* **2003,** 24 (12), 2077-2082.
19. Jeong, B.; Bae, Y. H.; Lee, D. S.; Kim, S. W. *Nature* **1997,** 388 (6645), 860-862.
20. Allen, T. M.; Cullis, P. R. *Science* **2004,** 303 (5665), 1818-1822.
21. Stanford, M. J.; Dove, A. P. *Chemical Society Reviews* **2010,** 39 (2), 486-494.
22. Kiesewetter, M. K.; Shin, E. J.; Hedrick, J. L.; Waymouth, R. M. *Macromolecules* **2010,** 43 (5), 2093-2107.
23. Kamber, N. E.; Jeong, W.; Waymouth, R. M.; Pratt, R. C.; Lohmeijer, B. G.; Hedrick, J. L. *Chemical reviews* **2007,** 107 (12), 5813-5840.
24. Nederberg, F.; Connor, E. F.; Möller, M.; Glauser, T.; Hedrick, J. L. *Angewandte Chemie International Edition* **2001,** 40 (14), 2712-2715.
25. MacMillan, D. W. *Nature* **2008,** 455 (7211), 304-315.
26. Dove, A. P.; Pratt, R. C.; Lohmeijer, B. G.; Waymouth, R. M.; Hedrick, J. L. *Journal of the American Chemical Society* **2005,** 127 (40), 13798-13799.

27. Pratt, R. C.; Lohmeijer, B. G.; Long, D. A.; Lundberg, P. P.; Dove, A. P.; Li, H.; Wade, C. G.; Waymouth, R. M.; Hedrick, J. L. *Macromolecules* **2006,** 39 (23), 7863-7871.
28. Makiguchi, K.; Satoh, T.; Kakuchi, T. *Macromolecules* **2011,** 44 (7), 1999-2005.
29. Mai, Y.; Eisenberg, A. *Chemical Society Reviews* **2012,** 41 (18), 5969-5985.
30. Zhang, L.; Eisenberg, A. *Polymers for Advanced Technologies* **1998,** 9 (10), 677-699.
31. Zhang, L.; Eisenberg, A. *Journal of the American Chemical Society* **1996,** 118 (13), 3168-3181.
32. Jain, S.; Bates, F. S. *Science* **2003,** 300 (5618), 460-464.
33. Zhang, L.; Yu, K.; Eisenberg, A. *Science* **1996,** 272 (5269), 1777-1779.
34. Doncom, K. E.; Blackman, L. D.; Wright, D. B.; Gibson, M. I.; O'Reilly, R. K. *Chemical Society Reviews* **2017,** 46 (14), 4119-4134.
35. Robin, M. P.; Mabire, A. B.; Damborsky, J. C.; Thom, E. S.; Winzer-Serhan, U. H.; Raymond, J. E.; O'Reilly, R. K. *Journal of the American Chemical Society* **2013,** 135 (25), 9518-9524.
36. Boal, A. K.; Ilhan, F.; DeRouchey, J. E.; Thurn-Albrecht, T.; Russell, T. P.; Rotello, V. M. *Nature* **2000,** 404 (6779), 746-752.
37. Toy, R.; Peiris, P. M.; Ghaghada, K. B.; Karathanasis, E. *Nanomedicine* **2014,** 9 (1), 121-134.
38. Cai, S.; Vijayan, K.; Cheng, D.; Lima, E. M.; Discher, D. E. *Pharmaceutical research* **2007,** 24 (11), 2099-2109.
39. Wang, F.; Xiao, J.; Chen, S.; Sun, H.; Yang, B.; Jiang, J.; Zhou, X.; Du, J. *Advanced Materials* **2018,** 30 (17), 1705674-1705680.
40. Christian, D. A.; Cai, S.; Bowen, D. M.; Kim, Y.; Pajerowski, J. D.; Discher, D. E. *European Journal of Pharmaceutics and Biopharmaceutics* **2009,** 71 (3), 463-474.
41. Kim, K. T.; Cornelissen, J. J.; Nolte, R. J.; van Hest, J. C. *Advanced Materials* **2009,** 21 (27), 2787-2791.
42. Du, J.; O'Reilly, R. K. *Soft Matter* **2009,** 5 (19), 3544-3561.
43. Lotz, B.; Kovacs, A.; Bassett, G.; Keller, A. *Kolloid-Zeitschrift und Zeitschrift für Polymere* **1966,** 209 (2), 115-128.
44. Vilgis, T.; Halperin, A. *Macromolecules* **1991,** 24 (8), 2090-2095.
45. Massey, J.; Power, K. N.; Manners, I.; Winnik, M. A. *Journal of the American Chemical Society* **1998,** 120 (37), 9533-9540.
46. Massey, J. A.; Temple, K.; Cao, L.; Rharbi, Y.; Raez, J.; Winnik, M. A.; Manners, I. *Journal of the American Chemical Society* **2000,** 122 (47), 11577-11584.
47. He, W.-N.; Zhou, B.; Xu, J.-T.; Du, B.-Y.; Fan, Z.-Q. *Macromolecules* **2012,** 45 (24), 9768-9778.
48. Sun, L.; Pitto-Barry, A.; Thomas, A. W.; Inam, M.; Doncom, K.; Dove, A. P.; O'Reilly, R. K. *Polymer Chemistry* **2016,** 7 (13), 2337-2341.
49. Lazzari, M.; Scalarone, D.; Hoppe, C.; Vazquez-Vazquez, C.; Lopez-Quintela, M. *Chemistry of Materials* **2007,** 19 (24), 5818-5820.
50. Patra, S. K.; Ahmed, R.; Whittell, G. R.; Lunn, D. J.; Dunphy, E. L.; Winnik, M. A.; Manners, I. *Journal of the American Chemical Society* **2011,** 133 (23), 8842-8845.
51. Schmelz, J.; Schacher, F. H.; Schmalz, H. *Soft Matter* **2013,** 9 (7), 2101-2107.
52. Cao, L.; Manners, I.; Winnik, M. A. *Macromolecules* **2002,** 35 (22), 8258-8260.

53. Finnegan, J. R.; He, X.; Street, S. T.; Garcia-Hernandez, J. D.; Hayward, D. W.; Harniman, R. L.; Richardson, R. M.; Whittell, G. R.; Manners, I. *Journal of the American Chemical Society* **2018,** 140 (49), 17127-17140.
54. He, W.-N.; Xu, J.-T. *Progress in Polymer Science* **2012,** 37 (10), 1350-1400.
55. Du, Z.-X.; Xu, J.-T.; Fan, Z.-Q. *Macromolecules* **2007,** 40 (21), 7633-7637.
56. Inam, M.; Cambridge, G.; Pitto-Barry, A.; Laker, Z. P.; Wilson, N. R.; Mathers, R. T.; Dove, A. P.; O'Reilly, R. K. *Chemical Science* **2017,** 8 (6), 4223-4230.
57. Shen, L.; Wang, H.; Guerin, G.; Wu, C.; Manners, I.; Winnik, M. A. *Macromolecules* **2008,** 41 (12), 4380-4389.
58. Hsiao, M.-S.; Yusoff, S. F. M.; Winnik, M. A.; Manners, I. *Macromolecules* **2014,** 47 (7), 2361-2372.
59. Schmelz, J.; Karg, M.; Hellweg, T.; Schmalz, H. *ACS Nano* **2011,** 5 (12), 9523-9534.
60. Wang, X.-Y.; Wang, R.-Y.; Fan, B.; Xu, J.-T.; Du, B.-Y.; Fan, Z.-Q. *Macromolecules* **2018,** 51 (5), 2138-2144.
61. Fan, B.; Xue, J.-Q.; Guo, X.-S.; Cao, X.-H.; Wang, R.-Y.; Xu, J.-T.; Du, B.-Y.; Fan, Z.-Q. *Macromolecules* **2018,** 51 (19), 7637-7648.
62. Rizis, G.; van de Ven, T. G.; Eisenberg, A. *ACS Nano* **2015,** 9 (4), 3627-3640.
63. Rizis, G.; van de Ven, T. G.; Eisenberg, A. *Angewandte Chemie International Edition* **2014,** 53 (34), 9000-9003.
64. Nazemi, A.; He, X.; MacFarlane, L. R.; Harniman, R. L.; Hsiao, M.-S.; Winnik, M. A.; Faul, C. F.; Manners, I. *Journal of the American Chemical Society* **2017,** 139 (12), 4409-4417.
65. He, X.; He, Y.; Hsiao, M. S.; Harniman, R. L.; Pearce, S.; Winnik, M. A.; Manners, I. *Journal of the American Chemical Society* **2017,** 139 (27), 9221-9228.
66. He, X.; Hsiao, M.-S.; Boott, C. E.; Harniman, R. L.; Nazemi, A.; Li, X.; Winnik, M. A.; Manners, I. *Nature Materials* **2017,** 16 (4), 481-491.
67. Qiu, H.; Gao, Y.; Boott, C. E.; Gould, O. E.; Harniman, R. L.; Miles, M. J.; Webb, S. E.; Winnik, M. A.; Manners, I. *Science* **2016,** 352 (6286), 697-701.
68. Mohd Yusoff, S. F.; Gilroy, J. B.; Cambridge, G.; Winnik, M. A.; Manners, I. *Journal of the American Chemical Society* **2011,** 133 (29), 11220-11230.
69. Cheng, J. Y.; Mayes, A. M.; Ross, C. A. *Nature Materials* **2004,** 3 (2), 823-831.
70. Darling, S. B. *Progress in Polymer Science* **2007,** 32 (10), 1152-1204.
71. Du, Z. X.; Xu, J. T.; Fan, Z. Q. *Macromolecular Rapid Communications* **2008,** 29 (6), 467-471.
72. Qian, J.; Li, X.; Lunn, D. J.; Gwyther, J.; Hudson, Z. M.; Kynaston, E.; Rupar, P. A.; Winnik, M. A.; Manners, I. *Journal of the American Chemical Society* **2014,** 136 (11), 4121-4124.
73. Taubert, A.; Napoli, A.; Meier, W. *Current Opinion in Chemical Biology* **2004,** 8 (6), 598-603.
74. Shenhar, R.; Norsten, T. B.; Rotello, V. M. *Advanced Materials* **2005,** 17 (6), 657-669.
75. Yeow, J.; Xu, J.; Boyer, C. *ACS Macro Letters* **2015,** 4 (9), 984-990.
76. Rieger, J.; Stoffelbach, F.; Bui, C.; Alaimo, D.; Jérôme, C.; Charleux, B. *Macromolecules* **2008,** 41 (12), 4065-4068.
77. Rieger, J.; Osterwinter, G.; Bui, C.; Stoffelbach, F.; Charleux, B. *Macromolecules* **2009,** 42 (15), 5518-5525.
78. Ladmiral, V.; Semsarilar, M.; Canton, I.; Armes, S. P. *Journal of the American Chemical Society* **2013,** 135 (36), 13574-13581.

79. Sugihara, S.; Blanazs, A.; Armes, S. P.; Ryan, A. J.; Lewis, A. L. *Journal of the American Chemical Society* **2011,** 133 (39), 15707-15713.
80. Blanazs, A.; Madsen, J.; Battaglia, G.; Ryan, A. J.; Armes, S. P. *Journal of the American Chemical Society* **2011,** 133 (41), 16581-16587.
81. Oliver, A. M.; Gwyther, J.; Boott, C. E.; Davis, S.; Pearce, S.; Manners, I. *Journal of the American Chemical Society* **2018,** 140 (51), 18104-18114.
82. Boott, C. E.; Gwyther, J.; Harniman, R. L.; Hayward, D. W.; Manners, I. *Nature Chemistry* **2017,** 9 (8), 785-798.
83. Gilroy, J. B.; Gädt, T.; Whittell, G. R.; Chabanne, L.; Mitchels, J. M.; Richardson, R. M.; Winnik, M. A.; Manners, I. *Nature Chemistry* **2010,** 2 (7), 566-579.
84. Wang, X.; Guerin, G.; Wang, H.; Wang, Y.; Manners, I.; Winnik, M. A. *Science* **2007,** 317 (5838), 644-647.
85. Guerin, G.; Rupar, P. A.; Manners, I.; Winnik, M. A. *Nature Communications* **2018,** 9 (1), 1158-1171.
86. Guerin, G.; Rupar, P.; Molev, G.; Manners, I.; Jinnai, H.; Winnik, M. A. *Macromolecules* **2016,** 49 (18), 7004-7014.
87. Rupar, P. A.; Chabanne, L.; Winnik, M. A.; Manners, I. *Science* **2012,** 337 (6094), 559-562.
88. Hudson, Z. M.; Boott, C. E.; Robinson, M. E.; Rupar, P. A.; Winnik, M. A.; Manners, I. *Nature Chemistry* **2014,** 6 (10), 893-900.
89. Hailes, R. L.; Oliver, A. M.; Gwyther, J.; Whittell, G. R.; Manners, I. *Chemical Society Reviews* **2016,** 45 (19), 5358-5407.
90. Arno, M. C.; Inam, M.; Coe, Z.; Cambridge, G.; Macdougall, L. J.; Keogh, R.; Dove, A. P.; O'Reilly, R. K. *Journal of the American Chemical Society* **2017,** 139 (46), 16980-16985.
91. Qiu, H.; Hudson, Z. M.; Winnik, M. A.; Manners, I. *Science* **2015,** 347 (6228), 1329-1332.
92. Li, X.; Gao, Y.; Harniman, R.; Winnik, M.; Manners, I. *Journal of the American Chemical Society* **2016,** 138 (39), 12902-12912.
93. Nazemi, A.; Boott, C. E.; Lunn, D. J.; Gwyther, J.; Hayward, D. W.; Richardson, R. M.; Winnik, M. A.; Manners, I. *Journal of the American Chemical Society* **2016,** 138 (13), 4484-4493.
94. Sun, L.; Pitto-Barry, A.; Kirby, N.; Schiller, T. L.; Sanchez, A. M.; Dyson, M. A.; Sloan, J.; Wilson, N. R.; O'Reilly, R. K.; Dove, A. P. *Nature Communications* **2014,** 5 (3), 5746-5752.
95. Li, Z.; Sun, L.; Zhang, Y.; Dove, A. P.; O'Reilly, R. K.; Chen, G. *ACS Macro Letters* **2016,** 5 (9), 1059-1064.
96. Hou, J.; Tan, Z. a.; Yan, Y.; He, Y.; Yang, C.; Li, Y. *Journal of the American Chemical Society* **2006,** 128 (14), 4911-4916.
97. Thomas, S. W.; Joly, G. D.; Swager, T. M. *Chemical Reviews* **2007,** 107 (4), 1339-1386.
98. Kamps, A. C.; Fryd, M.; Park, S.-J. *ACS Nano* **2012,** 6 (3), 2844-2852.
99. Li, X.; Wolanin, P. J.; MacFarlane, L. R.; Harniman, R. L.; Qian, J.; Gould, O. E.; Dane, T. G.; Rudin, J.; Cryan, M. J.; Schmaltz, T. *Nature Communications* **2017,** 8 (2), 15909-15919.
100. Jin, X.-H.; Price, M. B.; Finnegan, J. R.; Boott, C. E.; Richter, J. M.; Rao, A.; Menke, S. M.; Friend, R. H.; Whittell, G. R.; Manners, I. *Science* **2018,** 360 (6391), 897-900.

101. Nielsen, M. H.; Li, D.; Zhang, H.; Aloni, S.; Han, T. Y.-J.; Frandsen, C.; Seto, J.; Banfield, J. F.; Cölfen, H.; De Yoreo, J. J. *Microscopy and Microanalysis* **2014,** 20 (2), 425-436.
102. Ross, F. M. *Science* **2015,** 350 (6267), 9886-9897.
103. Friedrich, H.; Frederik, P. M.; de With, G.; Sommerdijk, N. A. *Angewandte Chemie International Edition* **2010,** 49 (43), 7850-7858.
104. Patterson, J. P.; Xu, Y.; Moradi, M.-A.; Sommerdijk, N. A.; Friedrich, H. *Accounts of Chemical Research* **2017,** 50 (7), 1495-1501.
105. Patterson, J. P.; Robin, M. P.; Chassenieux, C.; Colombani, O.; O'Reilly, R. K. *Chemical Society Reviews* **2014,** 43 (8), 2412-2425.
106. Giessibl, F. J. *Reviews of Modern Physics* **2003,** 75 (3), 949-960.
107. Canet-Ferrer, J.; Coronado, E.; Forment-Aliaga, A.; Pinilla-Cienfuegos, E. *Nanotechnology* **2014,** 25 (39), 395703-395723.

Chapter 2. Understanding the CDSA of polylactide containing triblock copolymers

2.1 Abstract

Crystallisation-driven self-assembly (CDSA) has become an extremely valuable technique in the preparation of well-defined nanostructures using diblock copolymers. The use of triblock copolymers is considerably less well-known on account of more complex syntheses and assembly methods despite the functional advantages provided by a third block. Herein, we show the simple preparation of well-defined tuneable 1D and 2D structures based on polylactide triblock copolymers of different block ratios synthesised by ring-opening polymerisation (ROP) and reversible addition-fragmentation chain transfer (RAFT) polymerisation. Single solvent CDSA processes revealed that comparatively hydrophilic polymers were liable to achieve. A phase diagram based on a novel unimer solubility approach is proposed. Using a series of poly(L-lactide)-*b*-poly(*N*,*N*-dimethylacrylamide) (PLLA-*b*-PDMA) diblock copolymers and PDMA-*b*-PLLA-*b*-PDMA triblock copolymers with different core/corona ratios, single solvent CDSA processes revealed that comparatively hydrophilic polymers were liable to achieve 2D platelets, while the less hydrophilic counterparts yield 'transition state' wide cylinders and pure 1D cylinders.

2.2 Introduction

The use of semi-crystalline polymers has provided an unprecedented route to the facile fabrication of cylindrical micelles using crystallisation-driven self-assembly (CDSA), where the formation of cylindrical structures is driven by the crystallisation of the core block to form micelles with low interfacial curvature.[1] As mentioned in **Chapter 1**, the size and morphology of the assemblies can be precisely adjusted with the instruction of a seed-growth methodology.[2-4]

Various functional groups have also been incorporated, including fluorescent marking,[5] metal nanoparticle incorporation,[6] and photo-responsibility,[7] demonstrating a diverse range of potential uses within drug delivery processes. As a semi-crystalline polymer, poly(L-lactide) (PLLA) is renowned for its outstanding biocompatibility and biodegradability, which allows use in bio-relevant applications. In our previous studies, PLLA block copolymers could be fabricated using a combination of reversible addition-fragmentation chain transfer (RAFT) and ring-opening polymerisation (ROP), where we have been able to achieve tuneable cylindrical micelles with a range of coronal blocks by CDSA.[8, 9] Further work was carried out to enrich the functionality of the PLLA-based cylinders,[10, 11] and successfully realize stereocomplexation-triggered morphological transitions,[12] which indicate the promising future of these cylindrical particles in the biomedical realm.

Similar to conventional phase separation-driven assembly, it can be expected that triblock copolymers will lead to an alternate morphology when undergoing CDSA as a consequence of the extra coil phase. Wang *et al.* prepared a series of coil-crystalline-coil poly(ferrocenylphenylphosphine)-*block*-poly(ferrocenyldimethylsilane)-*block*-poly(dimethylsiloxane) (PFP-*b*-PFDMS-*b*-PDMS) triblock copolymers and, upon increasing the degree of polymerisation of PFP from 6 to 11, the morphology transitioned from cylindrical to spherical micelles. It was proposed that the longer PFP block interfered with the crystallisation of the PFS block to a greater extent than the shorter blocks, thus leading to amorphous spheres.[13] Similarly, Schmalz *et al.* found that polystyrene-*b*-polyethylene-*b*-poly(methyl methacrylate)) (PS-*b*-PE-*b*-PMMA) triblock terpolymers formed worm-like micelles, whereas the

corresponding PE diblock copolymers (PE-*b*-PMMA) formed platelet-like structures. It was also found that, as the composition or molecular weight of the triblock terpolymer was changed, the morphology of the structures also changed, and, therefore, it was possible to control the type of structure formed, i.e. spherical, worm-like (cylindrical) or lamellar.[14] Although these studies focused on the CDSA behaviour of ABC type coil-crystalline-coil triblock copolymers, a systematic study of the assembly behaviour of a simplified triblock terpolymer model, i.e. ABA type copolymers have seldom been carried out. It is expected that these polymers will achieve different assembly morphologies compared to their corresponding coil-crystalline diblock copolymers as a consequence of the difference in solubility and crystallisation behaviour.

Herein, we report the preparation of well-defined amphiphilic diblock and triblock copolymers, PDMA-*b*-PLLA and PDMA-*b*-PLLA-*b*-PDMA, with a range of block lengths synthesised by ROP and RAFT polymerisation. Using a simple, single solvent assembly system, we show that the hydrophobicity of the polymer plays an important role in the assembly process for both *di*- and *tri*-block copolymer systems, where a clear transition from cylindrical to platelet structures can be observed on increasing polymer solubility.

2.3 Results and Discussion

2.3.1 Ring-opening polymerisation of L-lactide

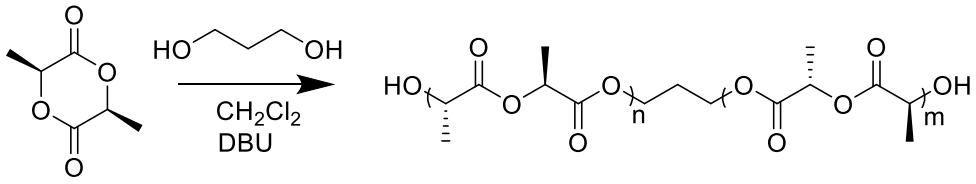

Scheme 2.1 Ring-opening polymerisation of L-lactide.

PLLA was synthesized by ROP using 1,3-propandiol and 1,8-Diazabicyclo[5.4.0]undec-7-ene (DBU) as the initiator and catalyst, respectively (**Scheme 2.1**). In order to investigate the effect of hydrophobic block length on the self-assembly morphology, three different degrees of polymerisation (DPs) values were targeted ($PLLA_{25}$, $PLLA_{32}$, $PLLA_{50}$ and $PLLA_{68}$). Analysis of the resultant polymers by ^1H NMR spectroscopy confirmed the successful polymerisation with the appearance of a quartet at δ = 5.13 ppm corresponding to the methine proton in the polymer backbone, in addition to a triplet at δ = 4.18 ppm corresponding to the methylene proton in the initiator (**Figure 2.1**). Comparison of the integration of these two peaks allowed for determination of the observed number-average molecular weight ($M_{n,\,obs.}$) for the PLLA homopolymers (**Table 2.1**). The theoretical number-average molecular weight ($M_{n,\,theo}$) was found to be in good agreement with the observed number-average molecular weight, confirming the controlled nature of the polymerisation. Analysis of the polymers using size exclusion chromatography (SEC) (**Figure 2.2**) indicated monomodal distributions for all homopolymers, with a shift in molecular weight as the DP of the polymer increased. Moreover, narrow size distribution for all the homopolymers were obtained ($Đ_M$ <1.1), which further indicates the controlled nature of the process.

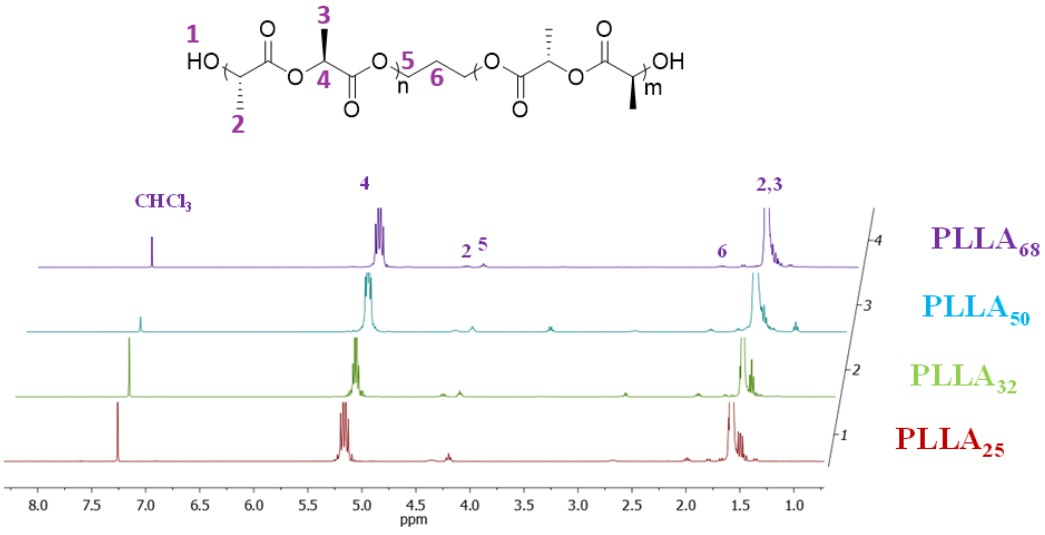

Figure 2.1 ^{1}H NMR spectra (400 MHz, $CDCl_3$) of various PLLA homopolymers $PLLA_{25}$, $PLLA_{32}$, $PLLA_{50}$ and $PLLA_{68}$.

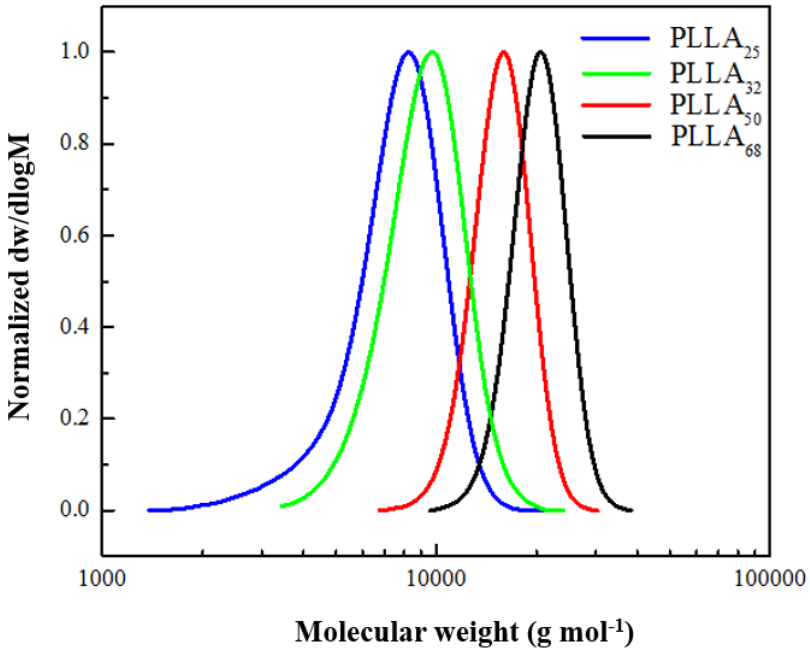

Figure 2.2 An overlay of SEC traces of homopolymers $PLLA_{25}$, $PLLA_{32}$, $PLLA_{50}$, $PLLA_{68}$ (DMF with 5 mM NH_4BF_4).

Table 2.1 Characterisation data of PLLA. The M_n determined by SEC is on the basis of polymer hydrodynamic volume of the polymer, the deviation mainly caused by the difference of the polymer PLLA from the standard calibration polymer PMMA.

Polymers	$M_{n,NMR}$ (kDa)[a]	$M_{n,SEC}$ (kDa)[b]	$Đ_M$[c]
$PLLA_{25}$	3.6	8.5	1.03
$PLLA_{32}$	4.6	9.8	1.04
$PLLA_{50}$	7.2	14.2	1.02
$PLLA_{68}$	9.8	17.6	1.05

[a]Measured by ^{1}H NMR spectroscopy (400 MHz, $CDCl_3$). [b]Measured by (DMF with 5 mM NH_4BF_4).

The homopolymers were analysed using matrix-assisted laser desorption/ionization-time of flight (MALDI-ToF) spectrometry (**Figure 2.3**). The absence of a secondary distribution in the spectra indicated minimal signs of chain transesterification or water initiation. Moreover, the molecular weight determined was in good agreement with that calculated from ^{1}H NMR spectroscopy, which confirms the controlled nature of the polymerisation.

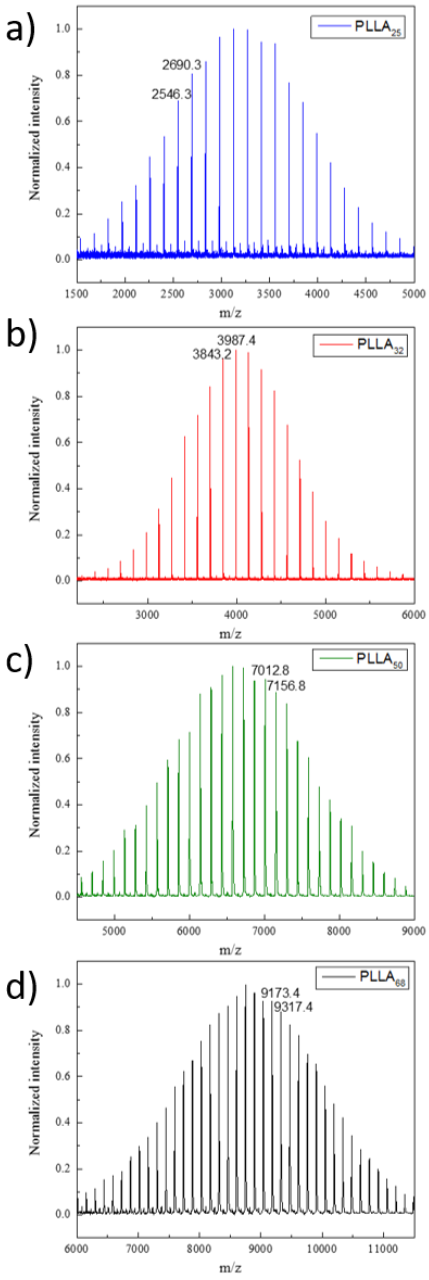

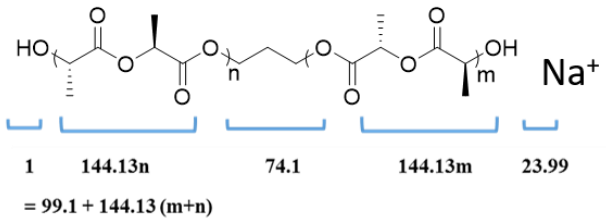

m+n	m/z
13	1681.4
14	1825.5
15	1969.68
16	2113.8
17	2258.02
18	2402.52
19	2546.62
20	2690.62
21	2834.72
22	2978.72
23	3122.72
24	3266.82
25	3410.82
26	3843.5
27	3987.7
28	4132.2
29	4276.3
30	4420.3
31	4564.4
32	4708.4

m+n	m/z
33	4852.4
34	4996.5
35	5140.5
46	6725.0
47	6869.0
48	7013.1
49	7157.1
50	7301.2
51	7445.2
52	7589.2
53	7733.3
63	9173.7
64	9317.7
65	9461.8
66	9605.8
67	9749.9
68	9893.9
69	10038.0
70	10182.0

Figure 2.3 MALDI-ToF mass spectra of (a) $PLLA_{25}$, (b) $PLLA_{32}$, (c) $PLLA_{50}$ and (d) $PLLA_{68}$.

2.3.2 Synthesis of 2-(Dodecylthiocarbonothioylthio)-2-methylpropionic acid (DDMAT)

In order to produce triblock copolymers, a RAFT chain transfer agent was coupled to the PLLA homopolymer to allow for chain extension of the other blocks. In addition to its suitability towards the polymerisation of acrylamide, DDMAT was selected owing to its carboxylic acid functionalities enabling facile coupling of the RAFT agent to the PLLA homopolymer. To this end, DDMAT was synthesized according to a previously reported method by Skey *et al.* (**Scheme 2.2**).[15] Following reaction for 72 h and purification *via* washing with hexane, the successful synthesis was confirmed by ^{1}H NMR spectroscopy (**Figure 2.4**), the methylene proton (δ = 3.24 ppm) appearing next to the thiocarbonyl functionality.

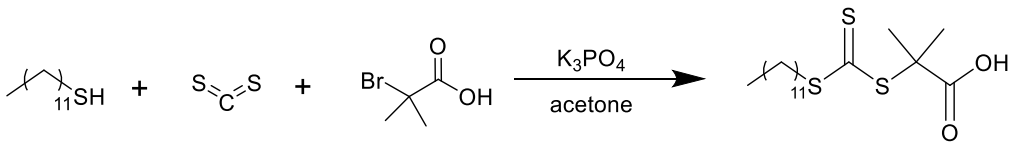

Scheme 2.2 Synthesis of RAFT agent DDMAT.

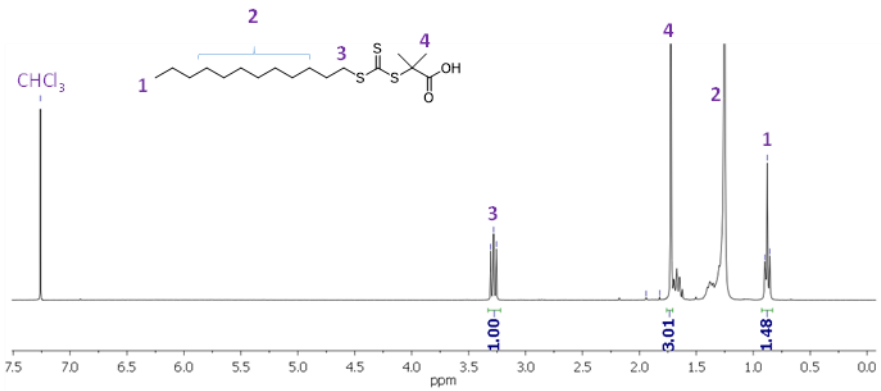

Figure 2.4 ^{1}H NMR spectrum of the RAFT agent DDMAT (400 MHz, $CDCl_3$).

2.3.3 Coupling the RAFT agent to the polymer

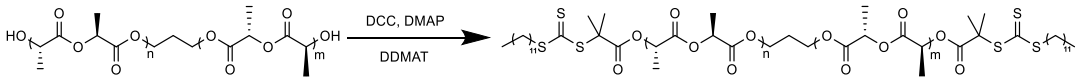

Scheme 2.3 Coupling of the RAFT agent DDMAT to PLLA.

The PLLA homopolymers bearing hydroxyl functional groups at both ends were reacted with the RAFT agent DDMAT using dicyclohexylcarbodiimide (DCC) and 4-dimethylaminopyridine (DMAP) as activating reagents (**Scheme 2.3**). The coupling reaction was carried out in a concentrated solution for an extensive period of time (3 days) using an excess of the carboxylic group functionality to promote quantitative attachment of the RAFT agent to both ends of the homopolymer. As observed in the ^{1}H NMR spectrum of the macro-initiator CTA-PLLA$_{32}$-CTA (**Figure 2.5 a** and **b**), the integral value of the triplet associated with the methylene proton of the thiocarbonyl group at δ = 3.24 ppm was equal to the corresponding value of the methylene protons in the initiator (δ = 4.18 ppm), which confirms that both ends of the polymer had been successfully functionalised with DDMAT. Comparable results were also achieved with the rest of the series (**Figure 2.5 c**).

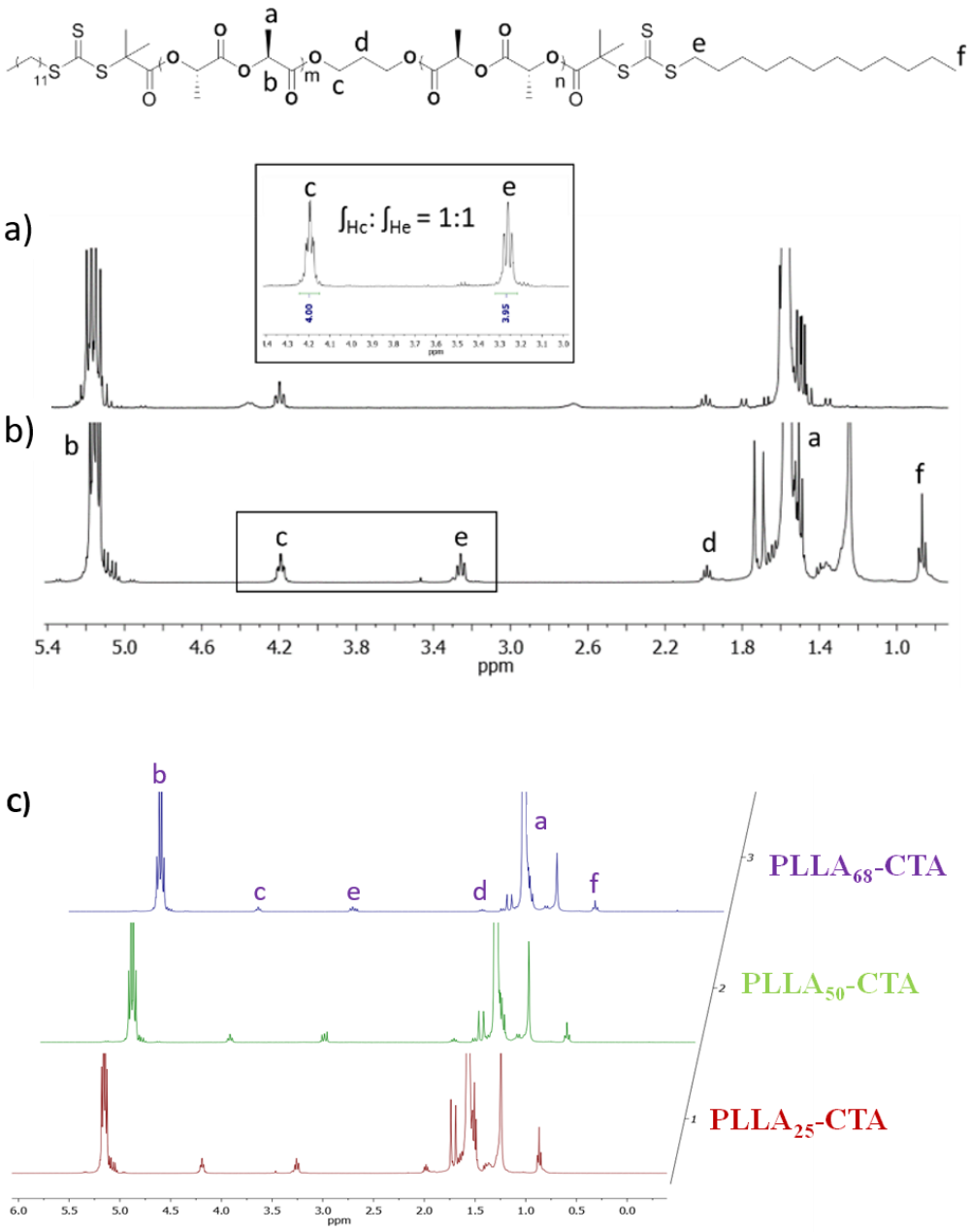

Figure 2.5 ^{1}H NMR spectra (400 MHz, $CDCl_3$) of $PLLA_{32}$(a), $PLLA_{32}$-CTA(b) and macro-initiator (c) $PLLA_{25}$-CTA, $PLLA_{50}$-CTA and $PLLA_{68}$-CTA.

SEC characterisation (**Figure 2.6**) shows a clear molecular weight shift (RI trace) and overlapping of the RI and UV traces (λ = 309 nm), which indicates successful attachment of the trithiocarbonate onto the polymer backbone. Furthermore, MALDI-ToF MS analysis of $PLLA_{32}$ and CTA-$PLLA_{32}$-CTA (**Figure 2.7**) also revealed a shift in mass distribution (Δm/z 692.25), which was calculated as exactly twice that of the

molecular weight of DDMAT, with no mass peaks existing between the main distribution, thus confirming that the attachment had occurred at both ends of the polymer.

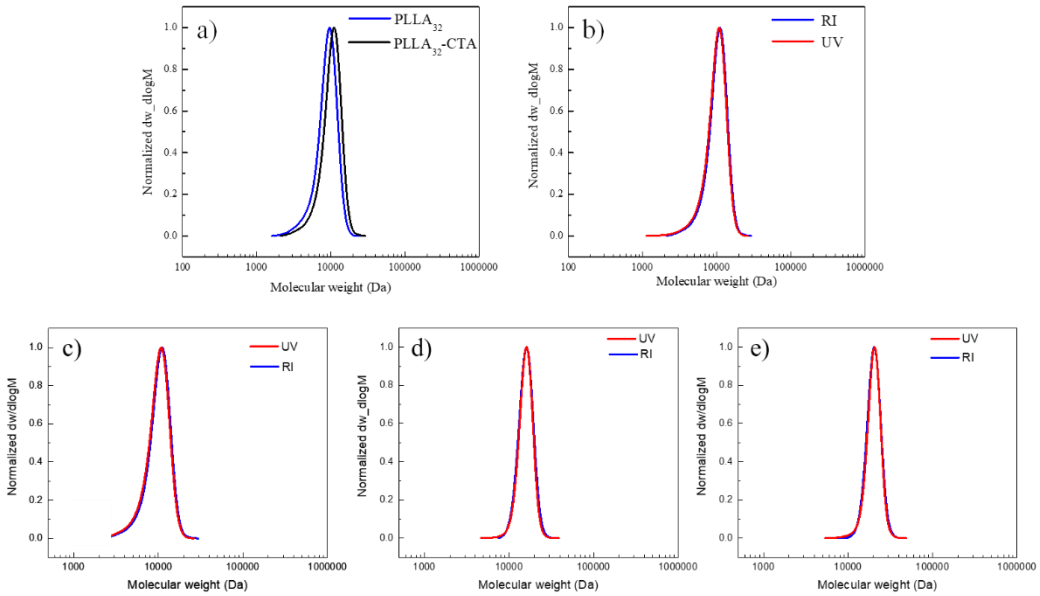

Figure 2.6 a) An overlay of SEC RI traces of homopolymers $PLLA_{32}$ and macro-CTA CTA-$PLLA_{32}$-CTA (DMF with 5 mM NH_4BF_4). b) An overlay of SEC RI and UV traces of b) CTA-$PLLA_{32}$-CTA, c) CTA-$PLLA_{25}$-CTA d) CTA-$PLLA_{50}$-CTA and e) CTA-$PLLA_{68}$-CTA macro-initiator.

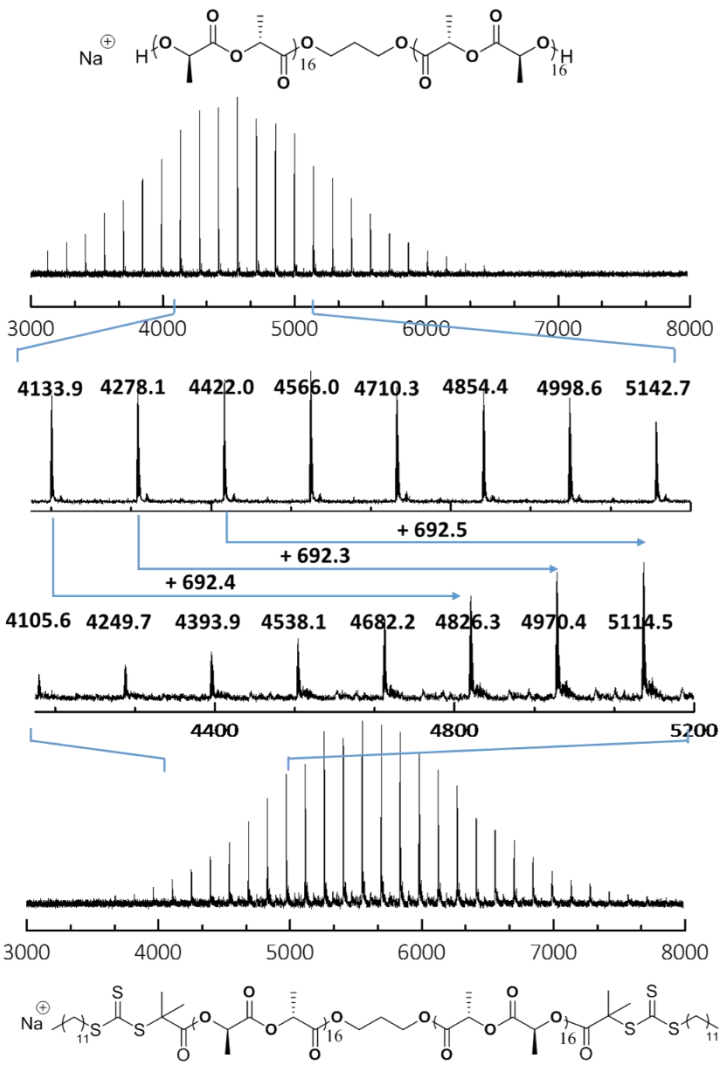

Figure 2.7 MALDI-ToF mass spectra of $PLLA_{32}$ and CTA-$PLLA_{32}$-CTA.

2.3.4. Chain-extension of dual-functionalised macro-CTA

The bifunctional macro-CTA was used to grow hydrophilic blocks of poly(*N*,*N*-dimethylacrylamide) (PDMA) to produce triblock copolymers displaying ABA sequence, PDMA-*b*-PLLA-*b*-PDMA via RAFT polymerisation. Typically, the reaction was executed at 70 °C for 5 h to give a monomer conversion of 90% as determined by ^{1}H NMR spectroscopy. Further ^{1}H NMR spectroscopic analysis of the purified polymer (**Figure 2.8**) was used to confirm the block ratio and

block length of the polymer blocks based on characteristic proton signals (δ = 2.90 and 5.14 ppm). The reaction conditions of the chain-growth of PDMA were adjusted, with respect to the core and corona lengths, to attain a range of well-defined triblock terpolymers **T1-T13** (**Table 2.2**) with different hydrophobic ratios (11, 15, 25 and 32%). SEC analysis confirmed narrow molecular weight distributions for all the polymers, $Đ_M$ < 1.2 (**Figure 2.9**).

Table 2.2 Characterisation data of PDMA-*b*-PLLA-*b*-PDMA triblock copolymers and PLLA-*b*-PDMA diblock copolymers [§].

T-triblock D-diblock	Block copolymers	$M_{n,NMR}$(kDa) [a]	$M_{n,SEC}$(kDa) [b]	$Đ_M$ [b]	Hydrophobic weight [c] (wt%)
T1	$PDMA_{42}$-*b*-$PLLA_{25}$-*b*-$PDMA_{42}$	11.3	17.8	1.05	32.1
T2	$PDMA_{60}$-*b*-$PLLA_{25}$-*b*-$PDMA_{60}$	14.4	18.7	1.12	25.2
T3	$PDMA_{105}$-*b*-$PLLA_{25}$-*b*-$PDMA_{105}$	24	32.5	1.10	15.1
T4	$PDMA_{160}$-*b*-$PLLA_{25}$-*b*-$PDMA_{160}$	32.8	39.7	1.13	11.0
T5	$PDMA_{45}$-*b*-$PLLA_{32}$-*b*-$PDMA_{45}$	13.5	19.5	1.04	32.2
T6	$PDMA_{66}$-*b*-$PLLA_{32}$-*b*-$PDMA_{66}$	18.5	22.7	1.07	25.1
T7	$PDMA_{122}$-*b*-$PLLA_{32}$-*b*-$PDMA_{122}$	28.9	38.4	1.08	15.3
T8	$PDMA_{188}$-*b*-$PLLA_{32}$-*b*-$PDMA_{188}$	41.9	46.7	1.13	11.1
T9	$PDMA_{75}$-*b*-$PLLA_{50}$-*b*-$PDMA_{75}$	22.1	30.9	1.04	32.2
T10	$PDMA_{225}$-*b*-$PLLA_{50}$-*b*-$PDMA_{225}$	51.8	58.2	1.14	15.1
T11	$PDMA_{295}$-*b*-$PLLA_{50}$-*b*-$PDMA_{295}$	65.5	69.6	1.17	11.0
T12	$PDMA_{115}$-*b*-$PLLA_{68}$-*b*-$PDMA_{115}$	32.6	47.4	1.03	32.0
T13	$PDMA_{315}$-*b*-$PLLA_{68}$-*b*-$PDMA_{315}$	72.3	73.5	1.14	15.0
D1	$PLLA_{25}$-*b*-$PDMA_{120}$	15.9	25	1.10	23.7
D2	$PLLA_{25}$-*b*-$PDMA_{225}$	26.3	36.3	1.17	13.9
D3	$PLLA_{48}$-*b*-$PDMA_{145}$	21.7	30.8	1.05	33.0
D4	$PLLA_{48}$-*b*-$PDMA_{240}$	31.1	41.5	1.05	22.8
D5	$PLLA_{48}$-*b*-$PDMA_{570}$	63.8	74.1	1.06	11.0
D6	$PLLA_{48}$-*b*-$PDMA_{950}$	101.5	122.2	1.10	6.9

[a] Measured by ^{1}H NMR spectroscopy (400 MHz, $CDCl_3$). [b] Measured by SEC using RI detection (DMF with 5 mM NH_4BF_4). [c] PLLA weight fraction in the block copolymer.

[§] $PLLA_n$-*b*-$PDMA_m$ diblock copolymers were prepared by Anaïs Pitto-Barry, Graeme Cambridge and Maria Inam.

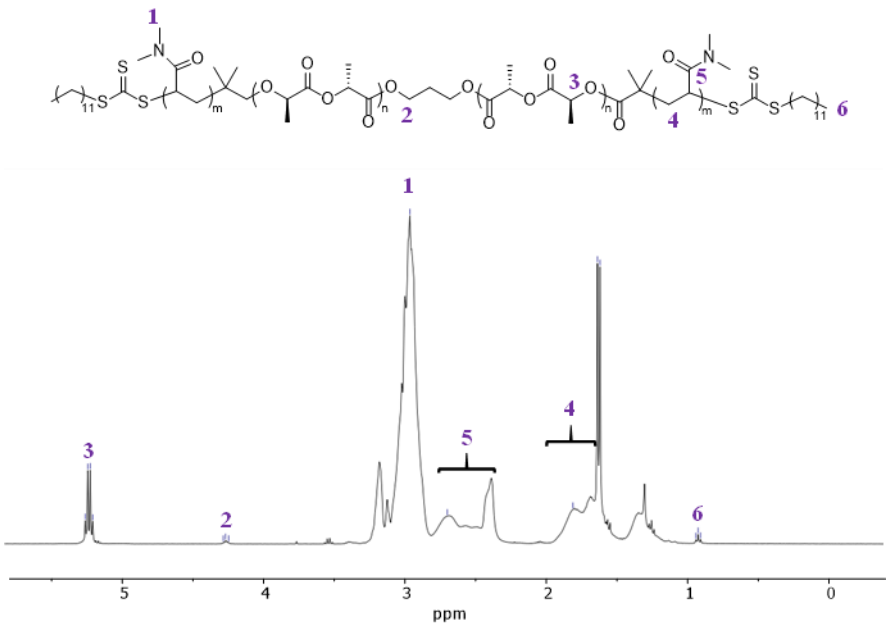

Figure 2.8 ^{1}H NMR spectrum of PDMA-*b*-PLLA-*b*-PDMA triblock copolymer **T7** (400 MHz, $CDCl_3$).

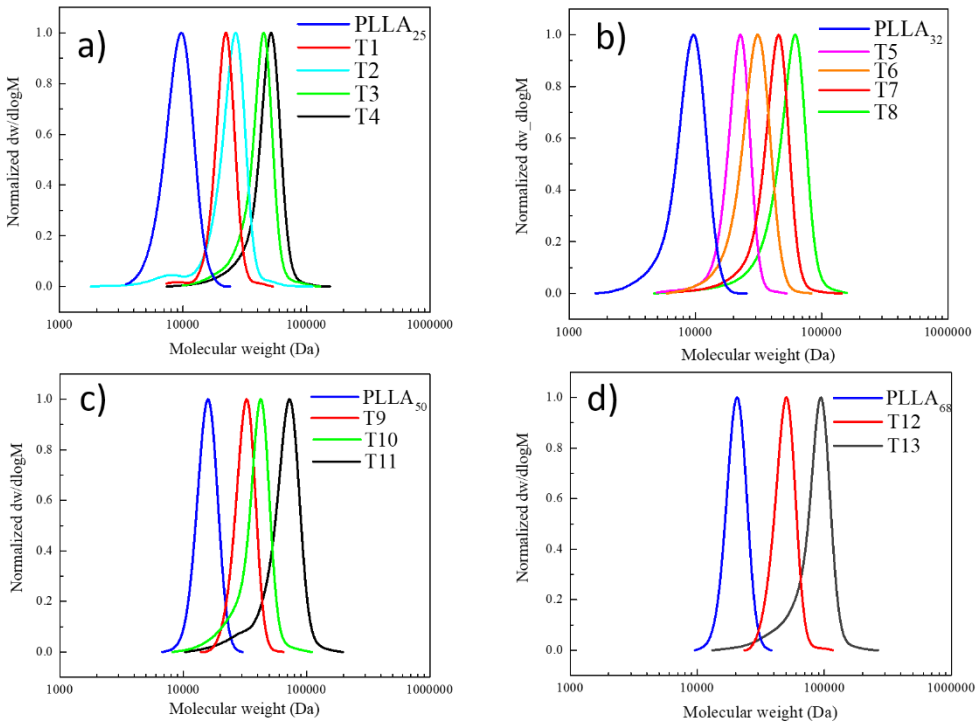

Figure 2.9 SEC curves of polymers (DMF with 5 mM NH_4BF_4). a) Macro-initiator **PLLA$_{25}$** and triblock copolymers **T1-T4**. b) Macro-initiator **PLLA$_{32}$** and triblock copolymers **T5-T8**. c) Macro-initiator **PLLA$_{50}$** and triblock copolymers **T9-T11**. d) Macro-initiator **PLLA$_{68}$** and triblock copolymers **T12, T13**.

^{1}H-DOSY NMR was also carried out to confirm the absence of homopolymer content since any contamination which has the potential to significantly influence the CDSA results.[16] The results obtained (**Figure 2.10**) clearly show the same diffusion coefficient value for protons corresponding to the PLLA core and the triblock terpolymer **T3**. This is distinguishably higher when compared to the $PLLA_{32}$ homopolymer and macro RAFT agent CTA-$PLLA_{32}$-CTA proton resonances, thus providing evidence for a pure triblock copolymer system without the presence of homopolymer.

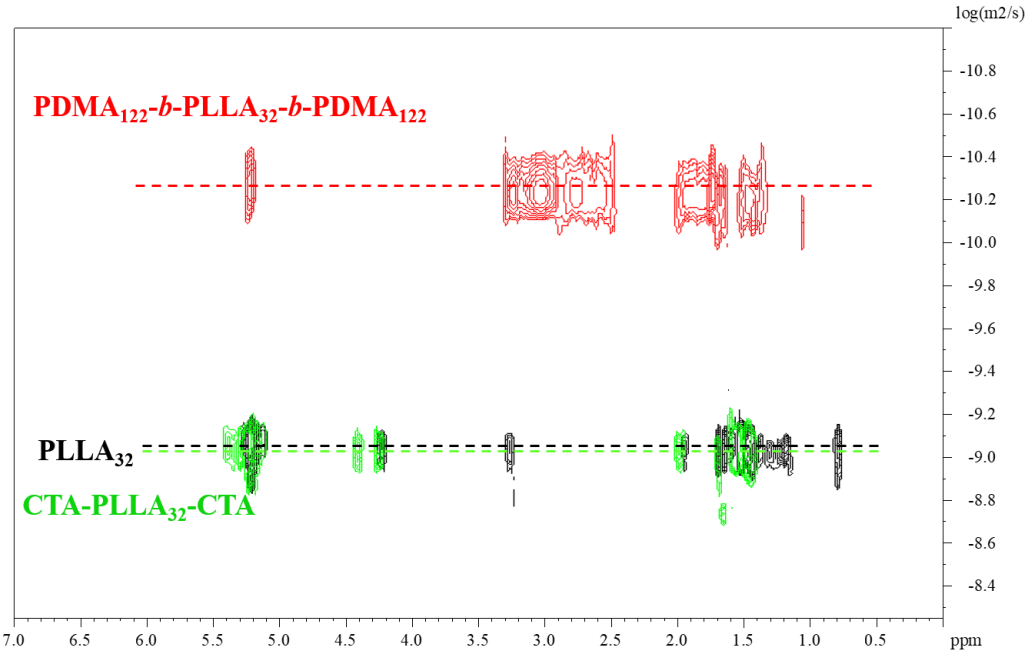

Figure 2.10 ^{1}H-DOSY NMR spectra (500 MHz, $CDCl_3$) of homopolymer $PLLA_{32}$, macro-initiator CTA-$PLLA_{32}$-CTA and triblock copolymer PDMA-*b*-PLLA-*b*-PDMA **T7**.

2.3.5 Crystallisation-Driven Self-Assembly of PDMA-*b*-PLLA-*b*-PDMA triblock copolymers

Previously, PLLA assemblies were prepared using a solvent switch and evaporation method which was time-consuming and laborious for further application.[17] Recently, we reported that a single alcoholic solvent could be

utilised to achieve CDSA for PLLA based diblock copolymers.[18] Upon examination, triblock terpolymers were found to completely dissolve in methanol at 5 mg mL^{-1} at room temperature. No Tyndall phenomenon was observed in solution for the first few hours, which indicates a lack of assembly into larger structures. After ageing at room temperature for 24 h, a strong Tyndall light path could be detected, which suggested the existence of large assemblies. Subsequent analysis of the sample using dynamic light scattering (DLS) confirmed the formation of monomodal assemblies (**Figure 2.11** and **Table 2.3**).

Table 2.3 DLS analysis of micelles from triblock copolymers PDMA-*b*-PLLA-*b*-PDMA.

Triblock copolymers	D_h^* / nm	PD
$PDMA_{45}$-*b*-P*L*LA_{32}-*b*-$PDMA_{45}$, **T5**	270.3	0.20
$PDMA_{122}$-*b*-P*L*LA_{32}-*b*-$PDMA_{122}$, **T7**	867.3	0.24
$PDMA_{75}$-*b*-P*L*LA_{50}-*b*-$PDMA_{75}$, **T9**	226.5	0.23
$PDMA_{225}$-*b*-P*L*LA_{50}-*b*-$PDMA_{225}$, **T10**	221.8	0.21
$PDMA_{115}$-*b*-P*L*LA_{68}-*b*-$PDMA_{115}$, **T12**	250.4	0.24
$PDMA_{315}$-*b*-P*L*LA_{68}-*b*-$PDMA_{315}$, **T13**	238.3	0.21

* D_h and PD by DLS in methanol.

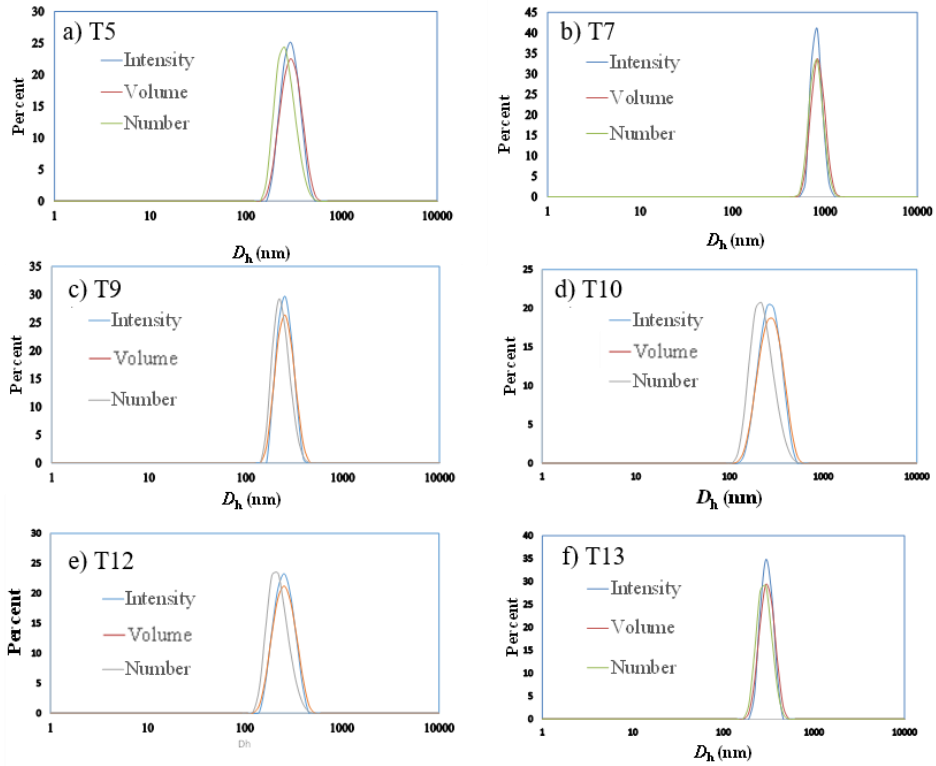

Figure 2.11 The dispersity trace of micelles achieved from polymer **T5** (a), **T7** (b), **T9** (c), **T10** (d), **T12** (e) and **T13** (f) by DLS analysis.

2.3.6 Tuning the size and morphology of the assemblies by changing the hydrophobic and hydrophilic block length

The morphology and size of all the assemblies were further characterised by transmission electron microscopy (TEM). Successful CDSA results were observed for all triblock terpolymers using this simple methanol dissolution methodology, where unique morphologies of low dispersity confirmed the results attained by DLS analysis. A clear transition from diamond-shaped lamellae to cylinders can be observed on changing the block lengths of the triblock copolymers towards less soluble unimers (**Figure 2.12**, where the white objects in **Figure 2.12 B** are artefacts from the staining). The morphological transition observed by changing copolymer composition is in agreement with our previous research,[18] and has also been observed by others.[19]

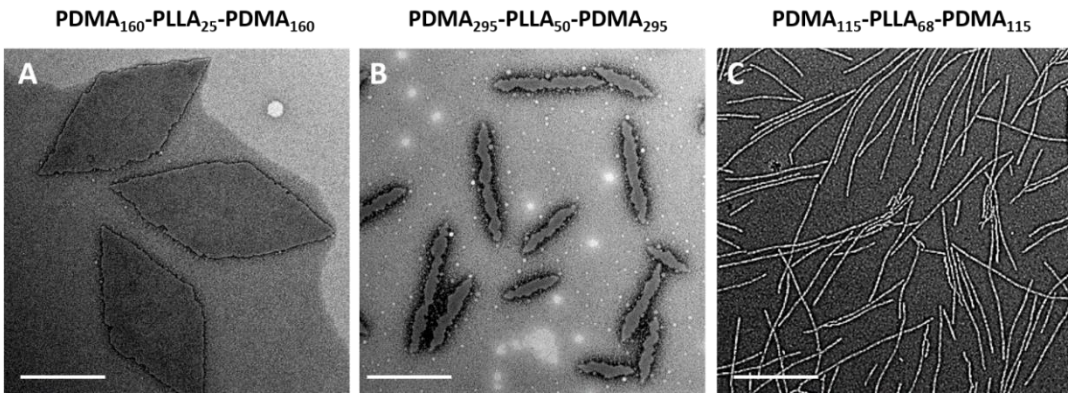

Figure 2.12 TEM images of micelles obtained from CDSA of the series of PDMA-*b*-PLLA-*b*-PDMA triblock copolymers **T4** (A), **T11** (B), **T12** (C). Samples were negatively stained using uranyl acetate. Scale bar = 1 μm.

Specifically, with shorter hydrophobic crystalline PLLA blocks (low degree of polymerisation DP = 32) and a sufficiently long hydrophilic coronal blocks (hydrophobic weight 11%, for example), diamond-shaped lamellae were achieved (**Figure 2.13 E**). Notably, these 2D sheets exhibited a regular diamond shape, where the average width and length is 1.0 ± 0.1 μm and 2.3 ± 0.2 μm respectively, which is in agreement with previous work. As the hydrophobic weight increased from 11% to 15% (**Figure 2.13 F**), sharp platelet assemblies were attained with slightly different average lengths and widths of 2.9 ± 0.2 and 0.9 ± 0.1 μm respectively. However, on decreasing the corona length, with a hydrophobic weight of 25%, elongated lamella or cylinders (width of 55 ± 6 nm) were obtained (**Figure 2.13 G**). Samples were further characterised by atomic force microscopy (AFM) and on graphene oxide (GO) covered grids by TEM to confirm that the staining method has no impact on the results (**Figure 2.14**). It should also be noted that all of these assemblies were left to age over a month to ensure analysis of thermodynamically stable morphologies as opposed to kinetically trapped structures (**Figure 2.15**).

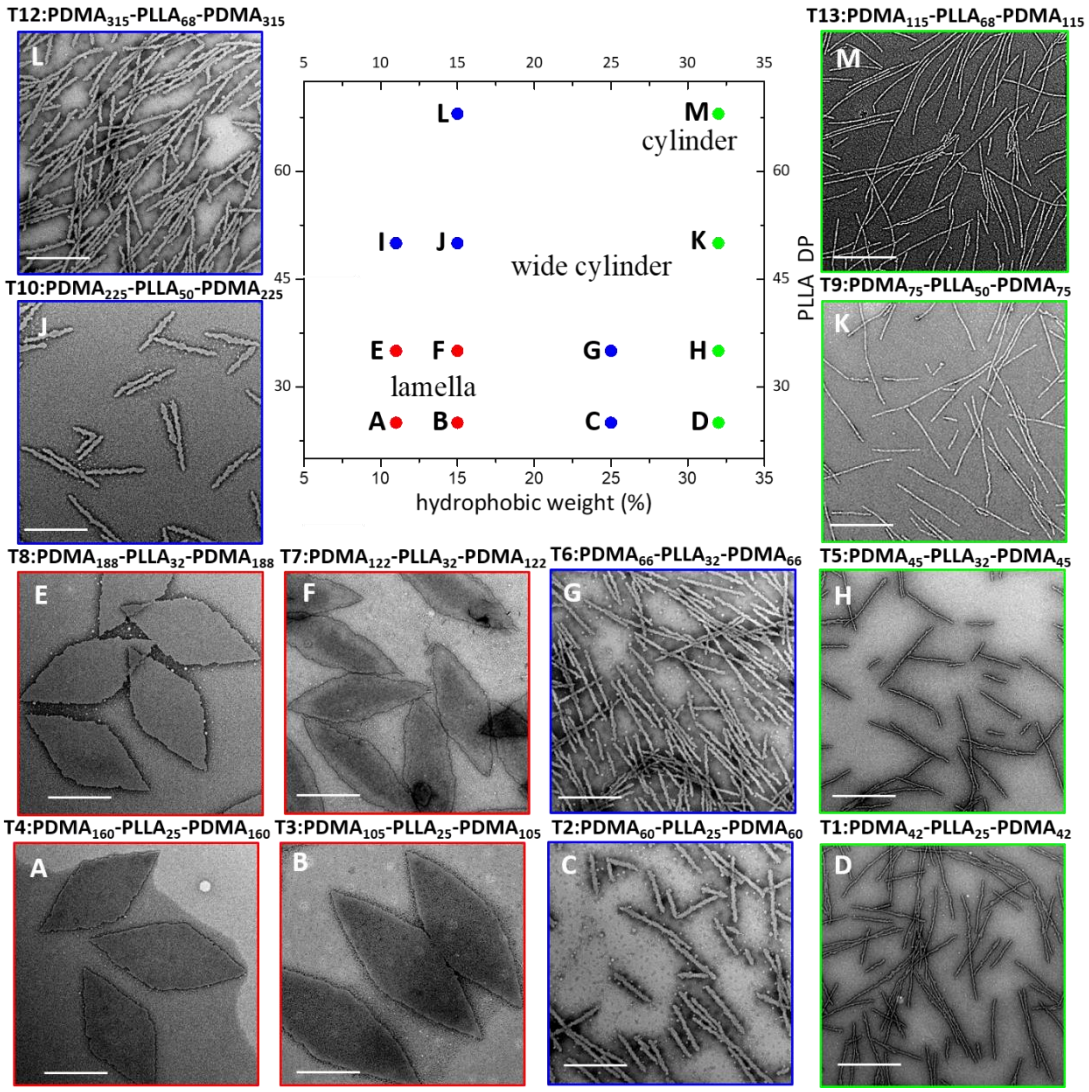

Figure 2.13 Phase diagram constructed for PDMA-*b*-PLLA-*b*-PDMA triblock terpolymers, **T1** (D), **T2** (C), **T3** (B), **T4** (A), **T5** (H), **T6** (G), **T7** (F), **T8** (E), **T9** (K), **T10** (J), **T11** (I), **T12** (L), **T13** (M). TEM characterisation of **T11** (I) is shown in **Figure 4** (B). As the target PLLA DP and the hydrophobic weight were systematically varied, the achieved morphology changed from lamellae (red) to wide cylinders (blue) and pure cylinders (green). Samples were negatively stained using uranyl acetate for TEM characterisation. Scale bar = 1 µm.

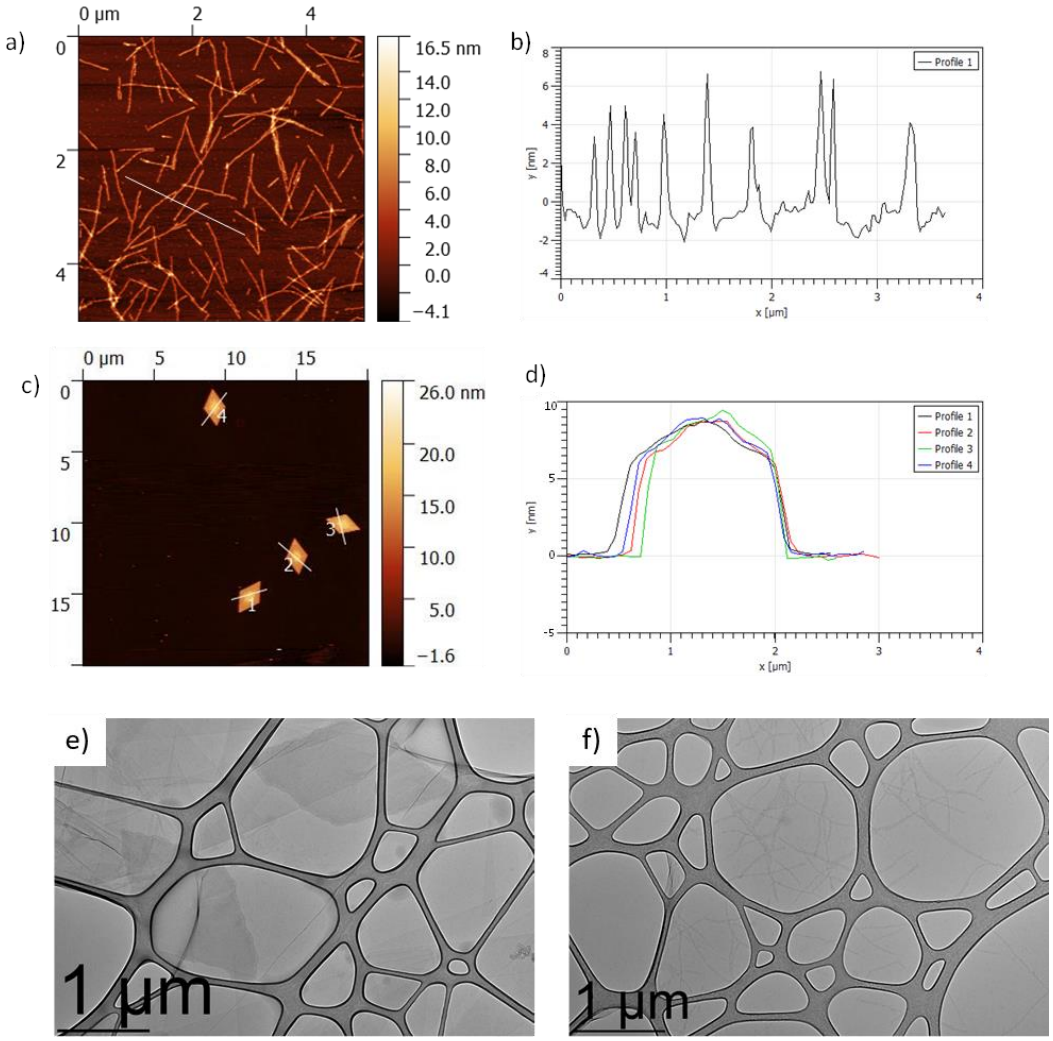

Figure 2.14 AFM and height profile of triblock copolymer **T9** cylinders (a, b) and **T8** diamond platelets (c, d). Samples were self-assembled in methanol at room temperature and aged for one day. TEM images of micelles obtained from the CDSA of triblock copolymers **T4** (e) and **T12** (f) prepared by a slow drying method on GO grids.

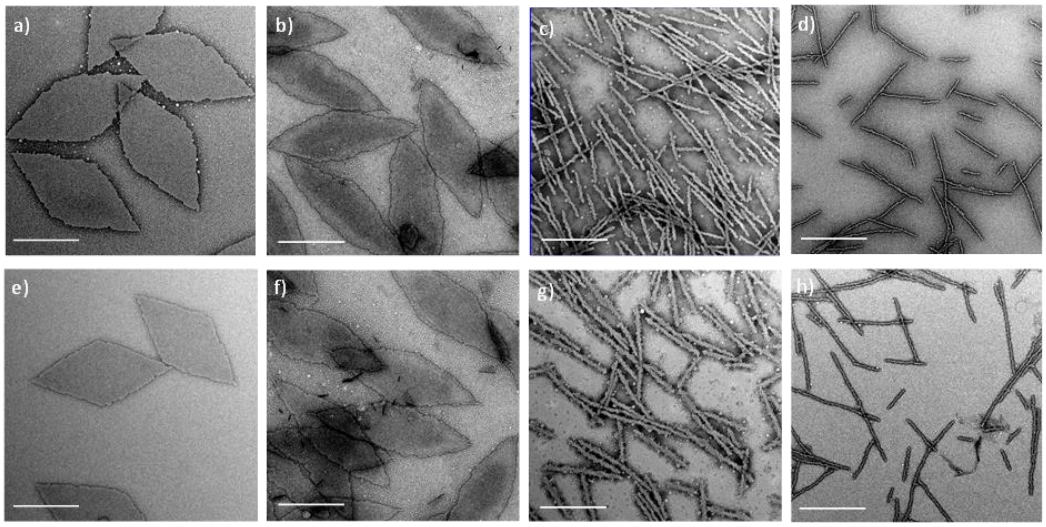

Figure 2.15 TEM images of micelles obtained from the CDSA of triblock copolymers **T8** (a), **T7** (b), **T6** (c), **T5** (d) after aging for one day. TEM images of the same assembled samples after one month (**T8** (e), **T7** (f), **T6** (g), **T5** (h)). Samples were negatively stained using uranyl acetate for TEM characterisation. Scale bar = 1 μm.

Based on these observations and in line with our previous results, we determined that the solubility of the polymers were of great significance in the CDSA process of these polymers. Block copolymers with a longer corona are more soluble, and thus remain as unimers undergoing a slower crystallisation process in forming large intact crystals (platelets), whereas, on the other hand, polymers with shorter corona are less soluble in methanol and thus may form aggregates before crystallisation, leading to a less-crystalline cylindrical morphology. This is further confirmed by wide angle X-ray scattering (WAXS) characterisation (**Figure 2.16**). Accordingly, our results (**Figure 2.13 H**) show thinner cylindrical assemblies (25.1 ± 3 nm in width) on increasing the hydrophobic ratio, which is consistent with our assumption.

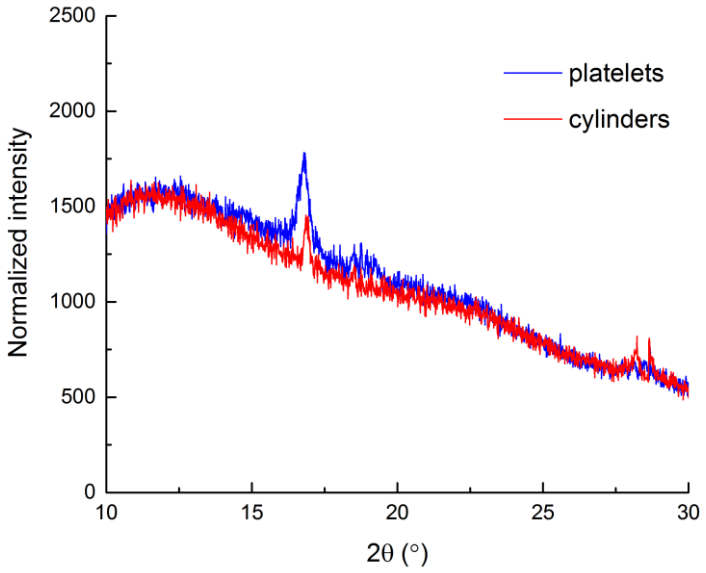

Figure 2.16 WAXS diffractogram of PDMA$_{188}$-*b*-PLLA$_{32}$-*b*-PDMA$_{188}$ (**T8**) diamond platelets and PDMA$_{66}$-*b*-PLLA$_{32}$-*b*-PDMA$_{66}$ (**T6**) cylinders showing the 2θ peak at *ca.* 16 ° characteristic of crystalline PLLA.

Based on our success in utilising corona block lengths to tune CDSA nanostructures, we then investigated the impact of altering core block lengths. Maintaining the same hydrophobic ratio, we decreased the core block length from PLLA$_{32}$ to PLLA$_{25}$ to probe the influence of a shorter core block. TEM imaging revealed assemblies similar to those achieved with the same hydrophobic weight (with PLLA$_{32}$), further confirming our solubility hypothesis (**Figure 2.13 A-D**). Similarly, when the core block was extended further (PLLA$_{50}$ and PLLA$_{68}$), the CDSA results of the corresponding triblock copolymers at 15% hydrophobic weight PDMA$_{225}$-*b*-PLLA$_{50}$-*b*-PDMA$_{225}$ (**T10**, **Figure 2.13 J**) and PDMA$_{315}$-*b*-PLLA$_{68}$-*b*-PDMA$_{315}$ (**T13**, **Figure 2.13 L**) revealed cylinders of greater width as opposed to 2D platelets, where the widths were measured at 55 ± 4 nm for both cylinders. Consistently, a similar phenomenon was obtained from a series with 11% hydrophobic ratio (**Figure 2.17**). This morphological transition can also be explained using a solubility approach.

Although the hydrophilic block was similar for each series of polymers, the comparatively longer core length resulted in a difficulty to solubilise as unimers. Therefore, shorter core length triblock copolymers led to 2D platelets, while a longer core length yielded cylindrical assemblies. As the corona block length of $PLLA_{50}$ and $PLLA_{68}$ was extended (**Figure 2.13, K** and **M**), thinner, conventional cylinders of widths 18.1 ± 2.0 nm, 17.3 ± 2.0 nm, respectively, were achieved, similar to the morphological transition from **G** to **H** (**Figure 2.13**). According to the summarized phase diagram (**Figure 2.13**), as a consequence of the gradual decrease of the solubility from left bottom to top right, the assembly morphology undergoes a gradual transition from 2D diamond platelets to 1D cylinders, where a 1D wide cylinders can be considered as a 'transition state' morphology.

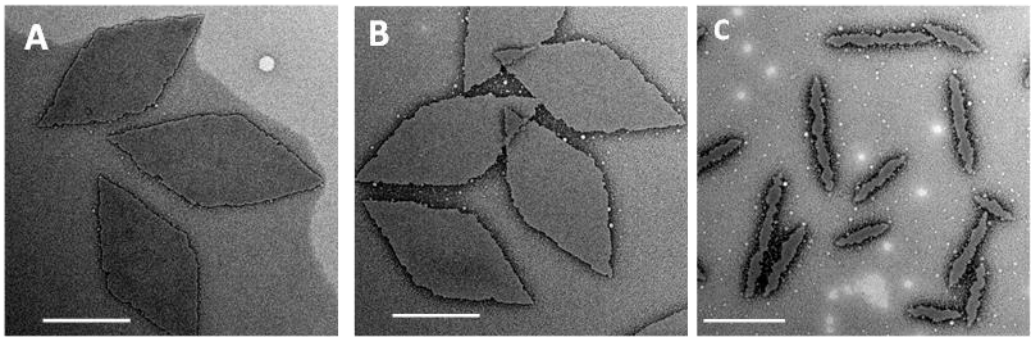

Figure 2.17 TEM images of micelles obtained from the CDSA of triblock copolymers **T4** (A), **T8** (B), **T11** (C). Scale bar = 1 μm.

2.3.7 Comparison of the diblock to triblock system

In order to draw comparisons between di- and tri- block systems, we investigated the behaviour of the diblock copolymers PDMA-*b*-PLLA as a comparison to the terpolymers discussed above. Assemblies in methanol at room temperature (using the same approach as triblock copolymer system) were unsuccessful (**Figure 2.18**) since clear solutions could not be obtained, presumably because of the lack of the third PDMA block solubilising the polymer. However, it was previously shown that the solubility of the polymer was required to match that of the solvent for optimum nanostructure formation. To apply this to triblock and diblock copolymers, we initially observed the Tyndall effect using a series of alcoholic solvents.

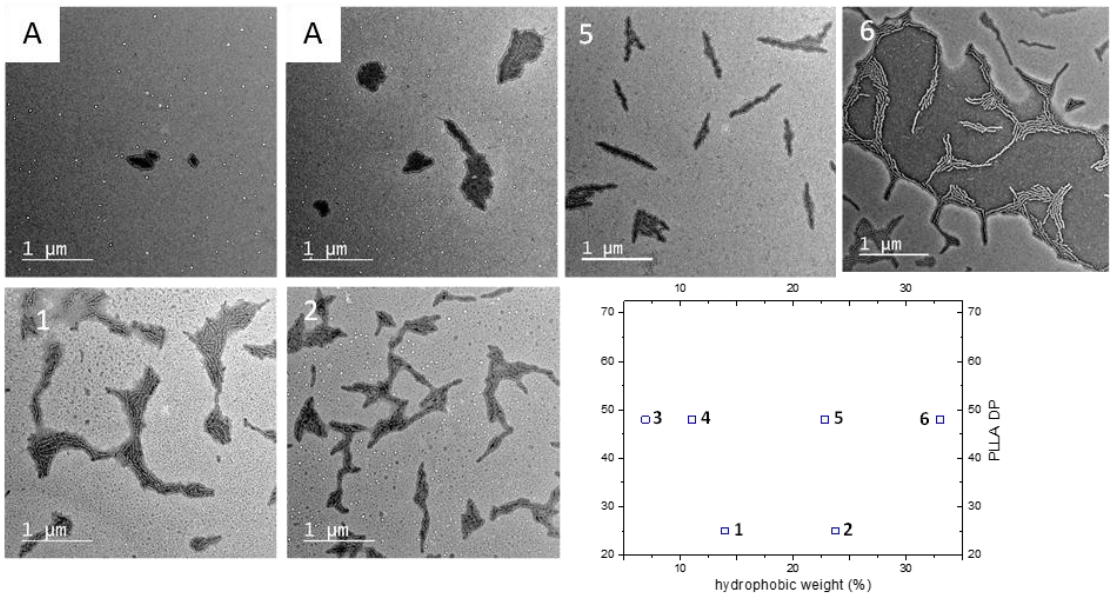

Figure 2.18 Assemblies achieved from PDMA-*b*-PLLA diblock copolymers **D6** (A)**, D5** (B), **D4** (C), **D3** (D), **D2** (E), **D1** (F) in methanol at room temperature. Samples were prepared by slow drying on carbon grids and were negatively stained using uranyl acetate for TEM characterisation. Scale bar = 1 µm.

In the triblock copolymer system, as expected, the strongest Tyndall effect could be observed in methanol (**Figure 2.19A**), which indicates a much larger morphology (or a greater number of assemblies), whereas, for the diblock system, the most outstanding Tyndall effect was observed in ethanol. For triblock copolymers, a blend of spheres, cylinders and incomplete platelets were obtained in ethanol (**Figure 2.19 E**). This can be attributed to the much greater solubilisation of the triblock copolymer, leading to limited crystallisation and , hence, mixed morphologies. The corresponding assemblies in methanol were pure intact diamonds (**Figure 2.19 C**), which supports the assumption that CDSA of triblock copolymers is easier to achieve in methanol. Similarly, for diblock copolymers, the cylindrical assemblies (**Figure 2.19 D**) achieved in methanol are less ordered than the 2D platelets (**Figure 2.19 F**), which indicates ethanol as the optimal alcoholic solvent.

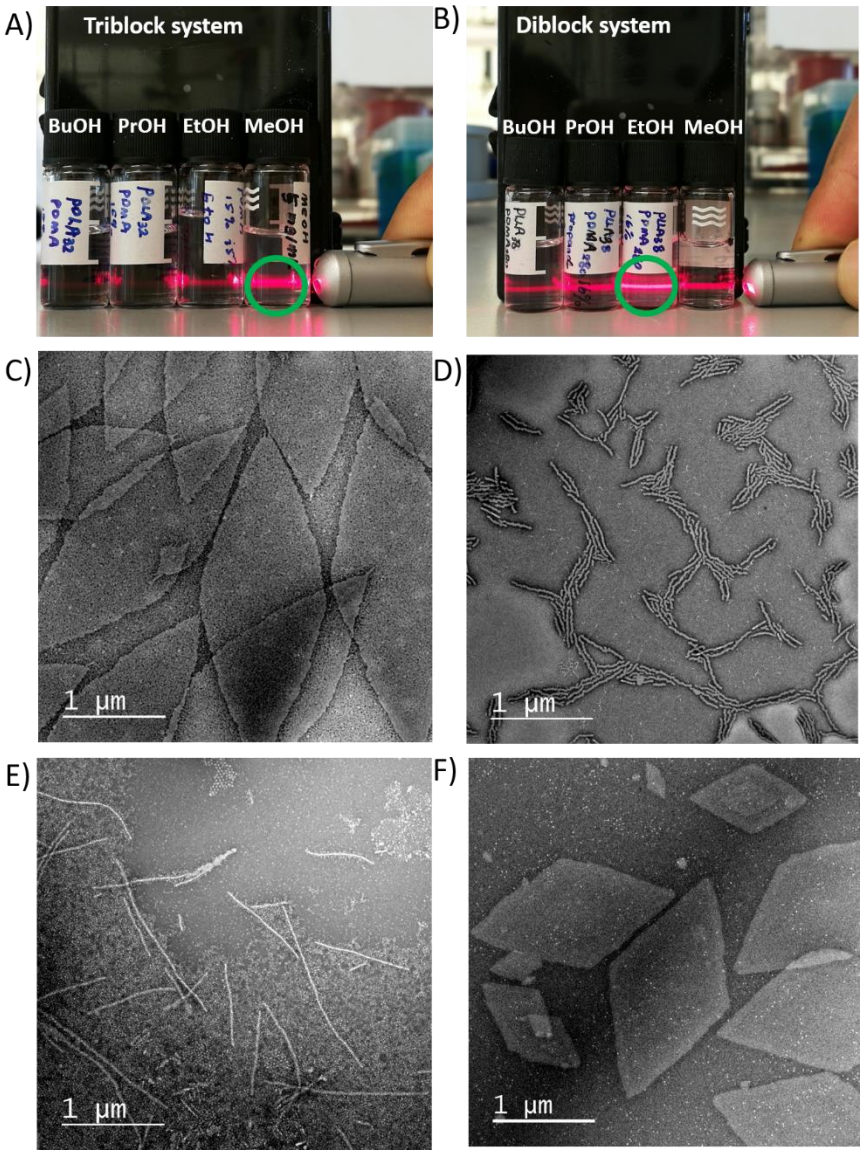

Figure 2.19 Triblock copolymer **T3** and diblock copolymer **D2** (with similar block lengths) were dissolved in different alcoholic solvents, i.e. methanol, ethanol, *n*-propanol, *n*-butanol, at a concentration of 5 mg mL^{-1}. The assembly solution was heated to 90 °C before cooling to room temperature and aged for one day. A laser pen was used to monitor the Tyndall effect of the triblock copolymer (A) and the diblock copolymer (B). TEM characterisation of the assemblies of polymers **T3** (C) and **D2** (D) in methanol and polymers **T3** (E) and **D2** (F) in ethanol. Samples were negatively stained using uranyl acetate for TEM characterisation.

To further confirm this assumption, d_4-methanol and d_6-ethanol were used to detect the assembly results of triblock copolymer on a smaller scale. After ageing, the d_4-methanol solution gradually became turbid and exhibited a stronger Tyndall effect than the corresponding d_6-ethanol solution (**Figure 2.20**). ^{1}H NMR spectroscopic

analysis revealed a considerable suppression of the L-lactide proton signals in d_4-methanol (**Figure 2.21**) after the assembly process (35% reduction compared to the original integral). The assemblies in d_6-ethanol revealed a much lower suppression such that, after the assembly process (**Figure 2.22**), a reduction of only 8% was observed. These results indicate that more unimers participate in the assembly process in methanol, which consolidates our initial conclusion from the Tyndall effect.

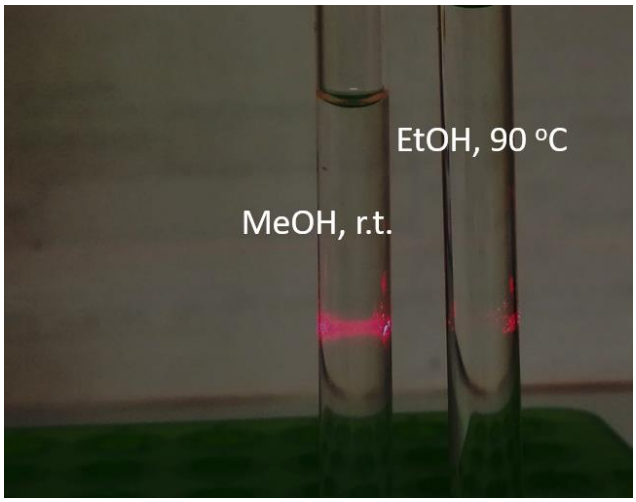

Figure 2.20 PLLA based triblock copolymer **T3** was assembled in methanol and ethanol (5 mg mL^{-1}). Tyndall phenomenon was observed.

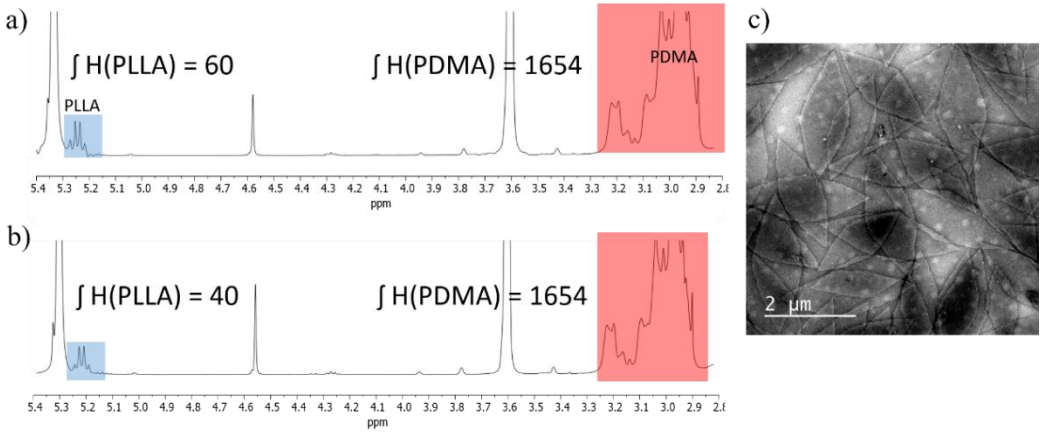

Figure 2.21 ^{1}H NMR spectra of PLLA based triblock copolymer **T3** assembled in d_4-methanol before aging (a) and after aging for two days (b). The corresponding TEM results showed intact diamonds (c).

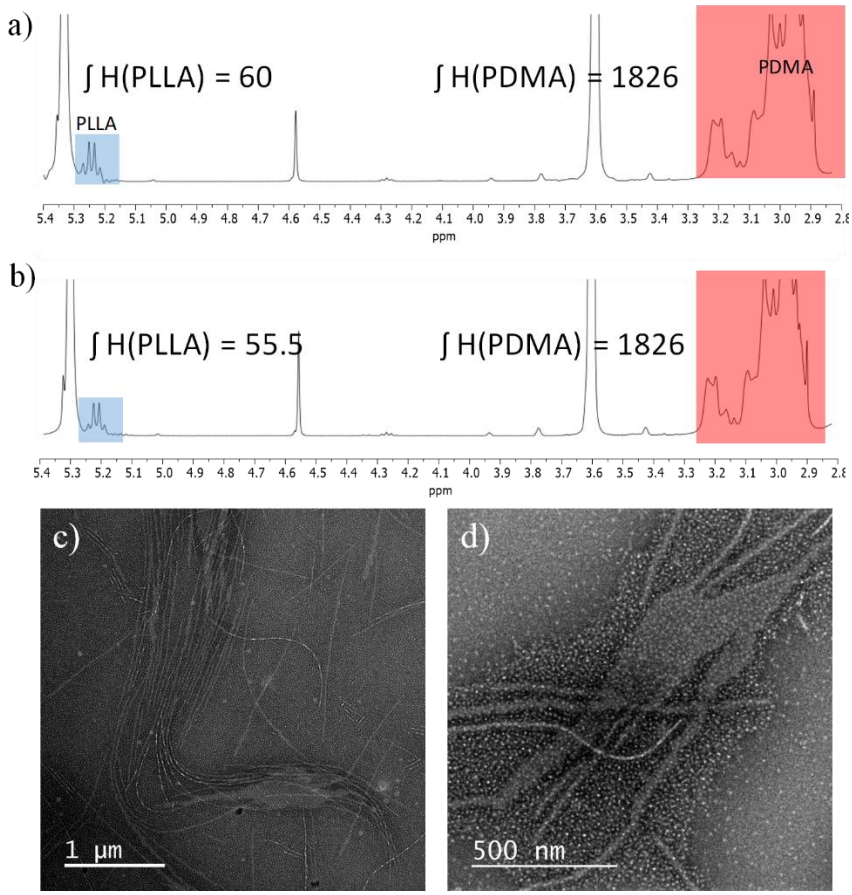

Figure 2.22 ^{1}H NMR spectra of PLLA based triblock copolymer **T3** assembled in d_6-ethanol before aging (a) and after aging for two days (b). The corresponding TEM results showed a blending of spheres, cylinders and incomplete platelet (c, d).

Similar to the triblock system, a phase diagram can be produced for our series of diblock copolymers assembled in ethanol (**Figure 2.23**). For $PLLA_{48}$-*b*-$PDMA_x$ diblock copolymers, as the corona lengths declined gradually (from 950 to 145), the assembly evolved from 2D platelets to a transition state (mixtures of diamond platelets and cylinders) and, finally, to a pure cylindrical phase. The same trend was also observed in the $PLLA_{25}$-$PDMA_x$ diblock copolymers on the basis of TEM characterisation. Using the same hypothesis, the enhanced solubility, as a consequence of the longer corona, contributes to the formation of well-ordered crystalline 2D platelets, while, conversely, the less soluble polymers (shorter corona blocks) lead to cylindrical assemblies.

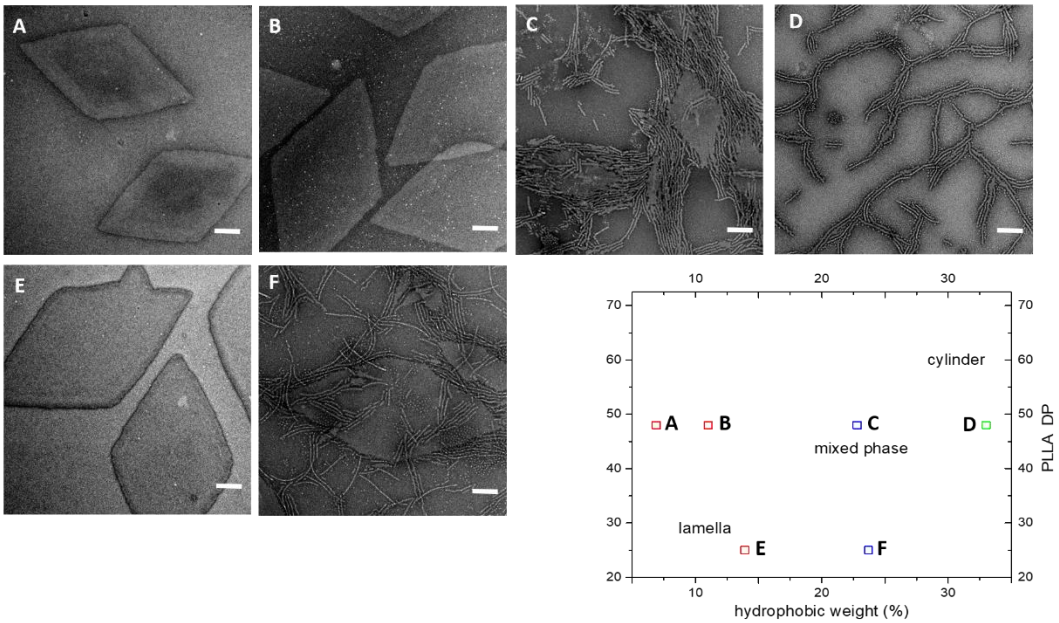

Figure 2.23 Phase diagram constructed for PDMA-*b*-P*L*LA diblock copolymers **D6** (A), **D5** (B), **D4** (C), **D3** (D), **D2** (E), **D1** (F). As target PLLA DP and the hydrophobic weight were systematically varied, the achieved morphology changed from lamella (red hollow square) to mixed phase (blue) and to cylinder (green). Scale bar = 1 μm.

As such, we propose a more generalised phase diagram encompassing both PLLA-containing di- and triblock copolymer systems (**Figure 2.24**), which consolidates our findings, i.e. for the CDSA process of PLLA based copolymers in a single alcoholic solvent, the solubility of the whole polymer plays an important role in determining the morphology of the assembly. The polymers that are more soluble in the assembly solvent achieve 2D platelets (red dots on the phase diagram), while the less soluble counterparts lead to 1D cylinders (green dots on the phase diagram) with a wide cylinder 'transition state' morphology in the middle (blue dots on the phase diagram).

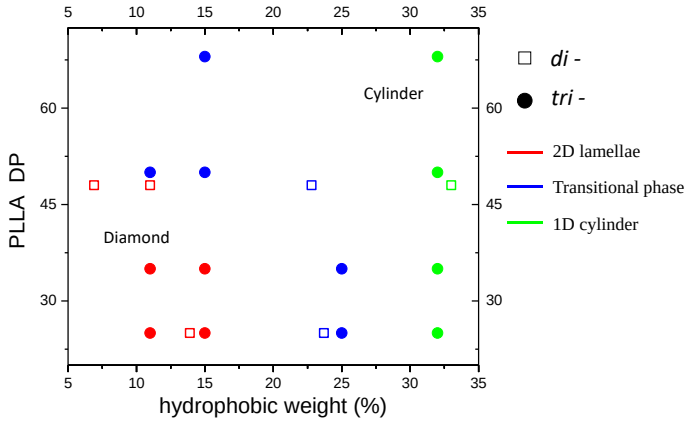

Figure 2.24 A combined phase diagram of PDMA-*b*-PLLA-*b*-PDMA triblock and PDMA-*b*-PLLA diblock copolymers. Triblock copolymers were assembled in methanol at room temperature, whereas diblock copolymers were assembled in ethanol after elevating the temperature to 90 °C for 8 hours. The solid circles represent the triblock copolymers, while the hollow squares represent the diblock copolymers. As the target PLLA DP and the hydrophobic weight were systematically varied, the achieved morphology ranged from 2D lamellae (red) to 'transition state' wide cylinders (blue) and pure cylinders (green).

2.4 Conclusion

We have prepared a series of well-defined PDMA-*b*-PLLA-*b*-PDMA triblock copolymers through a combination of RAFT polymerisation and ROP. We have used a simple single component solution-phase methodology, where we have been able to show shape-controlled CDSA for triblock copolymers through simple dissolution without any heating/cooling cycles.

A morphological transition from 2D platelets to 1D cylinders was revealed through detailed investigation of the CDSA process by alternating the core/corona block lengths. When the solvophilic corona length is increased, unimers are more soluble, leading to a slower crystallisation process and fully-formed 2D crystalline platelets. Similarly, shorter corona block copolymers are less soluble and thus aggregate before crystallisation, limiting the extent to which the crystalline block can adopt a preferred crystal conformation, forming cylindrical assemblies with a few crystal defects. While the trends observed are consistent across both di- and tri- block copolymer morphologies, we propose that the increased hydrophilicity of the copolymer system requires a more hydrophilic solvent to realise assemblies with controlled morphology.

Access to these uniform triblock copolymer organic nanomaterials with different morphologies, without the need of organic solvents and temperature control, greatly simplifies access to the sub-micro biocompatible assemblies which may show promise as new class of drug carrier for further biomedical application.[20, 21]

2.5 Experimental Section

2.5.1 Materials

Chemicals and solvents were purchased from Sigma-Aldrich, Acros, Fluka, TCI, Fisher Chemical, Alfa Aesar or VWR. L-Lactide was purchased from Corbion-Purac and recrystallised once from dichloromethane and twice from toluene. The monomer was dried over 3 Å molecular sieves for 3 days and recrystallised from toluene. 1,8-diazabicyclo[5.4.0]undec-7-ene (DBU) and (-)-sparteine were distilled over CaH_2 before use. Bis(trifluoromethyl)phenyl)-3-cyclohexyl-thiourea was prepared and purified as reported.[9] 2,2'-azobis(isobutyronitrile) (AIBN) was received from Molekula. After recrystallisation from methanol, it was stored at 4 °C. Deuterated solvents were used as received from Apollo Scientific. Raft agent 2-(dodecylthiocarbonothioylthio)-2-methylpropionic acid (DDMAT) was synthesised based on previous work.[22]

2.5.2 Instrument

Proton nuclear magnetic resonance (^{1}H NMR) spectra were recorded on a Bruker AV-400 spectrometer at 400 MHz. All spectra were recorded in $CDCl_3$ unless otherwise stated. The chemical shifts were reported as δ in parts per million and quoted downfield from the internal standard tetramethylsilane (δ = 0 ppm). Diffusion-ordered spectroscopy (DOSY) NMR spectroscopy was performed on a Bruker AV-500 AVANCE spectrometer equipped with a 5-mm broadband observe (BBO) z-axis gradient probe capable of generating nominal

maximum field strengths of 53.5 G cm^{-1}. The measurement was performed using stimulated echo and LED pulse sequences incorporating bipolar-gradient pulses for diffusion, using a diffusion time of 100 ms and a LED delay of 5 ms. For each experiment, pulsed field gradients with a duration of 2.5 ms followed by a recovery delay of 200 μs were applied with increases from 5% to 95% of the maximum strength in 32 equally spaced steps. Experiments were carried out on samples at a polymer concentration of 10 mg mL^{-1} in deuterated chloroform with active temperature regulation at 298 K. The DOSY spectrum was processed by the Bruker Topspin S3 software package (version 2.1).

Size exclusion chromatography (SEC) was performed using an Agilent 1260 Infinity Multi-Detector GPC System fitted with a refractive index and UV detector, and equipped with a guard column (Varian PLGel) and two PLGel 5 μm mixed-D columns. The mobile phase was DMF with 5 mM NH_4BF_4, at a flow rate of 1 mL min^{-1} at 50 °C. All data were analysed using Cirrus v3.3 and Agilent GPC/SEC software v1 with calibration curves produced using Varian Polymer Laboratories linear PMMA standards. Mass spectra were obtained using a Bruker Ultraflex II matrix-assisted laser desorption/ionization time-of-flight (MALDI-ToF) mass spectrometer. The MALDI-ToF samples were prepared using a trans-2-[3-(4-*t*-butyl-phenyl)-2-methyl-2-propenylidene] malononitrile (DCTB) matrix and sodium trifluoroacetate (NaTFA) as a cationization agent. Samples were prepared as follows: DCTB (2 μL, 10 mg mL^{-1} in tetrahydrofuran), sample (2 μL, 1 mg mL^{-1} in tetrahydrofuran) and NaTFA (2 μL, 0.1 mg mL^{-1} in tetrahydrofuran) were added to the MALDI-ToF plate successively. The samples were measured in reflection ion mode and calibrated using SpheriCal (1200-8000 g mol^{-1}) standards.

Transmission electron microscopy (TEM) was performed using a JEOL 2100FX at 200 kV. TEM samples were prepared on a formvar/carbon film TEM grid. In short, 2 μL of sample solution (1 mg mL^{-1}) was deposited on a grid and left air drying. 5 μL of uranyl acetate (UA, 1%) solution was then dropped on the grid and left for 60 seconds before blotting. The sample was kept in a desiccator overnight before characterisation. TEM samples were also prepared by using graphene oxide (GO)-covered TEM grids which are almost electron transparent and give excellent contrast.[23] Generally, one drop of the sample solution (2 μL) was added onto a GO grid, and, after 2 min, the solution was blotted away before drying. The GO grids were prepared as following: lacey carbon films on mesh copper grids (400 mesh, Cu, Elektron Technology UK LTD) were cleaned by air plasma from a glow-discharge system (2 min, 20 mA) to improve the hydrophilicity of the grid surface. One drop of GO solution (0.10−0.15 mg mL^{-1}) was deposited on each grid and left to air-dry.

Dynamic light scattering (DLS) was conducted using a Malvern Zetasizer Nano instrument equipped with a 4 mW He-Ne 633 nm laser module at 25 ℃, with data analysis using Malvern DTS 6.20 software. Measurements were carried out at a detection angle of 173° (backscattering). All determinations were made in triplicate unless otherwise stated (with 10 measurements recorded for each run).

Wide Angle X-ray Scattering (WAXS) was performed on a Panalytical X'Pert Pro MPD equipped with a Cu Kα1 hybrid monochromator as the incident beam optics. Typically, *ca.* 30 mg of freeze-dried particles was placed in a 10 mm sample holder, and standard "powder" 2θ−θ diffraction scans were carried out in the angular range from 10° to 30° 2θ at room temperature.

2.5.3 Synthesis of PLLA homopolymers

Ring opening polymerisation (ROP) of L-lactide was carried out using a dual-headed initiator, 1,3-propandiol, with an organic catalyst, DBU. Typically, for the synthesis of homopolymer $PLLA_{32}$, L-lactide (2.5 g, 17.35 mmol) monomer, 1,3-propandiol (34.59 µl, 0.48 mmol), DBU (25.94 µl, 0.17 mmol) and dichloromethane (25 mL) were mixed in an ampoule in a glove box, under nitrogen. The solution was left stirring at room temperature for 5 minutes for 100% monomer conversion. The mixture was purified by precipitation twice in hexane and once in methanol and dried *in vacuo* to yield a white powder (80% yield). $M_{n,\,NMR}$ = 4.6 kDa, DP = 32. $M_{n,\,SEC}$ = 10.4 kDa, $Đ_M$ = 1.05. ^{1}H NMR (400 MHz, $CDCl_3$): δ (ppm) 5.15 (q, 1 H, $^3J_{H\text{-}H}$ = 7.1, Hz OC*H*(CH_3)CO), 4.43–4.29 (m, 2 H, HOC*H*(CH_3)CO), 4.19 (t, 4 H, $^3J_{H\text{-}H}$ = 5.7 Hz, OC*H*$_2$CH_2C*H*$_2$O), 2.09–1.90 (m, 2 H, OCH_2C*H*$_2$CH_2O), 1.57 (d, 3 H, $^3J_{H\text{-}H}$ = 7.1 Hz, OCH(C*H*$_3$)CO).

2.5.4 Synthesis of dual functionalised macro-CTA

RAFT agent 2-(dodecylthiocarbonothioylthio)-2-methylpropionic acid (DDMAT), synthesised according to a previous method,[24] was coupled to the PLLA polymer backbone by esterification. In a typical coupling reaction, $PLLA_{32}$ (1.4 g, 0.324 mmol), DDMAT (1.18 g, 3.24 mmol), DMAP (0.0396 g, 0.324 mmol) and DCC (0.668 g, 3.24 mmol) were mixed together in an ampoule with 12 mL chloroform. The solution was left stirring at room temperature for 3 days. The solution was filtered and the filtrate precipitated in diethyl ether three times and the resultant polymer was dried *in vacuo* (1.1 g, 70% yield). $M_{n,\,NMR}$ = 5.2 kDa, $M_{n,\,SEC}$ = 9.9 kDa, $Đ_M$ = 1.06. ^{1}H NMR

(400 MHz, $CDCl_3$): δ (ppm) 5.15 (q, 1 H, $^3J_{H\text{-}H}$ = 7.1 Hz, OC*H*(CH_3)CO), 4.43 – 4.29 (m, 1 H, HOC*H*(CH_3)CO), 4.19 (t, 4 H, $^3J_{H\text{-}H}$ = 5.7 Hz, OC*H*$_2$$CH_2$C*H*$_2$O), 3.26 (t, 4 H, $^3J_{H\text{-}H}$ = 7.5 Hz, SC*H*$_2$$CH_2$), 2.09 – 1.90 (m, 2 H, OCH$_2$C*H*$_2$$CH_2$O), 1.57 (d, 3 H, $^3J_{H\text{-}H}$ = 7.1 Hz, OCH(C*H*$_3$)CO). 1.24 (s, 21 H, $C_{10}H_{21}$), 0.87 (t, 3 H, $^3J_{H\text{-}H}$ = 6.8 Hz, C*H*$_3$$CH_2$).

2.5.5 Synthesis of triblock copolymers poly(*N*,*N*-dimethylacrylamide)-*b*-poly(L-lactide)-*b*-poly(*N*,*N*-dimethylacrylamide)

Dual functionalised macro-CTA was chain-extended using RAFT polymerisation with DMA as the monomer. In a typical reaction of PDMA$_{122}$-*b*-PLLA$_{32}$-*b*-PDMA$_{122}$, CTA-PLLA$_{32}$-CTA (50 mg, 0.01 mmol), DMA (0.33 ml, 3.2 mmol) and 10 mg ml^{-1} AIBN solution (16.42 µl, 0.001 mmol) were mixed in 1 mL dioxane in an ampoule. The solution was degassed *via* three freeze-pump-thaw cycles and refilled with argon. The solution was placed in an oil bath at 70 °C for 5 h. The product was precipitated in diethyl ether three times and dried in *vacuo* (90% conversion, 0.18 g, 60% yield). $M_{n,\,NMR}$ = 28.9 kDa, DP = 245. $M_{n,\,SEC}$ = 38.4 kDa, $Đ_M$ = 1.08. ^{1}H NMR (400 MHz, $CDCl_3$): δ (ppm) 5.15 (q, 1 H, $^3J_{H\text{-}H}$ = 7.1 Hz, OC*H*(CH_3)CO), 4.19 (t, 4 H, $^3J_{H\text{-}H}$ = 5.7 Hz, OC*H*$_2$$CH_2$C*H*$_2$O), 2.88 (s, 6 H, CON(C*H*$_3$)$_2$), 1.57 (d, $^3J_{H\text{-}H}$ = 7.1 Hz, 3 H, OCH(C*H*$_3$)CO), 1.24 (s, 21 H, $C_{10}H_{21}$), 0.87 (t, 6 H, $^3J_{H\text{-}H}$ = 6.8 Hz, C*H*$_3$$CH_2$).

2.5.6 Crystallisation-driven self-assembly of PDMA-*b*-PLLA-*b*-PDMA triblock copolymers and PDMA-*b*-PLLA diblock copolymers

All triblock copolymers were assembled in HPLC grade methanol. Typically, 5 mg of polymer was totally dissolved in 1 mL methanol with vortexing and sonication at room temperature. The assembly solution was left to age in a sealed vial at room temperature for one day. Diblock copolymers were assembled in ethanol. Typically, 5 mg of polymer was dissolved in 1 mL of ethanol and heated to 90 °C for 8 h before cooling to room temperature and ageing overnight.[18]

2.6 References

1. Tritschler, U.; Pearce, S.; Gwyther, J.; Whittell, G. R.; Manners, I. *Macromolecules* **2017,** 50 (9), 3439-3463.
2. Presa Soto, A.; Gilroy, J. B.; Winnik, M. A.; Manners, I. *Angewandte Chemie International Edition* **2010,** 49 (44), 8220-8223.
3. Gädt, T.; Ieong, N. S.; Cambridge, G.; Winnik, M. A.; Manners, I. *Nature materials* **2009,** 8 (2), 144-160.
4. Wang, X.; Guerin, G.; Wang, H.; Wang, Y.; Manners, I.; Winnik, M. A. *Science* **2007,** 317 (5838), 644-647.
5. Hudson, Z. M.; Lunn, D. J.; Winnik, M. A.; Manners, I. *Nature communications* **2014,** 5 (2), 3372-3380.
6. Schöbel, J.; Karg, M.; Rosenbach, D.; Krauss, G.; Greiner, A.; Schmalz, H. *Macromolecules* **2016,** 49 (7), 2761-2771.
7. Zhou, H.; Lu, Y.; Qiu, H.; Guerin, G.; Manners, I.; Winnik, M. A. *Macromolecules* **2015,** 48 (7), 2254-2262.
8. Petzetakis, N.; Walker, D.; Dove, A. P.; O'Reilly, R. K. *Soft Matter* **2012,** 8 (28), 7408-7414.
9. Pitto-Barry, A.; Kirby, N.; Dove, A. P.; O'Reilly, R. K. *Polymer Chemistry* **2014,** 5 (4), 1427-1436.
10. Sun, L.; Pitto-Barry, A.; Thomas, A. W.; Inam, M.; Doncom, K.; Dove, A. P.; O'Reilly, R. K. *Polymer Chemistry* **2016,** 7 (13), 2337-2341.
11. Li, Z.; Sun, L.; Zhang, Y.; Dove, A. P.; O'Reilly, R. K.; Chen, G. *ACS Macro Letters* **2016,** 5 (9), 1059-1064.
12. Sun, L.; Pitto-Barry, A.; Kirby, N.; Schiller, T. L.; Sanchez, A. M.; Dyson, M. A.; Sloan, J.; Wilson, N. R.; O'Reilly, R. K.; Dove, A. P. *Nature Communications* **2014,** 5 (3), 5746-5752.
13. Wang, X. S.; Winnik, M. A.; Manners, I. *Macromolecules* **2002,** 35 (24), 9146-9150.
14. Schmalz, H.; Schmelz, J.; Drechsler, M.; Yuan, J.; Walther, A.; Schweimer, K.; Mihut, A. M. *Macromolecules* **2008,** 41 (9), 3235-3242.
15. Skey, J.; O'Reilly, R. K. *Chemical Communications* **2008,** 6 (35), 4183-4185.
16. Rizis, G.; van de Ven, T. G.; Eisenberg, A. *Angewandte Chemie International Edition* **2014,** 53 (34), 9000-9003.
17. Sun, L.; Petzetakis, N.; Pitto-Barry, A.; Schiller, T. L.; Kirby, N.; Keddie, D. J.; Boyd, B. J.; O'Reilly, R. K.; Dove, A. P. *Macromolecules* **2013,** 46 (22), 9074-9082.
18. Inam, M.; Cambridge, G.; Pitto-Barry, A.; Laker, Z. P. L.; Wilson, N. R.; Mathers, R. T.; Dove, A. P.; O'Reilly, R. K. *Chemical Science* **2017,** 8 (6), 4223-4230.
19. Hsiao, M.-S.; Yusoff, S. F. M.; Winnik, M. A.; Manners, I. *Macromolecules* **2014,** 47 (7), 2361-2372.
20. Ding, M.; Li, J.; Tan, H.; Fu, Q. *Soft Matter* **2012,** 8 (20), 5414-5428.
21. Oh, J. K. *Soft Matter* **2011,** 7 (11), 5096-5108.
22. Moughton, A. O.; O'Reilly, R. K. *Chemical Communications* **2010,** 46 (7), 1091-1093.
23. Patterson, J. P.; Sanchez, A. M.; Petzetakis, N.; Smart, T. P.; Epps III, T. H.; Portman, I.; Wilson, N. R.; O'Reilly, R. K. *Soft Matter* **2012,** 8 (12), 3322-3328.
24. Wilks, T. R.; Pitto-Barry, A.; Kirby, N.; Stulz, E.; O'Reilly, R. K. *Chemical Communications* **2014,** 50 (11), 1338-1340.

Chapter 3. Monodisperse cylindrical micelles with controlled length and composition from polylactide based block copolymers *via* living crystallization driven self-assembly

3.1 Abstract

In this chapter, PLLA core polymers were synthesised and self-assembled using different hydrophilic corona-forming blocks, i.e. poly(4-vinyl pyridine) (P4VP), poly(*N*-acryloylmorpholine) (PNAM), and poly(*N*-Hydroxyethyl acrylate) (PHEA) to expand the scope of the crystallisation-driven self-assembly of PLLA-based ABA type copolymers. By generating crystalline seeds using these polymers, fine control over particle size could be achieved by carefully changing the unimer to seed ratio. Finally, it was demonstrated that triblock co-micelles with spatially distinct PDMA and P4VP coronal segments can be accessed from the sequential addition of dissolved P4VP-*b*-PLLA-*b*-P4VP to preformed PDMA-*b*-PLLA-*b*-PDMA micelles.

3.2 Introduction

The precise control of the size and uniformity of non-spherical micelles such as 1D or 2D polymer nanostructures remains a major challenge.[1, 2] As illustrated in **Chapter 1**, the discovery of a seeded growth or 'living' CDSA method has emerged as a promising approach to solve this problem.[3] Living CDSA is analogous to living covalent polymerisation of monomers whereby crystalline chain ends of micelles can initiate the growth of larger structures by continuous addition of unimers. The length of the resultant nanostructures formed by living CDSA is dependent on the unimer to seed ratio just as living polymerisation protocols provide access to polymers with tunable length. Following the success of living CDSA with poly(ferrocenylphenylmethylsilane) (PFDMS) based block copolymers,[4, 5] other semi-crystalline polymers (e.g. polycaprolactone,[6, 7] polyethylene,[8, 9] poly(3-hexylthiophene),[10, 11] and poly(*p*-phenylenevinylene),[12-14] have also been reported. The precise control over these nanoparticles provides advancement in a variety of research fields.[15]

One of the major applications of nano-sized structures formed using CDSA techniques is biomedicine, when cylindrical micelles exhibit increased circulation times and enhanced targeting to specific tissues compared to spherical particles.[16] However, very few biocompatible and biodegradable semi-crystalline polymers are known to undergo CDSA, thus precise anisotropic nanoparticles that could be valuable for applications in biomedicine remain rare. Of the few examples, block copolymers with stereoregular PLLA cores have been reported to form cylindrical micelles *via* CDSA.[17, 18] However, in these cases, the micelle formation was not capable of living CDSA, thus limiting the control of micelle lengths. Although these structures have been investigated for

cellular uptake and this behavior correlated to the overall shape of the assemblies,[19] the lack of control over the micelle dimension and composition precludes a deeper understanding of the interaction between these nanoparticles and cells.

Recently, we reported a simplified CDSA method for PLLA-*b*-PDMA diblock copolymers where the unimers were directly assembled in polar protic solvents to produce 2D platelets, while the analogous ABA polymers formed wormlike 1D assemblies under similar assembly conditions.[20, 21] In this study we have expanded the corona chemistry from PDMA to poly(4-vinyl pyridine) (P4VP), poly(*N*-acryloylmorpholine) (PNAM) and poly(*N*-Hydroxyethyl acrylate) (PHEA) while keeping the PLLA core consistent in ABA type triblock polymers. Even though the hydrophilic block was varied considerably, most of the polymers were capable of assembling into fibre-like micelles using this single solvent approach. Cylindrical micelles with controllable lengths could be precisely tuned using a seeded-growth strategy and the seeds were also manipulated by the growth of polymers that contained different block arrangements and/or corona compositions.

3.3 Result and discussion

3.3.1 Synthesis of ABA type triblock copolymers

Similar to the protocol mentioned in **Chapter 2**, the triblock copolymers were synthesized with a combination of reversible addition-fragmentation chain-transfer (RAFT) polymerisation and ring-opening polymerisation (ROP) (**Scheme 3.1**). The core block of PLLA was produced after the organo-base catalysed ROP of stereo-pure lactide. Subsequently, the hydroxyl terminated PLLA was end-capped with a dithiocarbonate using a dicyclohexylcarbodiimide (DCC) esterification protocol to form a macro chain-transfer agent (CTA) suitable for a controlled radical polymerisation. Various hydrophilic vinyl monomers i.e. 4-vinyl pyridine (4-VP), *N*-acryloylmorpholine (NAM) and *N*-Hydroxyethyl acrylate (HEA) were then polymerised from the dual macro CTA (prepared in **Chapter 2**) *via* RAFT polymerisation to afford the PLLA-core triblock copolymers.

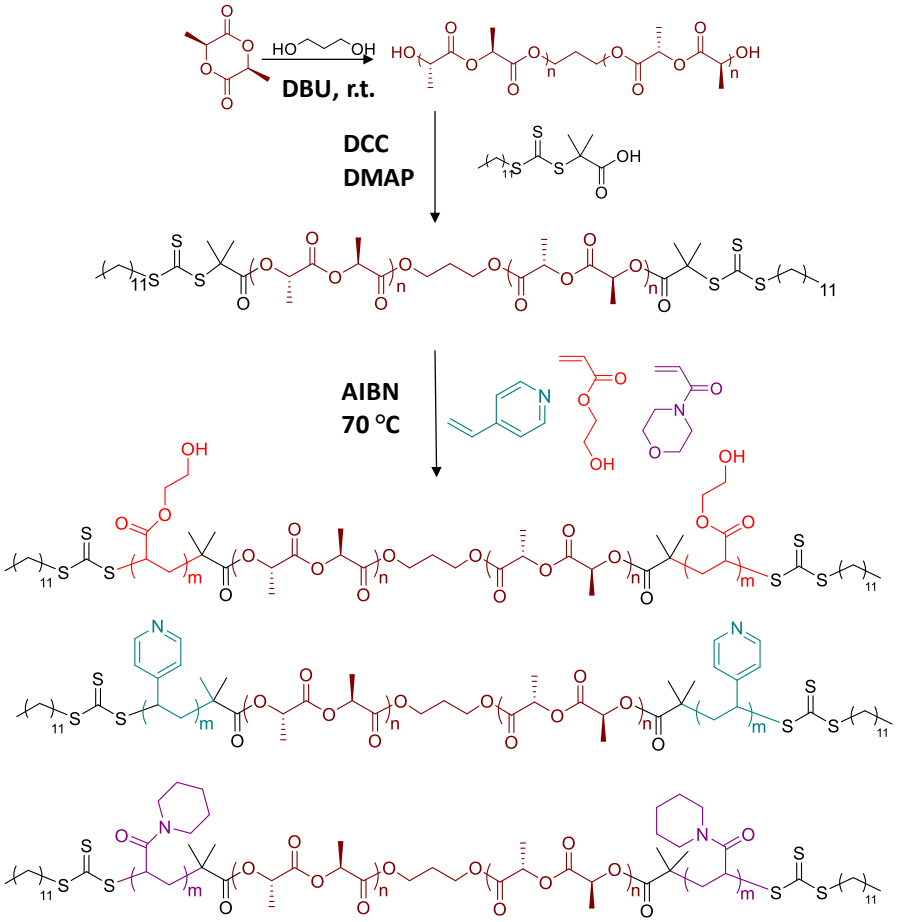

Scheme 3.1 Synthetic route for the preparation of PHEA-*b*-PLLA-*b*-PHEA, P4VP-*b*-PLLA-*b*-P4VP and PNAM-*b*-PLLA-*b*-PNAM triblock copolymers.

For each RAFT polymerisation, the monomer conversion was stopped at ≤ 70% (*ca.* 30% when using HEA as a monomer since it is notoriously challenging to polymerise in a controlled manner) in order to prevent undesirable termination reactions. The length of each block was calculated using ^{1}H NMR spectroscopy by integrating and determining the ratio of the proton on the tertiary carbon of PLLA (δ = 5.13 ppm) and the signals corresponding to protons in the hydrophilic blocks (see specific numbering in **Figure 3.1 a** (proton 1)**, b** (proton 1) and **c** (proton 3 and 4)). SEC analysis for each triblock copolymer also showed a monomodal distribution, in both UV and RI traces, and narrow dispersity ($Đ_M$ = 1.15–1.30) (**Figure 3.2 a–c**), which indicates that these polymers were suitable for self-assembly study. Full characterisation data for the

important properties of each polymer used in this chapter is provided in **Table 3.1** (polymer **4-6** were synthesized in **Chapter 2**).

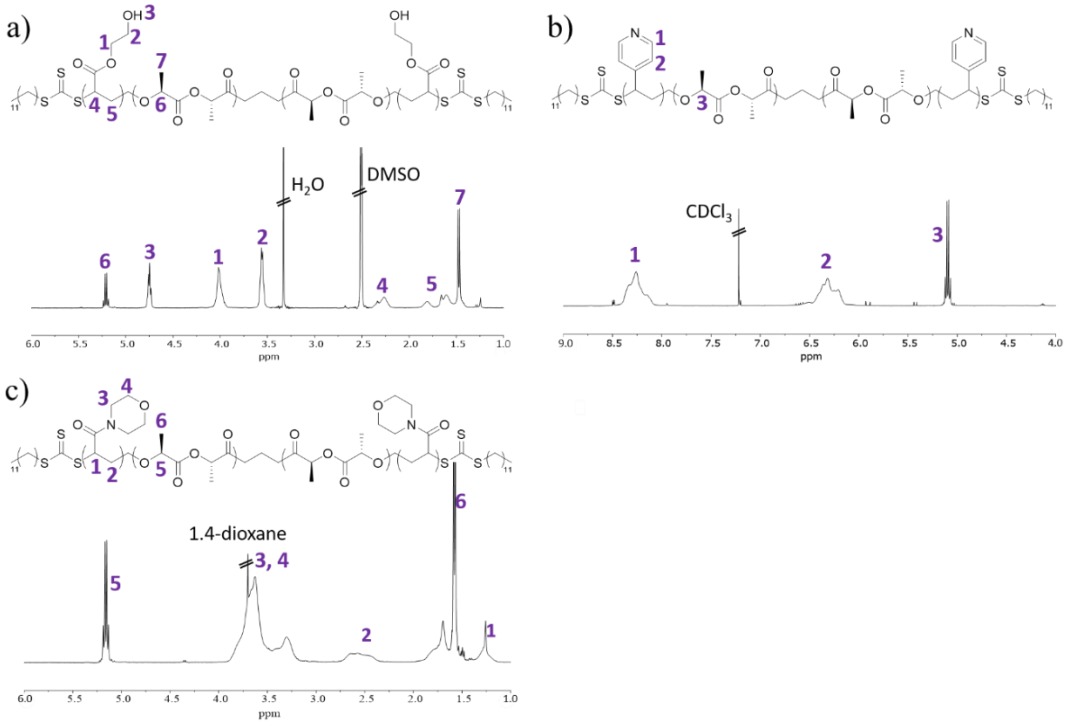

Figure 3.1 Characterisation data for ^{1}H NMR spectra (400 MHz) of (a) $PHEA_{75}$-*b*-$PLLA_{50}$-*b*-$PHEA_{75}$ (d_6-DMSO) (b) $P4VP_{70}$-*b*-$PLLA_{50}$-*b*-$P4VP_{70}$ ($CDCl_3$) (c) $PNAM_{80}$-*b*-$PLLA_{50}$-*b*-$PNAM_{80}$ ($CDCl_3$).

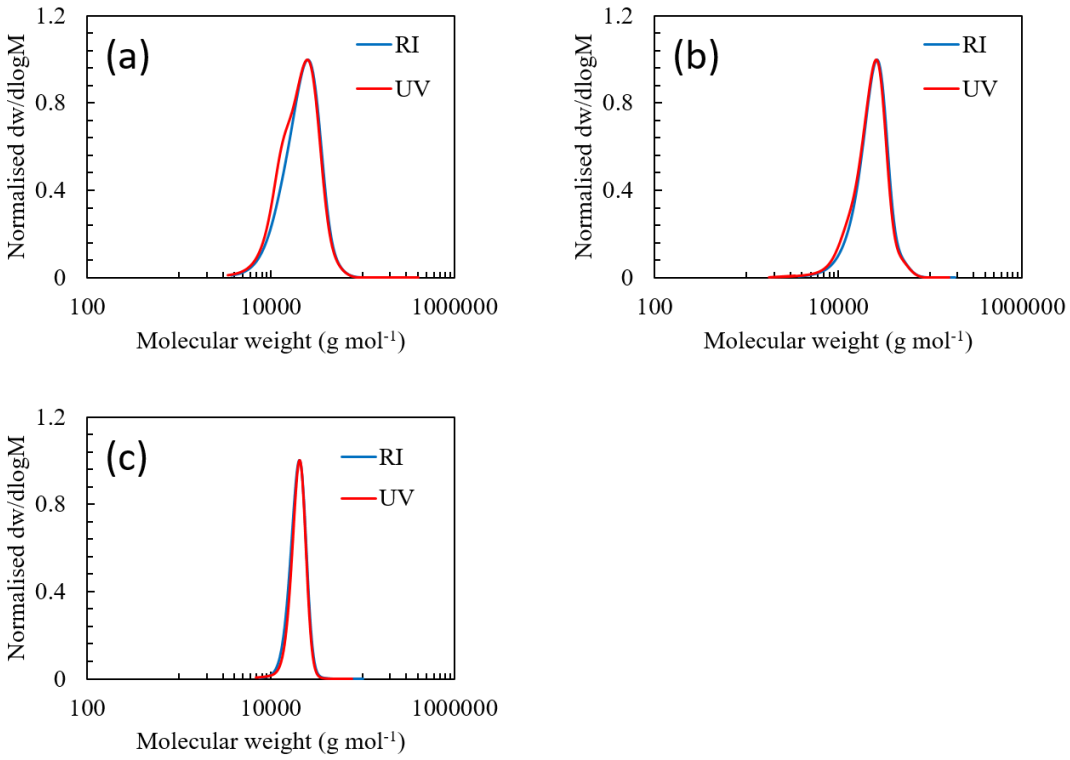

Figure 3.2 SEC chromatograms of (a) $PHEA_{75}$-*b*-$PLLA_{50}$-*b*-$PHEA_{75}$, (b) $P4VP_{70}$-*b*-$PLLA_{50}$-*b*-$P4VP_{70}$ and (c) $PNAM_{80}$-*b*-$PLLA_{50}$-*b*-$PNAM_{80}$, DMF (5 mM NH_4BF_4) was used as the eluent.

Table 3.1 Characterisation data of PXX-*b*-PLLA-*b*-PXX ABA type triblock copolymers.

Triblock copolymers	M_n **(kDa)**[a]	$Đ_M$[b]	***Conversion***
$PHEA_{75}$-*b*-$PLLA_{50}$-*b*-$PHEA_{75}$, **1**	24.6	1.28	30%
$P4VP_{70}$-*b*-$PLLA_{50}$-*b*-$P4VP_{70}$, **2**	22.0	1.23	70%
$PNAM_{80}$-*b*-$PLLA_{50}$-*b*-$PNAM_{80}$, **3**	27.0	1.15	100%
$PDMA_{75}$-*b*-$PLLA_{50}$-*b*-$PDMA_{75}$, **4**	22.1	1.14	90%
$PDMA_{115}$-*b*-$PLLA_{68}$-*b*-$PDMA_{115}$, **5**	32.6	1.13	90%
$PDMA_{122}$-*b*-$PLLA_{32}$-*b*-$PDMA_{122}$, **6**	28.9	1.08	90%

[a] Measured by ^{1}H NMR spectroscopy in (400 MHz, d_6-DMSO or $CDCl_3$). [b] Measured by SEC (DMF, 5 mM NH_4BF_4).

3.3.2 Preparation of cylindrical micelles from PXX-*b*-PLLA-*b*-PXX ABA triblock copolymers

We demonstrated in **Chapter 2** that triblock copolymers of PDMA-*b*-PLLA-*b*-PDMA (polymer **4, 5**) assembled into cylindrical micelles. In order to expand the scope of the corona functionality on the PLLA based wormlike micelles, three new ABA triblock copolymers were screened for CDSA behavior. Importantly, the dispersity of the polymers was controlled, with $Đ_M \leq 1.30$ (**Table 3.1**), in order to minimise possible disturbances to the resultant morphologies in the nanoparticles as a consequence of homopolymer presence.[22, 23] Using the previously identified assembly method for PDMA-*b*-PLLA-*b*-PDMA, the new polymers were assembled in methanol (5 mg mL^{-1}) at ambient temperature (25 °C). After two days, cylindrical micelles were obtained (**Table 3.1**, polymer **1, 2**) according to TEM analysis (**Figure 3.3**). This observation suggests that this assembly method for PLLA core-block copolymers of ABA type, reliably generates cylindrical micelles irrespective of the corona block chemistry. However, polymer **3** was not soluble in methanol, and thus did not self-assemble, precluding further analysis.

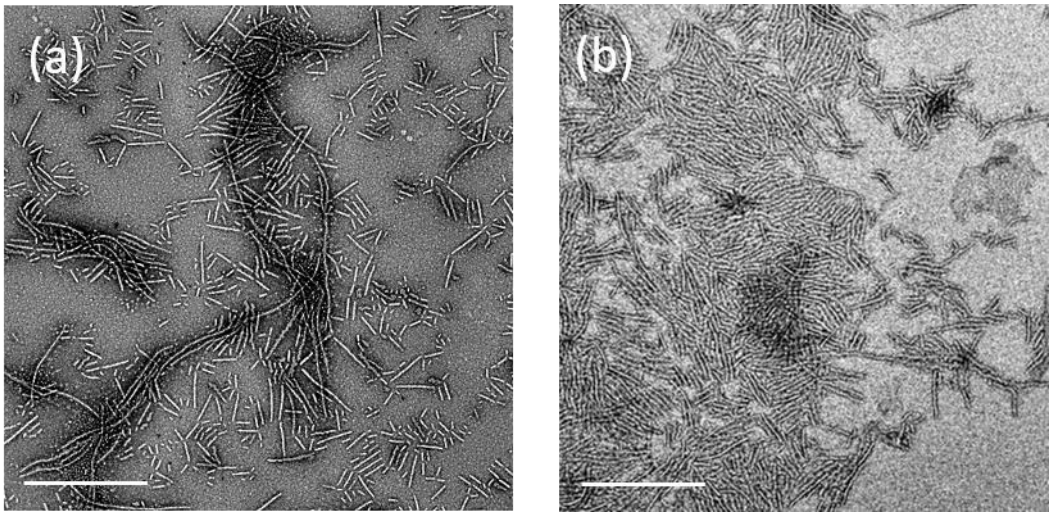

Figure 3.3 TEM micrographs of micelles obtained from the CDSA of triblock copolymers (a) polymer **1**, (b) polymer **2**. Samples were negatively stained using uranyl acetate (0.5 wt %). Scale bar = 1 μm.

3.3.3 Preparation of crystalline seeds from PLA-based block copolymers

In order to control the size and uniformity of the micelles, it is necessary to prepare well-defined crystalline seeds that serve as nuclei for living CDSA. The assembly solution (polymer **4**) was cooled to 0 °C using an ice bath and sonicated with a probe to fracture the micelles into smaller particles that were suitable as seeds. Each polymer solution was sonicated for 10 cycles of 2 min each with 10 min between the cycles in order to cool down the probe and thus prevent unwanted crystallisation as a result of local heating. Several aliquots were taken during the sonication process and characterised using TEM to monitor the changes in the micelles length (**Figure 3.4**). After sonication for 20 min in total (10 cycles), short and uniform 1D seeds *ca.* 65 nm (**Figure 3.5**, **Table 3.2**) were obtained, as analysed by TEM. Moreover, the seeds appeared to be stable in solution for at least 30 days without any undesired end-coupling or aggregation into larger particles (**Figure 3.4 e**). In particular, SEC analysis

of the seeds revealed monomodal distributions which suggests no degradation occurred during the sonication process (**Figure 3.6**).

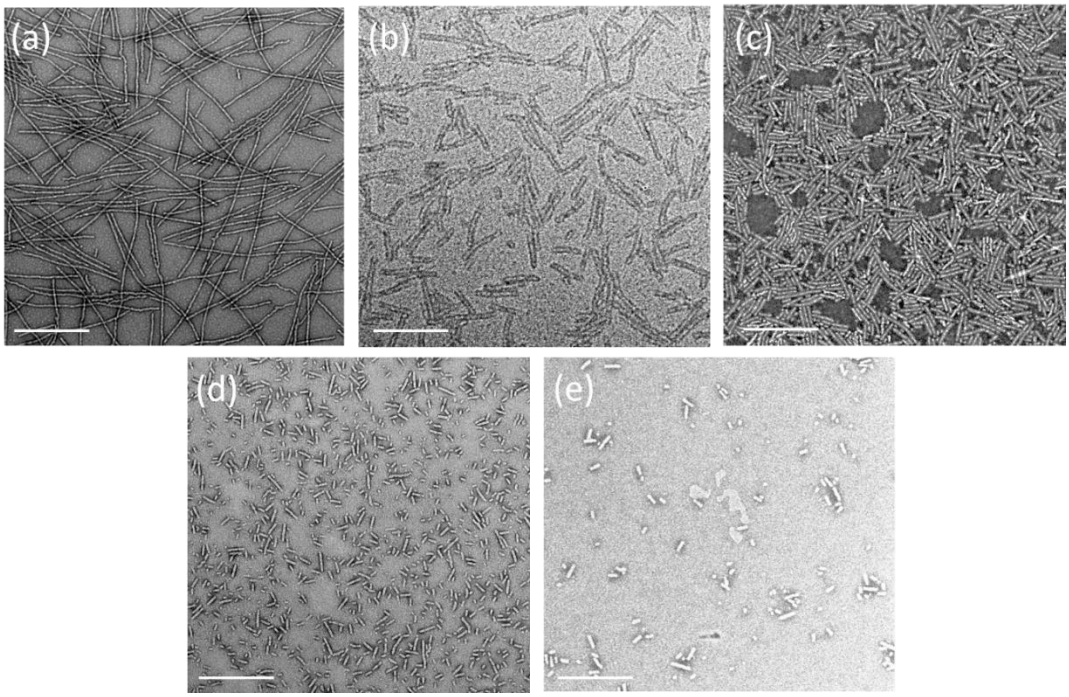

Figure 3.4 TEM micrographs of polymer **4** cylinders assembled in methanol after sonication at 0 °Cusing a sonic probe (a) 0, (b) 4, (c) 10 and (d) 20 min. (e) Seeds aged for one month in solution. Samples were negatively stained using uranyl acetate (0.5 wt %). Scale bar = 0.5 μm.

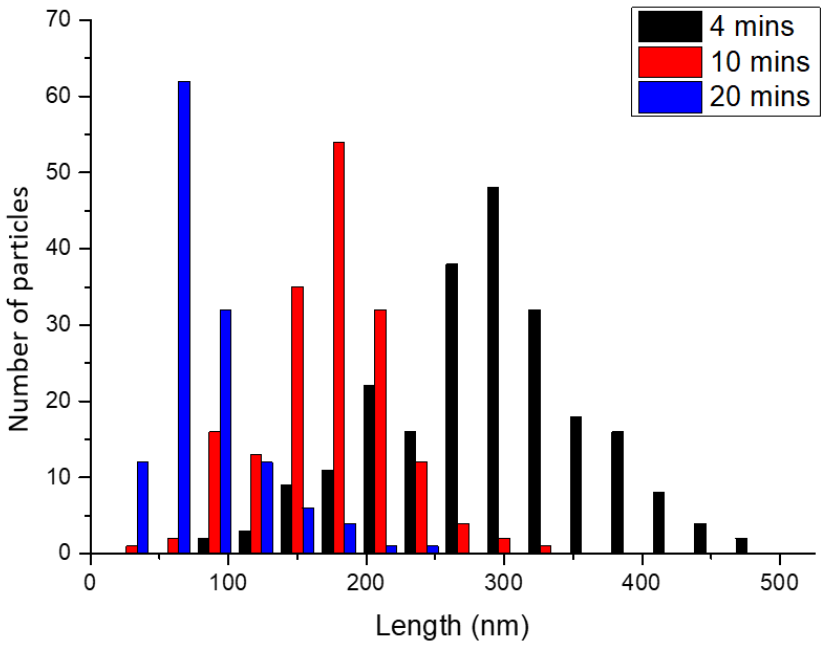

Figure 3.5 Histogram showing the length distribution of sonicated cylinders after 4, 10 and 20 min of sonication at 0 °C using a sonic probe.

Table 3.2 Length distribution for cylinders formed upon sonication of cylindrical micelles (polymer **4**) at 0 °C using a sonic probe.

Time (min)	L_w[a]	L_n[b]	L_w / L_n
4	374	317	1.18
10	224	185	1.21
20	70	65	1.06
Aging for a week	72	68	1.07

[a] *Weight average length.* [b] *Number average length.*

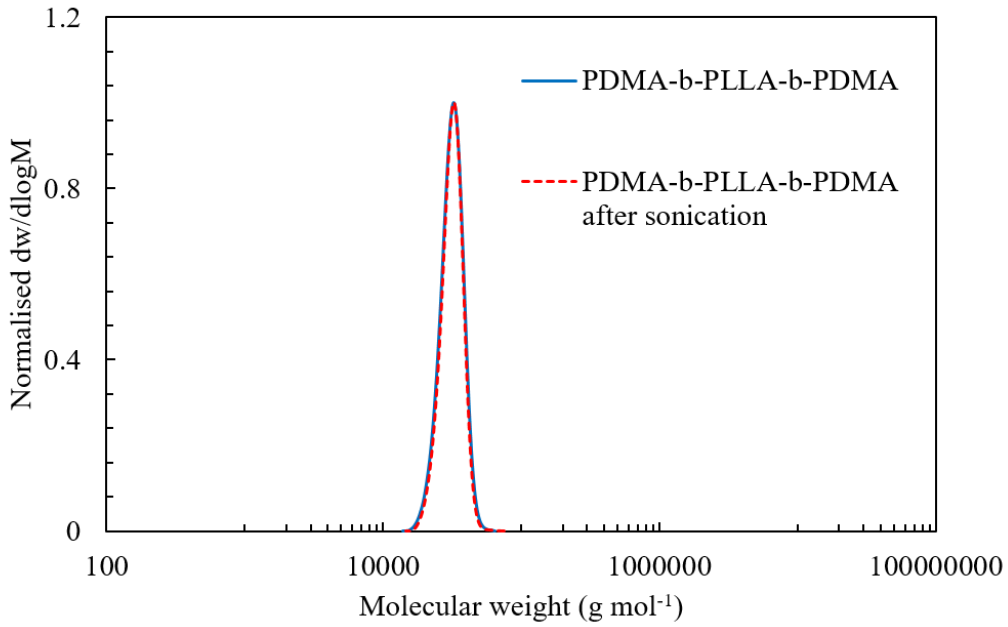

Figure 3.6 Overlaid RI SEC chromatography of polymer **4** before self-assembly (solid, red line) and after sonication of the assembled cylinders for 20 min at 0 °C using a sonic probe (dashed, blue line). DMF (5 mM NH_4BF_4) was used as the eluent.

3.3.4 Epitaxial growth of cylindrical micelles

3.3.4.1 The effect of common good solvent for both blocks

Analogous to the living covalent polymerisation of monomers, the seed nucleus is able to initiate crystallisation of unimers to form larger cylinders with uniform sizes. The seeded-growth process was accomplished by dissolving polymer **4** in a common good solvent able to solubilise the core and corona block to form a solution of unimers. Subsequently, unimers were added to the seed solution dissolved in methanol (selective solvent for core) and aged for 2 days to evolve the micelle structures. Various common solvents (Tetrahydrofuran (THF), dimethylformamide (DMF), dichloromethane (DCM)) were found to be suitable solvents and screened in order to investigate the effects of common good solvent on the final micelle properties. For each solvent, 30 μL unimer stock solution (5 mg mL^{-1}) was added to 1 mL of the seed solution (0.01 mg mL^{-1}), i.e. 15/1 unimer/seed ratio (w/w), and aged for 2 days. The resultant assemblies (**Figure 3.7**) were all cylindrical and possessed similar lengths (*ca.* 500 nm), which indicated negligible effects of the choice of common good solvent on the living CDSA process in this system. This is very important and makes the living CDSA process much more universal because polymers with diverse corona chemistries sometimes necessitate the use of different common good solvents.

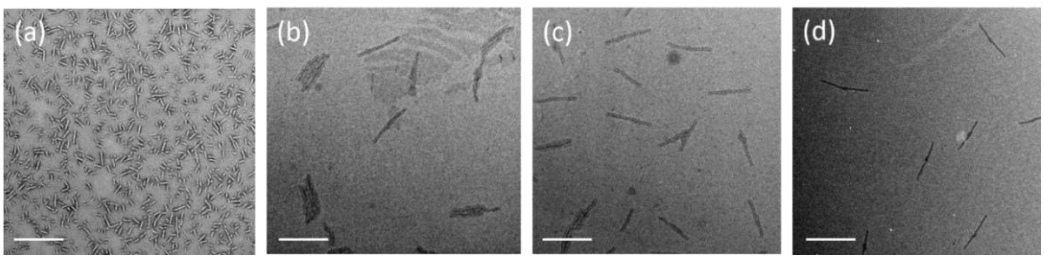

Figure 3.7 TEM images of cylindrical micelles of $PDMA_{75}$-*b*-$PLLA_{50}$-*b*-$PDMA_{75}$ obtained by adding equivalent mass of unimers (5 mg mL^{-1}) in (b) chloroform, (c) DMF and (d) THF to the (a) seeds micelles in methanol (1 mL, 0.01 mg mL^{-1}) at room temperature (25 °C). Scale bar = 0.5 μm. Samples were negatively stained using uranyl acetate (0.5 wt %).

Though many solvents were suitable in the seeded-growth process, when the ratio of common solvent to seeds solvent was increased, detrimental effects to the assembly process were observed. For example, adding 200 μL unimer solution in THF (5 mg mL^{-1}) to 1 mL seed solution (methanol, 0.01 mg mL^{-1}) produced nanoparticles non-uniform in both size and shape, with short cylinders and narrow platelets appearing observed by TEM (**Figure 3.8**).

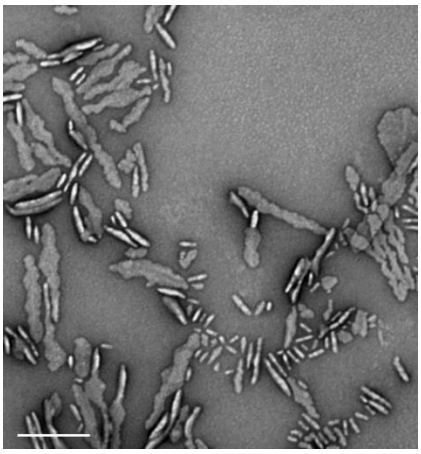

Figure 3.8 TEM micrograph obtained from mixing 200 μL of unimer solution in THF (5 mg mL^{-1}) and 1 mL seed solution (methanol, 0.01 mg mL^{-1}) and aging for 2 days. Scale bar = 0.5 μm. Samples were negatively stained using uranyl acetate (0.5 wt %).

In efforts to access larger nanostructured materials, it was proposed to use the same solvent system for both solutions (unimer and seeds) since higher amounts of the unimer solution could be added thus increasing the likelihood of forming larger structures without disturbing the living CDSA process. As previously stated in **Chapter 2**, when polymer **4** was dissolved in methanol at 5 mg mL^{-1} a minimal Tyndall effect was initially observed, however the solution became turbid after 24 h. However, when it was placed in methanol (5 mg mL^{-1}) and heated to 90 °C (in a firmly sealed vial since the boiling point of methanol is near 65 °C) for 1 h, the solution became clear and no Tyndall effect could be observed. After the solution was cooled

down to ambient temperature (25 °C) and aged for a few days no turbidity was observed, which indicated that the unimer solution was stable and no assemblies were formed. After the preparation of the stable methanol unimer solution (5 mg mL^{-1}), 80 μL (40/1 unimer/seed), and 200 μL (100/1 unimer/seed) unimer solution, respectively, was added to 1 mL of seed solution (0.01 mg mL^{-1}). The combined solutions were aged 7 days under ambient conditions before TEM analysis (**Figure 3.9**). Disappointingly, the size and shape of the polymer seeds remained consistent without any growth likely as a consequence of irreversible conformational adjustment caused by heating the unimers to high temperatures in the dissolution step.

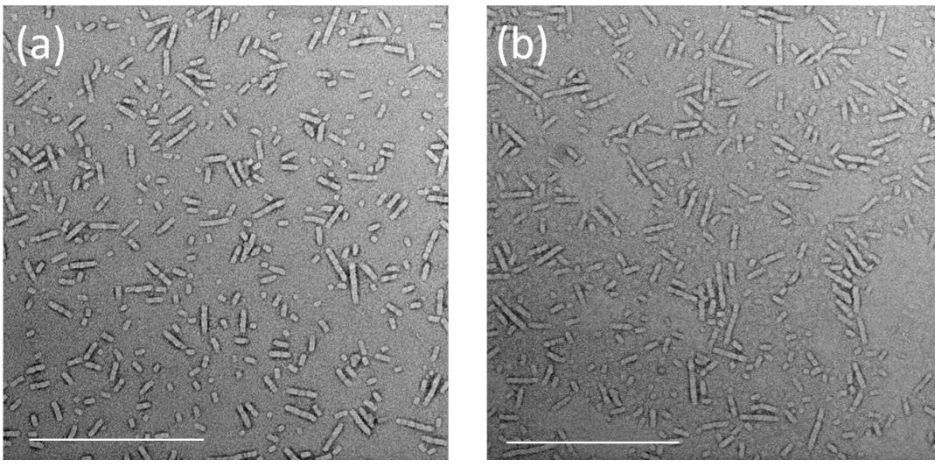

Figure 3.9 TEM micrographs of polymer **4** fibres grown from polymer **4** seed micelles with m_{unimer}/m_{seed} of (a) 40/1 and (b) 100/1. Scale bar = 0.5 μm. Samples were negatively stained using uranyl acetate (0.5 wt %).

3.3.4.2 Epitaxial growth of unimer 4 on micelle seeds 4

Further experiments using unimer solutions dissolved in THF were conducted to assess the effect of unimer/seed ratio on the epitaxial growth process. A known amount of unimer solution of polymer **4** was added to a solution of the seed micelles (polymer **4**) at various unimer/seed ratios (from 3/1 to 30/1 w/w). The combined solution was then stirred vigorously for 5 seconds and then left to age for 2 days at ambient

temperature (25 °C). For each solution, an aliquot was removed and the solvent evaporated for TEM and atomic force microscopy (AFM) analyses. At each ratio, a living CDSA process was observed and afforded micelles ranging from 120 to 810 nm (**Figure 3.10**) with small length dispersity (L_w/L_n < 1.10, where L_w and L_n are the weight and number-average length respectively, **Table 3.3**). Most important of all, the final length of the structure was dependent on the total amount of unimers added (red line, **Figure 3.10 b**).

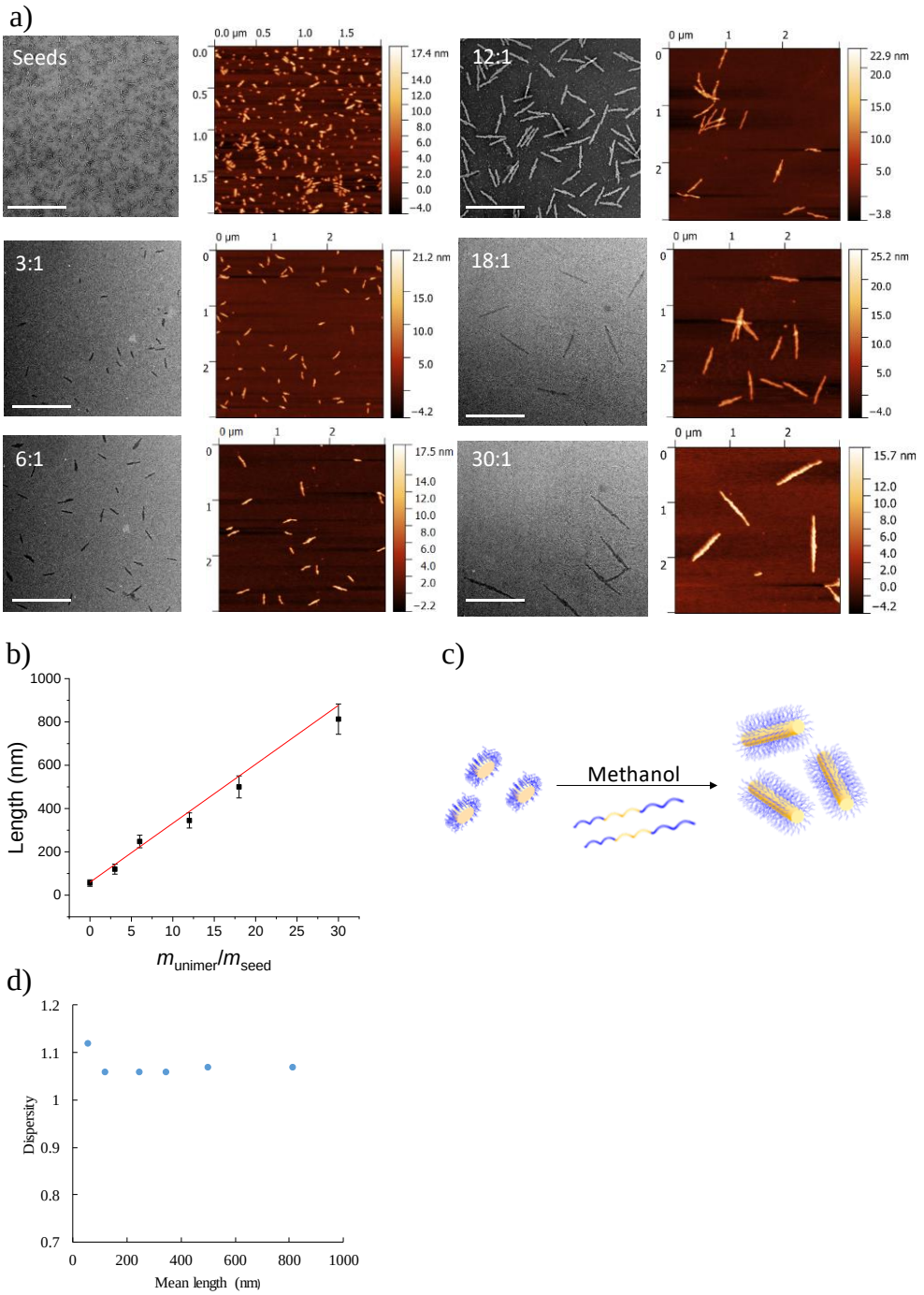

Figure 3.10 (a) TEM and AFM micrographs of seed micelles of polymer **4** prepared by sonication for 20 min at 0 °C (L_n = 65 nm, L_w/L_n = 1.06) and near monodisperse cylindrical micelles drop-cast from methanol prepared by living CDSA by the addition of 3 equiv, 6 equiv, 12 equiv, 18 equiv, and 30 equiv of unimer (polymer **4**); (b) Graph showing the linear dependence of micelle length on the unimer-to-seed ratio of polymer **4**. Scale bar = 1 μm. Samples were negatively stained using uranyl acetate (0.5 wt %). (c) Schematic representation of the preparation of near monodisperse fibres. (d) Graph displaying the degree of variation of the length of the nanoparticles by plotting dispersity against the particle sizes on average.

Table 3.3 Length dispersity of cylinders formed upon epitaxial growth of $PDMA_{75}$-*b*-$PLLA_{50}$-*b*-$PDMA_{75}$ (polymer **4**) cylindrical micelles.

m_{unimer}:m_{seeds} Polymer **4**: Polymer **4**	L_w[a]	L_n[a]	L_w / L_n
3:1	127	120	1.06
6:1	258	248	1.04
12:1	365	345	1.06
18:1	541	500	1.09
30:1	885	813	1.09

[a] *Lengths as determined by TEM analysis, see Experimental for details.*

When unimer solution is added to the seeds, the free polymer chain can either self-nucleate or attach to the exposed crystalline end of the seed. In order to further elucidate the mechanism of the CDSA process, a control experiment was performed by adding stock unimer solution (36 μL) to 1 mL of methanol (18/1 unimer/seed ratio if a standard seed solution was employed). After 2 days of aging, irregular narrow platelets were formed as a consequence of a self-seeding process (**Figure 3.11**). Since the unimers aggregated without seed crystals, it is believed that free polymer crystallisation is favoured on the seed crystal chain ends rather than *via* a self-nucleation mechanism.

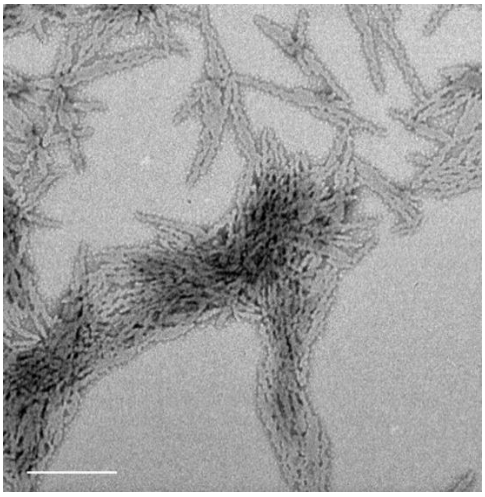

Figure 3.11 TEM images of assemblies obtained when 36 μL of unimer solution (polymer **4** at 5 mg mL^{-1}) was added to 1 mL methanol. Scale bar = 1 μm. Samples were negatively stained using uranyl acetate (0.5 wt %).

3.3.4.3 Epitaxial growth of unimer 1, 2, 5 and 6 on micelle seeds 4

After demonstrating seeded-growth using unimers and seeds with the same composition and topology, the growth behavior of unimers/seed mixtures possessing polymers with different block lengths was also investigated. According to a previous study (**Chapter 2**), $PDMA_{115}$-*b*-$PLLA_{68}$-*b*-$PDMA_{115}$ (polymer **5**) self-assembled into cylindrical micelles, whereas $PDMA_{122}$-*b*-$PLLA_{32}$-*b*-$PDMA_{122}$ (polymer **6**) yielded diamond platelets after CDSA in methanol. Different amount of unimer (polymer **5**, 5 mg mL^{-1} in THF) were added to seed solutions (0.01 mg/mL) prepared from polymer **4** to create a series of tests (the unimer/seed ratio 6/1, 12/1 and 25/1 w/w) for seeded growth study. Even though there was a large discrepancy in both core and corona lengths between the samples, the seed micelles underwent epitaxial growth to furnish cylindrical particles (**Figure 3.12 a-c, e and f**). However, polymer **6** that possesses longer hydrophilic block ratio did not show any further seeded-growth behavior after aging for 7 days under similar assembly conditions (unimer/seed ratio 25/1 w/w).

Seeds were still prevalent in the solution and longer fibres and/or 2D micelles were absent according to TEM analysis (**Figure 3.12 d**).

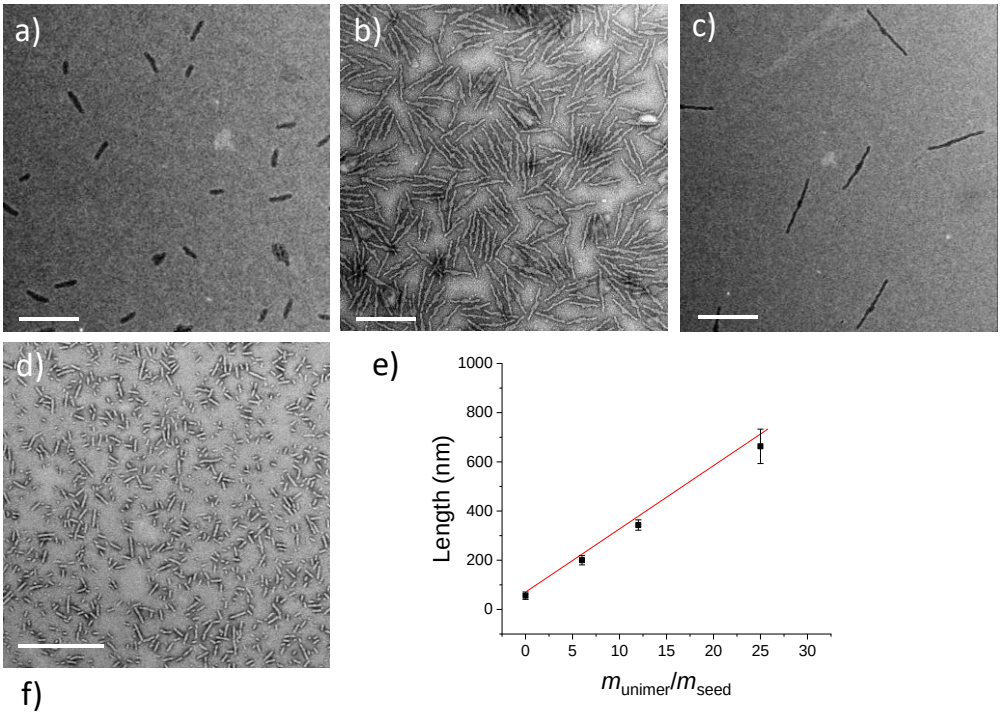

f)

m_{unimer}:m_{seeds} Polymer **5**: Polymer **4**	L_w[a]	L_n[a]	L_w / L_n
3:1	213	200	1.07
6:1	365	343	1.06
25:1	712	663	1.07

[a] *Lengths as determined by TEM analysis, see Experimental for details.*

g)

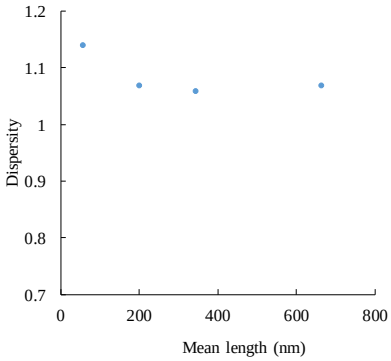

Figure 3.12 TEM micrographs of polymer **5** fibres grown from polymer **4** seed micelles with m_{unimer}/m_{seed} of (a) 6/1, (b) 12/1, and (c) 25/1. (d) unimers of polymer **6** were added in the seeds (polymer **4**) and aged for 7 days showing no growth over the time period. Scale bar = 0.5 μm. Samples were negatively stained using uranyl acetate (0.5 wt %). (e) Plot showing experimentally obtained fibre length (L_n) is consistent with theoretical lengths (red line) based on different m_{unimer}/m_{seed} mass ratios. (f)

Length dispersity of cylinders formed upon epitaxial growth of polymer **5** cylindrical micelles. (g) Graph displaying the degree of variation of the length of the nanoparticles by plotting dispersity value against the particle sizes on average.

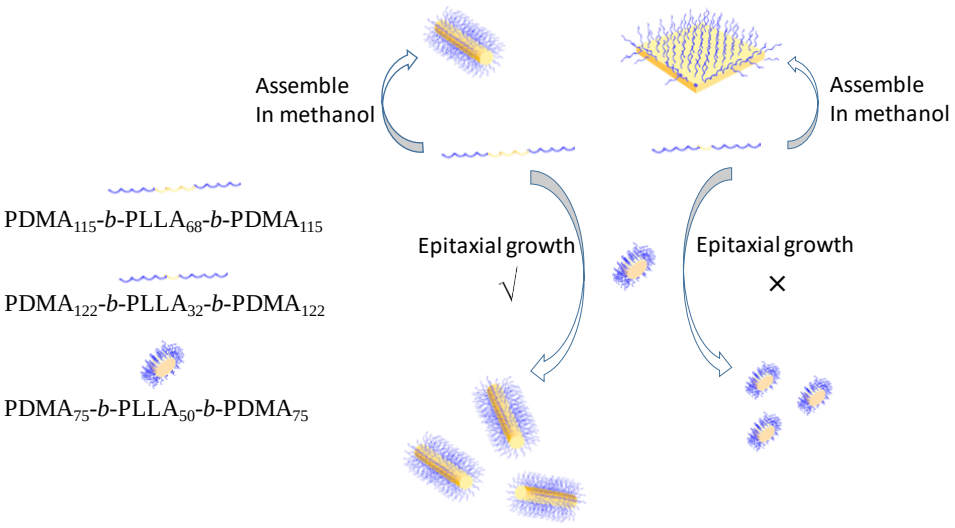

Scheme 3.2 Schematic representation of the process of epitaxial growth of unimer on seeds with different block lengths.

This observation is likely caused by the increased hydrophilicity of the polymer where a polymer with a larger corona to core ratio can interfere with the crystallisation as a consequence of the different solubility. Although we demonstrated that polymers with different block lengths were compatible for the living CDSA process, this is still limited to a certain regime since the unimers and seed micelles should have similar block ratio (**Scheme 3.2**).

The living CDSA process was also investigated for various PLLA core-block polymers where both unimers and seeds possessed different hydrophilic blocks (coronas). A stock solution (5 mg mL^{-1} in DMF) containing $PHEA_{75}$-*b*-$PLLA_{50}$-*b*-$PHEA_{75}$ (polymer **1**) was added to a polymer **4** seed solution (0.01 mg mL^{-1} in methanol) at various unimer/seed ratios (3/1, 6/1 and 18/1). After aging for 2 days, the seed growth ceased (**Figure 3.13**) and the micelle length remained consistent near the

predicted values of epitaxial deposition assuming all the unimers were consumed (red line, **Figure 3.13 e**). This result is particularly interesting since it shows that polymers with divergent corona chemistries are compatible in the seeded-growth process for core-block PLLA copolymers.

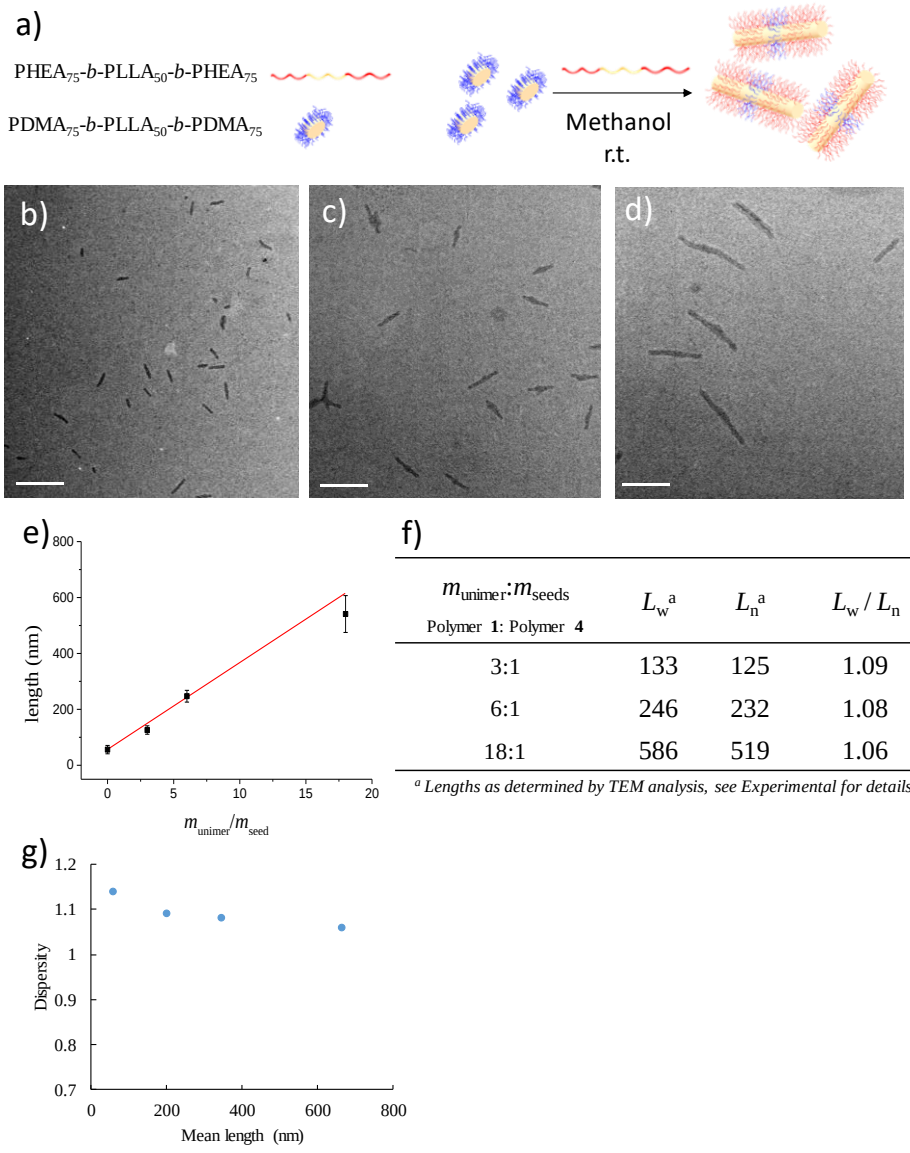

m_{unimer}:m_{seeds} Polymer **1**: Polymer **4**	L_w[a]	L_n[a]	L_w / L_n
3:1	133	125	1.09
6:1	246	232	1.08
18:1	586	519	1.06

[a] *Lengths as determined by TEM analysis, see Experimental for details.*

Figure 3.13 (a) Schematic representation of the preparation of near monodisperse fibres. TEM micrographs of polymer **1** fibres grown from polymer **4** seed micelles with m_{unimer}/m_{seed} of (b) 3:1, (c) 6:1 and (d) 18:1. Scale bar = 0.5 μm. Samples were negatively stained using uranyl acetate (0.5 wt %). (e) Plot showing experimentally obtained fibre length (L_n) ± standard deviation is consistent with theoretical lengths (red line) based on different m_{unimer}/m_{seed} mass ratios, 100 particles in the TEM images were counted for analysis. (f) Length dispersity of cylinders formed upon epitaxial growth of polymer **4** cylindrical micelles. (g) Graph displaying the degree of variation

of the length of the nanoparticles by plotting dispersity values against the particle sizes on average when the dispersity refers to L_w/L_n value.

In addition to yielding uniform 1D micelles, the living CDSA process provides access to complex architectures e.g. segmented assemblies[24] *via* the step-wise addition of different (various corona compositions) block copolymers to the micelle solutions (**Figure 3.14 a**). To prepare triblock co-micelles, polymer **4** unimers were firstly added to polymer **4** seeds solution obtaining uniform and short cylinders (L_n = 345 nm, L_w/L_n = 1.06, **Figure 3.14 b**) and then polymer **2** unimers were added in subsequently. After 2 days of aging, the co-micelles displayed discernible coronal segments according to TEM analysis (**Figure 3.14 c**). Notably, the TEM images were obtained without staining as a consequence of the higher electron density of P4VP compared to the central PDMA segment.[26] Furthermore, the co-micelles were found to be uniform in size (L_n = 1184 nm, L_w/L_n = 1.07).

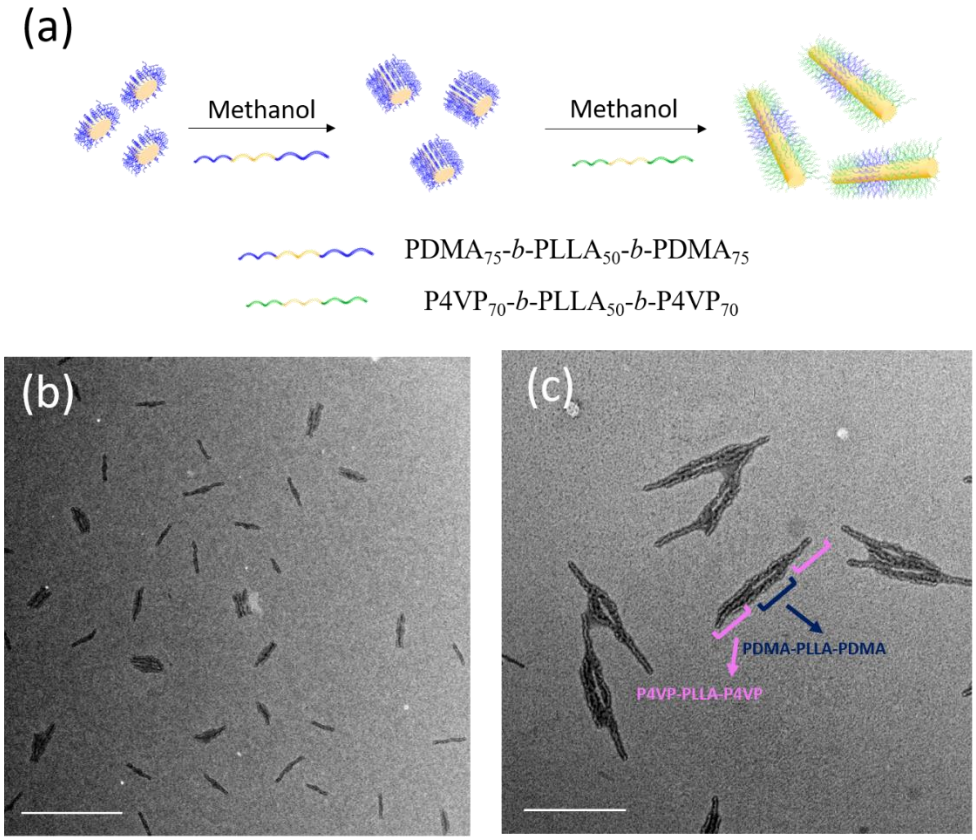

(d)

	L_w [a]	L_n [a]	L_w / L_n
Longer seeds	365	345	1.06
B-A-B comicelles	1270	1184	1.07

[a] *Lengths as determined by TEM analysis, see Experimental for details.*

Figure 3.14 (a) Schematic representation of the formation of ABA block co-micelles. TEM micrographs of representative triblock co-micelles prepared from monodisperse seed micelles when drop-casted from methanol: (b) the long seed micelles composed of polymer **4** and (c) a triblock co-micelle with a central seed segment composed of polymer **4**, with outer blocks derived from unimers of polymer **2**. Scale bar = 1 μm. Samples were negatively stained using uranyl acetate (0.5 wt %) for sample (b). (d) Length dispersity of cylinders of ABA block co-micelles.

3.3.5 Epitaxial growth of PDMA-b-PLLA-b-PDMA 2D platelets

After demonstrating that 1D seeds could initiate crystallisation of unimers to form cylindrical micelles, the growth of 2D diamond platelet seeds was investigated. For the 2D assemblies composed of $PDMA_{122}$-*b*-$PLLA_{32}$-*b*-$PDMA_{122}$ (polymer **6**) the platelets were also sonicated at reduced temperatures (0 °C) to prepare 2D seeds and the solution was sampled at various time points (*ca.* every 2 min) for TEM analysis to monitor the disassembly of the platelets. TEM images showed the diamond morphology was fragmented into irregular seeds after 20 min of sonication (10 cycles) and most particles were smaller than 100 nm in diameter (**Figure 3.15**). Similar to the 1D seeds, these 2D particles display good stability in methanol without noticeable growth or coupling processes after aging at room temperature for 30 days (**Figure 3.15 e**).

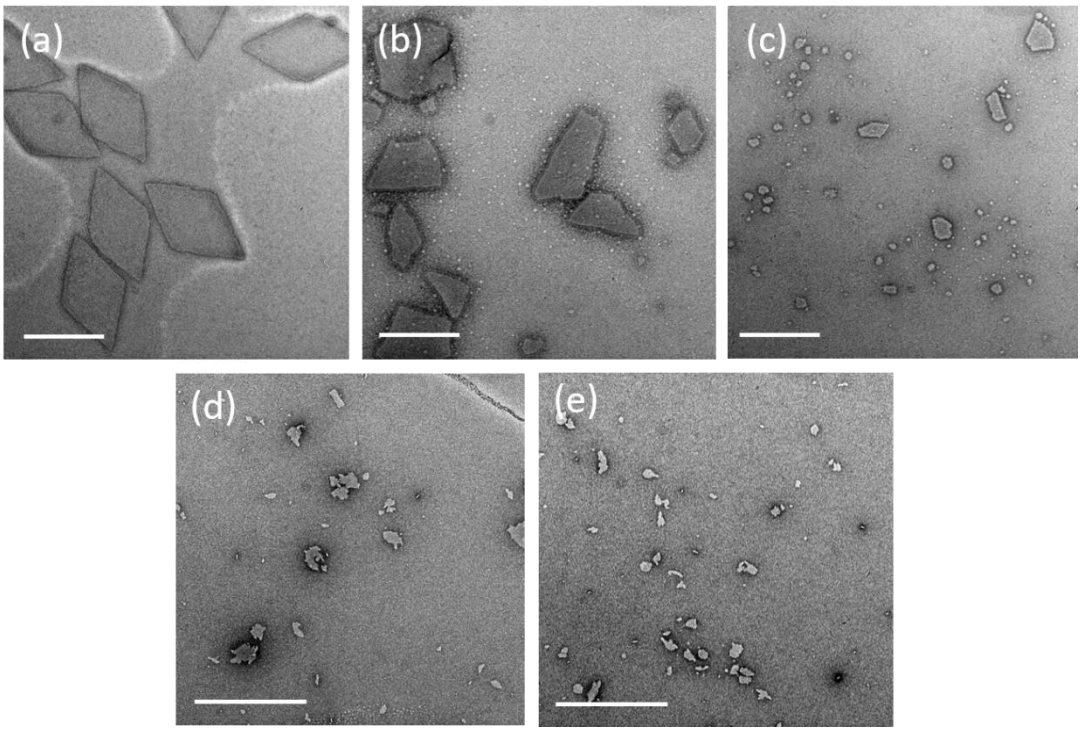

Figure 3.15 TEM micrographs of polymer **6** platelets assembled in methanol after sonication at 0 °C using a sonic probe at (a) 0, (b) 4, (c) 10, (d) 20 min. (e) Seeds aged for one month. Scale bar = 1 μm. Samples were negatively stained using uranyl acetate (0.5 wt %).

Similar to the seeded-growth protocol to form 1D cylinders, various unimer solutions (polymer **6**) were added to the 2D seed solution (polymer **6**) respectively and subsequently aged for 2 days under ambient conditions (25 °C). The seeds grew uniformly in both dimensions to furnish larger 2D diamond platelets and, analogous to the seeded growth for the 1D cylinders, the area of the platelets was found to be linearly dependent on the m_{unimer}/m_{seed} ratio (**Figure 3.16 b-d, f**). To account for the potential influence of a self-nucleating process, an aliquot of unimer solution was added into methanol without any seeds. After 2 days, TEM analysis indicated irregular platelets formed suggesting the seeds play a vital role in controlling the seeded-growth process of the micelles by suppressing the self-seeding process (**Figure 3.16 e**). For PLLA based triblock copolymers the seeded-growth process was leveraged to form 1D cylinders and 2D diamond platelets.

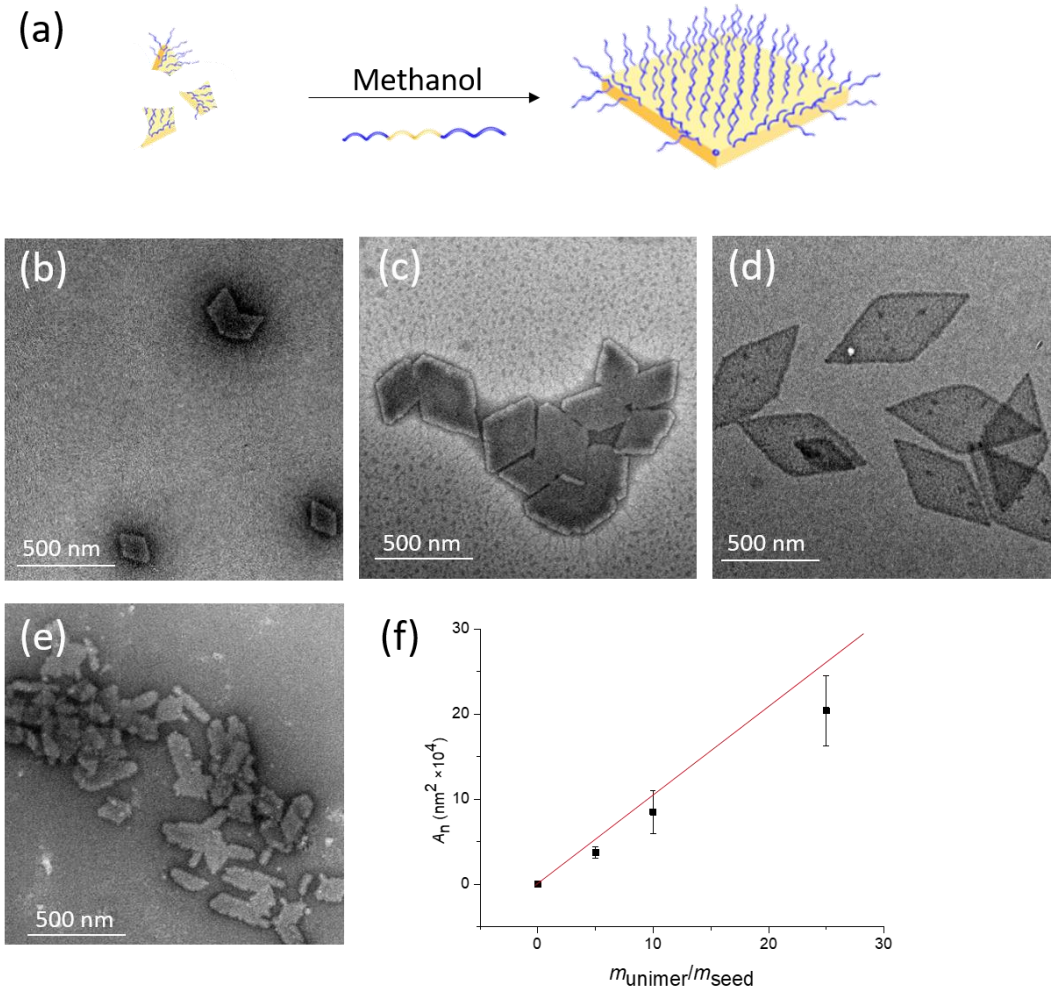

Figure 3.16 (a) Schematic representation of the preparation of uniform platelets. TEM micrographs of polymer **6** 2D platelets grown from polymer **6** seed micelles with m_{unimer}/m_{seed} of (b) 5/1, (c) 10/1, and (d) 25/1. (e) TEM images of final structures obtained when 50 μL of unimer solution was added to methanol solution without seeds. Scale bar = 0.5 μm. Samples were negatively stained using uranyl acetate (0.5 wt %). (f) Plot showing linear dependence between micelle area and the m_{unimer}/m_{seed} ratio with error bars and standard deviation.

3.4 Conclusion

The ability to prepare PLLA assemblies with well-defined shape and dimensions is of great significance on account of their profound potentials in bio-relevant applications. Although there are some breakthrough to elegantly tune the dimensions and spatial functionality of PLLA based 2D soft materials,[25-27] obtaining precise control over the 1D assemblies still represent as a key challenge. Herein, by taking advantage of crystalline properties of the PLLA segments, monodisperse 1D cylinders with uniform width (24 nm) and length ranging from 127 to 850 nm were able to be prepared. The micelle length is consistent with the predicted L_n value as a function of unimer to seeds ratio. The seeded-growth route could also be applied to prepare complex structures e.g. ABA type triblock co-micelles, taking advantage of the PLLA crystalline core. This is the first example where controlled PLLA based ABA triblock copolymers could be used to obtain 1D assemblies by living CDSA methodology, opening avenues to prepare complex and functioned micelles for the application in drug delivery and nanomedicine.

3.5 Experimental Section

3.5.1 Materials

Chemicals and solvents were purchased from Sigma-Aldrich, Acros, Fluka, TCI, Fisher Chemical, Alfa Aesar or VWR. L-Lactide was purchased from Corbion-Purac and recrystallised once from dichloromethane and twice from toluene. The monomer was dried over 3 Å molecular sieves for 3 days and recrystallised from toluene. 1,8-Diazabicyclo[5.4.0]undec-7-ene (DBU) and (−)-sparteine were distilled over CaH_2 before use.1-(3,5-Bis(trifluoromethyl)phenyl)-3-cyclohexyl-thiourea was prepared and purified as reported. 2,2′-Azobis(isobutyronitrile) (AIBN) was received from Molekula. After recrystallisation from methanol it was stored at 4 °C. Deuterated solvents were used as received from Apollo Scientific. Raft agent 2-(dodecylthiocarbonothioylthio)-2-methylpropionic acid (DDMAT) was synthesised in **Chapter 2**. All the monomer used for polymerisation will go through basic aluminium oxide to remove the inhibitor.

3.5.2 Instrument

Proton nuclear magnetic resonance (^{1}H NMR) spectra were recorded on a Bruker AV-400 spectrometer at 400 MHz. All spectra were recorded in $CDCl_3$ and d_6-DMSO unless otherwise stated. The chemical shifts were reported as δ in parts per million and quoted downfield from the internal standard tetramethylsilane (δ = 0 ppm).

Size exclusion chromatography (SEC) was performed using an Agilent 1260 Infinity Multi-Detector GPC System fitted with a refractive index and UV detector, and

equipped with a guard column (Varian PLGel) and two PLGel 5 μm mixed-D columns. The mobile phase was DMF and 5 mM NH_4BF_4, at a flow rate of 1 mL min^{-1} at 50 °C. All data was analysed using Cirrus v3.3 and Agilent GPC/SEC software v1 with calibration curves produced using Varian Polymer Laboratories linear PMMA standards.

Transmission electron microscopy (TEM) was performed using a JEOL 2100FX at 200 kV. TEM samples were prepared on a formvar/carbon film TEM grid. In short, 2 μL of sample solution (1 mg mL^{-1}) was deposited on a grid and left air dry. 5 μL of uranyl acetate (UA, 1%) solution was then dropped on the grid and left for 60 seconds before blotting. The sample was kept in a desiccator overnight before characterisation. Generally, one drop of the Transmission electron microscopy (TEM) was performed using a JEOL 2100FX at 200 kV. TEM samples were prepared on a formvar/carbon film TEM grid. In short, 2 μL of sample solution (1 mg mL^{-1}) was deposited on a grid and left air dry. 5 μL of uranyl acetate (UA, 1%) solution was then dropped on the grid and left for 60 seconds before blotting. The sample was kept in a desiccator overnight before characterisation. TEM images were analysed by ImageJ software, where at least 100 particles were counted for each sample to obtain the number-average length (L_n) and weight-average length (L_w). L_n and L_w were calculated by using the following equations:

$$L_n = \frac{\sum_{i=1}^{n} N_i L_i}{\sum_{i=1}^{n} N_i}$$

$$L_w = \frac{\sum_{i=1}^{n} N_i {L_i}^2}{\sum_{i=1}^{n} N_i L_i}$$

Where L_i is the length each counted cylindrical micelle and N_i is the number of the cylindrical micelles with the length L_i.

Atomic Force Microscopy (AFM). Samples for AFM analysis were prepared by drop casting 7 μL of polymer in methanol (0.25 mg mL^{-1}) onto silicon wafer followed by drying with compressed air. Imaging and analysis were performed on an Asylum Research MFP3D-SA atomic force microscope in alternate contact (tapping) mode

3.5.3 Synthesis of poly(4-vinylpyridine)-*block*-poly(L-lactide)-*block*-poly(4-vinylpyridine) (P4VP-*b*-PLLA-*b*-P4VP)

CTA-$PLLA_{32}$-CTA, (60.0 mg, 6.1 μmol), 4-VP (96.5 mg, 918.2 μmol) and AIBN (10.1 μL of a 10 mg mL^{-1} solution in dioxane) were dissolved in dioxane (0.5 mL) before transferring to a dried ampoule. After three freeze-pump-thaw cycles, the solution was sealed under argon and heated for 18 hours at 80 ℃ for 35% conversion. The reaction was quenched in ice bath and purified by precipitation one time into ethyl acetate and two times into diethyl ether. The resultant pale yellow solid was dried in *vacuo* before use. M_n, NMR = 24.1 kDa, DP = 140. M_n, SEC = 28.1 kDa, $Đ_M$ = 1.23. ^{1}H NMR (400 MHz, $CDCl_3$, 298 K): δ (ppm) 8.31 (br s, 1 H, NC*H*CH), 6.32 (q, 1 H, $^3J_{H\text{-}H}$ = 6.9 Hz, NCHC*H*), 5.16 (q, 1 H, $^3J_{H\text{-}H}$ = 6.9 Hz, OC*H*(CH3)CO).

3.5.4 Synthesis of Poly(*N*-acryloylmorpholine)-*block*-poly(L-lactide)-*block*-Poly(*N*-acryloylmorpholine) (PNAM-*b*-PLLA-*b*-PNAM)

CTA-$PLLA_{50}$-CTA, (40.0 mg, 5.6 μmol), NAM (250.0 mg, 35.0 μmol) and AIBN (10.0 μL of a 10 mg mL^{-1} solution in 1, 4-dioxane) were dissolved in dioxane (1 mL) before transferring to a dried ampoule. After three freeze-pump-thaw cycles, the solution was sealed under argon and heated for 5 hours at 70 ℃ for 100% conversion.

The reaction was quenched in ice bath and purified by precipitation three times into cold diethyl ether. The resultant pale yellow solid was dried in *vacuo* before use. M_n, NMR = 42.2 kDa, DP = 300. M_n, SEC = 50.0 kDa, $Đ_M$ = 1.21. ^{1}H NMR (400 MHz, $CDCl_3$, 298 K): δ (ppm) 5.16 (q, 1 H, $^3J_{H\text{-}H}$ = 6.9 Hz, OC*H*(CH_3)CO) 3.31-3.63 (br s, 4 H, -OC*H*$_2$C*H*$_2$N-) 2.57 (br s, 1 H, CH_2C*H*CO) 1.57 (d, 3 H, $^3J_{H\text{-}H}$ = 7.1 Hz, OCH(C*H*$_3$)CO) 1.25 (br s, 2 H, C*H*$_2$CHCO) 0.87 (t, 6 H, $^3J_{H\text{-}H}$ = 6.8 Hz, C*H*$_3$$CH_2$).

3.5.5 Synthesis of poly(*N*-Hydroxyethyl acrylate)-*block*-poly(L-lactide)-*block*-poly(*N*-Hydroxyethyl acrylate) (PHEA-*b*-PLLA-*b*-PHEA)

CTA-$PLLA_{32}$-CTA, (40.0 mg, 9.0 μmol), HEAA (261.9 mg, 2255.1 μmol) and AIBN (14.2 μL of a 10 mg mL^{-1} solution in DMSO) were dissolved in DMSO (0.5 mL) before transferring to a dried ampoule. After three freeze-pump-thaw cycles, the solution was sealed under argon and heated for 3 hours at 65 °C for 30% conversion. The reaction was quenched in ice bath and purified by precipitation one time into cold ethyl acetate and two times into cold diethyl ether. The resultant pale yellow solid was dried in *vacuo* before use. M_n, NMR = 24.1 kDa, DP = 150. M_n, SEC = 28.3 kDa, $Đ_M$ = 1.25. ^{1}H NMR (400 MHz, d_6-DMSO, 298 K): δ (ppm) 5.16 (q, 1 H, $^3J_{H\text{-}H}$ = 6.9 Hz, OC*H*(CH_3)CO) 4.73 (br s, 2 H, $COCH_2CH_2O$*H*) 4.02 (br s, 2 H, COC*H*$_2$$CH_2OH$) 1.46 (d, 3 H, $^3J_{H\text{-}H}$ = 7.1 Hz, OCH(*CH*$_3$)CO) 0.87 (t, 6 H, $^3J_{H\text{-}H}$ = 6.8 Hz, C*H*$_3$$CH_2$).

3.5.6 Typical crystallisation driven self-assembly method for PLLA based block copolymers

All triblock copolymers were assembled in methanol using the following general protocol: polymer was dissolved in methanol at a concentration of 5 mg mL^{-1} and the resultant solution was stirred at ambient temperature in a sealed vial for 2 days.

3.5.7 Sonication of $PDMA_{75}$-*b*-$PLLA_{50}$-*b*-$PDMA_{75}$ cylindrical micelles

Cylindrical micelles achieved from the polymer $PDMA_{75}$-*b*-$PLLA_{50}$-*b*-$PDMA_{75}$ in methanol (5 mg mL^{-1}) were sonicated into seeds using a sonicating probe at 0 °C. An aliquot of the solution was taken at various time intervals and analysed using TEM. The crystalline seeds were prepared after 20 minutes sonication (10 cycles of 2 minutes) with 10 minutes between cycles.

3.5.8 Typical crystallinzation driven self-assembly method for the epitaxial growth of PLLA block copolymers

Polymer $PDMA_{75}$-*b*-$PLLA_{50}$-*b*-$PDMA_{75}$ was dissolved in THF (5 mg mL^{-1}) making a stock solution. Unimers in the stock solution was added into the seeds (0.01 mg mL^{-1}) and aged for two days before TEM characterisation. The unimers to seeds ratio was controlled by the volume of the stock solution to the dispersion of seeds micelles.

3.6 References

1. Tritschler, U.; Gwyther, J.; Harniman, R. L.; Whittell, G. R.; Winnik, M. A.; Manners, I. *Macromolecules* **2018,** 51 (14), 5101-5113.
2. Blanazs, A.; Armes, S. P.; Ryan, A. J. *Macromolecular rapid communications* **2009,** 30 (4), 267-277.
3. Wang, X.; Guerin, G.; Wang, H.; Wang, Y.; Manners, I.; Winnik, M. A. *Science* **2007,** 317 (5838), 644-647.
4. Qiu, H.; Gao, Y.; Boott, C. E.; Gould, O. E.; Harniman, R. L.; Miles, M. J.; Webb, S. E.; Winnik, M. A.; Manners, I. *Science* **2016,** 352 (6286), 697-701.
5. Qiu, H.; Hudson, Z. M.; Winnik, M. A.; Manners, I. *Science* **2015,** 347 (6228), 1329-1332.
6. Arno, M. C.; Inam, M.; Coe, Z.; Cambridge, G.; Macdougall, L. J.; Keogh, R.; Dove, A. P.; O'Reilly, R. K. *Journal of the American Chemical Society* **2017,** 139 (46), 16980-16985.
7. He, W.-N.; Zhou, B.; Xu, J.-T.; Du, B.-Y.; Fan, Z.-Q. *Macromolecules* **2012,** 45 (24), 9768-9778.
8. Schmalz, H.; Schmelz, J.; Drechsler, M.; Yuan, J.; Walther, A.; Schweimer, K.; Mihut, A. M. *Macromolecules* **2008,** 41 (9), 3235-3242.
9. Schmelz, J.; Schedl, A. E.; Steinlein, C.; Manners, I.; Schmalz, H. *Journal of the American Chemical Society* **2012,** 134 (34), 14217-25.
10. Patra, S. K.; Ahmed, R.; Whittell, G. R.; Lunn, D. J.; Dunphy, E. L.; Winnik, M. A.; Manners, I. *Journal of the American Chemical Society* **2011,** 133 (23), 8842-8845.
11. Qian, J.; Li, X.; Lunn, D. J.; Gwyther, J.; Hudson, Z. M.; Kynaston, E.; Rupar, P. A.; Winnik, M. A.; Manners, I. *Journal of the American Chemical Society* **2014,** 136 (11), 4121-4124.
12. Shin, S.; Menk, F.; Kim, Y.; Lim, J.; Char, K.; Zentel, R.; Choi, T. L. *Journal of the American Chemical Society* **2018,** 140 (19), 6088-6094.
13. Tao, D.; Feng, C.; Cui, Y.; Yang, X.; Manners, I.; Winnik, M. A.; Huang, X. *Journal of the American Chemical Society* **2017,** 139 (21), 7136-7139.
14. Tao, D.; Feng, C.; Lu, Y.; Cui, Y.; Yang, X.; Manners, I.; Winnik, M. A.; Huang, X. *Macromolecules* **2018,** 51 (5), 2065-2075.
15. Jin, X.-H.; Price, M. B.; Finnegan, J. R.; Boott, C. E.; Richter, J. M.; Rao, A.; Menke, S. M.; Friend, R. H.; Whittell, G. R.; Manners, I. *Science* **2018,** 360 (6391), 897-900.
16. Sakurai, Y.; Kajimoto, K.; Hatakeyama, H.; Harashima, H. *Expert opinion on drug delivery* **2015,** 12 (1), 41-52.
17. Petzetakis, N.; Walker, D.; Dove, A. P.; O'Reilly, R. K. *Soft Matter* **2012,** 8 (28), 7408-7414.
18. Sun, L.; Pitto-Barry, A.; Thomas, A. W.; Inam, M.; Doncom, K.; Dove, A. P.; O'Reilly, R. K. *Polymer Chemistry* **2016,** 7 (13), 2337-2341.
19. Li, Z.; Sun, L.; Zhang, Y.; Dove, A. P.; O'Reilly, R. K.; Chen, G. *ACS Macro Letters* **2016,** 5 (9), 1059-1064.
20. Yu, W.; Inam, M.; Jones, J. R.; Dove, A. P.; O'Reilly, R. K. *Polymer Chemistry* **2017,** 8 (36), 5504-5512.
21. Inam, M.; Cambridge, G.; Pitto-Barry, A.; Laker, Z. P.; Wilson, N. R.; Mathers, R. T.; Dove, A. P.; O'Reilly, R. K. *Chemical science* **2017,** 8 (6), 4223-4230.
22. Rizis, G.; van de Ven, T. G.; Eisenberg, A. *ACS nano* **2015,** 9 (4), 3627-3640.

23. Das, A.; Petkau-Milroy, K.; Klerks, G.; van Genabeek, B.; Lafleur, R. P. M.; Palmans, A. R. A.; Meijer, E. W. *ACS Macro Letters* **2018,** 7 (5), 546-550.
24. Kynaston, E. L.; Nazemi, A.; MacFarlane, L. R.; Whittell, G. R.; Faul, C. F. J.; Manners, I. *Macromolecules* **2018,** 51 (3), 1002-1010.
25. Inam, M.; Jones, J. R.; Pérez-Madrigal, M. M.; Arno, M. C.; Dove, A. P.; O'Reilly, R. K. *ACS Central Science* **2017,** 4 (1), 63-70.
26. He, X.; He, Y.; Hsiao, M. S.; Harniman, R. L.; Pearce, S.; Winnik, M. A.; Manners, I. *Journal of the American Chemical Society* **2017,** 139 (27), 9221-9228.
27. He, X.; Hsiao, M.-S.; Boott, C. E.; Harniman, R. L.; Nazemi, A.; Li, X.; Winnik, M. A.; Manners, I. *Nature Materials* **2017,** 16 (4), 481-491.

Chapter 4. Structural reorganization of cylindrical nanoparticles triggered by polylactide stereocomplexation in aqueous solution

4.1 Abstract

The stereocomplexation of enantiomeric poly(lactic acid) (PLA) (i.e. isotactic poly(L-lactide) (PLLA) and poly(D-lactide) (PDLA)) opens up an avenue for the formation of new materials with enhanced performance, specifically regarding their mechanical, thermal-resistance, and hydrolysis-resistance response. Despite this fact, the study of the stereocomplexation between block copolymers based on PLA in solution is very limited. Hence, a comprehensive understanding of this phenomenon is needed. In this chapter, a series of triblock copolymers (i.e. poly(*N*-hydroxyethyl acrylamide)-*b*-PL(D)LA-*b*-poly(*N*-hydroxyethyl acrylamide); (PHEAAm$_y$-*b*-PL(D)LA$_x$-*b*-PHEAAm$_y$)) were synthesized and assembled into cylindrical micelles *via* the crystallisation-driven self-assembly (CDSA) technique. Then, the sterecomplexation between enantiomeric micelles triggered their morphological transition, which was investigated considering different factors: aging temperature, block composition and solvent. In general, increasing the solubility of the copolymer in a specific solvent promotes the exchanging speed between the micelles and the unimers, thus accelerating the transition process. Based on this principle, we attempted to realize the transformation process under physiological conditions after optimising the hydrophilicity of the polymer by modifying the end-group into a charged functionality.

4.2 Introduction

The chiral center of the lactic acid unit yields enantiomeric poly(lactic acid) polymers (i.e. PLLA or PDLA) for which the thermodynamically favored CH_3•••O=C hydrogen-bonding is present.[1, 2] The stereocomplexation between left-handed PLLA and right-handed PDLA polymeric helices improves the mechanical and thermal properties of the material compared to the equivalent homochiral polymers, which results in a new strategy to prepare biomaterials with enhanced performance, such as hydrogels and nanoparticles for drug-delivery.[3, 4] For instance, Leroux *et al.* obtained stereocomplex block copolymer micelles in aqueous solution by mixing equimolar quantities of enantiomeric PLLA-*b*-PEO and PDLA-*b*-PEO block copolymers. The sterecomplex micelles showed lower critical micellization concentration and higher kinetical stability than the equivalent enantiomeric pure micelles (i.e. PLLA-*b*-PEO) as a consequence of their more compact chain conformation in the core.[5]

In our previous study, cylindrical micelles were successfully prepared by crystallisation-driven self-assembly (CDSA) from two different diblock copolymers based on PLA and poly(acrylic acid) (PAA), PLLA-*b*-PAA and PDLA-*b*-PAA.[6] Most notably, the enantiomer micelle mixture underwent morphological reorganization from cylinders to crystalline spheres, which demonstrates the promising application of these assemblies as stimuli-responsive vectors in a biorelevant context.[7] However, the harsh experimental conditions used to facilitate the extraction of the unimer from the crystalline assemblies, i.e. high temperature (65 °C) and organic solvent (20% THF), hinder the further development of these nanostructures. In that regard, triblock copolymers with ABA architecture showed distinct advantages over the diblock counterpart (i.e. greater solubility,[8] and accelerated unimer assembly exchange rate[9]).

Hence, this specific polymer architecture reduces the energy barrier of the unimer extraction from the crystalline assemblies, and therefore demonstrate the potential to realize morphological transformation under physiological conditions (i.e. in aqueous media at 37 °C).

Taking into consideration that PAA is toxic, we screened several biocompatible and hydrophilic polymers to be used as corona, and thus render the assemblies suitable for biotechnological applications. *N*-hydroxyethyl acrylamide stands out because of its facile synthesis and assembly methodology. Hence, in this work, a series of triblock copolymers with various corona and core ratio have been synthesized, and a comprehensive study has been carried out to understand the effect of different factors, such as temperature and block composition, on the transformation process. Moreover, by removing the alkane RAFT end-group, we have been able to increase the stability of the assemblies in aqueous solution and, more importantly, partially charge the end group, which potentially allows the morphological transition to occur under physiological conditions. Our approach, which is based on using the enantiomeric assembly as stimulus to trigger the morphological transition and then release certain chemicals or recombine two chemistries, is a new concept in the stimuli-responsive drug vector field. Indeed, the findings described in this chapter demonstrate the significant potential of such strategy for biomedical applications.

4.3 Results and Discussion

4.3.1 Selection of the polymer model for the stereocomplex-triggered morphological transition study

As mentioned in the introduction the stereocomplex-triggered morphological transition of PL(D)LA-*b*-PAA is explained by the "unimer-exchange" mechanism. In order to realize the transition under physiological conditions, the polymer being used needs to be carefully reconsidered.

4.3.1.1 Polymer architecture

Frank S. Bates and Timothy P. Lodge studied the molecular exchange kinetics of poly(styrene)-*b*-poly(ethylene-alt-propylene) block copolymers and found that polymer architecture plays a vital role in the exchange process, while the additional corona block in an ABA type triblock greatly facilities the movement of the core block into the solvent by a factor of 2000 compared with the AB diblock counterpart.[10] In addition to that, the coil-crystalline-coil architecture promotes the polymer solubility in comparison with the coil-crystalline one, which potentially lowers the energy barrier of the unimer extraction from the crystalline assemblies. For example, the solubility of $PDMA_{60}$-*b*-$PLLA_{25}$-*b*-$PDMA_{60}$ and $PLLA_{25}$-*b*-$PDMA_{120}$ (prepared in **Chapter 2**) in methanol and ethanol, respectively, was assessed by UV-Vis spectroscopy. In contrast to the diblock copolymer, the triblock copolymer showed outstanding solubility, with much higher transmittance values being obtained within a temperature range varying from 25 to 90 ℃ (**Figure 4.1**). Hence, this evidence rationalizes the design of copolymers with specific architectures (i.e. ABA triblock copolymers) to achieve the stereocomplexation-triggered morphological transition under physiological conditions.

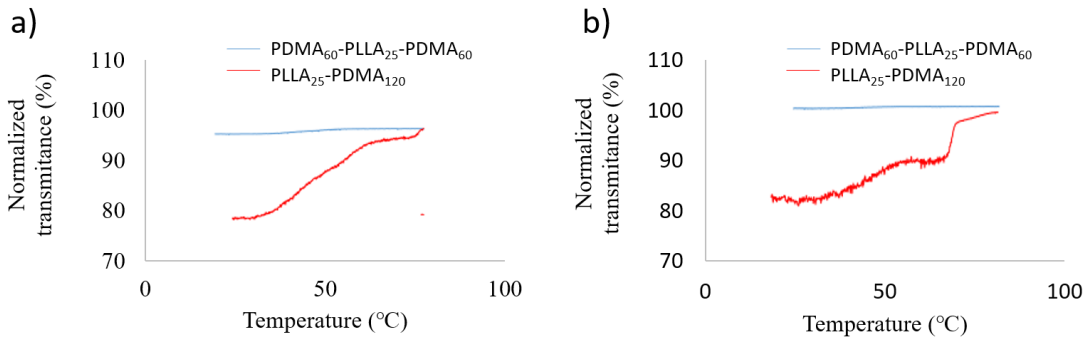

Figure 4.1 Plots of normalized transmittance versus temperature obtained for polymers $PDMA_{60}$-b-$PLLA_{25}$-b-$PDMA_{60}$ and $PLLA_{25}$-b-$PDMA_{120}$ (5 mg mL^{-1}) in (a) methanol and (b) ethanol.

4.3.1.2 Corona chemistry optimisation

Since the propensity for unimer formation when block copolymers dissolve in water and alcohols largely depends on hydrophobicity, the choice of a proper corona chemistry is of significant importance to realize the morphological transition in physiological condition. To predict hydrophobicity of the coil-crystalline-coil triblock copolymers, a series of homopolymers (corona block) were investigated by calculating normalized octanol-water partition coefficients ($LogP_{oct}$/SA) for oligomeric models. $LogP_{oct}$/SA values were derived from computer simulations and represent the respective hydrophilicity of the homopolymer, whereby negative values refer to overall hydrophilic properties and positive values indicate hydrophobicity in proportion to the absolute value. It was discovered that homopolymers such as poly(hydroxyethyl acrylamide), poly(acryoylmorpholine) and poly(*N*-vinylpryyolidone) have a high probability of unimer formation in water based on those $LogP_{oct}$/SA values (**Figure 4.2**).[11] Considering other properties, such as biocompatibility,[12] and easy of synthesis,[13] PHEAAm is chosen as the corona block

and PHEAAm-*b*-PL(D)LA-*b*-PHEAAm triblock copolymers are taken as the model polymer for study in this chapter.

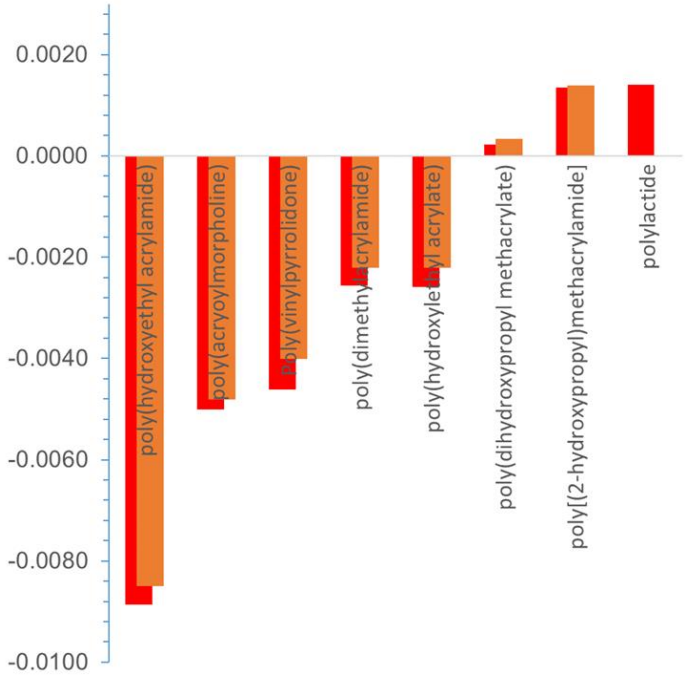

Figure 4.2 Normalized octanol-water partition coefficients ($LogP_{oct}$/SA) for oligomeric models based on hexamers (orange bars) and decamers (red bars).§

4.3.2 Synthesis of ABA type triblock copolymers PHEAAmy-b-PL(D)LAx-b-PHEAAmy

The triblock copolymers were synthesized by combining reversible addition-fragmentation chain-transfer polymerisation (RAFT) and ring-opening polymerisation (ROP) as described in **Chapter 2**. 1,3-propanediol was firstly used to initiate the polymerisation with DBU as organic catalyst, which yielded the homochiral polymer PL(D)LA with barely no racemization as observed by ^{1}H homodecoupled NMR and quantitative ^{13}C NMR spectroscopy (**Figure 4.3**). As mentioned in **Chapter 2**, the DP of the polymer was determined by end group analysis.

§ $LogP_{oct}$ analysis was carried out by Robert T. Mathers.

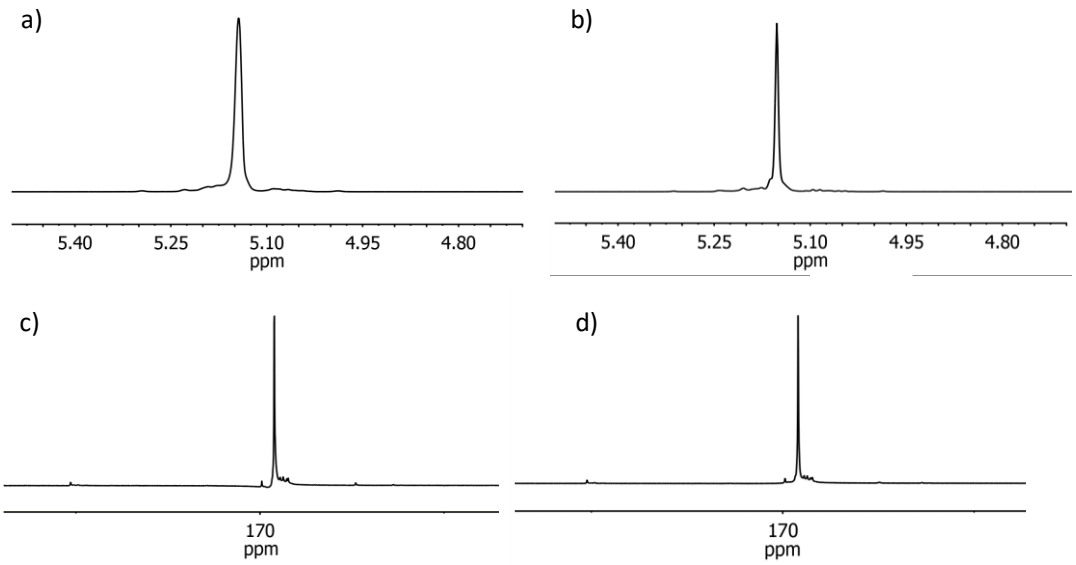

Figure 4.3 Homonuclear decoupled ^{1}H spectra of the methine region of (a) $PLLA_{32}$ and (b) $PDLA_{32}$ (500 MHz, $CDCl_3$). Quantitative ^{13}C NMR of (c) $PLLA_{32}$ and (d) $PDLA_{32}$.

Besides, the chirality of poly(L(D)-lactide) was further verified by optical rotation, which was determined to be $[\alpha]^{25}_{D} = +127$ and $[\alpha]^{25}_{L} = -123$ ($c = 0.1$ mg mL^{-1}, $CHCl_3$, 25 °C). Similar to the procedure mentioned in **Chapter 2**, the RAFT agent 2-(dodecylthiocarbonothioylthio)-2-methylpropionic acid (DDMAT) was coupled to the end of the polymer backbone. In the ^{1}H NMR spectrum of an example (i.e. $PDLA_{32}$, **Figure 4.4 a**), the integral of the methylene protons (proton 6) is equal to the integral of the initiator $OC\mathit{H_2}CH_2C\mathit{H_2}O$ (proton 2), which verifies the successful attachment of the RAFT agent to the polymer backbone at both ends. The highly overlapping signals collected from both the UV and RI detectors in SEC analysis (**Figure 4.4 b**) further supports this conclusion.

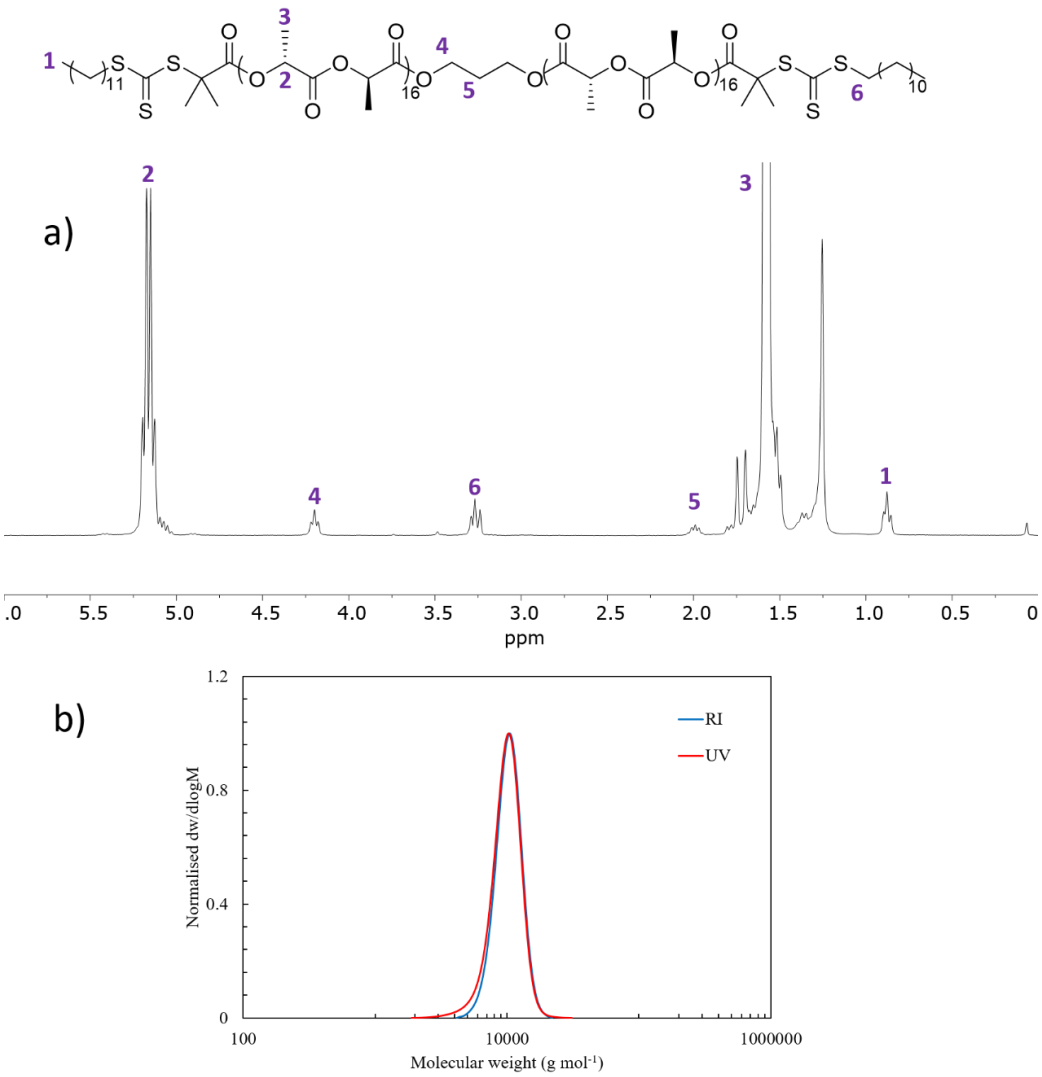

Figure 4.4 (a) ^{1}H NMR spectrum of CTA-PDLA$_{32}$-CTA (400 MHz, $CDCl_3$). (b) SEC analysis of CTA-PDLA$_{32}$-CTA (DMF with 5 mM NH_4BF_4).

In the next step, the corona block HEAAm was subsequently grown from the dual-headed macro-initiator through RAFT polymerisation. The reaction was carried out in DMSO to minimise the hydrogen bonding, and the conversion of the polymerisation was controlled to reach 70% to prevent termination. The composition of each block was calculated by ^{1}H NMR spectroscopy using the known integral for the methane protons in the PLLA unit (δ = 5.14 ppm) and the new peaks corresponding to the HEAAm side chain (δ = 7.95 ppm) (**Figure 4.5**).

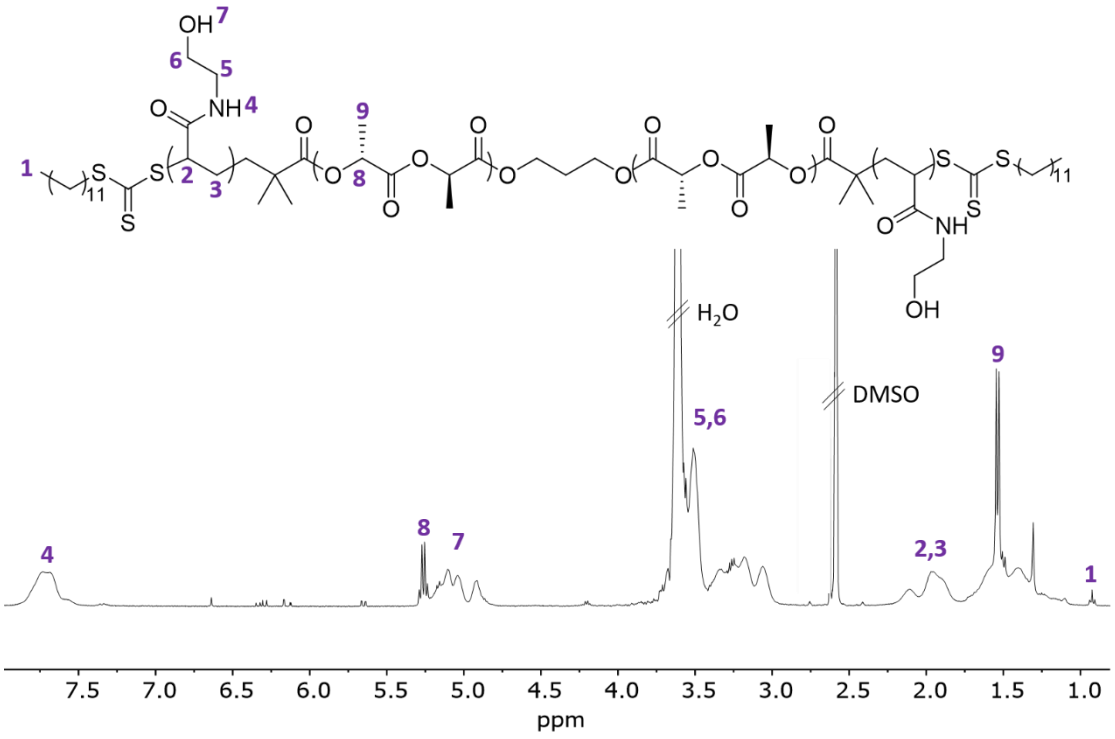

Figure 4.5 ^{1}H NMR spectrum (400 MHz, d_6-DMSO) of PHEAAm$_{92}$-*b*-PDLA$_{32}$-*b*-PHEAAm$_{92}$.

In order to have a comprehensive understanding of the effect of the polymer composition on the morphological transition process, a series of ABA type block copolymers were synthesized with different core and corona length. All the triblock copolymers listed below (**Table 4.1**) showed monomodel dispersity ($Đ_M$ < 1.3) as calculated by SEC analysis (**Figure 4.6**), while the molar mass determined from SEC is a bit higher than that determined by ^{1}H NMR, because of the deviation of the gyration ratio of the calibration standard.

Table 4.1 PHEAAm$_y$-*b*-PL(D)LA$_x$-*b*-PHEAAm$_y$ triblock copolymers prepared with varying core and corona lengths.

Triblock copolymers	M_n (kDa)[a]	M_n (kDa)[b]	$Đ_M$[b]	Hydrophobic %wt[c]	Assemblies
PHEAAm$_{42}$-*b*-PLLA$_{32}$-*b*-PHEAAm$_{42}$, **L1**	14.3	20.1	1.21	32%	**SA-L1**
PHEAAm$_{92}$-*b*-PLLA$_{32}$-*b*-PHEAAm$_{92}$, **L2**	25.8	30.6	1.25	18%	**SA-L2**
PHEAAm$_{65}$-*b*-PLLA$_{50}$-*b*-PHEAAm$_{65}$, **L3**	22.2	28.5	1.19	33%	**SA-L3**
PHEAAm$_{95}$-*b*-PLLA$_{50}$-*b*-PHEAAm$_{95}$, **L4**	29.1	34.2	1.23	25%	**SA-L4**
PHEAAm$_{50}$-*b*-PDLA$_{32}$-*b*-PHEAAm$_{50}$, **D1**	16.1	21.3	1.16	29%	**SA-D1**
PHEAAm$_{86}$-*b*-PDLA$_{32}$-*b*-PHEAAm$_{86}$, **D2**	24.4	29.6	1.18	19%	**SA-D2**
PHEAAm$_{70}$-*b*-PDLA$_{50}$-*b*-PHEAAm$_{70}$, **D3**	23.3	28.7	1.21	30%	**SA-D3**
PHEAAm$_{100}$-*b*-PDLA$_{50}$-*b*-PHEAAm$_{100}$, **D4**	30.2	34.2	1.24	24%	**SA-D4**

[a] Measured by ^{1}H NMR (400 MHz, d_6-DMSO). [b] Measured by SEC (DMF with 5 mM NH_4BF_4). [c] PLLA weight fraction in the PHEAAm$_y$-*b*-PLLA$_x$-*b*-PHEAAm$_y$ triblock copolymers. All the assemblies were obtained by solubilizing (5 mg mL^{-1}) and aging polymer in methanol at room temp (25 °C).

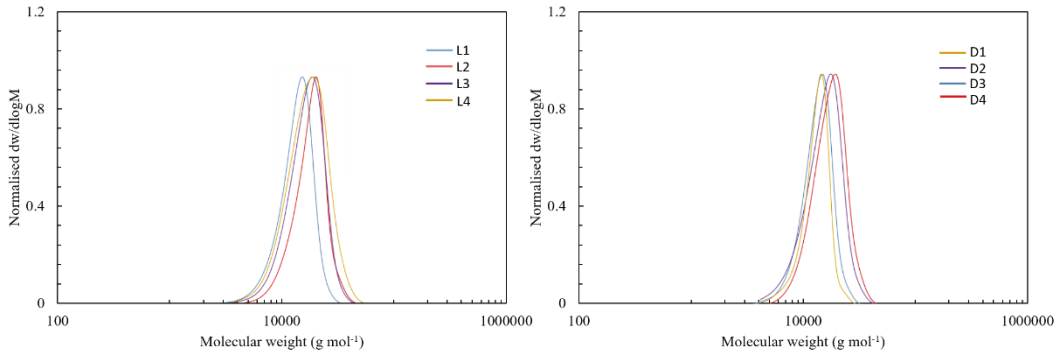

Figure 4.6 SEC traces of copolymers (a) **L1-L4** and (b) **D1-D4** from refractive index signals (DMF with 5 mM NH_4BF_4).

Overall, a range of triblock copolymers PHEAAm$_x$-*b*-PL(D)LA$_{32}$-*b*-PHEAAm$_x$ with varying core/corona lengths were fabricated by combining ROP and RAFT polymerisation techniques which could be further utilised for the assembly study.

4.3.3 Crystallisation-Driven Self-Assembly of PHEAAm$_y$-*b*-PL(D)LA$_x$-*b*-PHEAAm$_y$ triblock copolymers

One of the main conclusions derived from **Chapter 2** states that singular alcoholic solvents (e.g. methanol or ethanol) can be used to prepare 1D and 2D micelles of stereoregular PLA-based block copolymers *via* CDSA approaches. Additionally, in **Chapter 3**, the scope of the work was extended to include other corona polymers, such as 4-vinylpyridine and *N*-hydroxyethyl acrylate. The assembly methodology described in **Chapter 2** and **3** is followed in the current chapter. Specifically, the copolymers listed in **Table 1** were dissolved in methanol (5 mg mL^{-1}) after vortexing and sonication, with barely no Tyndall effect being observed for the first hour at room temperature (i.e. 25 °C). After aging for 24 hours, the assembly solution got turbid (Tyndall effect), which indicates the formation of micelles (**SA-L1** to **SA-D4** in **Table 1)**.

As a general procedure, transmission electron microscopy (TEM) was used as a characterisation technique to determine the morphology of the assemblies. Judged by TEM, polymer **L1** assembled into micelles with length values ranging from 200 nm to 2 μm, while the width was *ca.* 30 nm (**Figure 4.7 a**). When the corona to core ratio was increased from 2:1 to 4:1 (**L2**), the width of the resulting cylinders also increased to 40 nm (**Figure 4.7 b**). In contrast, the increase of core length (from DP = 32 to DP = 50) had no effect on the assembly morphology. Indeed, the structures obtained were well-defined fibre-like nanoparticles (**Figure 4.7 c** and **d**). Meanwhile, the results obtained for the enantiomer assemblies of copolymers PHEAAm$_y$-*b*-PDLA$_x$-*b*-PHEAAm$_y$ (**Figure 4.7 e-h**) are in good agreement with those obtained for the PLLA counterpart. Hence, in general, cylindrical micelles were achieved from PHEAAm$_y$-*b*-PL(D)LA$_x$-*b*-PHEAAm$_y$ triblock copolymers following this singular alcoholic

solvent approach regardless of their block ratio (corona to core ratio varied from 4:1 to 2:1) or their chiral characteristics.

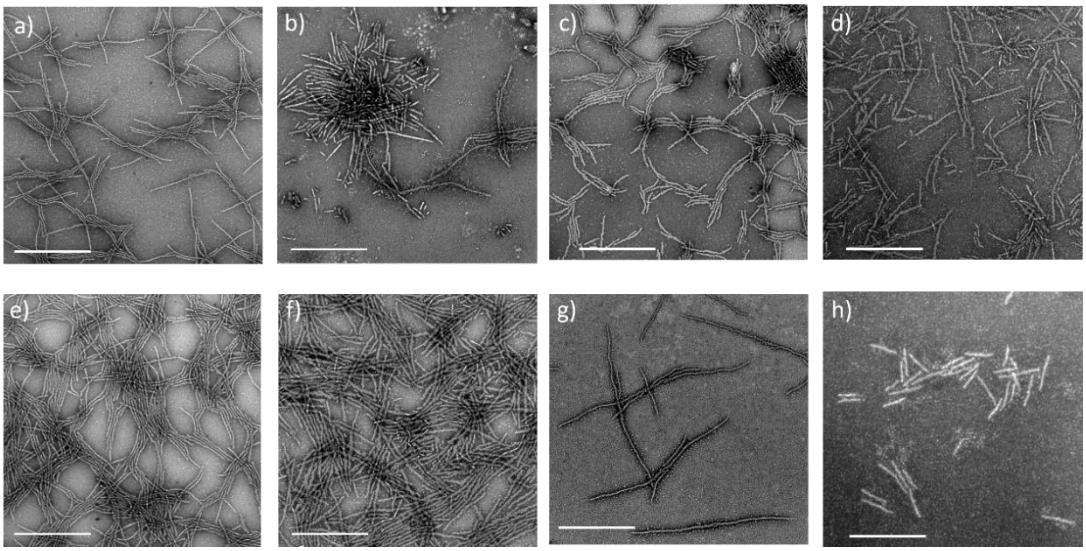

Figure 4.7 TEM micrographs of copolymers assembled in methanol 5 mg mL^{-1} at room temperature (25 °C) for two days: (a) **SA-L1,** (b) **SA-L2**, (c) **SA-L3**, (d) **SA-L4**, (e) **SA-D1**, (f) **SA-D2**, (g) **SA-D3** and (h) **SA-D4**. Samples were negatively stained using uranyl acetate (0.5 wt %). Scale bar = 1 μm.

Finally, in order to confirm the stability of the assemblies in methanol, the nanoparticles were aged for a longer period (i.e. one month) at room temperature. Assemblies **SA-L1** and **SA-L2** displayed negligible morphological differences (**Figure 4.8**) in comparison to the original morphology (aging time two days, **Figure 4.7 a** and **b**), which evidences the robustness of the self-assembled cylindrical micelles.

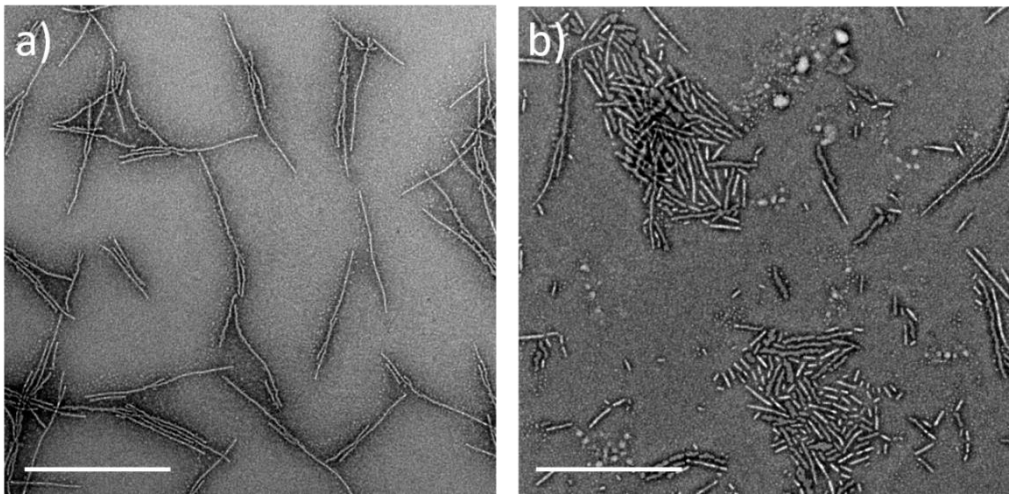

Figure 4.8 TEM micrographs of assemblies **SA-L1** and **SA-L2** after aging for one month. Samples were negatively stained using uranyl acetate (0.5 wt %). Scale bar = 1 μm.

4.3.4 Stereocomplexation-triggered morphological transition in methanol: from homochiral cylinders to aggregates

After "verifying" the formation of enantiomer pure fibre-like micelles, their morphological transition triggered by stereocomplexation was subsequently investigated. To that end, equal amounts of enantiomer cylindrical assemblies (1 mg mL^{-1}) (**SA-L1** and **SA-D1**) were mixed together in methanol at body temperature (i.e. 37 °C) and aged for 24 h. Surprisingly, after that period, few cylindrical micelles were spotted on the TEM grid, whereas a new morphology defined as aggregated worm had appeared (**Figure 4.9 c**). This result is of great significance since the morphological transition proceeded at body temperature, which is a step closer to our target conditions, i.e. physiological conditions.

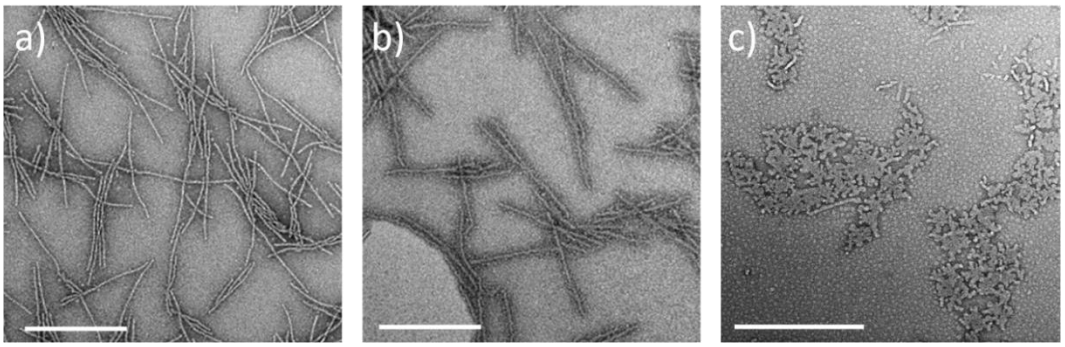

Figure 4.9 TEM micrographs of the cylindrical assemblies (a) **SA-L1** and (b) **SA-L2**. (c) Image showing the resulting morphology after mixing the enantiomer pure cylinders for one day at body temperature. Samples were negatively stained using uranyl acetate (0.5 wt %). Scale bar = 1 μm.

In order to understand this transition process, a kinetic study was carried out. The long cylindrical micelles (**SA-L1** and **SA-D1**) were sonicated separately into shorter cylinders (50-300 nm) in an ice bath to obtain comparatively uniform micelles. After sonication, both solutions were mixed together in methanol, and the resulting structures were observed by TEM to reveal truncated fibre-like micelles (< 500 nm) (**Figure 4.10 a**). Then, as previously done, the assembly solution was aged at body temperature (37 ºC) in methanol, and aliquots were taken at specific time points (i.e. 2 h, 5 h, 8 h and 24 h) for characterisation. Interestingly, the formation of stereocomplex structures was already detected after aging for two hours (**Figure 4.10 b**), which indicated the quick initiation of such morphological transformation. As the aging time evolved, the amount of cylinders spotted on the grid gradually decreased as the newly formed morphology increased accordingly. After 24 hours, fibre-like micelles were hardly detected, which suggested that the morphological transition was almost finalized. A control experiment was performed by aging the pure chiral micelles (**SA-L1**) in the same conditions (methanol, 37 ºC) for 24 h. The micelles remained in the original state, i.e. cylindrical morphology (**Figure 4.10 f**).

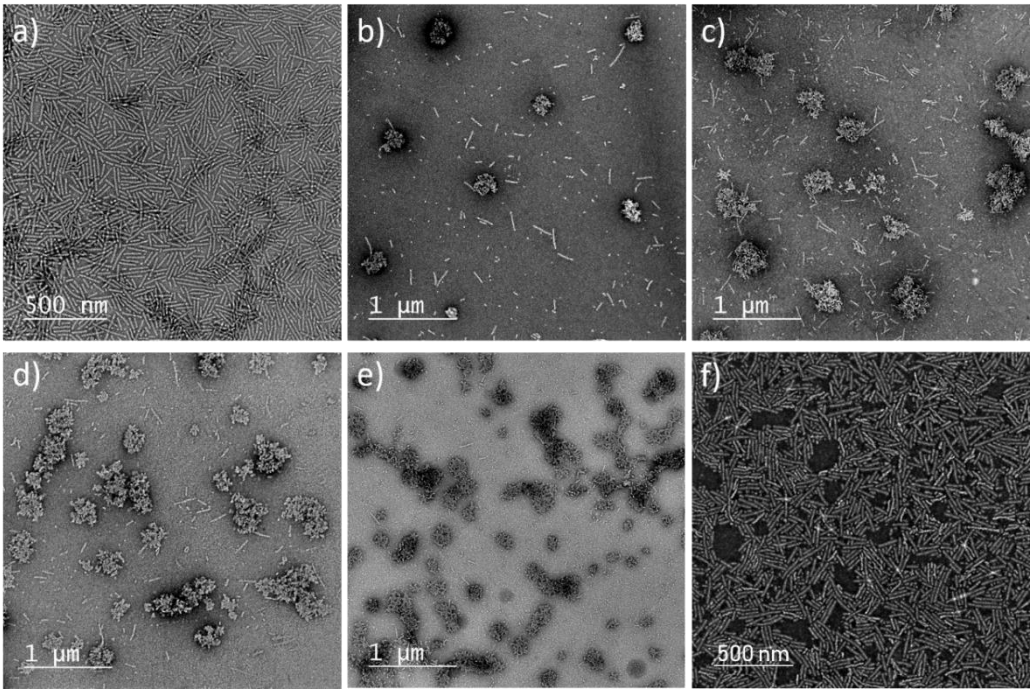

Figure 4.10 TEM micrographs of the mixed assembly solution **SA-L1** and **SA-D1** after aging at 37 ℃ for (a) 0 h, (b) 2 h, (c) 5 h, (d) 8 h and (e) 24 h. (f) Homo-chiral micelles **SA-L1** aged at body temperature (37 ℃) for 24 h. Samples were negatively stained using uranyl acetate (0.5 wt %).

According to these results, it was hypothesized that the morphological transformation was triggered by the interaction between the stereocenters of the enantiomer copolymers. Fourier-transform infrared (FTIR) is a suitable characterisation technique to confirm the formation of sterecomplex lactide enantiomer[7] since the vibrational wavenumber of the carboxyl functional group of homo-chiral lactide will shift from 1758 cm^{-1} to 1750 cm^{-1}. According to the IR spectra of the samples (mixture micelle solution of **SA-L1** and **SA-D1**), the vibrational signal of carboxyl do shift from 1758 to 1750 cm^{-1} in 24 hours (**Figure 4.11 a**), which consolidates the assumption explained above. The spectrum between 1720 cm^{-1} and 1780 cm^{-1} was deconvoluted into two isolated peaks, based on which the transition process could be monitored and compared in value.

Specifically, the progression of the transformation (P) was defined by the area integration percentage of signal corresponding to 1750 cm^{-1}. Although there are some limitations to predict the transition process using this approach, the data collected and analysed under the same condition within this system is still informative to draw a conclusion.

$$P = \frac{A_{1750}}{A_{1750}+A_{1758}} \qquad \text{(Equation. 1)}$$

Noticeably, in two hours, the progression of the transformation reached a value of 41%, which reveals how fast the process is (**Figure 4.11 b**).

a)

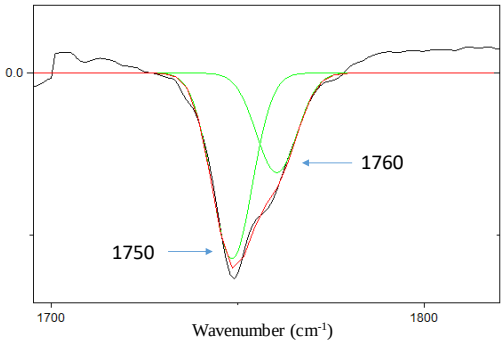

b)

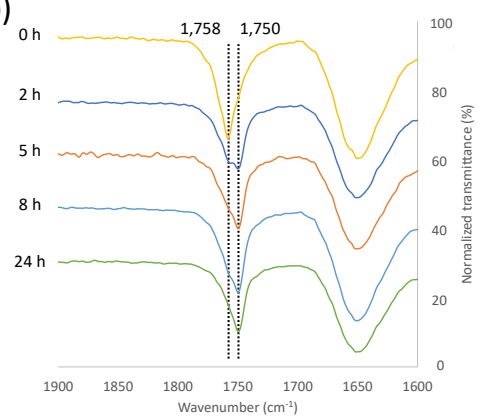

c)

Time (h)	Progression of the transition
0	0%
2	41%
5	60%
8	83%
24	91%

Figure 4.11 The mixed assembly solution **SA-L1** and **SA-D1** after sonication was aged at body temperature (37 °C) and monitored at different time interval: (a) Example curve fit of the FT-IR spectra measured in methanol at 5 hours. The red line represent the fitted curve, while the black line represent the measured spectrum. The green line represent curves of peak 1750 cm^{-1} and 1760 cm^{-1} after deconvolution (b) FTIR spectra revealed that the wavenumber of the carbonyl group vibration of PLA shifted from 1758 to 1750 cm^{-1} over time during the morphological transition process. (c) Quantification of the transformation process by FTIR.

Moreover, to corroborate the formation of stereocomplex micelles, assembled samples aged for 24 hours were prepared for Wide-angle X-ray scattering (WAXS) analysis. The presence of sharp Bragg peaks at a 2θ value of 12° and 23.8°, which correspond to the sterecomplex, definitively proved the formation of crystalline stereocomplexation (**Figure 4.12**), while the Bragg peak attributed to the homochiral polymer at a 2θ value of 16.6° was barely detected, thus confirming that the transition was almost completed after aging for 24 hours.

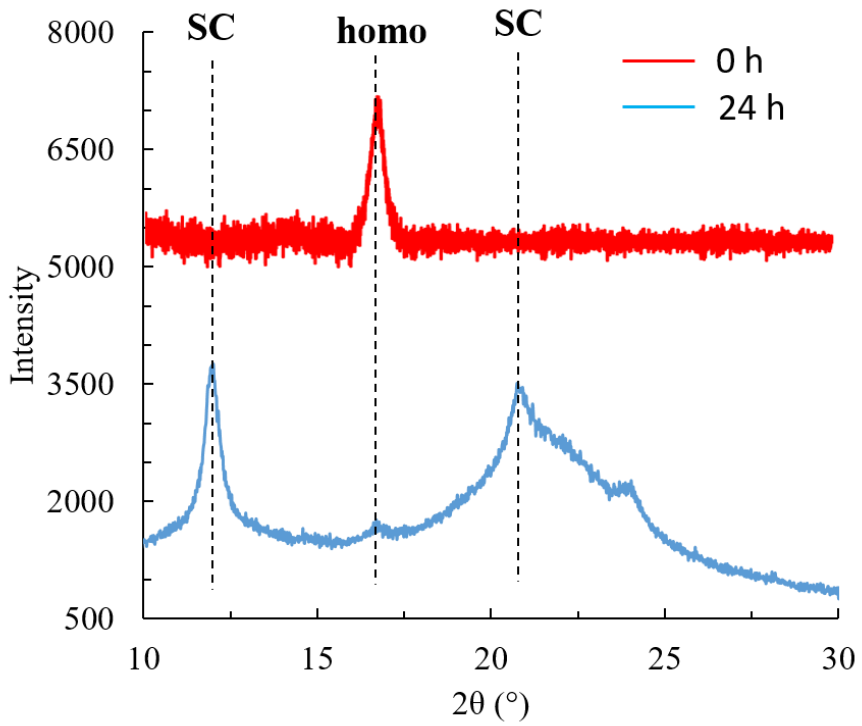

Figure 4.12 The mixed assembly solution **SA-L1** and **SA-D1** after sonication was aged at body temperature (37 ℃). WAXD diffractograms evidenced the appearance of stereocomplex Bragg peak at a *2θ* value of 12° and 23.8° and the disappearance of homochiral Bragg peak at a 2θ value of 16.6° after aging for 24 hours.

4.3.5 Elucidating the mechanism of stereocomplexation

According to previous work in the group, the morphological transition from cylinders to spheres of PL(D)LA-*b*-PAA polymers has been explained by considering the

"unimer-exchange" mechanism.[7] It is assumed that a balance between unimers and the crystalline assemblies exists. The mixed enantiomer polymers prefer to reorganize into new particles on account of the intermolecular hydrogen bonding between the enantiomer and, consequently, the original micelles would continuously disassemble into unimers. Because of the similarity between the systems, the "unimer-exchange" theory is also applied to the triblock copolymers studied herein.

To further clarify this point, copolymers **L1** and **D1** were mixed together directly and aged in methanol at 37 °C for one day, which also resulted in aggregated worm assemblies (**Figure 4.13 a**), similarly to those achieved from the enantiomer cylinders (**Figure 4.13 b**). This result strongly supports the "unimer-exchange" theory as explanation for the morphological transition process of this specific system, which is illustrated in **Figure 4.13 c**.

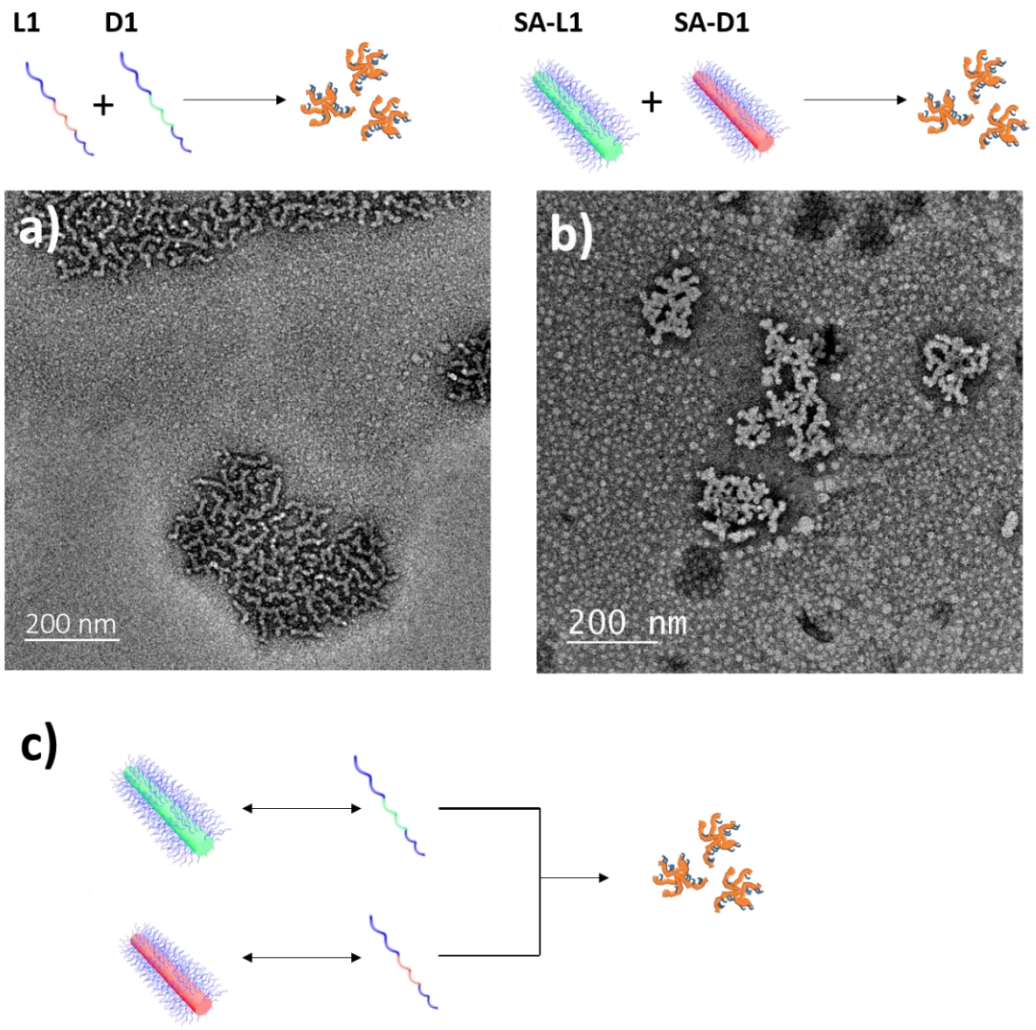

Figure 4.13 (a) TEM micrographs of aggregated worm-like structures obtained after mixing polymers **L1** and **D1** at body temperature (37 °C) in methanol. (b) TEM images of aggregated worm-like structures obtained after mixing micelles **SA-L1** and **SA-D1** at 37 °C in methanol. Samples were negatively stained using uranyl acetate (0.5 wt %). (c) Schematic representation of the formation of the new morphology triggered by sterecomplexation.

4.3.6 Study of the parameters affecting the morphological transition

4.3.6.1 The effect of core length

Polymer block composition plays a vital role in the dynamic balance between assemblies and unimers. Since the "unimer-exchange" mechanism was used to explain the morphological transition process, polymers with different block composition are expected to affect the transition speed. The influence of the core block length was investigated firstly. To that end, copolymers with longer core length (i.e. **L3** and **D3**) were synthesized and assembled keeping the block ratio close to 2:1 (corona to core), which corresponds to copolymers **L1** and **D1**. The assemblies (**SA-L3** and **SA-D3**), which were sonicated into shorter fibres before mixing them in MeOH (1 mg mL^{-1}), were aged at 37 °C. By means of TEM monitoring (**Figure 4.14 a-c**), it was observed that their morphological transition was dramatically slowed down compared to that displayed by copolymers with shorter core length values (**SA-L1** and **SA-D1** mixture). Indeed, a large amount of cylinders were still detectable on the grid after aging for three days. The IR spectra (**Figure 4.14 d**) further supports this observation since only a progression value of 55% was determined after 3 days of aging, while it took 7 days to accomplish the morphological transformation in majority (89%). Since the block ratio for **L3** and **D3** is pretty similar to that of samples **L1** and **D1**, the difference in solubility cannot be accounted responsible for the delay in the morphological transformation. However, it was reported that core block length displayed a dramatic influence on the chain exchange kinetics of poly(styrene)-*b*-poly(ethylene-alt-propylene) (SEP) diblock copolymers, i.e. longer core results in slower exchanging rate.[14] It is also believed that longer core length values slow down the unimer-assembly exchange rate in this system as well, thus delaying the formation of stereocomplex structures.

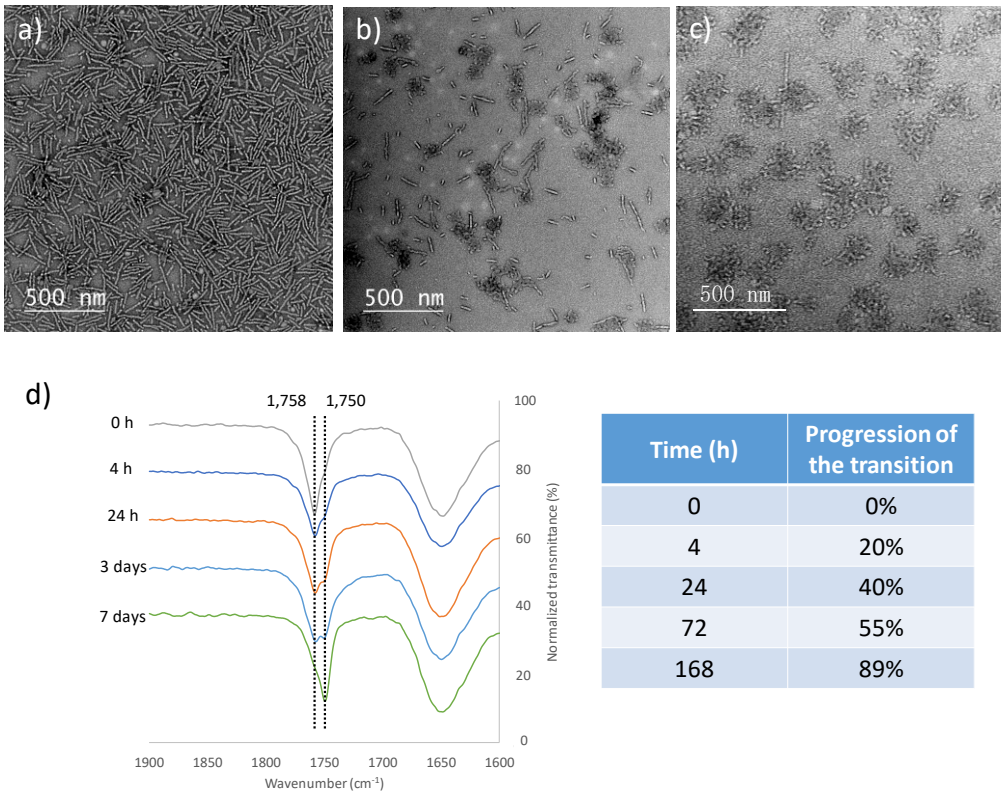

Time (h)	Progression of the transition
0	0%
4	20%
24	40%
72	55%
168	89%

Figure 4.14 TEM micrographs of the mixed assembly solution **SA-L3** and **SA-D3** after aging at 37 °C in methanol for (a) 0 h, (b) 3 d, and (c) 7 d. Samples were negatively stained using uranyl acetate (0.5 wt %). (d) FTIR spectra revealed that the wavenumber of the carbonyl group vibration of PLA shifted from 1758 to 1750 cm^{-1} over time during the morphological transition process.

4.3.6.2 The effect of corona length

The effect of the corona block length values in the morphological transition was also studied at the same time. In particular, the hydrophilic block was extended from DP= 84 to DP = 184 (**L2** and **D2**) for a fixed hydrophobic core PLA_{32}. The corresponding assemblies **SA-L2** and **SA-D2** were sonicated in shorter micelles and underwent the morphological transition test. According to the data collected from TEM and FTIR (**Figure 4.15**), the transition process showed negligible difference in comparison to the shorter corona counterparts (**SA-L1** and **SA-D1**). Specifically, after aging for 2 h, a blend of cylinders and stereoaggregates was observed on the grid, while the quantification by FTIR signals determined a progression value of 43%, which is close to that observed for the mixture of **SA-L1** and **SA-D1** samples (i.e. 41%). Besides, the morphological transition was close to completion within one day, which is again in good agreement with the response shown by the shorter corona counterpart. The influence of the corona block length on the chain exchange is a controversial topic because of its complexity. In fact, it is generally assumed to be less important than the effect of the core block in the exchange process.[10] From a solubility point of view, it was postulated that the increased solubility introduced by the longer corona length showed no difference since the polymer was already very soluble in methanol. Indeed, for this system, varying the core block length showed a more significant effect on the transition process than changing the corona block length.

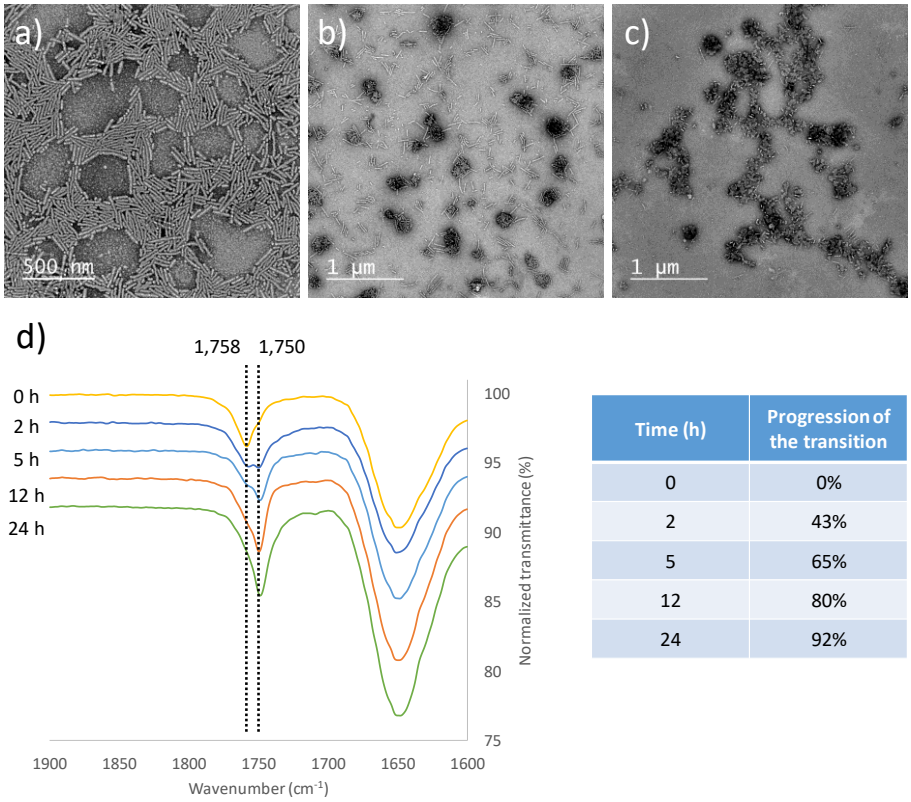

Time (h)	Progression of the transition
0	0%
2	43%
5	65%
12	80%
24	92%

Figure 4.15 TEM micrographs of the mixed assembly solution **SA-L2** and **SA-D2** after aging at 37 °C in methanol for (a) 0 h, (b) 2 h, and (c) 1 d. Samples were negatively stained using uranyl acetate (0.5 wt %). (d) FTIR spectra revealed that the wavenumber of the carbonyl group vibration of PLA shifted from 1758 to 1750 cm^{-1} over time during the morphological transition process.

4.3.6.3 The effect of aging temperature

In addition to the block length values, the aging temperature was also inspected with respect to its effect on the morphological transition process. Cylindrical micelles **SA-L1** and **SA-L2** were aged at room temperature (25 °C) for comparison. The process was observed by TEM (**Figure 4.16 a-c**): fibre-like micelles were detected as the dominant shape on day 4, whereas a large amount of cylinders still coexisted with stereoaggregates on day 20. Further supported by FTIR monitoring, it was determined that the transition process was significantly slowed down at room temperature, only 49% and 61% of progression being reached after 9 and 20 days of aging, respectively

(**Figure 4.16 d**). Not only does the lower temperature decelerate the "unimer-assembly" exchanging rate, but also decreases the polymer solubility, which altogether slows down the transition to a great extent. This result exemplified the important role played by temperature on the kinetics of the morphological transition process.

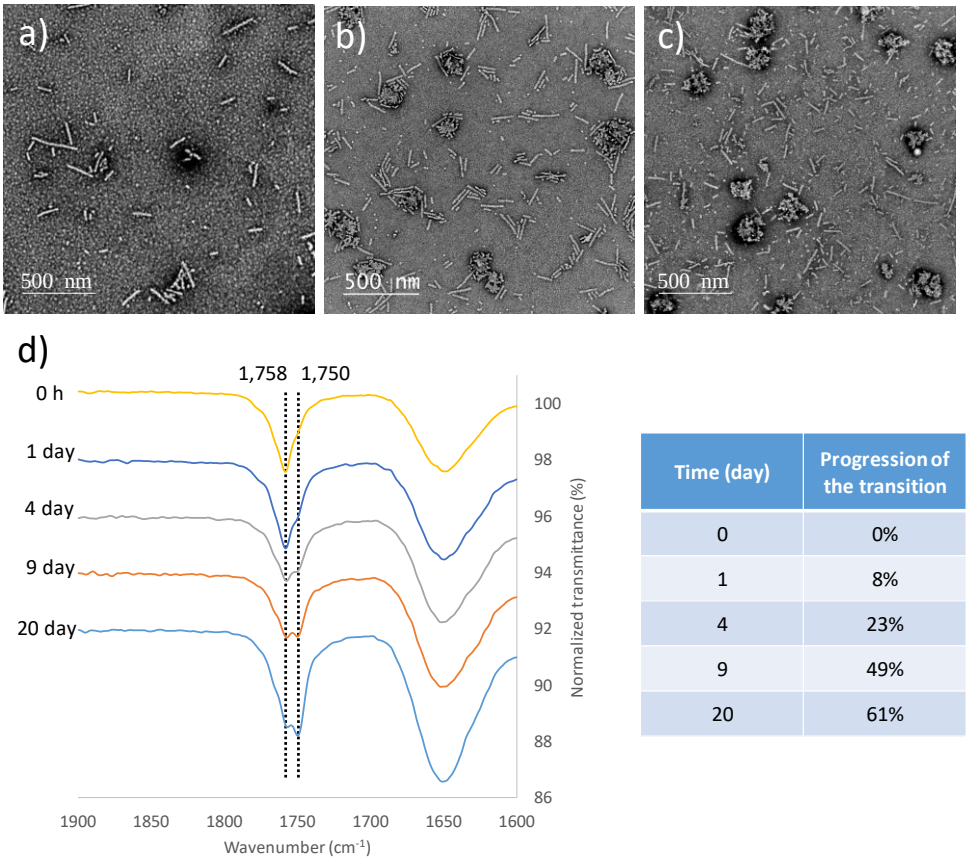

Time (day)	Progression of the transition
0	0%
1	8%
4	23%
9	49%
20	61%

Figure 4.16 TEM micrographs of the mixed assembly solution **SA-L1** and **SA-D1** after aging at room temperature (25 °C) in methanol for (a) 4 d, (b) 9 d, and (c) 20 d. Samples were negatively stained using uranyl acetate (0.5 wt %). Samples were negatively stained using uranyl acetate (0.5 wt %). (d) FTIR spectra revealed that the wavenumber of the carbonyl group vibration of PLA shifted from 1758 to 1750 cm^{-1} over time during the morphological transition process.

4.3.6.4 The effect of corona chemistry

Although the variation of corona length has been demonstrated to show no discernable effect on the morphological transition process, the alteration of its chemistry is believed to influence the process as a consequence of the solubility difference. Poly(*N*,*N*-dimethyl acrylamide)-*b*-PLLA-*b*-poly(*N*,*N*-dimethyl acrylamide) ($PDMA_{45}$-*b*-$PLLA_{32}$-*b*-$PDMA_{45}$) as described in **Chapter 2** assembled into cylinders and so did its enantiomer ($PDMA_{50}$-*b*-$PDLA_{32}$-*b*-$PDMA_{50}$) (**Figure 4.17 a** and **b**). Following the procedure applied previously, the mixed micelles were aged in methanol at 37 °C; however, in this case, no morphological transition was detected after 7 days (**Figure 4.17 c**), while the FTIR spectra evidenced the absence of the stereocomplex structure since the characteristic signal of sterecomplexation at 1750 cm^{-1} is missing (**Figure 4.17 d**). The Hildebrand solubility parameter of PHEAAm (δ_h = 24.0 $MPa^{1/2}$) is much closer to methanol (δ_h = 29.8 $MPa^{1/2}$) than PDMA (δ_h = 18.0 $MPa^{1/2}$)[15], which indicates better solubility of PHEAAm over PDMA in methanol. Therefore, the energy barrier for the unimer ($PDMA_{45}$-*b*-$PLLA_{32}$-*b*-$PDMA_{45}$) to be extracted from the crystalline assemblies is much higher, which dramatically slows down the chain exchange process or even freezes the dynamic balance, thus inhibiting the formation of the sterecomplex structure. This result underlines the importance of the corona chemistry on the transition process, which in turn guides the optimisation of the morphological transition in aqueous solutions, as discussed in **Section 4.3.8**.

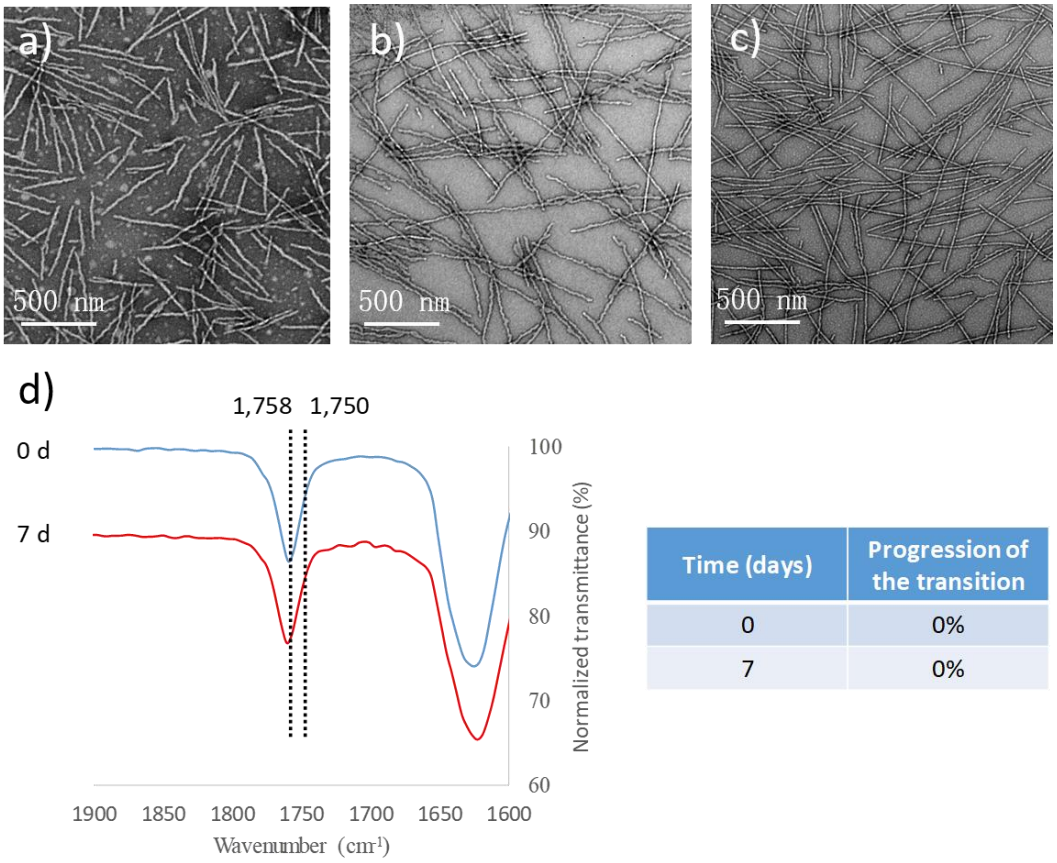

Time (days)	Progression of the transition
0	0%
7	0%

Figure 4.17 TEM micrographs of cylindrical micelles from polymer (a) $PDMA_{45}$-*b*-$PLLA_{32}$-*b*-$PDMA_{45}$ and (b) $PDMA_{50}$-*b*-$PDLA_{32}$-*b*-$PDMA_{50}$ as prepared. They were mixed at body temperature (37 ℃) in methanol and aged for 7 days before another analysis (c). Samples were negatively stained using uranyl acetate (0.5 wt %). (d) FTIR spectra of the mixture assembly solution (37 ℃, MeOH) after 7 d.

4.3.7 Stabilising the assemblies in aqueous solution

Since the stereocomplex-triggered morphological transition of $PHEAAm_y$-*b*-$PL(D)LA_x$-*b*-$PHEAAm_y$ assemblies had been well understood in methanol, the next step focused on investigating their performance in water considering their potential biotechnological applications. Hence, cylindrical micelles derived from $PHEAAm_{42}$-*b*-$PL(D)LA_{32}$-*b*-$PHEAAm_{42}$ copolymers were transferred into an aqueous solution by dialysis; however, the assemblies precipitated out in a few minutes. The assembled structures in water were characterised by TEM to show that the cylinders had piled up

into aggregation (**Figure 4.18 b**), which reveals the instability of such nanoparticles in water.

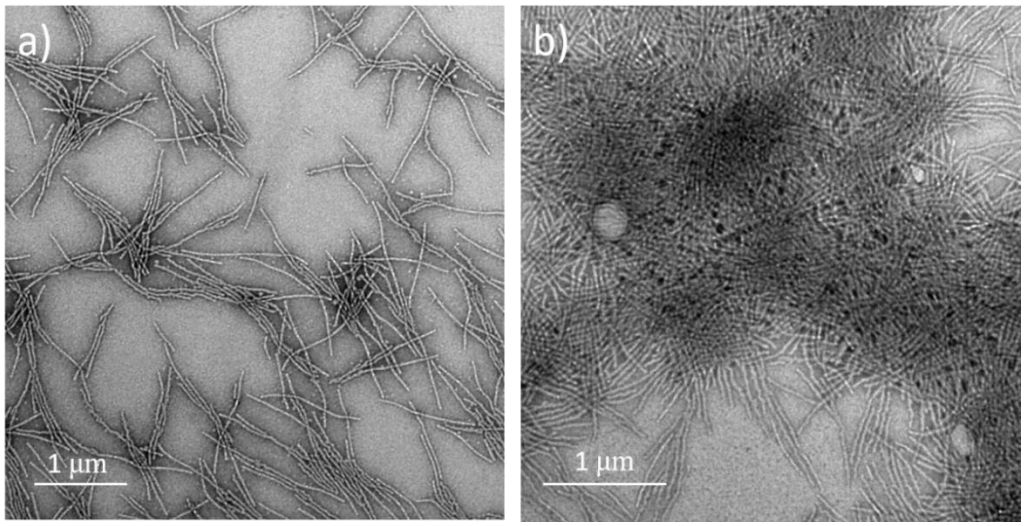

Figure 4.18 TEM micrographs of the assemblies **SA-L1** in methanol (a) and after being transferred to water at room temperature, which resulted in an aggregated morphology (b). Samples were negatively stained using uranyl acetate (0.5 wt %).

4.3.7.1 Preparation of pentablock copolymers

In a previous work[16], the cylindrical micelles derived from PCL-*b*-PDMA diblock copolymers also showed this stability problem in water, which was attributed to the swelling of the corona block after transferring into water, causing stress to the crystalline structure and its subsequent fracture. For that system, it was found that an intermediate hydrophobic block between the core and the corona successfully stabilised the micelles in water. Hence, taking inspiration from that work, a pentablock copolymer (i.e. PHEAAm-*b*-PMMA-*b*-PLLA-*b*-PMMA-*b*-PHEAAm) was designed by firstly growing short, glassy methyl methacrylate (MMA) blocks from a dual-headed macro-CTA, the block ratio was calculated from protons 1 and 3 of the ^{1}H NMR spectra (**Figure 4.19**). According to the SEC analysis (**Figure 4.20**), a high

molecular weight shoulder was always found in the spectra, even when the monomer conversion was controlled to be under 10%, which was mainly ascribed to the poor controllability of the RAFT agent DDMAT over the methacrylate.[17]

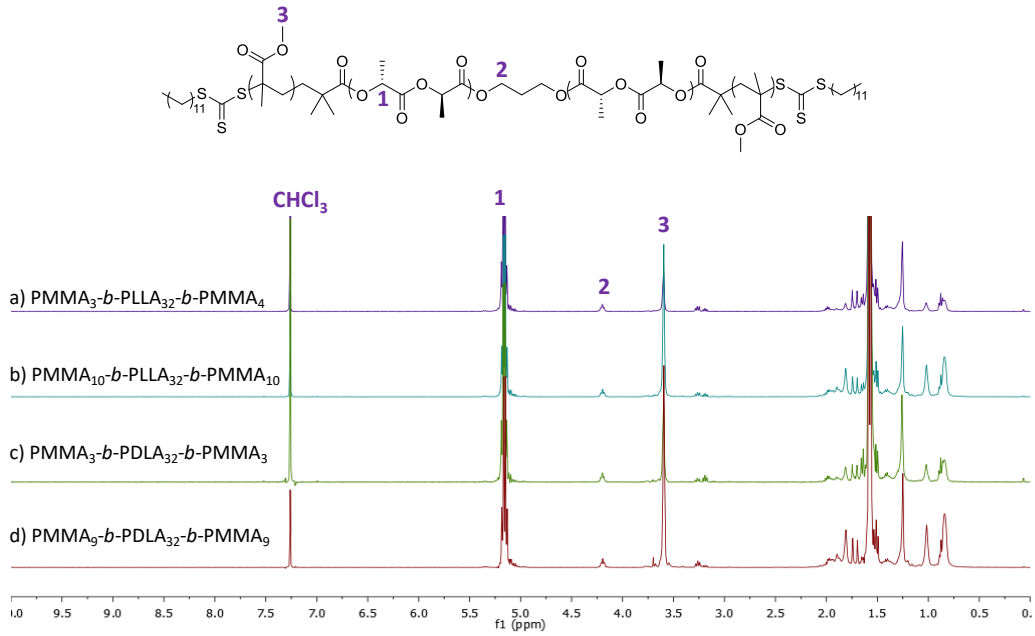

Figure 4.19 ^{1}H NMR spectra (400 MHz, $CDCl_3$) of (a) $PMMA_4$-*b*-$PLLA_{32}$-*b*-$PMMA_4$, (b) $PMMA_{10}$-*b*-$PLLA_{32}$-*b*-$PMMA_{10}$, (c) $PMMA_3$-*b*-$PDLA_{32}$-*b*-$PMMA_3$ and (d) $PMMA_9$-*b*-$PDLA_{32}$-*b*-$PMMA_9$.

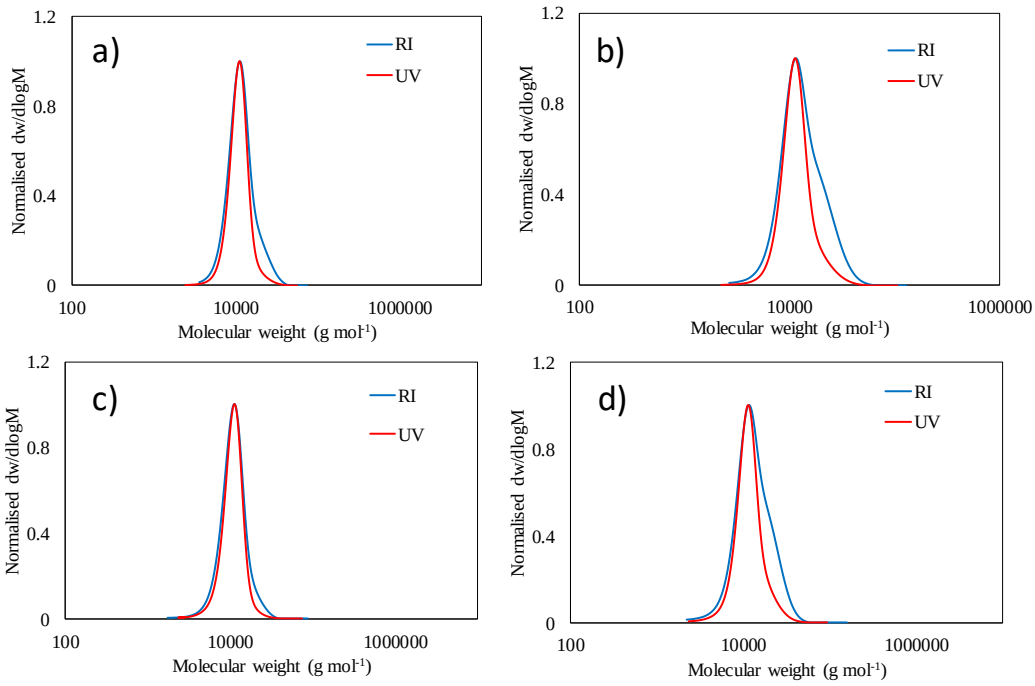

Figure 4.20 SEC analysis (DMF with 5 mM NH_4BF_4) of copolymers (a) $PMMA_4$-*b*-$PLLA_{32}$-*b*-$PMMA_4$, (b) $PMMA_{10}$-*b*-$PLLA_{32}$-*b*-$PMMA_{10}$, (c) $PMMA_3$-*b*-$PDLA_{32}$-*b*-$PMMA_3$ and (d) $PMMA_9$-*b*-$PDLA_{32}$-*b*-$PMMA_9$.

Another hydrophobic block (i.e. n-butyl acrylate) was selected to replace MMA based on its straightforward and controllable polymerisation with respect to DDMAT. ^{1}H NMR spectroscopy verified that the monomer had been attached to the macro-CTA (**Figure 4.21**), with the block ratio being calculated based on the specific proton signals (1 and 2), whereas the SEC trace showed that the polymerisation had been under control (**Figure 4.22**).

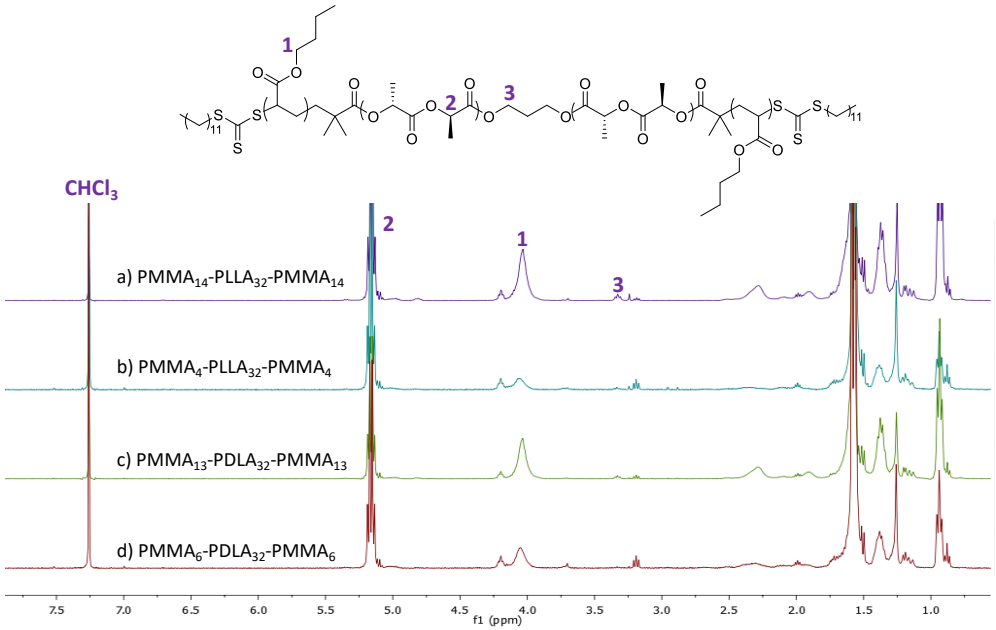

Figure 4.21 ^{1}H NMR spectra (400 MHz, $CDCl_3$) of (a) $PBuA_{14}$-*b*-$PLLA_{32}$-*b*-$PBuA_{14}$, (b) $PBuA_4$-*b*-$PLLA_{32}$-*b*-$PBuA_4$, (c) $PBuA_{13}$-*b*-$PDLA_{32}$-*b*-$PBuA_{13}$ and (d) $PBuA_6$-*b*-$PDLA_{32}$-*b*- $PBuA_6$.

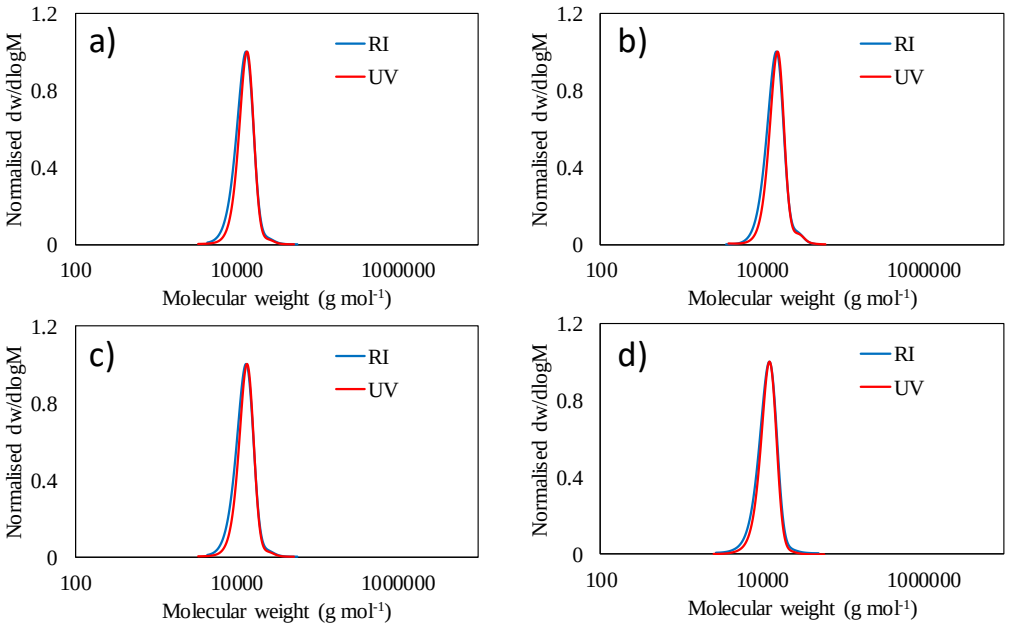

Figure 4.22 SEC analysis (DMF with 5 mM NH_4BF_4) of copolymers (a) $PBuA_{14}$-*b*-$PLLA_{32}$-*b*-$PBuA_{14}$, (b) $PBuA_4$-*b*-$PLLA_{32}$-*b*-$PBuA_4$, (c) $PBuA_{13}$-*b*-$PDLA_{32}$-*b*-$PBuA_{13}$ and (d) $PBuA_6$-*b*-$PDLA_{32}$-*b*- $PBuA_6$.

Finally, the PBuA$_{14}$-*b*-PL(D)LA$_{32}$-*b*-PBuA$_{14}$ triblock copolymers were chain-extended to pentablock copolymers (i.e. PHEAAm$_{100}$-*b*-PBuA$_{14}$-*b*-PL(D)LA$_{32}$-*b*-PBuA$_{14}$-*b*-PHEAAm$_{100}$), step that was confirmed by ^{1}H NMR spectroscopy (**Figure 4.23**). Surprisingly, the SEC traces from the RI detector (**Figure 4.24**) showed high molecular weight peaks suggesting that the control over the polymerisation had been lost, which was possibly ascribed to the comparatively poor solubility of the macro-initiator (i.e. PBuA$_{14}$-*b*-PLLA$_{32}$-*b*-PBuA$_{14}$) in DMSO. Overall, it was concluded that synthesizing pentablock copolymers with adequate dispersity was extremely challenging, which would have made in turn the morphological transition of the derived polymer assembly more complicated to understand.

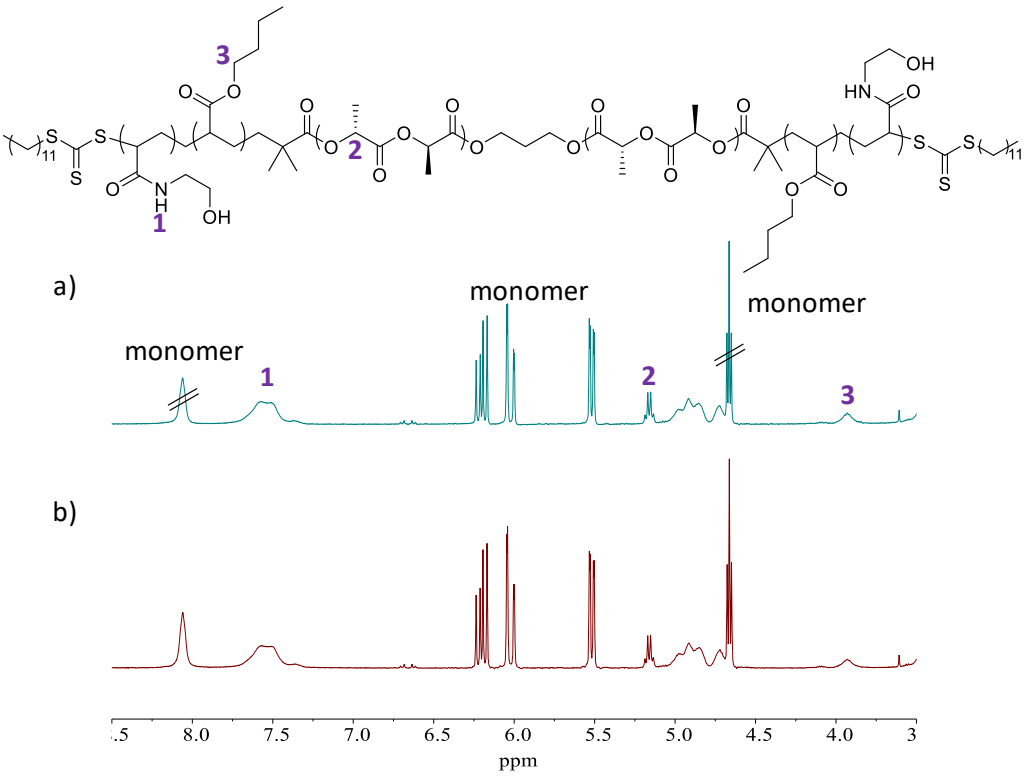

Figure 4.23 ^{1}H NMR spectra (400 MHz, *d*$_6$-DMSO) of (a) PHEAAm$_{100}$-*b*-PBuA$_{14}$-*b*-PLLA$_{32}$-*b*-PBuA$_{14}$-*b*-PHEAAm$_{100}$ and (b) PHEAAm$_{93}$-*b*-PBuA$_{13}$-*b*-PDLA$_{32}$-*b*-PBuA$_{13}$-*b*-PHEAAm$_{93}$.

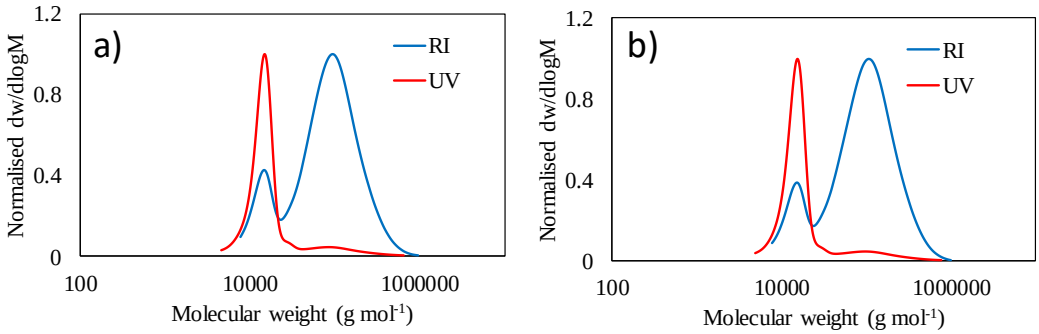

Figure 4.24 SEC analysis (DMF with 5 mM NH_4BF_4) of copolymers (a) $PHEAAm_{100}$-*b*-$PBuA_{14}$-*b*-$PLLA_{32}$-*b*-$PBuA_{14}$-*b*-$PHEAAm_{100}$ and (b) $PHEAAm_{93}$-*b*-$PBuA_{13}$-*b*-$PDLA_{32}$-*b*-$PBuA_{13}$-*b*-$PHEAAm_{93}$.

4.3.7.2 Removal of the RAFT end group

To increase the stability of the assemblies in aqueous solution, another approach was followed that was based on removing the polymer end group since the RAFT end group dodecyl contributes significantly to the hydrophobicity of the micelles.[18] Thus, using a previously reported method[19], all functionality from the polymer ends were effectively substituted with a hydrogen atom (**Scheme 4.1**). Such achievement was confirmed by the SEC UV traces at 309 nm after performing the reaction (**Figure 4.25**). The polymers after end-group removal and their assemblies are cataloged in **Table 4.2**.

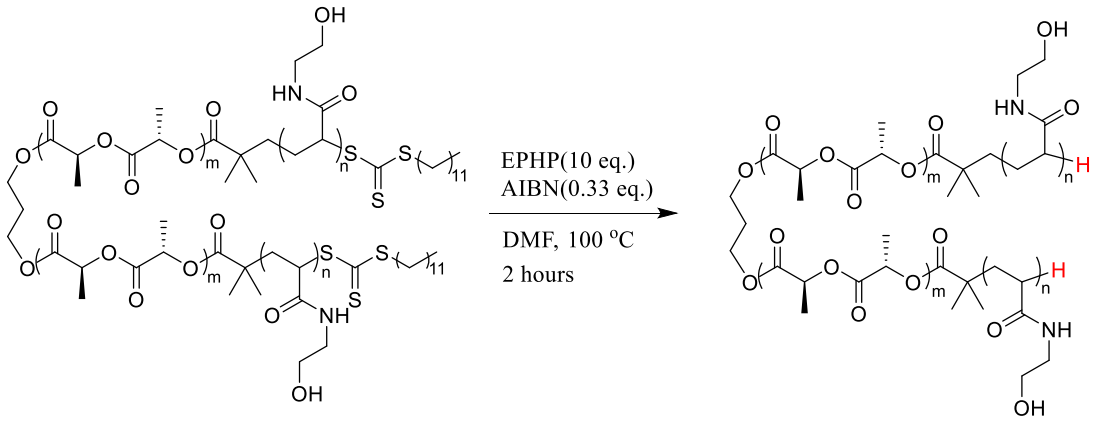

Scheme 4.1 Modification of the RAFT end group of polymers **L1** and **D1** with 1-Ethylpiperidine hypophosphite (EPHP).

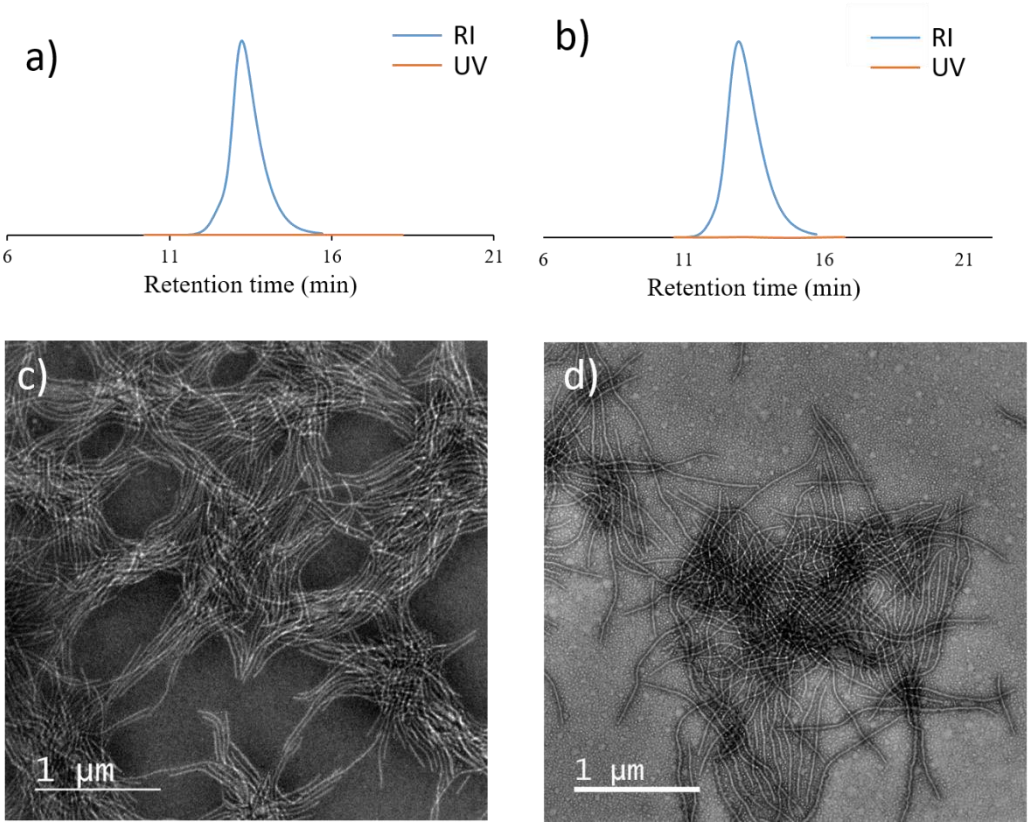

Figure 4.25 Removal of the trithiocarbonate group using EPHP and AIBN. UV-vis (309 nm) and RI SEC traces of a) polymer **L5** and b) polymer **D5**. TEM micrographs of the micelles c) **SA-L5** and d) **SA-D5**. Samples were negatively stained using uranyl acetate (0.5 wt %).

Table 4.2 The RAFT end group of polymers **L1** and **D1** was modified into different functionalities to yield new polymers.

Original polymer	Polymer after end group removal	Assemblies obtained from polymers after end group removal
$PHEAAm_{42}$-*b*-$PLLA_{32}$-*b*-$PHEAAm_{42}$, **L1**	Protonated, **L5**	**SA-L5**
$PHEAAm_{50}$-*b*-$PDLA_{32}$-*b*-$PHEAAm_{50}$, **D1**	Protonated, **D5**	**SA-D5**
$PHEAAm_{42}$-*b*-$PLLA_{32}$-*b*-$PHEAAm_{42}$, **L1**	Tertiary amine, **L6**	**SA-L6**
$PHEAAm_{50}$-*b*-$PDLA_{32}$-*b*-$PHEAAm_{50}$, **D1**	Tertiary amine, **D6**	**SA-D6**

RAFT end group (DDMAT) was removed by two approaches. "Protonated" refers to the method where the polymers were reacted with EPHP and AIBN. "Tertiary amine" means that the RAFT agent was replaced with an acrylate monomer bearing a tertiary amine functional group, *i.e.* 2-(Dimethylamino)ethyl acrylate. Polymers were assembled in MeOH (5 mg mL^{-1}) at r.t..

Then, the polymers after end-group modification , i.e. **L5** and **D5,** were assembled in methanol (5 mg mL^{-1}) at room temperature and characterised by TEM after aging for two days to confirm that the removal of the RAFT end group had no impact on the final morphology of the assemblies (cylindrical micelles, **Figure 4.25 c** and **d**). The assemblies were subsequently dialyzed against water for 5 days without any precipitants being observed. Additional dynamic light scattering (DLS) characterisation further corroborated the stability of the micelles in aqueous solution since the correlation coefficient function and intensity distribution of the nanoparticles in methanol and water highly overlapped (**Figure 4.26**).

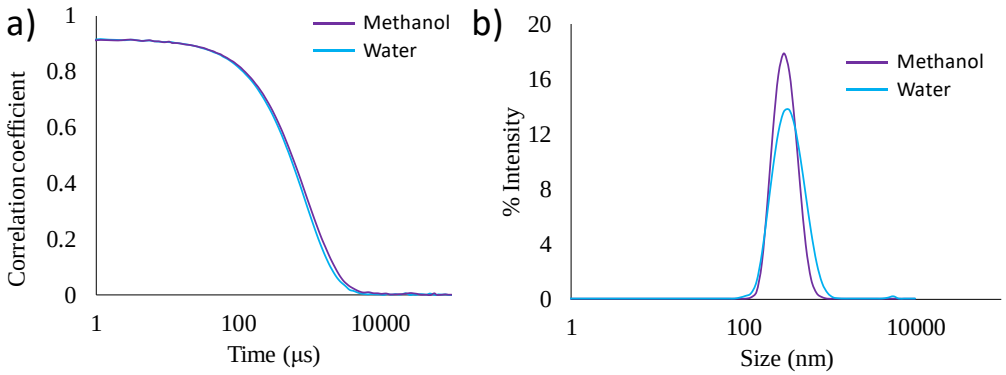

Figure 4.26 Assemblies **SA-L5** in methanol were transferred to an aqueous solution and characterised by DLS: (a) Correlation coefficient function of the nanoparticles in methanol and water. (b) Size distribution by intensity of the assemblies in methanol and water.

Considering these results, the instability of the assemblies **SA-L1** in water is mainly ascribed to the presence of long alkane groups at the polymer ends. In methanol, the dodecyl group is buried into the corona layer (PHEAAm), which isolates it from the solvent. However, when the micelles are transferred to an aqueous solution, the corona itself collapses to a certain extent as a consequence of its poorer solubility in water (compared to methanol), which in turn exposes the protected long alkane group to the immiscible solvent (water) (**Figure 4.27**). In order to minimise this interaction with

water, the micelles prefer to aggregate into bundles, as it is shown in **Figure 4.18 b**. Therefore, eliminating the RAFT end group significantly enhances the stability of the copolymer assemblies in water.

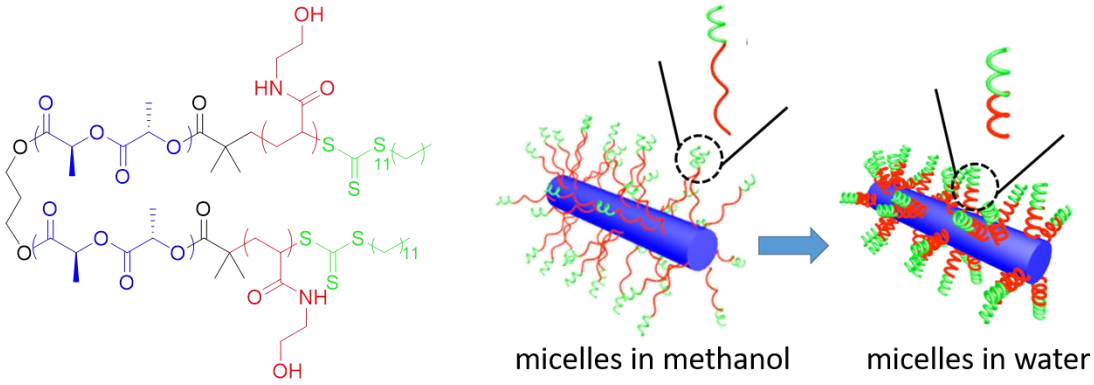

Figure 4.27 Schematic representation showing the corona conformation of the assemblies derived from PHEAAm$_y$-*b*-PL(D)LA$_x$-*b*-PHEAAm$_y$ in methanol and water.[§]

4.3.8 Morphological transition under physiological conditions

After the end-group removal, all the assemblies showed higher stability in aqueous solutions, which was exploited to study their morphological transition under physiological conditions. To that end, equal amounts of cylindrical micelles, **SA-L5** and **SA-D5** (**Table 4.2**), were mixed together in water (1 mg mL^{-1}) and aged at body temperature (37 °C). After aging for four days, the fibre-like micelles were still prevalent in the assembly solution without any morphological transformation being observed (**Figure 4.28 a-c**). The results were further consolidated by IR analysis, since almost all the C=O stretching vibration signal from the lactide unit stays in the homo-chiral state (wavenumber 1758 cm^{-1}) (**Figure 4.28 d**).

[§]Figure 4.27 was plotted with the help of Yujie Xie.

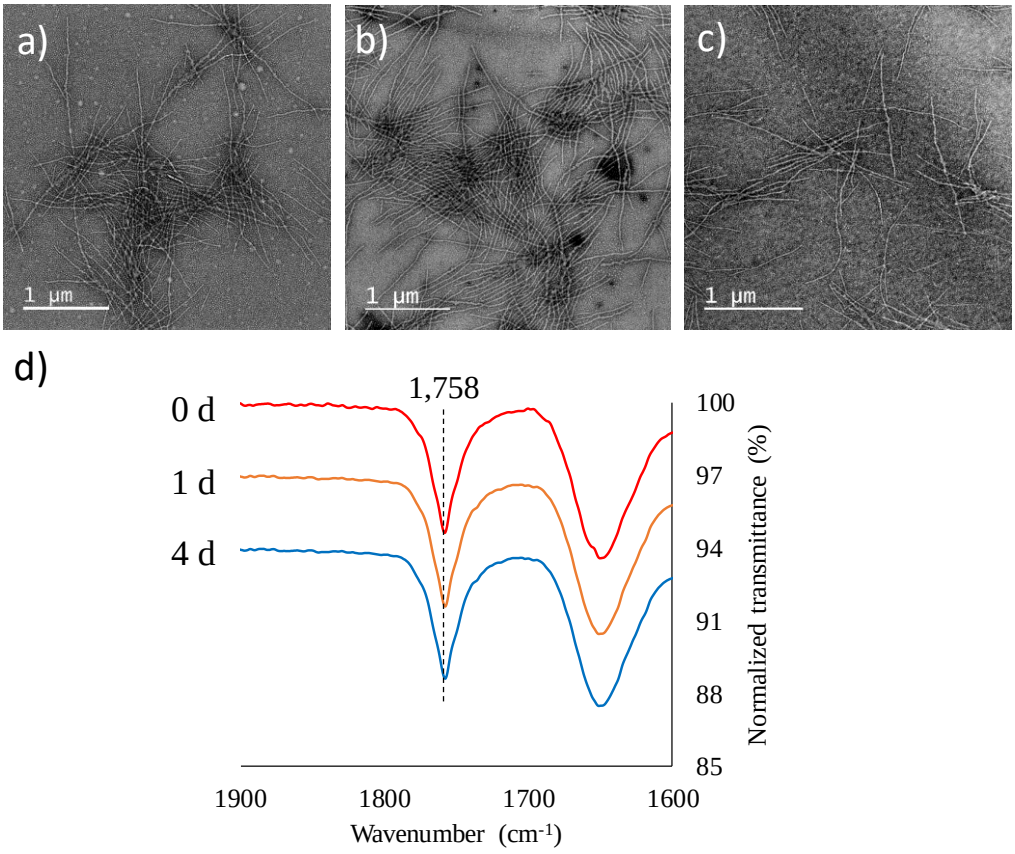

Figure 4.28 TEM micrographs of the mixed assembly solution **SA-L5** and **SA-D5** after aging at 37 °C in methanol for (a) 0 d, (b) 1 d, and (c) 4 d. Samples were negatively stained using uranyl acetate (0.5 wt %). (d) FTIR spectra of the mixture assemblies over time.

Similar to the results obtained from mixing enantiomer assemblies of $PDMA_{45}$-*b*-$PLLA_{32}$-*b*-$PDMA_{45}$ and $PDMA_{50}$-*b*-$PDLA_{32}$-*b*-$PDMA_{50}$ in methanol (**Section 4.3.6.4**), it is suspected that the solubility of the copolymers **L5** and **D5** was much lower in water than in methanol, which prevented the extraction of the unimers from the assemblies. Even though the dodecyl end group had been removed, the energy barrier for the morphological transition in water was still too high. To overcome this drawback, either a small amount of an organic biocompatible solvent, i.e. DMSO, MeOH, EtOH, glycerol or *N*-Methyl-2-pyrrolidone (NMP) was added to the aqueous solution (10% v/v) or the aging temperature was raised up to 50 °C in a series of tests

(**Table 4.3**). After aging for 4 days, the TEM images (**Figure 4.29 a-f**) showed that the cylindrical micelles remained without any new morphology being observed. Meanwhile, IR analysis (**Figure 4.29 g**) demonstrated that the signal of the carboxylic function stayed at 1758, which unfortunately indicated that none of the applied approaches induced the morphological transition of the enantiomeric mixture of micelles.

Table 4.3 Morphological transition tests performed with assemblies **SA-L5** and **SA-D5** applying different experimental conditions.

Assemblies used for the transition test	**Condition for morphological transition test**	**Test number**
SA-L5 (1 mg mL^{-1}) mixed with **SA-D5** (1 mg mL^{-1})	10% (v/v) DMSO + 90% H_2O, 37 °C	**Test 1**
	10% (v/v) EtOH + 90% H_2O, 37 °C	**Test 2**
	10% (v/v) MeOH + 90% H_2O, 37 °C	**Test 3**
	10% (v/v) NMP+ 90% H_2O, 37 °C	**Test 4**
	10% (v/v) Glycerol + 90% H_2O, 37 °C	**Test 5**
	100% H_2O, 50 °C	**Test 6**

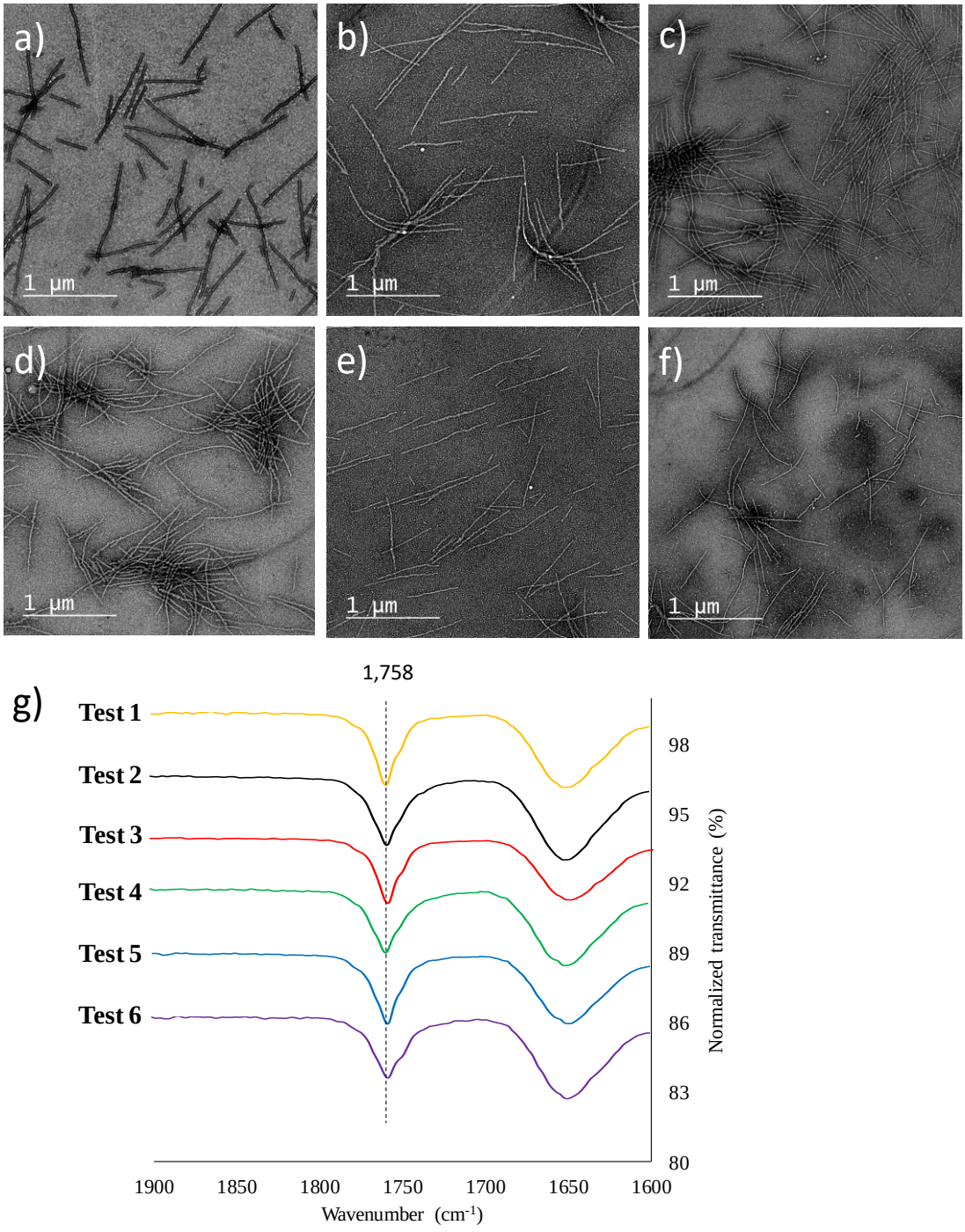

Figure 4.29 Cylindrical micelles **SA-L5** and **SA-D5** were mixed together and aged under different conditions (**Test 1-6, Table 4.3**). TEM micrographs of the assemblies after four days of aging: (a) **Test 1**, (b) **Test 2**, (c) **Test 3**, (d) **Test 4**, (e) **Test 5**, and (f) **Test 6**. Samples were negatively stained using uranyl acetate (0.5 wt %). (g) FTIR spectra of mixture assemblies **Test 1-6** after aging for 4 days.

At this point, since the morphological transformation still failed in aqueous solution, possibly as a consequence of the poor solubility of the copolymer, another straightforward and practical route was followed to increase the copolymer hydrophilicity by replacing the RAFT agent with a charged functional group. Using a previously reported aminolysis and Michael addition process[20], the RAFT end-group was removed, followed by addition of acrylate monomer, i.e. 2-(dimethylamino)ethyl acrylate (DMAEA) in a one-pot procedure, which rendered it a positively charged copolymer (**Scheme 4.2**).

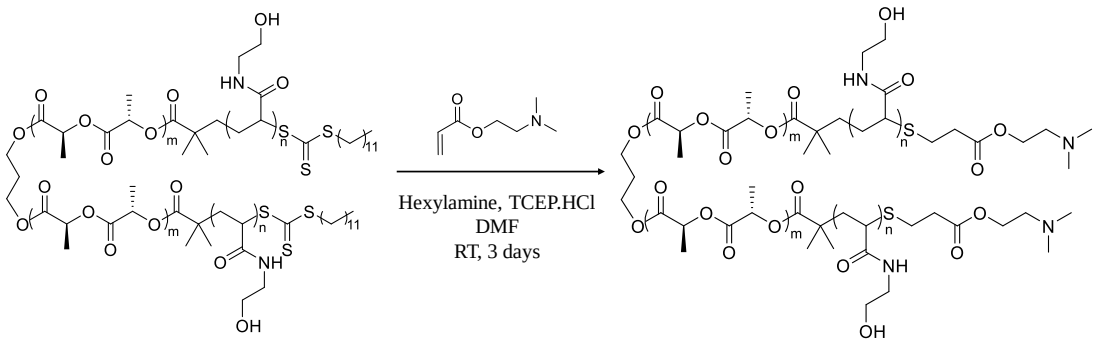

Scheme 4.2 Modification of the RAFT end group of **L1** and **D1** block copolymers with a tertiary amine group.

The modification of the RAFT end group of copolymer **L1** with a positively charged tertiary amine was verified by ^{1}H NMR spectroscopy, which clearly showed the successful attachment of DMAEA at the polymer end with the appearance of singlet methyl proton (δ = 2.17 ppm) (**Figure 4.30 a**). Moreover, SEC analysis further corroborated this statement based on the disappearance of the UV signal after the end group modification (**Figure 4.30 b**). The copolymers obtained after such end group modifications are listed in **Table 4.2** (**L6** and **D6**).

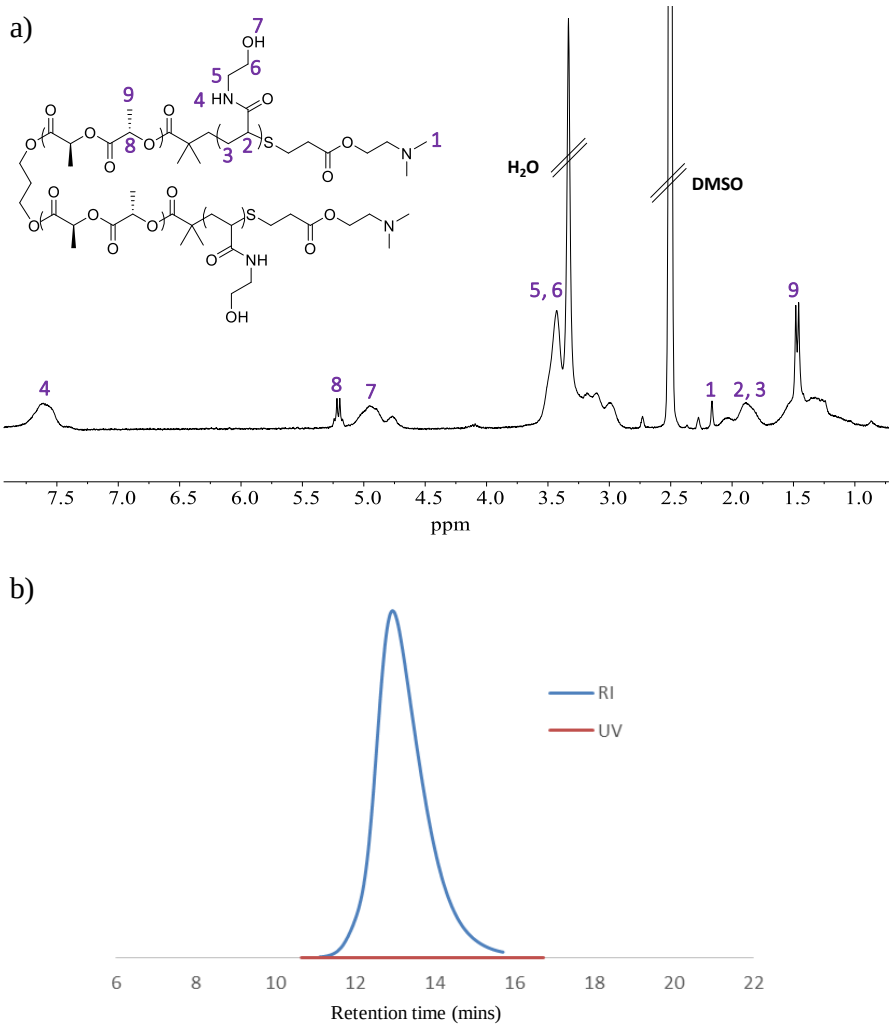

Figure 4.30 (a) ^{1}H NMR ($CDCl_3$, 400 MHz) spectrum of polymer **L6**. (b) SEC analysis of polymer **L6** (DMF with 5 mM NH_4BF_4).

Polymers **L6** and **D6** were assembled into cylinders (**SA-L6** and **SA-D6**) in methanol (5 mg mL^{-1}) at room temperature (**Figure 4.31 a** and **b**), which indicates that the end group modification had no impact on their assembly response and final morphology. Such nanoparticles were subsequently transferred to aqueous solution by dialysis, and their stability in water was evidenced by TEM analysis (**Figure 4.31 c** and **d**), which further verifies the assumption that the instability of the micelles in water is ascribed to the RAFT end group. Moreover, it was hypothesized that the tertiary amine functionality would greatly improve the unimer solubility in water as a consequence

of its partial ionization, which might help to trigger the morphological transition in aqueous solution.

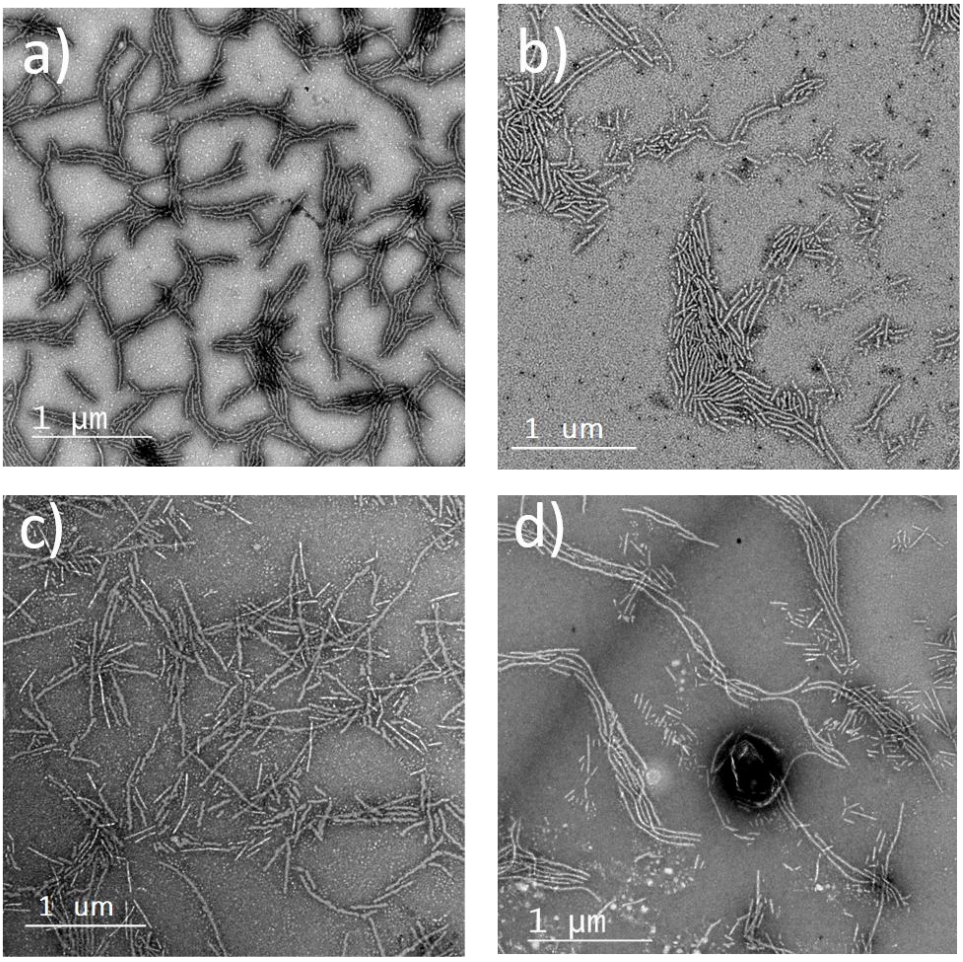

Figure 4.31 TEM micrographs of assemblies **SA-L6** in methanol (a) and water (c). Assemblies **SA-D6** in methanol (b) and water (d). Samples were negatively stained using uranyl acetate (0.5 wt %).

To verify such reasoning, cylindrical micelles **SA-L6** and **SA-D6** were mixed at 37 °C in water. Unfortunately, no discernible morphological transformation was observed for these assemblies even after aging for 4 days judged by TEM and IR analysis (**Figure 4.32 a** and **b**). Hence, based on these results, it was postulated that the unimer-assembly exchange is still frozen in the aqueous solution, which accounts for the failure regarding the morphological transition. Even though the copolymer end-group

is partially charged, the solubility of the copolymer is not significantly enhanced since the pH value of the solution (pH = 7) is quite close to the pKa of DMAEA (i.e. 7.2)[21]. Bearing this in mind, in future work, the tertiary amine should be permanently charged by quaternization to further increase the solubility of the copolymer.

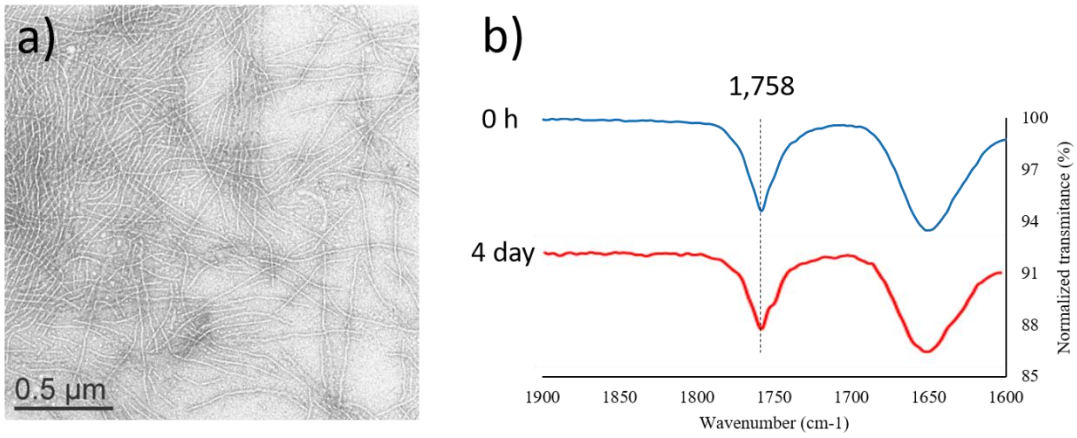

Figure 4.32 Micelles **SA-L6** and **SA-D6** were mixed at body temperature (37 °C) in water for 4 days before analysis. (a) TEM image of the micelles. Samples were negatively stained using uranyl acetate (0.5 wt %). (b) FTIR spectra of the mixture assembly solution.

4.4 Conclusions

A series of PHEAAm$_y$-*b*-PL(D)LA$_x$-*b*-PHEAAm$_y$ triblock copolymers, which were successfully synthesized by combining ROP and RAFT polymerisation techniques, assembled into well-defined cylinders by CDSA. Then, the comprehensive study of the stereocomplex-triggered morphological transition between enantiomeric cylindrical micelles allowed us to determine the effect of several parameters, such as polymer composition and aging temperature, on this phenomenon. Indeed, we observed that increasing the copolymer solubility accelerated the unimer-assembly exchanging rate during the transition, thus significantly facilitating the process. Most notably, in order to stabilise the micelles in aqueous solutions, the alkane RAFT end-group was removed or substituted with a charged functional group to enhance the copolymer solubility. Although the morphological transition of the optimised copolymers did not proceed as expected under physiological conditions, the exhaustive understanding gained of this process, as well as the versatile modification approaches developed herein, represent useful guidelines to design copolymers and their corresponding assemblies for potential biotechnological applications.

4.5 Experimental Section

4.5.1 Materials

Chemicals and solvents were purchased from Sigma-Aldrich, Acros, Fluka, TCI, Fisher Chemical, Alfa Aesar or VWR. L-Lactide was purchased from Corbion-Purac and recrystallised once from dichloromethane and twice from toluene. The monomer was dried over 3 Å molecular sieves for 3 days and recrystallised from toluene. 1,8-Diazabicyclo[5.4.0]undec-7-ene (DBU) and (-)-sparteine were distilled over CaH_2 before use.1-(3,5-Bis(trifluoromethyl)phenyl)-3-cyclohexyl-thiourea was prepared and purified as reported. 2,2′-Azobis(isobutyronitrile) (AIBN) was received from Molekula. After recrystallisation from methanol, it was stored at 4 °C. Deuterated solvents were used as received from Apollo Scientific. Raft agent 2-(dodecylthiocarbonothioylthio)-2-methylpropionic acid (DDMAT) was synthesized following the procedure described in **Chapter 2**. All the monomers used for polymerisation went through basic aluminium oxide to remove the inhibitor.

4.5.2 Characterisation techniques

Proton nuclear magnetic resonance (^{1}H NMR) spectra were recorded on a Bruker AV-400 spectrometer at 400 MHz. All spectra were recorded in d_6-DMSO unless otherwise specified. The chemical shifts were reported as δ in parts per million and quoted downfield from the internal standard tetramethylsilane (δ = 0 ppm).

Size exclusion chromatography (SEC) was performed using an Agilent 1260 Infinity Multi-Detector GPC System fitted with a refractive index and UV detectors, and equipped with a guard column (Varian PLGel) and two PLGel 5 μm mixed-D

columns. The mobile phase was DMF and 5 mM NH_4BF_4, at a flow rate of 1 mL min^{-1} at 50 °C. All data was analysed using Cirrus v3.3 and Agilent GPC/SEC software v1, and the calibration curves were produced using Varian Polymer Laboratories linear PMMA standards.

Transmission electron microscopy (TEM) was performed using a JEOL 2100FX at 200 kV. TEM samples were prepared on a formvar/carbon film TEM grid. In short, 2 μL of sample solution (1 mg mL^{-1}) was deposited on the grid and left to air dry. 5 μL of uranyl acetate (UA, 1%) solution was then dropped on the grid for 60 seconds before blotting. The sample was kept in a desiccator overnight before characterisation. TEM images were analysed by ImageJ software.

Dynamic light scattering (DLS) was conducted using a Malvern Zetasizer Nano instrument equipped with a 4 mW He–Ne 633 nm laser module at 25 °C, with data being analysed using Malvern DTS 6.20 software. Measurements were carried out at a detection angle of 173° (backscattering). All determinations were made in triplicate unless otherwise specified (with 10 measurements recorded for each run).

Wide Angle X-ray Scattering (WAXS) was performed on a Panalytical X'Pert Pro MPD equipped with a Cu Kα1 hybrid monochromator as the incident beam optics. Typically, freeze-dried particles (*ca.* 30 mg) were placed on a 10 mm sample holder, and standard "powder" 2θ–θ diffraction scans were carried out in the angular range from 10° to 30° 2θ at room temperature.

Fourier-transform infrared spectroscopy (FTIR) data were recorded (neat) on a Perkin Elmer Spectrum 100 FTIR Spectrometer. 5 μL assembly solution (5 mg mL^{-1}) was deposited on top of the detectors using attenuated total reflection to measure, the scan wavelength start from 1600 to 1900 cm^{-1}. The data was exported to analyse using

Origin 2019. Deconvolution and curve fitting of the spectra in the region of 1780 to 1720 cm^{-1}. The fitting parameters are listed below: Peak Type (Gaussian), Centre gravity (1750 cm^{-1}, 1760 cm^{-1}), FWHM (12 for 1750 cm^{-1} and 1760 cm^{-1}).

4.5.3 Synthesis of poly(N-hydroxyethyl acrylamide)-block-poly(L(D)-lactide)-block-poly(N-hydroxyethyl acrylamide); (PHEAAmy-b-PL(D)LAx-b-PHEAAmy)

CTA-$PLLA_{32}$-CTA, (40.0 mg, 8.7 μmol), HEAAm (99.8 mg, 867.2 μmol) and AIBN (14.2 μL of a 10 mg mL^{-1} solution in DMSO) were dissolved in DMSO (0.5 mL) before transferring to a dried ampoule. After three freeze-pump-thaw cycles, the solution was sealed under argon and heated for 2 hours at 65 ℃ (70% conversion). The reaction was quenched in ice-cold bath and purified by precipitation into cold ethyl acetate (once) and cold diethyl ether (twice). The resultant pale yellow solid (yield 40%) was dried under vacuum: M_n, ^{1}H NMR = 14.4 kDa, DP = 84. M_n, SEC = 20.1 kDa, $Đ_M$ = 1.16. ^{1}H NMR (400 MHz, d_6-DMSO, 298 K): δ (ppm) 7.71 (br s, 1 H, N*H*CH_2CH_2), 5.16 (q, 2 H, $^3J_{H\text{-}H}$ = 6.9 Hz, OC*H*(CH3)CO), 4.96 (br s, 2 H, CH_2OH), 3.43 (br s, 2 H, CH_2CH_2OH), 1.46 (d, 3 H, $^3J_{H\text{-}H}$ = 7.1 Hz, OCH(CH_3)CO), 0.87 (t, 3 H, $^3J_{H\text{-}H}$ = 6.8 Hz, CH_3CH_2).

4.5.4 Synthesis of poly(n-butyl acrylate)-*block*-poly(L-lactide)-*block*-poly(n-butyl acrylate); ($PBuA_y$-*b*-$PLLA_x$-*b*-$PBuA_y$)

CTA-$PLLA_{32}$-CTA, (40.0 mg, 8.7 μmol), n-butyl acrylate (11.1 mg, 86.7 μmol) and AIBN (14.0 μL of a 10 mg mL^{-1} solution in 1, 4-dioxane) were dissolved in dioxane (0.3 mL) before transferring to a dried ampoule. After three freeze-pump-thaw cycles, the solution was sealed under argon and heated for 2 hours at 70 ℃ (20% conversion).

The reaction was quenched in an ice-cold bath and purified by precipitation into cold pet ether (three times). The resultant pale yellow solid was dried under vacuum (yield 70%). M_n, NMR = 7.8 kDa, DP = 25. M_n, SEC = 20.1 kDa, $Đ_M$ = 1.09. ^{1}H NMR (400 MHz, $CDCl_3$, 298 K): δ (ppm) 5.16 (q, 1 H, $^3J_{H\text{-}H}$ = 6.9 Hz, OC*H*(CH_3)CO), 4.03 (br s, 2 H, COOC*H*$_2$), 2.28 (br s, 1 H, C*H*COO), 1.57 (d, 3 H, $^3J_{H\text{-}H}$ = 7.1 Hz, OCH(C*H*$_3$)CO), 1.25 (br s, 4 H, C*H*$_2$C*H*$_2$$CH_2COO$), 0.87 (t, 3 H, $^3J_{H\text{-}H}$ = 6.8 Hz, C*H*$_3$$CH_2CH_2COO$).

4.5.5 Synthesis of poly(*N*-hydroxyethyl acrylamide)-*block*-poly(n-butyl acrylate)-*block*-poly(L-lactide)-*block*-poly(n-butyl acrylate)-*block*-poly(*N*-hydroxyethyl acrylamide); (PHEAAm$_z$-*b*-PBuA$_y$-*b*-PLLA$_x$-*b*-PBuA$_y$-*b*-PHEAAm$_z$)

CTA-PLLA$_{32}$-CTA, (60.0 mg, 8.4 μmol), HEAAm (288.8 mg, 2504.5 μmol) and AIBN (13.7 μL of a 10 mg mL^{-1} solution in DMSO) were dissolved in DMSO (0.8 mL) before transferring to a dried ampoule. After three freeze-pump-thaw cycles, the solution was sealed under argon and heated for 2 hours at 65 °C (60% conversion). The reaction was quenched in an ice-cold bath and purified by precipitation into cold ethyl acetate (once) and into cold diethyl ether (twice). The resultant pale yellow solid was dried under vacuum before using (yield 60%). M_n, NMR = 38.2 kDa, DP = 300. M_n, SEC =48.4 kDa, $Đ_M$ = 1.51. ^{1}H NMR (400 MHz, d_6-DMSO, 298 K): δ (ppm) 7.71 (br s, 1 H, N*H*CH_2CH_2), 5.16 (q, 3 H, $^3J_{H\text{-}H}$ = 6.9 Hz , OCH(C*H*$_3$)CO), 4.96 (br s, 2 H, C*H*$_2$OH), 4.03 (br s, 2 H, COOC*H*$_2$), 3.43 (br s, 2 H, CH_2C*H*$_2$OH), 1.46 (d, 3 H, $^3J_{H\text{-}H}$ = 7.1 Hz, OCH(C*H*$_3$)CO), 1.25 (br s, 4 H, C*H*$_2$C*H*$_2$$CH_2COO$), 0.87 (t, 3 H, $^3J_{H\text{-}H}$ = 6.8 Hz, C*H*$_3$$CH_2$).

4.5.6 Removal of the RAFT end group

In a typical end-group removal, PHEAAm-*b*-P*L*LA$_{32}$-*b*-PHEAAm (83.0 mg, 0.0033 mmol), 1-ethylpiperidine hypophosphate (EPHP) (11.9 mg, 0.0664 mmol) and 10 mg mL^{-1} AIBN solution (14.26 µL, 0.00087 mmol) were mixed in 1.6 mL DMF in an ampoule. The solution was degassed *via* three freeze-pump-thaw cycles and refilled with argon. The solution was placed in an oil bath at 100 °C for 2 h. The product (30 mg, 60% yield) was precipitated in diethyl ether and dried under vacuum, yield 37%. M_n, SEC = 36.8 kDa, $Đ_M$ = 1.11. ^{1}H NMR (400 MHz, $CDCl_3$, 298 K): δ (ppm) 7.71 (br s, 1 H, N*H*CH$_2$CH$_2$), 5.15 (q, 4 H, $^3J_{H-H}$ = 7.1 Hz, OC*H*(CH$_3$)CO), 4.19 (t, 4 H, $^3J_{H-H}$ = 5.7 Hz OC*H*$_2$CH$_2$C*H*$_2$O), 2.88 (s, 3 H, CON(C*H*$_3$)$_2$), 1.57 (d, 3 H, $^3J_{H-H}$ = 7.1 Hz OCH(C*H*$_3$)CO), 1.24 (s, 21 H, C$_{10}$*H*$_{21}$).

4.5.7 Synthesis of the amine-terminated PHEAAm$_{42}$-*b*-PLLA$_{32}$-*b*-PHEAAm$_{42}$ copolymer

TCEP·HCl (0.142 mg, 0.496 µmol) and *N*,*N*-dimethylaminoethyl acrylate (7.1 mg, 49.6 µmol) were added to a solution of PHEAAm$_{42}$-*b*-PLLA$_{32}$-*b*-PHEAAm$_{42}$ copolymer (35.0 mg, 2.48 µmol) dissolved in DMF (0.5 mL). The solution was transferred to a dried ampoule under nitrogen. After three freeze-pump-thaw cycles, n-hexylamine (2.5 mg, 24.8 µmol) was added under a flow of nitrogen. After another freeze-pump-thaw cycle, the solution was sealed under nitrogen and allowed to stir at room temperature for 3 days. The reaction was quenched by opening to air and purified by precipitation into ice-cold diethyl ether (three times). M_n, NMR = 14.2 kDa, M_n, SEC = 19.3 kDa, $Đ_M$ = 1.19. ^{1}H NMR (400 MHz, d_6-DMSO, 298 K): δ (ppm) 7.71 (br s, 1 H, N*H*CH$_2$CH$_2$), 5.16 (q, 4 H, $^3J_{H-H}$ = 6.9 Hz, OC*H*(CH$_3$)CO), 4.96 (br s, 2 H,

C*H*$_2$OH), 3.43 (br s, 2 H, CH$_2$C*H*$_2$OH), 2.18 (s, 6 H, N(C*H*$_3$)$_2$), 1.46 (d, 3 H, $^3J_{H\text{-}H}$ = 7.1 Hz, OCH(C*H*$_3$)CO).

4.5.8 Crystallisation-driven self-assembly method for PHEAAm$_y$-*b*-PL(D)LA$_x$-*b*-PHEAAm$_y$ block copolymers

All the triblock copolymers prepared in this chapter were assembled in methanol as follows: the copolymer was dissolved in methanol at a concentration of 5 mg mL^{-1}, and the solution was stirred at room temperature (25 °C) in a sealed vial for two days.

4.5.9 Sonication of PHEAAm$_y$-*b*-PL(D)LA$_x$-*b*-PHEAAm$_y$ cylindrical micelles

The cylindrical micelles derived from PHEAAmy-b-PL(D)LAx-b-PHEAAmy copolymers in methanol (5 mg mL-1) were transformed into shorter fibres by probe sonication in an ice-cold bath for 4 minutes.

4.5.10 Calculation Details

LogPoct values for 8 common monomers were calculated with the following software programs: EPI Suite v. 4.11 using KOWWINTM v. 1.68, ChemBioDraw Ultra 13.0, and Virtual Computational Chemistry Laboratory (accessed on 24 July 2016). In addition, LogPoct were also extracted from the ChemSpider.com database for ChemAxon and ACD/Laboratories (accessed on 21 July 2015). For homopolymers and copolymers, Chem3D Pro version 13.0.2.3021 was used. Each structure was built and minimized with the MM2 force field. Then, the LogPoct values were extracted

from the chemical properties module, and the Connolly molecular surface area was calculated using a probe of 1.4 Å.[11]

4.6 References

1. Tsuji, H. *Macromolecular bioscience* **2005,** 5 (7), 569-597.
2. Urayama, H.; Kanamori, T.; Fukushima, K.; Kimura, Y. *Polymer* **2003,** 44 (19), 5635-5641.
3. Xu, H.; Teng, C.; Yu, M. *Polymer* **2006,** 47 (11), 3922-3928.
4. Fujiwara, T.; Mukose, T.; Yamaoka, T.; Yamane, H.; Sakurai, S.; Kimura, Y. *Macromolecular Bioscience* **2001,** 1 (5), 204-208.
5. Kang, N.; Perron, M.-È.; Prud'Homme, R. E.; Zhang, Y.; Gaucher, G.; Leroux, J.-C. *Nano letters* **2005,** 5 (2), 315-319.
6. Petzetakis, N.; Walker, D.; Dove, A. P.; O'Reilly, R. K. *Soft Matter* **2012,** 8 (28), 7408-7414.
7. Sun, L.; Pitto-Barry, A.; Kirby, N.; Schiller, T. L.; Sanchez, A. M.; Dyson, M. A.; Sloan, J.; Wilson, N. R.; O'Reilly, R. K.; Dove, A. P. *Nature Communications* **2014,** 5 (3), 5746-5752.
8. Yu, W.; Inam, M.; Jones, J. R.; Dove, A. P.; O'Reilly, R. K. *Polymer Chemistry* **2017,** 8 (36), 5504-5512.
9. Lu, J.; Bates, F. S.; Lodge, T. P. *Macromolecules* **2015,** 48 (8), 2667-2676.
10. Wang, E.; Lu, J.; Bates, F. S.; Lodge, T. P. *Macromolecules* **2018,** 51 (10), 3563-3571.
11. Magenau, A. J.; Richards, J. A.; Pasquinelli, M. A.; Savin, D. A.; Mathers, R. T. *Macromolecules* **2015,** 48 (19), 7230-7236.
12. Zhao, C.; Patel, K.; Aichinger, L. M.; Liu, Z.; Hu, R.; Chen, H.; Li, X.; Li, L.; Zhang, G.; Chang, Y. *RSC Advances* **2013,** 3 (43), 19991-20000.
13. Truong, N. P.; Dussert, M. V.; Whittaker, M. R.; Quinn, J. F.; Davis, T. P. *Polymer Chemistry* **2015,** 6 (20), 3865-3874.
14. Choi, S.-H.; Bates, F. S.; Lodge, T. P. *Macromolecules* **2011,** 44 (9), 3594-3604.
15. Ochiai, B.; Shimada, Y. *Technologies* **2018,** 6 (3), 80-90.
16. Arno, M. C.; Inam, M.; Coe, Z.; Cambridge, G.; Macdougall, L. J.; Keogh, R.; Dove, A. P.; O'Reilly, R. K. *Journal of the American Chemical Society* **2017,** 139 (46), 16980-16985.
17. Perrier, S. b. *Macromolecules* **2017,** 50 (19), 7433-7447.
18. Du, J.; Willcock, H.; Patterson, J. P.; Portman, I.; O'Reilly, R. K. *Small* **2011,** 7 (14), 2070-2080.
19. Wilks, T. R.; Pitto-Barry, A.; Kirby, N.; Stulz, E.; O'Reilly, R. K. *Chemical Communications* **2014,** 50 (11), 1338-1340.
20. Inam, M.; Jones, J. R.; Pérez-Madrigal, M. M.; Arno, M. C.; Dove, A. P.; O'Reilly, R. K. *ACS Central Science* **2017,** 4 (1), 63-70.
21. Bütün, V.; Armes, S.; Billingham, N. *Polymer* **2001,** 42 (14), 5993-6008.

Chapter 5. Understanding the CDSA of poly(ε-caprolactone) containing triblock copolymers

5.1 Abstract

The assembly study of polymers based on semi-crystalline core poly(ε-caprolactone) (PCL) is currently an area of high interest on account of PCL's well-known biocompatibility and biodegradability, yet a systematic study of coil-crystalline-coil type triblock copolymers assembly behaviour with respect to the core chemistry is rarely reported. Herein, we demonstrate the simple preparation of a variety of 1D and 2D micelles based on PCL triblock copolymers of different block ratios synthesized by ring-opening polymerisation (ROP) and reversible addition–fragmentation chain transfer (RAFT) polymerisation. The solubility of PCL-based amphiphiles in assembly solvent were investigated to tune the morphology and sizes of the assemblies, whereby 2D platelets and cylinders were obtained with soluble coronal blocks in high corona/core ratios or in good assembly solution. By contrast, less soluble PCL-containing block copolymers or unfavourable solvent composition yielded short cylinders. Furthermore, variation of solvent composition or temperature was found to drive the self-nucleation process to achieve cylinders ranged from 84 nm to 1207 nm with narrow length dispersity.

5.2 Introduction

In addition to the seeded-growth approach mentioned in **Chapter 1**, self-seeding is also a commonly utilised strategy to control the micelles size and dispersity in the CDSA process. In a typical self-seeding process, a crystalline polymer suspended in a solvent and the solution is heated above the polymer's apparent dissolution temperature with very few crystallites surviving. The solubilised unimers subsequently deposit on the remaining nuclei resulting in larger crystals. Semi-crystalline polymers such as poly(ferrocenyldimethylsilane) (PFS),[1] poly(3-hexylthiophene) (P3HT),[2] poly(2-perfluorooctyl ethyl methacrylate) (PFMA),[3] and PEO,[4] have been reported to yield uniform 1D or 2D micelles with controllable size by varying aging temperature to control the population of seeds. Apart from the effect of aging temperature, solvent property is also of significant importance in controlling the self-nucleation process. For instance, the sizes of the uniform diamond lamellae obtained from poly(L-lactide)-*block*-poly(dimethyl acrylamide) (PLLA-*b*-PDMA) diblock copolymers could be exquisitely tuned by varying the amount of common solvent.[5] More surprisingly, as described in **Chapter 2**, the triblock copolymer PDMA-*b*-PLLA-*b*-PDMA assembled at room temperature were able to fabricate uniform diamond platelets, which suggested the self-seeding process could even occur at room temperature for specific polymer compositions and solvent systems.[6]

PCL-based diblock copolymers have been reported to assemble into cylinders and platelets *via* CDSA approach,[7, 8] and those 1D micelles were capable of living seeded-growth to controlled lengths.[9, 10] However, most of the CDSA studies of PCL are based on coil-crystalline diblock copolymers with very few example of coil-crystalline-coil triblock copolymers.[11] Herein, a comprehensive CDSA study of PCL-based ABA type

triblock copolymers was presented. It was found that the polymer block composition could determine the self-assembly morphology, which ranged from hexagonal platelets to cylinders with varying lengths. The properties of the solvent utilised in the system were also demonstrated to affect the morphologies from hairy cylinders to short seeds. Furthermore, it is proved for the first time that PCL-based block copolymers are able to carry out self-nucleation at room temperature, while the size of the micelles could be tuned by varying the aging temperature or solvent composition.

5.3 Result and discussion

5.3.1 Ring-opening polymerisation of ε-caprolactone

The synthetic strategy to prepare PCL-based ABA type triblock copolymers was quite similar to the PLLA counterpart described in **Chapter 2**. The first step was to prepare PCL homopolymers with hydroxyl functional groups at both ends. 1, 3-propanediol was used to initiate the polymerisation of ε-caprolactone catalysed by diphenyl phosphate (DPP)[12] (**Scheme 5.1**). The reactions were carried out in two solvents i.e. benzene and chloroform at room temperature, respectively. An aliquot of the reaction mixture was taken every few hours to investigate the kinetics, when the conversion of the monomer was deduced by the integral ratio of proton 1 and 1' by ^{1}H NMR (**Figure 5.1**). The reaction was found much slower in chloroform than benzene (**Figure 5.2**), presumably because the more polar solvent impaired the activation between monomer and catalyst. The SEC analysis (**Figure 5.3**) evidenced the low polydispersity of the homopolymers in both reacting solutions and because of the toxicity of benzene, chloroform was selected for further polymerisation studies.

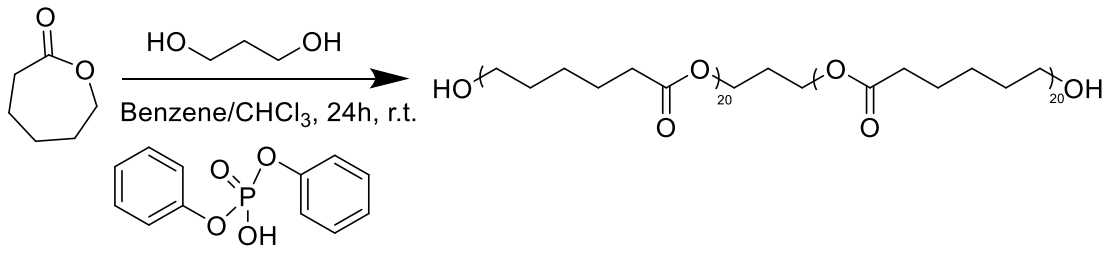

Scheme 5.1 Ring-opening polymerisation of ε-caprolactone.

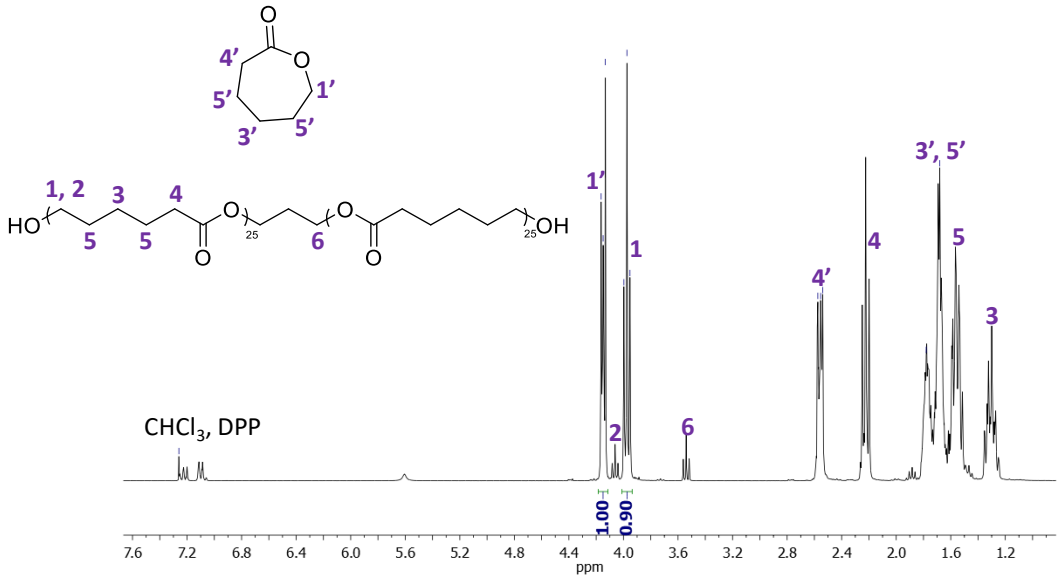

Figure 5.1 ^{1}H NMR spectrum (400MHz, $CDCl_3$) of the reaction mixture of PCL polymerisation initiated by 1, 3-propanediol and catalysed by DPP.

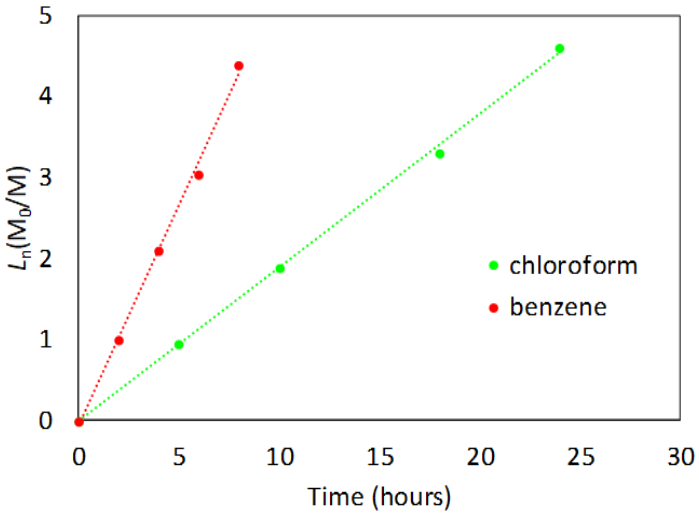

Figure 5.2 Ring-opening polymerisation of ε-caprolactone with initiator 1, 3-propanediol. First order kinetics of ε-CL consumption with linear fit.

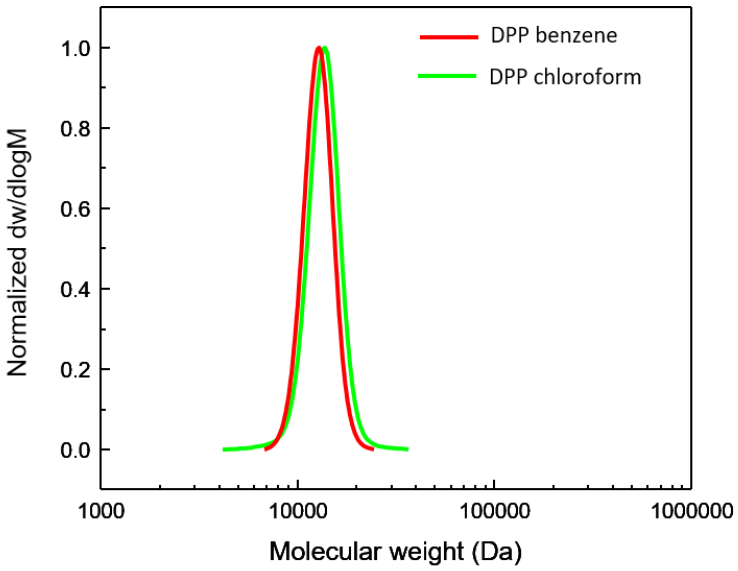

Figure 5.3 SEC chromatogram (DMF with 5 mM NH_4BF_4) of PCL polymerised in different solvents (benzene and chloroform).

A range of homopolymers (PCL_{30}, PCL_{40} and PCL_{60}) were prepared in chloroform with acidic catalyst (DPP) after reactions for one day. ^{1}H NMR characterisation (**Figure 5.4)** was utilised to predict the block length by end group analysis (integral between proton 1 and proton 4) and SEC results demonstrated the narrow dispersity of the polymers (**Figure 5.5**). Furthermore, matrix-assisted laser desorption/ionization time of flight (MALDI-TOF) mass spectrometry analysis of a homopolymer example (PCL_{40}) demonstrated no transesterification (**Figure 5.6**) and confirmed the molecular weight calculated by ^{1}H NMR spectroscopy.

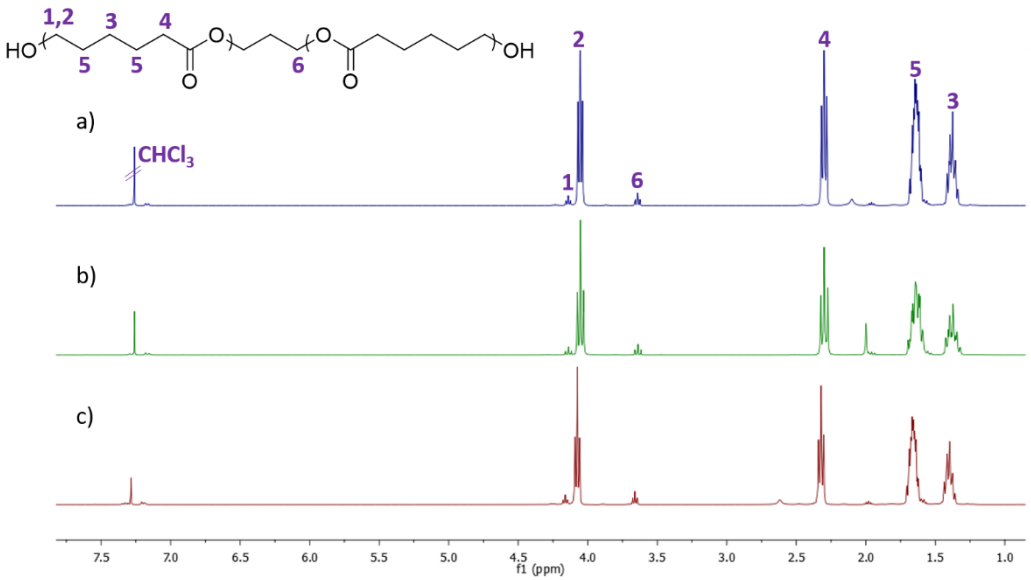

Figure 5.4 ^{1}H NMR spectra (400MHz, $CDCl_3$) of PCL_{60} (a), PCL_{40} (b) and PCL_{30} (c).

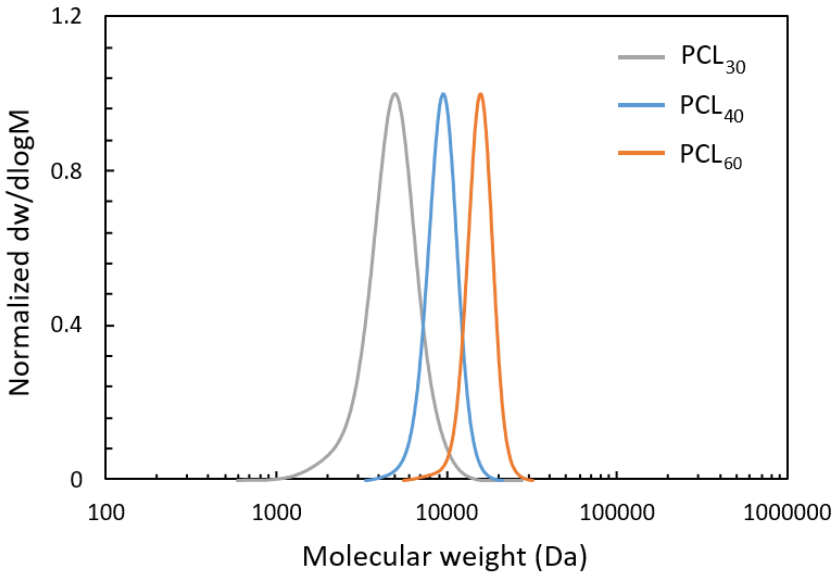

Figure 5.5 SEC chromatograms (DMF with 5 mM NH_4BF_4) of PCL_{30}, PCL_{40} and PCL_{60}. Signals were collected from RI detectors.

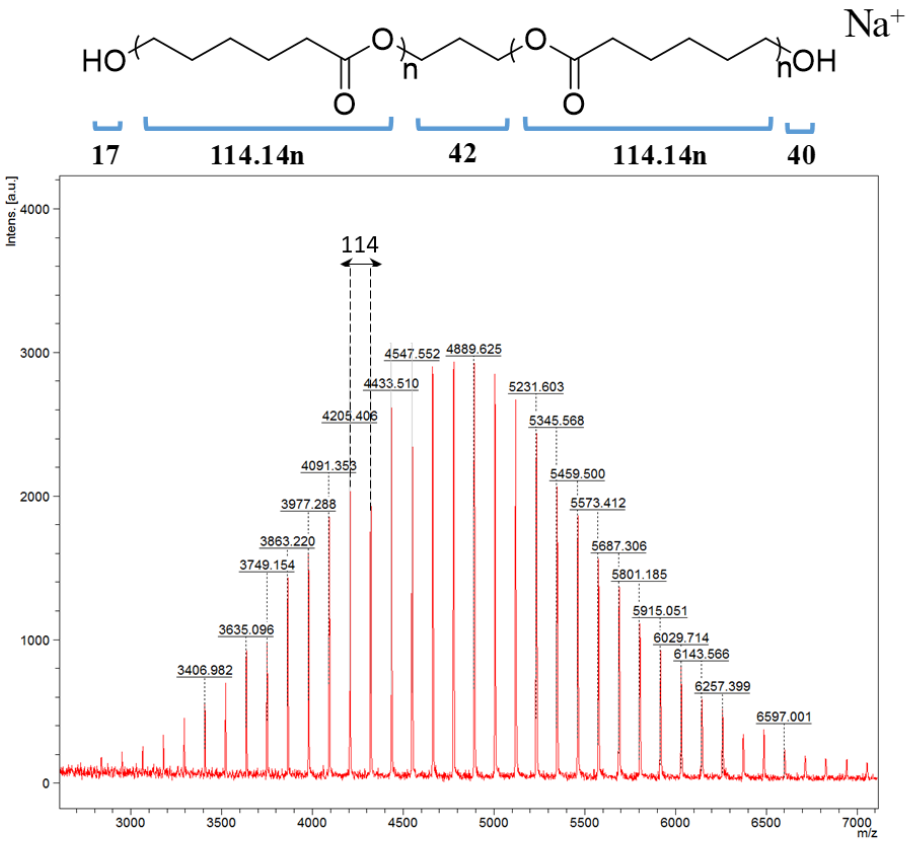

2n	m/z
28	3294.92
29	3409.06
30	3523.2
31	3637.34
32	3751.48
33	3865.62
34	3979.76
35	4093.9
36	4208.04
37	4322.18
38	4436.32
39	4550.46

2n	m/z
40	4664.6
41	4778.74
42	4892.88
43	5007.02
44	5121.16
45	5235.3
46	5349.44
47	5463.58
48	5577.72
49	5691.86
50	5806
51	5920.14

Figure 5.6 MALDI-ToF MS spectrum of homopolymer PCL_{40} showing minimal no transesterification.

5.3.2 Conjugation of RAFT agent DDMAT to PCL homopolymers

DDMAT was coupled to PCL with the activation of dicyclohexylcarbodiimide (DCC) and 4-dimethylaminopyridine (DMAP) (**Scheme 5.2**). The success of the reaction was confirmed by ^{1}H NMR spectroscopy (**Figure 5.7**) with the presence of a new signal at δ = 3.24 ppm, attributable to the SC*H*$_2$CH$_2$ from DDMAT. The comparison of the integrals associated with δ = 3.24 ppm, and the OC*H*$_2$CH$_2$C*H*$_2$O in the initiator (δ = 4.18 ppm) revealed a ratio of approximately 1:1, which indicated both ends of the polymer had been functionalised with the RAFT agent.

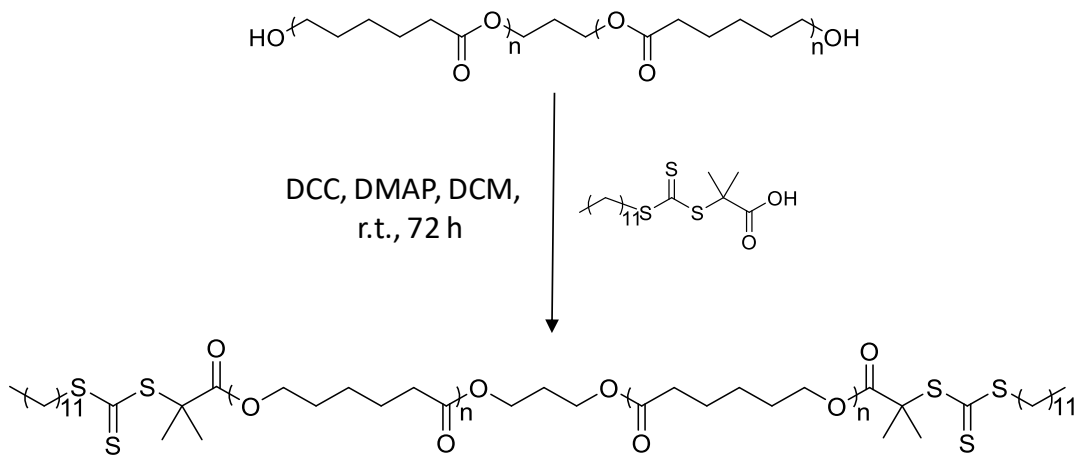

Scheme 5.2 Coupling reaction of the RAFT DDMAT to PCL homopolymer.

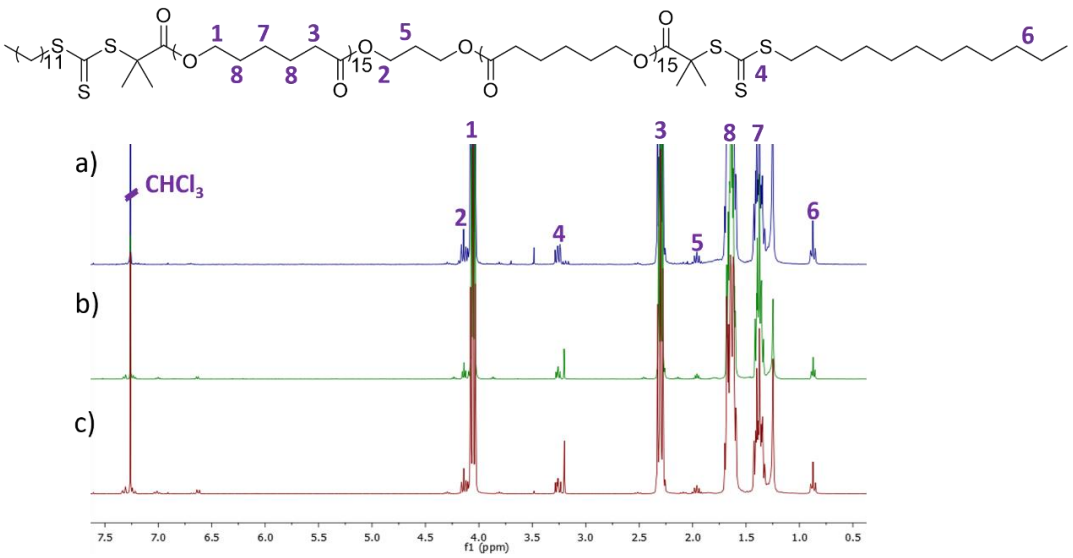

Figure 5.7 ^{1}H NMR spectra (400 MHz, $CDCl_3$) of PCL_{30}-CTA (a), PCL_{40}-CTA (b), and PCL_{60}-CTA (c).

Further characterisation of the polymers were carried out using SEC analysis fitted with a UV-vis detector set at λ = 309 nm, the wavelength attributable to the trithiocarbonate functionality of the RAFT CTA. A good overlap between the RI and UV (309 nm) traces of the polymers indicated the success of RAFT agent conjugation (**Figure 5.8**).

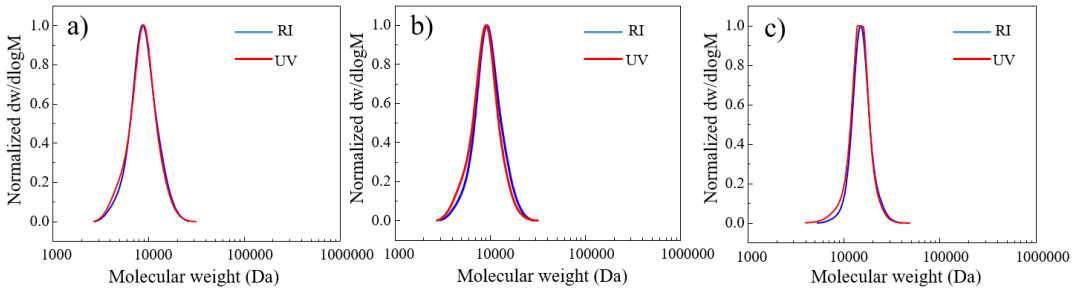

Figure 5.8 SEC chromatograms (DMF with 5 mM NH_4BF_4) of PCL_{30}-CTA (a), PCL_{40}-CTA (b) and PCL_{60}-CTA (c).

5.3.3 Chain-extension of dual-functionalised Macro-CTA

The PCL-based macro-CTA was chain-extended with dimethylacrylamide (DMA) to produce PDMA-*b*-PCL-*b*-PDMA triblock copolymers using the radical initiator 2,2'-azobis(2-methylpropionitrile) (AIBN). ^{1}H NMR spectroscopy analysis of the triblock copolymers (**Figure 5.9**) confirmed the success of the polymerisation, as the signal of methyl (δ = 2.90 ppm, proton 2) next to the amide functionality was observed in the spectrum. PDMAs with varying DPs were synthesized to explore the effect of hydrophobic weight fraction upon the dimensions of the resultant particles (**Table 5.1**). SEC analyses demonstrated all the triblock copolymers used in this chapter showed narrow molecular weight distributions ($Đ_M$ < 1.2) (**Figure 5.10**). Diffusion-ordered spectroscopy (DOSY) NMR was also carried out to confirm the absence of homopolymer, which displayed great impact on the CDSA results as described in **Chapter 1**. Alignment of all the proton signals along a single diffusion coefficient suggested no homopolymer was present (**Figure 5.11**).

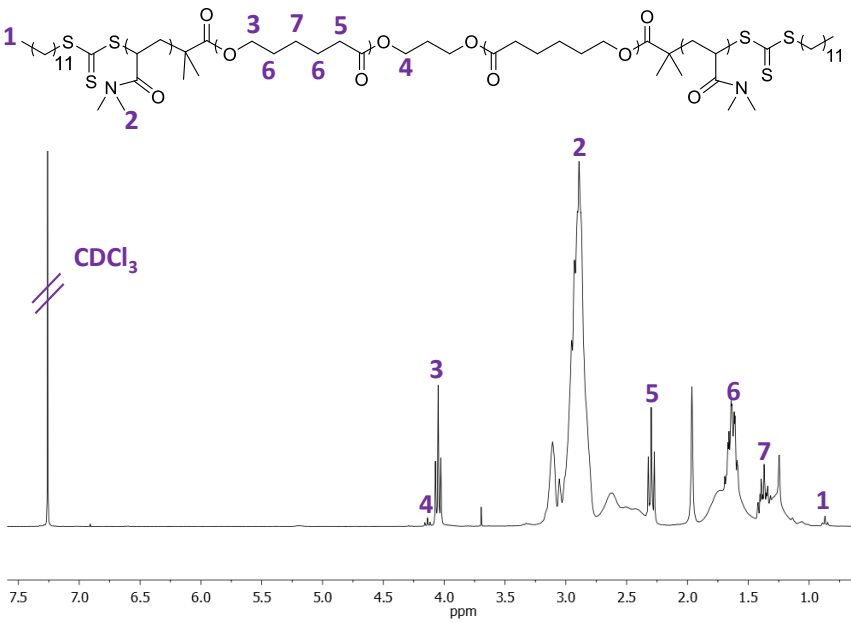

Figure 5.9 ^{1}H NMR spectrum (400 MHz, $CDCl_3$) of $PDMA_{150}$-*b*-PCL_{30}-*b*-$PDMA_{150}$.

Table 5.1 Properties of the triblock copolymer $PDMA_x$-*b*-PCL_y-*b*-$PDMA_x$ with varying core and corona lengths.

Triblock copolymer	$M_{n,NMR}$[a] (kDa)	$M_{n,SEC}$[b] (kDa)	$Đ_M$[b]	Hydrophobic content (wt%)[c]
$PDMA_{40}$-*b*-PCL_{30}-*b*-$PDMA_{40}$, **T1**	10.7	13.5	1.09	32
$PDMA_{96}$-*b*-PCL_{30}-*b*-$PDMA_{96}$, **T2**	22.8	27.4	1.15	15
$PDMA_{150}$-*b*-PCL_{30}-*b*-$PDMA_{150}$, **T3**	34.2	38.4	1.18	10
$PDMA_{47}$-*b*-PCL_{40}-*b*-$PDMA_{47}$, **T4**	14.3	19.2	1.13	32
$PDMA_{124}$-*b*-PCL_{40}-*b*-$PDMA_{124}$, **T5**	30.4	36.2	1.14	15
$PDMA_{203}$-*b*-PCL_{40}-*b*-$PDMA_{203}$, **T6**	44.6	48.3	1.17	10
$PDMA_{75}$-*b*-PCL_{60}-*b*-$PDMA_{75}$, **T7**	21.4	25.3	1.08	32
$PDMA_{190}$-*b*-PCL_{60}-*b*-$PDMA_{190}$, **T8**	45.6	49.3	1.13	15
$PDMA_{302}$-*b*-PCL_{60}-*b*-$PDMA_{302}$, **T9**	68.4	71.3	1.18	10

[a] Measured by ^{1}H NMR spectroscopy (400 MHz, $CDCl_3$). [b] Measured by SEC (DMF with 5 mM NH_4BF_4). [c] PCL weight fraction in the $PDMA_y$-*b*-PCL_x-*b*-$PDMA_y$ triblock copolymers was calculated by ^{1}H NMR spectroscopy.

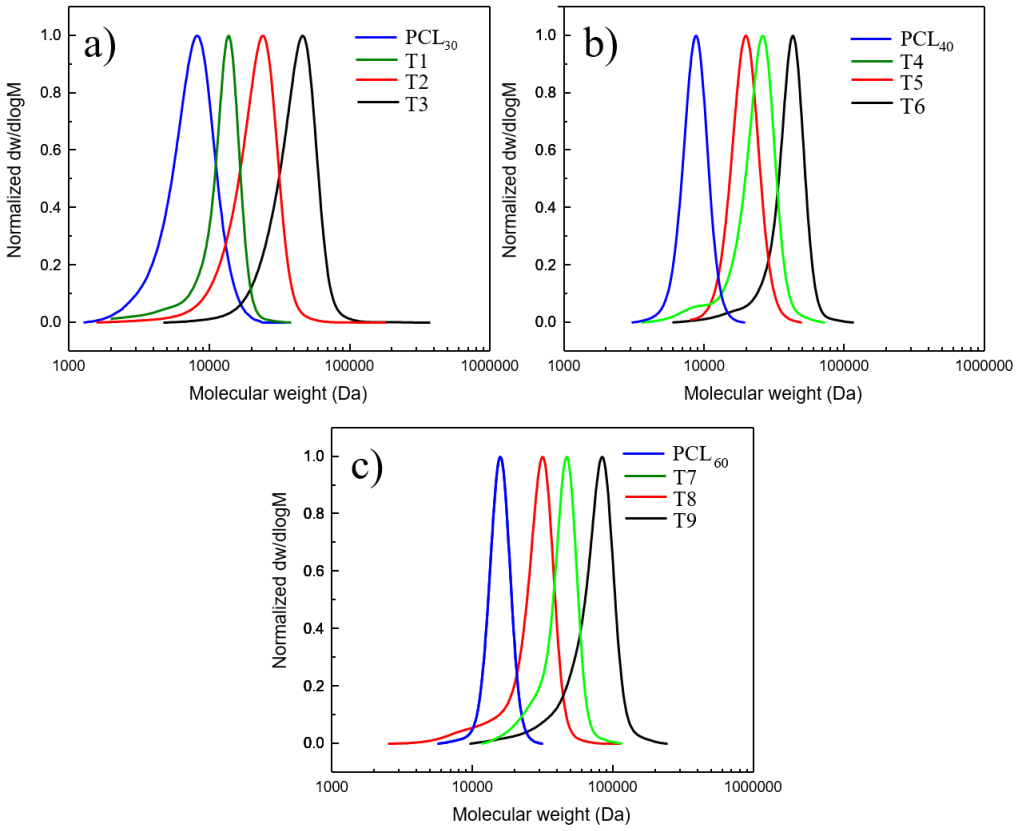

Figure 5.10 Overlaid SEC chromatograms (DMF with 5 mM NH_4BF_4) of different PCL homopolymers and copolymers. a) Macro-CTA PCL_{30} and triblock copolymers **T1-T3**. b) Macro-initiator PCL_{40} and triblock copolymers **T4-T6**. c) Macro-initiator PCL_{60} and triblock copolymers **T7-T9**.

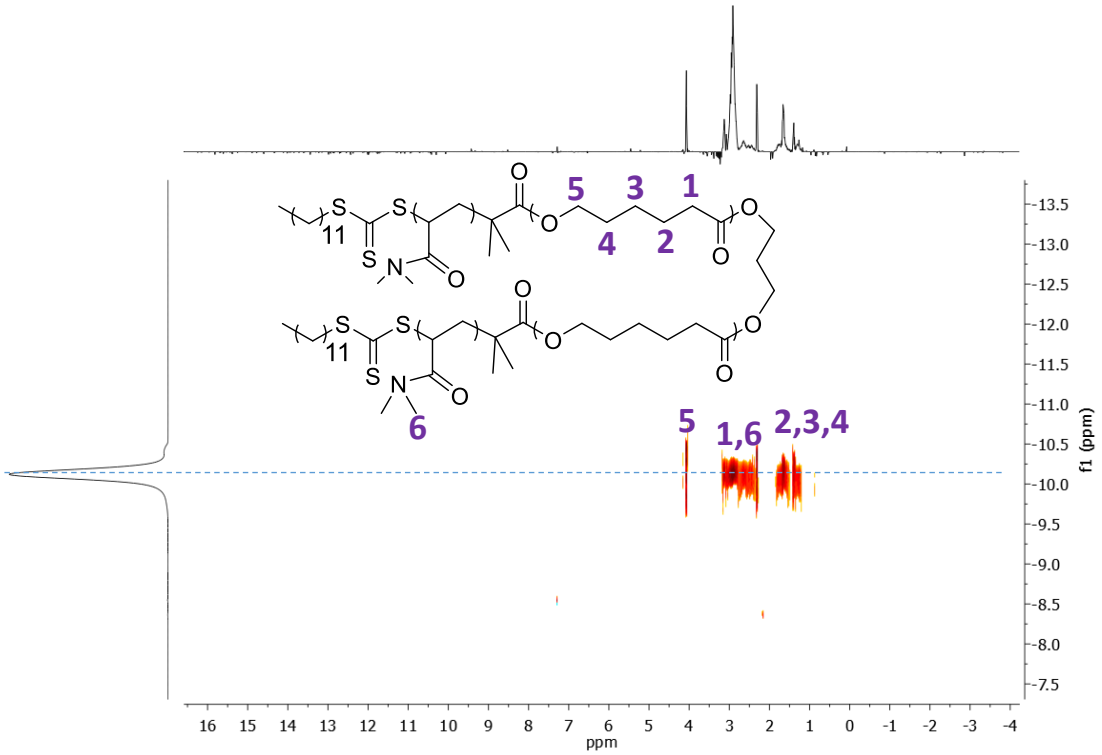

Figure 5.11 ^{1}H-DOSY NMR spectrum (500 MHz, $CDCl_3$) of triblock copolymer $PDMA_{150}$-*b*-PCL_{30}-*b*-$PDMA_{150}$ in $CDCl_3$ at 298 K.

5.3.4 Optimisation of the self-assembly methodology

5.3.4.1 The selection of a proper assembly solution

It was previously demonstrated that PCL-*b*-PDMA diblock copolymers could yield cylindrical morphologies in single alcoholic solvent.[37] Based on the developed assembly methodology of ABA type triblock copolymers in the last three chapters, a series of alcoholic solvents (i.e. methanol, ethanol, 1-propanol, 1-butanol) were screened to assemble PDMA-*b*-PCL-*b*-PDMA at room temperature. In contrast to the PCL-*b*-PDMA diblock copolymer, the triblock counterpart (polymer **T5** was taken for example) could be totally solubilized in all four alcoholic solvents (5 mg mL^{-1}) with barely any Tyndall effect observed initially. The assembly solution gradually became turbid after aging for two days at room temperature. Transmission electron microscopy

(TEM) showed that cylindrical micelles could be obtained from all the alcoholic solvents listed above. To be specific, in methanol very long micelles (> 4 μm) were observed (**Figure 5.12 a**), whilst changing the assembly solution to a less polar alcoholic solvent i.e. ethanol yielded a blend of long and short nanoparticles (**Figure 5.12 b**). Furthermore, when the least polar solvents herein (1-propanol and 1-butanol) were used, much shorter nanoparticles were observed instead (< 2 μm) (**Figure 5.12 c** and **d**). The self-assembly process was postulated as follows: Initially, most of the polymer chains solubilize as unimers in the alcoholic solvent with a few nuclei left. Subsequently, free polymer chains deposit on those remained crystals evolving into larger crystallites i.e. crystalline cylinders. In that regard, the solvent property played a vital role in the CDSA process: increased solubility not only diminishes the remaining nuclei in the assembly solution but also increases the polymer flexibility to pack into crystals. These factors accounts for the long micelles achieved from methanol and short cylinders from 1-butanol, when methanol was assumed to provide better solubilisation for the polymers.

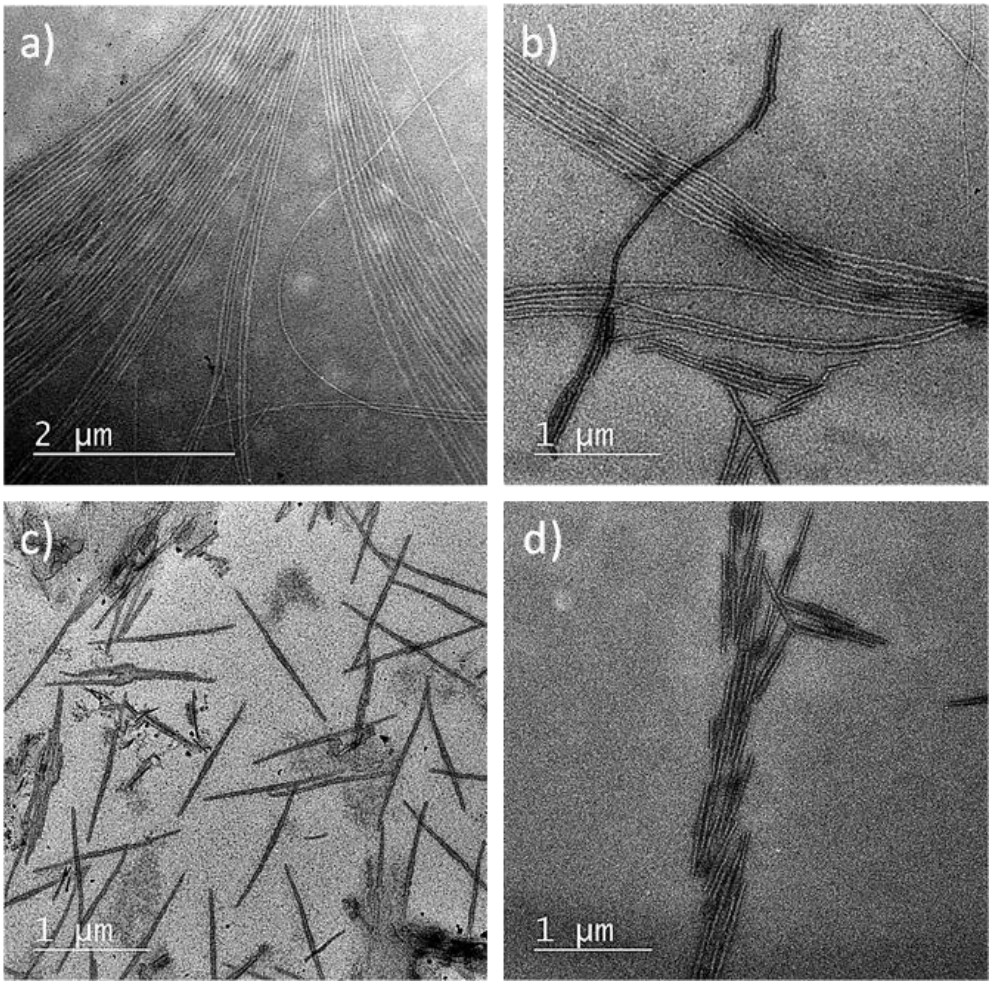

Figure 5.12 TEM micrographs of the micelles achieved from polymer **T5** in (a) methanol, (b) ethanol, (c) 1-propanol and (d) 1-butanol at room temperature aging for 2 d. Samples were negatively stained using uranyl acetate (0.5 wt %).

To further prove this assumption that the solubility determines the micelle length, a mixed solvent system in varying proportion was used. Polymer **T5** was assembled under the same conditions i.e. 5 mg mL^{-1} at room temperature but in different solvent systems (water in methanol varying from 20% to 40 vol %). After aging for two days, TEM analysis (**Figure 5.13 b**) revealed that a 20 vol % water mixture in methanol still resulted in cylindrical micelles, but a dramatic decrease in the micelle length (L_n = 550 nm) was observed (in comparison to 100% methanol, L_n > 4 µm, **Figure 5.13 a**). In addition, as the water ratio increased to 30 vol % and 40 vol %, the micelles became

even shorter *ca.* 200 nm and less than 100 nm, respectively, (**Figure 5.13 c** and **d**), which supported the assumption that decreased micelle length was caused by lower solubility. In order to avoid the interference of solvent effect with the assembly morphologies, all further assemblies were prepared in 100% methanol solution only.

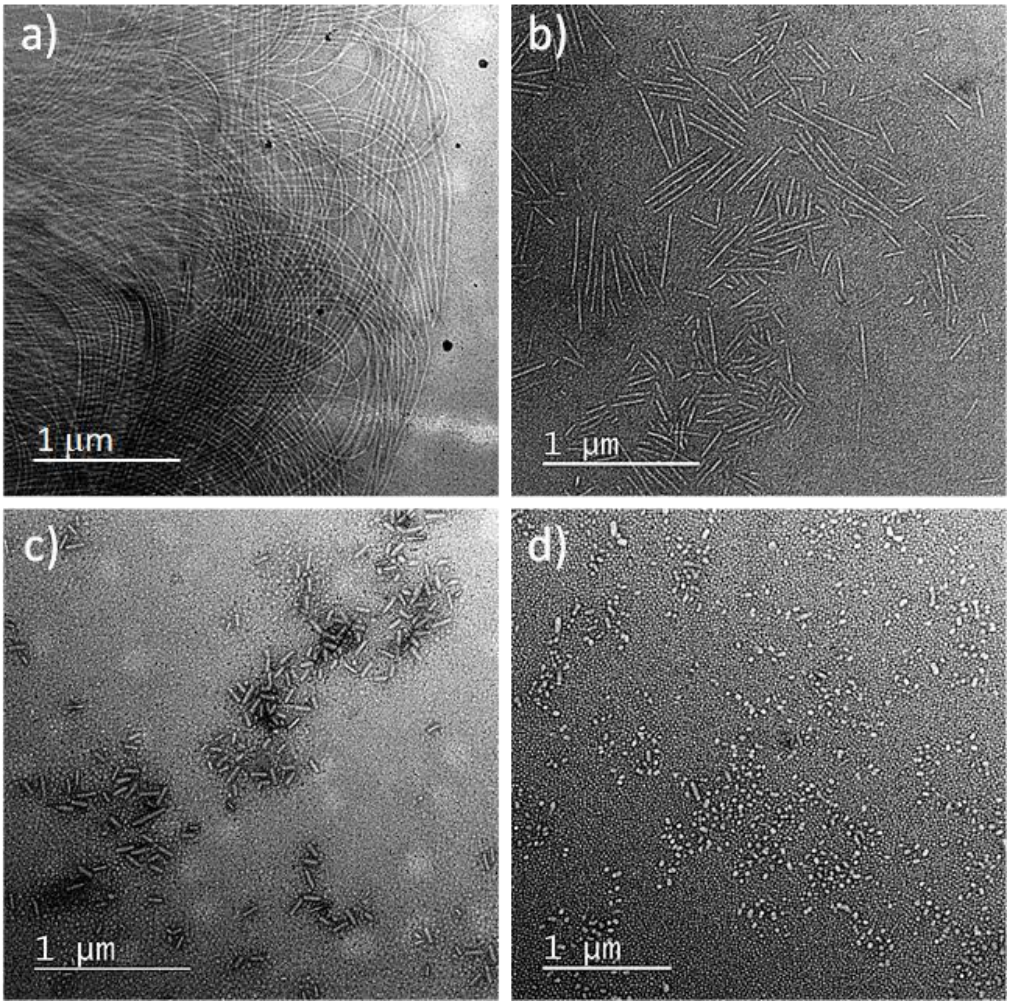

Figure 5.13 TEM micrographs of the micelles achieved from polymer **T5** in (a) 100 vol % methanol, (b) 80 vol % methanol and 20% water, (c) 70 vol % methanol and 30% water and (d) 60 vol % methanol and 40% water at room temperature. Samples were negatively stained using uranyl acetate (0.5 wt %).

5.3.4.2 Optimisation of assembly concentration

Since there are limited examples in the literature reporting the effect of polymer concentration on the CDSA process,[13] it was of interest to probe this problem herein. The assembly concentration of polymer **T5** was adjusted to 0.5 mg mL^{-1} and 20 mg mL^{-1} (in methanol), respectively, and then aged at room temperature for two days. TEM images (**Figure 5.14**) revealed that, the obtained micelles at these two assembly concentrations (0.5 mg mL^{-1} and 20 mg mL^{-1}) were both long cylinders, which is the same as the particles achieved from 5 mg mL^{-1} counterpart. Thus, it could be concluded that the polymer concentration had barely any effect on the size or morphology of the micelles in this system. For consistency, the assembly concentration applied below is 5 mg mL^{-1}.

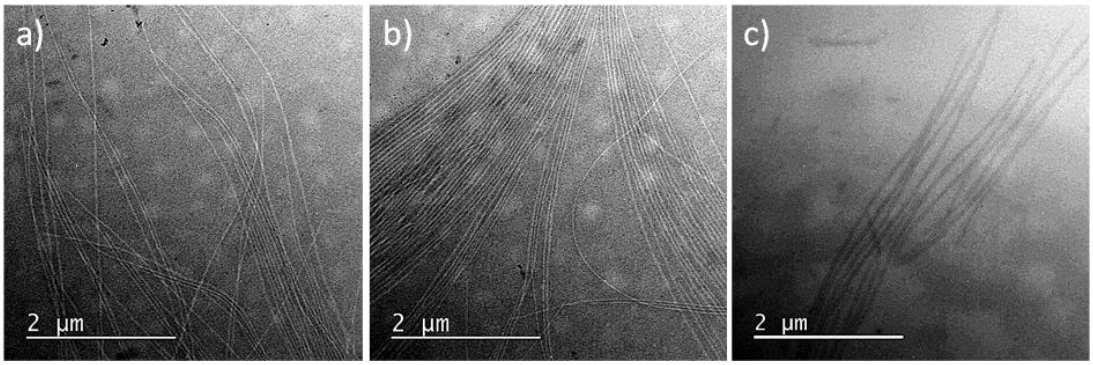

Figure 5.14 TEM micrographs of the micelles achieved from polymer **T5** in methanol at different polymer concentration: (a) 0.5 mg mL^{-1} (b) 5 mg mL^{-1}, (c) 20 mg mL^{-1} at room temperature. Samples were negatively stained using uranyl acetate (0.5 wt %).

5.3.5 Kinetic study of the self-assembly process

The assumed CDSA process of such polymer system is that the polymer dissolves in methanol as unimers, with a few nuclei left as seeds for the subsequent crystallisation and growth. To prove this assumption, a kinetic self-assembly study (polymer **T5** as the example) was performed using the standard assembly condition (5 mg mL^{-1} in

methanol at r.t.). An aliquot was taken from the assembly solution at 10 min, 30 min and 3 h (aging time), respectively, for TEM inspection. Surprisingly, after aging for 10 min, spherical micelles were exclusively observed on the TEM grid (**Figure 5.15 a**). However, as the aging time passed by, short cylinders began to emerge (30 min, **Figure 5.15 b**) and by 3 h longer fibres (**Figure 5.15 c**) were formed eventually.

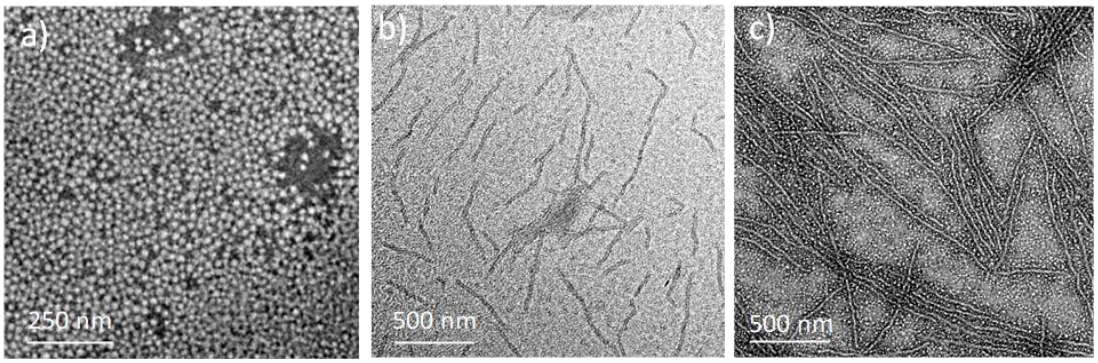

Figure 5.15 TEM micrographs of the micelles achieved from polymer **T5** in methanol at room temperature: (a) 10 min (b) 30 min (c) 3 h. Samples were negatively stained using uranyl acetate (0.5 wt %).

Other than the example polymer (**T5**), the coexistence of spheres and cylinders (or lamellae) were also spotted in other assembly tests in their initial assembly stage, such as polymer **T4** and **T6** (aging for 3 h, **Figure 5.16 a** and **b**). Similarly, the amount of spherical micelles considerably declined as the assembly solution aged longer (1 d, **Figure 5.16 c** and **d**).

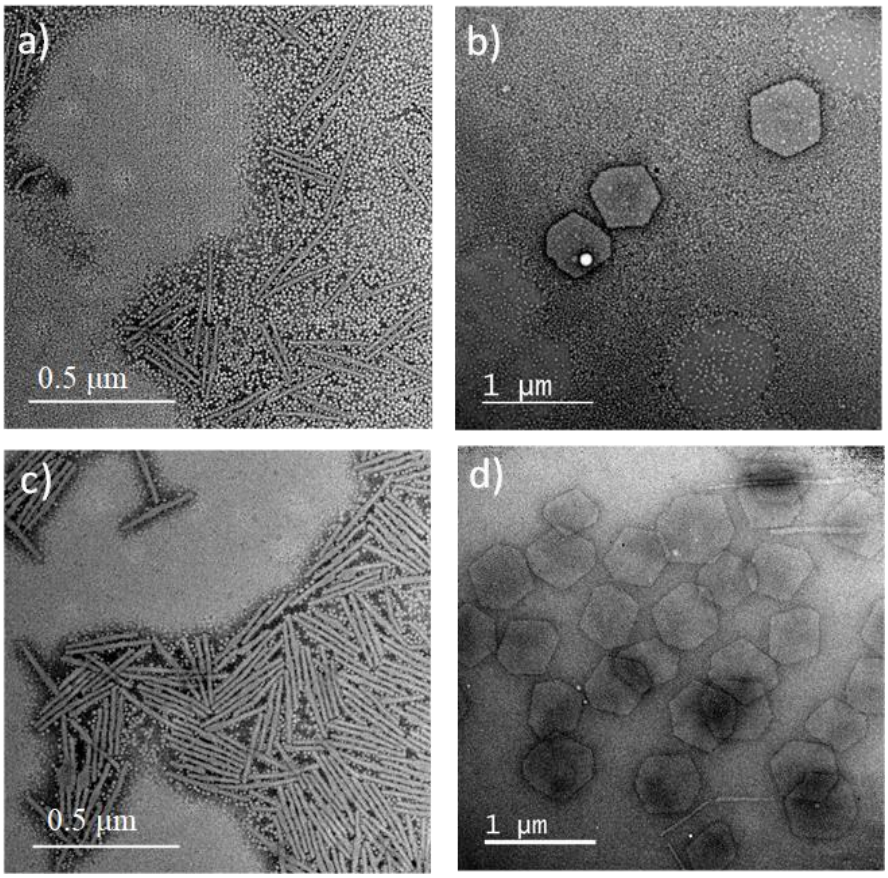

Figure 5.16 TEM micrographs of the micelles achieved from polymer **T4** and **T6** in methanol at room temperature: (a) polymer **T4,** 3 h (b) polymer **T4,** 3 h (c) polymer **T6,** 1 d. (d) polymer **T6,** 1 d. Samples were negatively stained using uranyl acetate (0.5 wt %).

Contrary to our assumption in the first place, polymers didn't stabilise as unimers initially but formed spherical micelles instead. Those spheres could be considered as a reservoir of unimers, which gradually released free polymer chain to the assembly solution. In the progression of the crystallisation, unimers kept depositing on the nucleus front, which evolve the nucleus to long cylinders (lamellas) as shown in **Figure 5.17**. In that regard, the amount of spherical micelles diminished accordingly to replenish consumed unimers.

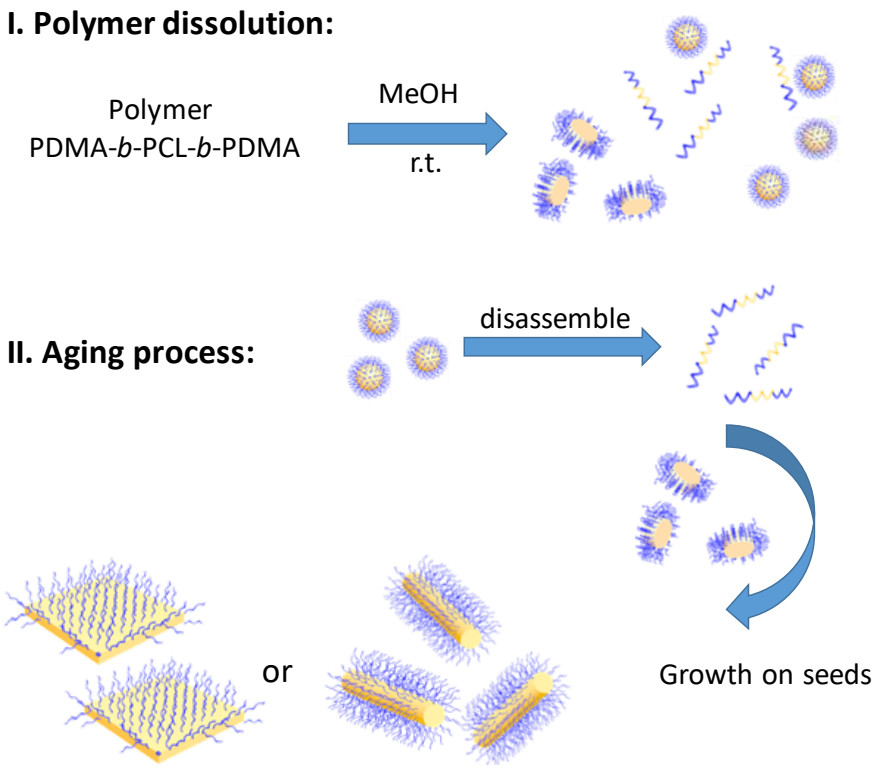

Figure 5.17 Schematic representation of the preparation of crystalline micelles by PDMA-*b*-PCL-*b*-PDMA triblock copolymer.

In addition to TEM characterisation, the assembly process was also monitored *in situ* by dynamic light scattering (DLS). Particles in a dispersion are assumed to be in a constant, random Brownian motion, which causes the intensity of scattered light to fluctuate as a function of time. A correlator i.e. a signal comparator was used to compare one signal with itself at varying time intervals, when correlation function could be defined based on this variable. It is known that the correlation of the signal decays more rapidly in samples containing smaller particles.[14] In the example assembly (polymer **T5**, in methanol, 1 mg mL^{-1}), the correlation coefficient function (**Figure 5.18 a**) decayed rapidly (less than 1000 µs) in the initial stage (0 min) and the scattering signal is actually very low (< 0.6) indicating the absence of micelles at first. However, as the aging time evolved (5 min interval for signal collection), the relaxation time gradually extended (more than 1000 µs) accompanied by the rise of

the signal intensity. By 3 h, the correlation function came to steady state with much slower signal decay (> 1000 μs), which suggested large nanoparticles were formed. The information is more straightforward in the size distribution by intensity (**Figure 5.18 b**). The signals around 10 nm corresponding to unimers or spheres diminished step by step whereas the distribution around 700 nm increased accordingly, which was consistent with the morphological transition from small particles or unimers to large micelles. After aging for three hours the size distribution curve by intensity exclusively showed large aggregates, with the disappearance of the small particle signal, which suggested that larger particles dominated in the assembly solution. Since the light scattering results are in line with the conclusion drawn from TEM analysis, the hypothesis that spherical micelles continuously release unimers to support crystallisation on the remaining nuclei, which eventually grow into larger nanostructures is therefore highly probable.

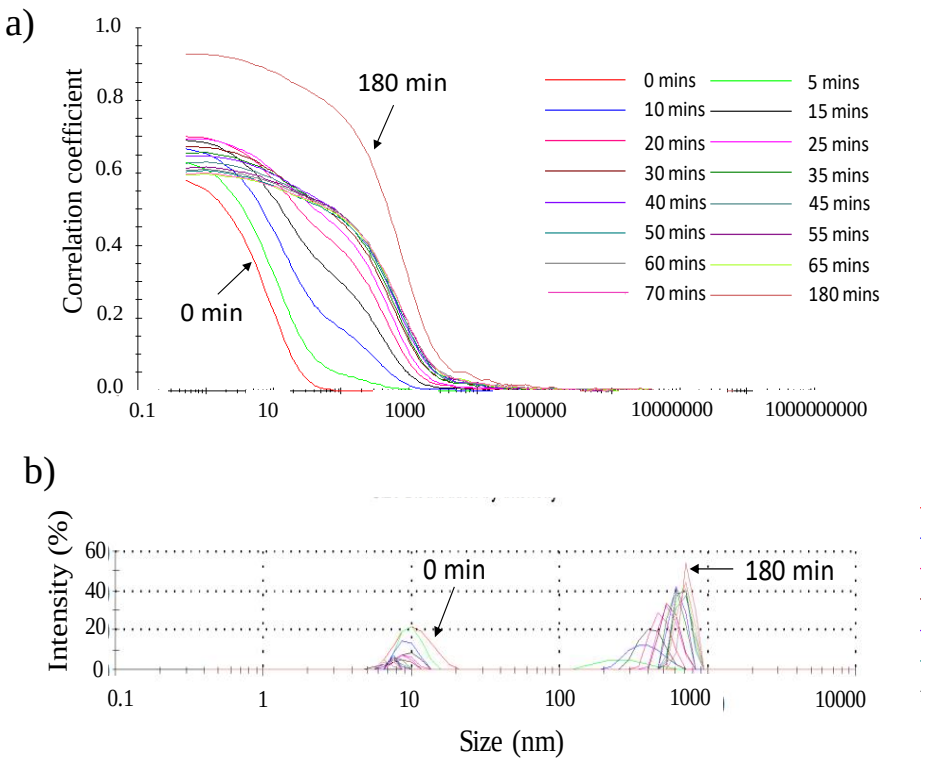

Figure 5.18 a) Correlation coefficient function of polymer **T5** assemblies *in situ* with a measurement interval of 5 min. b) Size distribution by intensity with the same time period.

5.3.6 Study of the effect of block length on the resultant assembly morphology

In order to understand how the block length and ratio of PCL based triblock copolymers influence the CDSA behaviour, a series of PDMA-*b*-PCL-*b*-PDMA triblock copolymers, i.e. polymer **T1-T9,** were synthesized and assembled under the standard conditions (5 mg mL^{-1} in methanol, r.t.). After aging for two days, all assembly solutions showed a visible Tyndall effect, indicating the formation of particles. TEM analysis (**Figure 5.19**) was performed to illustrate the morphology and size of the micelles.

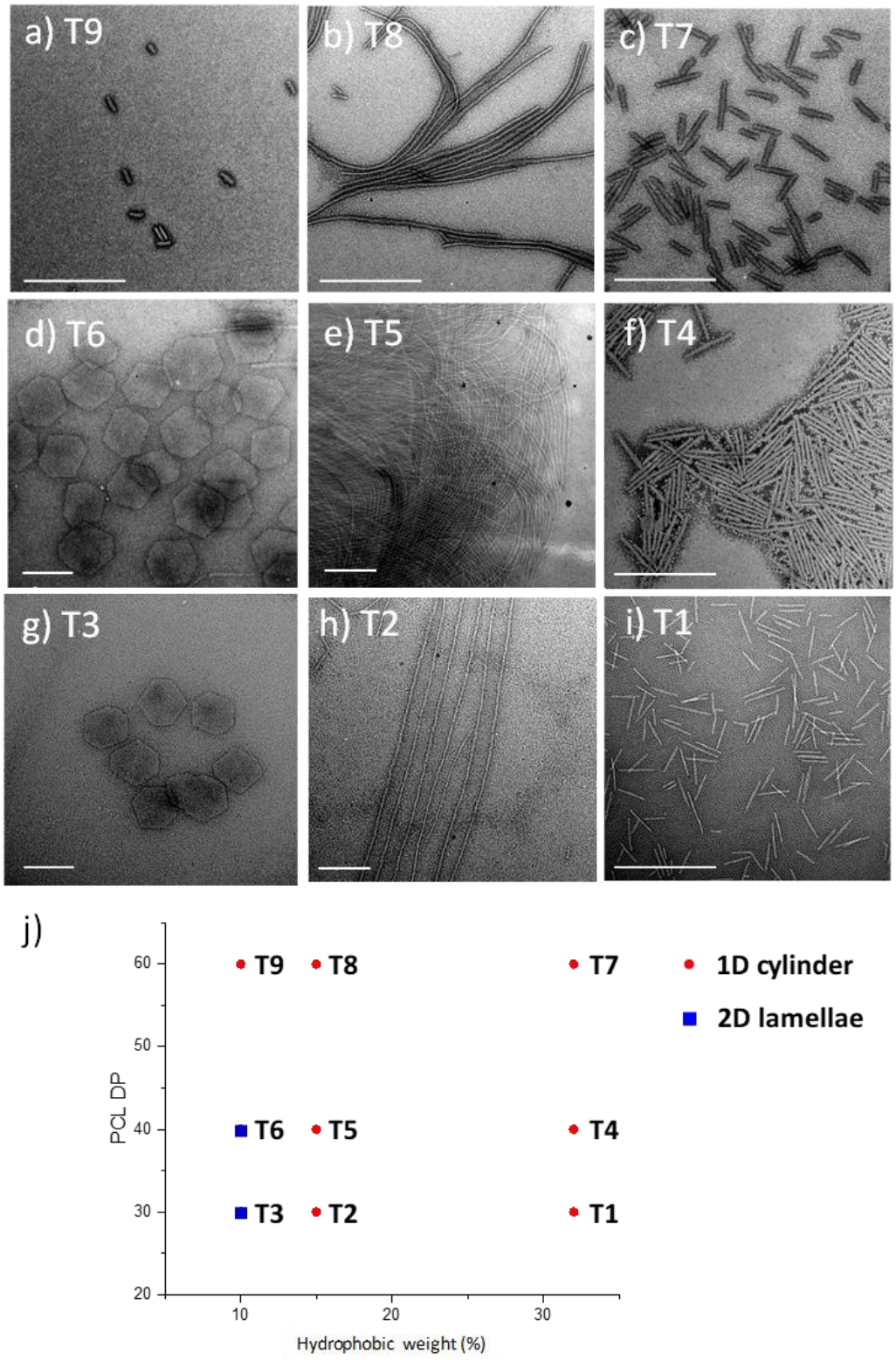

Figure 5.19 TEM micrographs of the micelles obtained from polymers PDMA-*b*-PCL-*b*-PDMA: (a) **T9**, (b) **T8**, (c) **T7**, (d) **T6**, (e) **T5**, (f) **T4**, (g) **T3**, (h) **T2** and (i) **T1**. Samples were negatively stained using uranyl acetate (0.5 wt %). Scale bar = 0.5 µm. (j) Phase diagram constructed for PDMA-*b*-PCL-*b*-PDMA triblock terpolymers.

It was already known that the example polymer **T5** ($PDMA_{124}$-*b*-PCL_{40}-*b*-$PDMA_{124}$) assembled into hair-like fibres (**Figure 5.19 e**). Thereafter, the core length was fixed at DP = 40, and corona length was varied to DP = 96 (polymer **T4**) and DP = 406 (polymer **T6**) for assembly study. As mentioned in **section 5.3.5**, longer corona (polymer **T6**) resulted in 2D hexagonal platelets (**Figure 5.19 d**), whereby the shorter counterpart (polymer **T4**) formed short fibres (**Figure 5.19 f**), as shown in the phase diagram (**Figure 5.19 j**). Studies of the formation of di- and tri-BCP micelles with a PLLA crystalline core and PDMA corona in **Chapter 2** revealed a preference for 2D lamellae over 1D cylinders when the percentage composition of corona-forming block was increased. This behaviour is in stark contrast with the widely accepted packing parameter considerations[15] but could also be attributed to the fact that the increased solubility of the polymer (with longer corona composition) gives adequate time for the semi-crystalline polymer chain to adopt a preferred crystal conformation thus leading to well-defined structures (2D platelets). This explanation also properly rationalize the results here.

Since varying the corona block lengths successfully enables to tune the CDSA of the nanostructures, the impact of altering core block length was then investigated. The length of the core block was reduced from PCL_{40} to PCL_{30} to probe the influence of a shorter core block (polymer **T1**-**T3**) on the assembly behaviour while the same hydrophobic ratio was maintained, Under the standard assembly condition, the obtained morphologies were quite similar to the PCL_{40} counterparts: Longer corona (polymer **T3**) led to 2D hexagonal platelets, the medium one (polymer **T2**) produced hairy cylinders and shorter corona (polymer **T1**) formed short fibres (**Figure 5.19 g-i**). In contrast, as the core block length extended to DP = 60 (polymer **T7-T9**) the obtained micelles are slightly different. To be specific, polymer **T7** still assembled

into short cylinders showing similar length (L_n = 199 nm) to **T4** counterpart L_n = 283 nm (same hydrophobic ratio 32%). However, the nanoparticles obtained from **T8** are much shorter (L_n = 819 nm) than the expectation based on **T5** (L_n > 4 μm). More surprisingly, as the corona length extended to DP = 600 (polymer **T9**), short fibres (L_n = 84 nm, **Figure 5.19 a** and **j**) were achieved instead of platelets. This is explained by the fact that the corona block is so long that it potentially hindered the crystallisation on the crystal front leading to truncated fibres. Additionally, from the solubility point of view, though the block ratio of PCL_{60} series are the same to the PCL_{40} counterparts, the longer core block still makes the hydrophobic area less soluble, which impede the formation of favoured conformation (lamella structure) during the crystallisation process. Similar results were also observed in **Chapter 2**.

It was worth noting the assemblies obtained from coil-crystalline-coil triblock copolymers PDMA-*b*-PCL-*b*-PDMA by the single component solution-phase approach showed remarkable uniformity (except for polymer **T2** and **T5** since the micelles are too long to be estimated). Indeed, the length dispersity (L_w/L_n) of the cylindrical micelles were all controlled below 1.08 (**Table 5.2** and **Figure 5.20**).

Table 5.2 Characterisation data of cylinder dimensions

Sample	L_n[a] (nm)	L_w[a] (nm)	L_w/L_n
T1	204	211	1.03
T4	283	290	1.02
T7	199	211	1.06
T8	819	881	1.08
T9	84	87	1.03

[a] Determined by TEM analysis from the uranyl acetate stained samples.

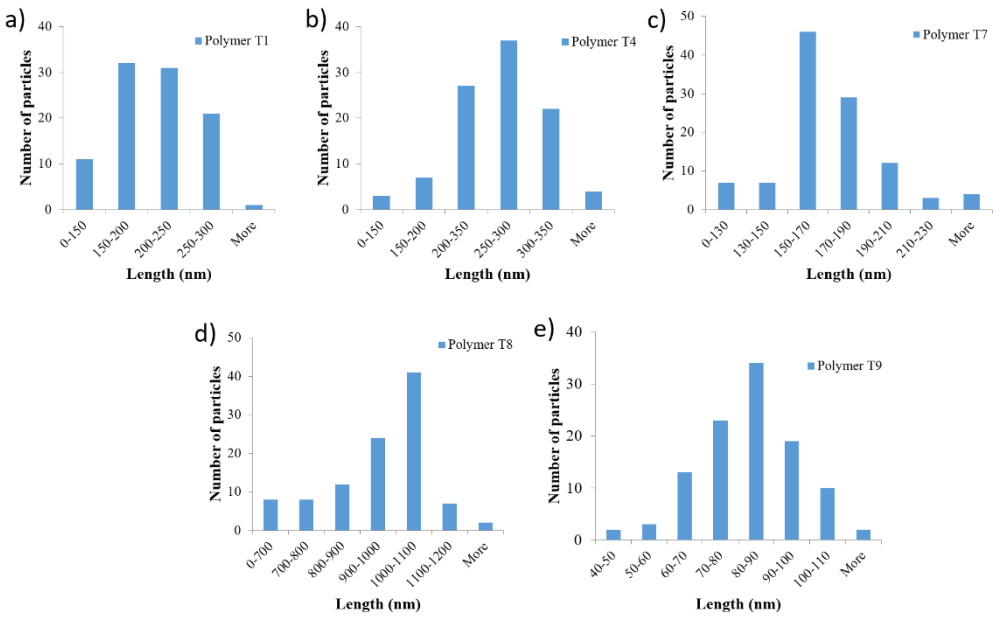

Figure 5.20 Histograms of the lengths of PDMA-*b*-PCL-*b*-PDMA cylindrical micelles, a) **T1**, b) **T2**, c) **T3**, d) **T4** and e) **T5** as determined by TEM analysis.

5.3.7 Self-seeding process of PCL based triblock copolymers

As mentioned before, in the PCL based triblock copolymers system, the polymer dissolution process consumed most of the crystalline domains leaving a few ordered nuclei to initiate nanoparticle growth. Interestingly, as a consequence of the particular polymer composition and solvent conditions, this could be realized without any heating in single solvent. Similar assembly behavior has previously been observed in PLLA based triblock copolymer systems, when it was shown that uniform diamond platelets could be fabricated at room temperature.[25] In order to further corroborate the hypothesis of a self-nucleation process, the assembly solution, polymer $PDMA_{302}$-*b*-PCL_{60}-*b*-$PDMA_{302}$ (Polymer **T9**) for instance, was annealed at 30 °C and 35 °C for 4 hours before cooling to room temperature (25 °C) and aged for two days. TEM analysis of the annealed samples at 30 °C demonstrated longer micelles (*ca.* 432 nm, **Figure 5.21 b**) with narrow length distribution (L_w/L_n = 1.05). As the aging temperature

increased to 35 °C, the obtained fibres were even longer (*ca.* 1207 nm, **Figure 5.21 c**) and the size dispersity still remained low ($L_w/L_n < 1.03$). These data demonstrated that the number of surviving seeds diminished as the annealing temperature increased. However, if the annealing temperature was too high e.g.70 °C, which is above the melting temperature of PCL (60 °C), spheres were obtained instead (**Figure 5.21 d**). This was presumably because all the crystalline nuclei melted at that temperature and on cooling the unimers preferred to assemble into spherical micelles since there was no crystal front available to initiate the crystallisation. This result emphasizes the importance of the nucleus in the formation of uniform cylindrical micelles.

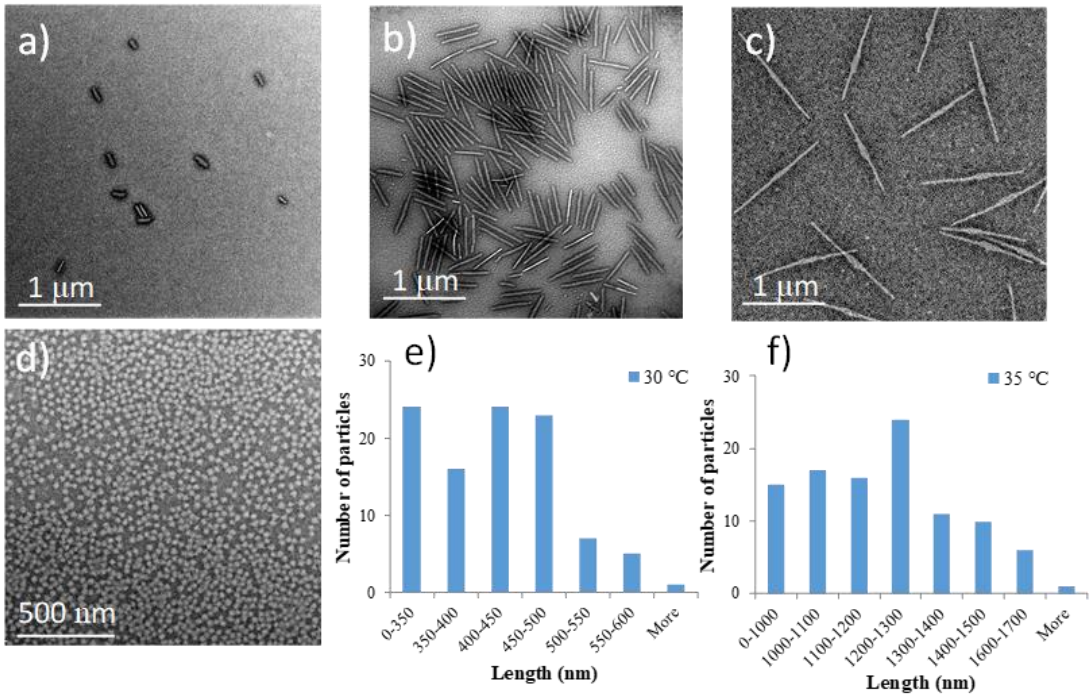

Figure 5.21 TEM analysis of $PDMA_{302}$-*b*-PCL_{60}-*b*-$PDMA_{302}$ self-assembled in methanol at 5 mg mL^{-1} following heating at (a) 25 °C (b) 30 °C (c) 35 °C and (d) 70 °C for 4 hours before cooling down in 25 °C and aging for two days. Samples were negatively stained using uranyl acetate (0.5 wt %). Histograms of the lengths of the samples aging at (e) 30 °C and (f) 35 °C.

Apart from the influence of temperature, the effect of solvent on the number of remaining seeds was also investigated. To be specific, polymer **T9** was assembled

under the similar condition (5 mg mL^{-1}, r.t. aging for 2 d), but in a mixture of THF and methanol. It was found that a small amount of good solvent (THF, 4 vol %) promoted an increase in micelle length from 84 nm to 265 nm (L_w/L_n = 1.04, **Figure 5.22 b**). Furthermore, as the THF content increased to 10 vol %, the cylindrical micelles grew to about 762 nm in length (**Figure 5.22 c**) with good size dispersity (L_w/L_n = 1.02). In general, the addition of common solvent or heating were both able to manipulate the number of seeds in the assembly solution, which makes it possible to tune the resultant cylindrical micelle length as a self-seeding process (**Figure 5.23**).

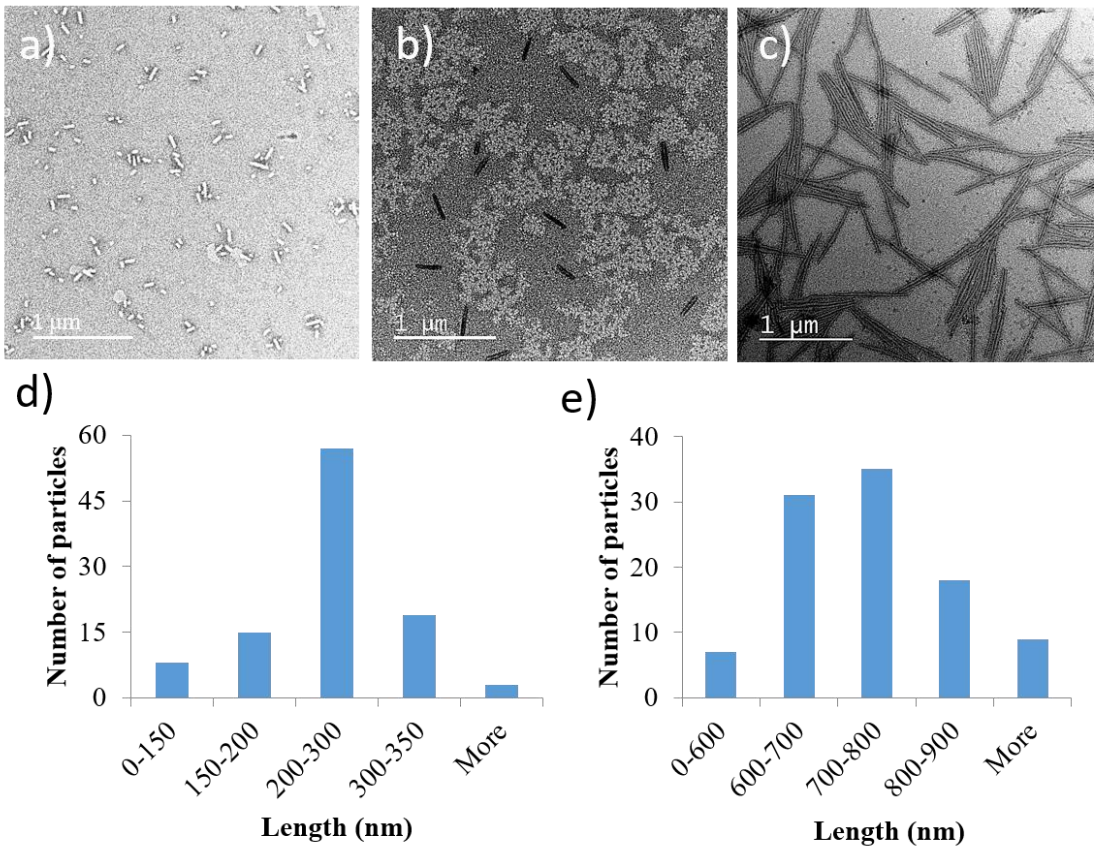

Figure 5.22 TEM analysis of $PDMA_{302}$-*b*-PCL_{60}-*b*-$PDMA_{302}$ self-assembled in a) 100% methanol b) 96% methanol + 4% THF c) 90% methanol + 10% THF 5 mg mL^{-1} at room temperature and for 2 d. Samples were negatively stained using uranyl acetate (0.5 wt %). Histograms of the lengths of the samples aging in (d) 4% THF and (e) 10% THF.

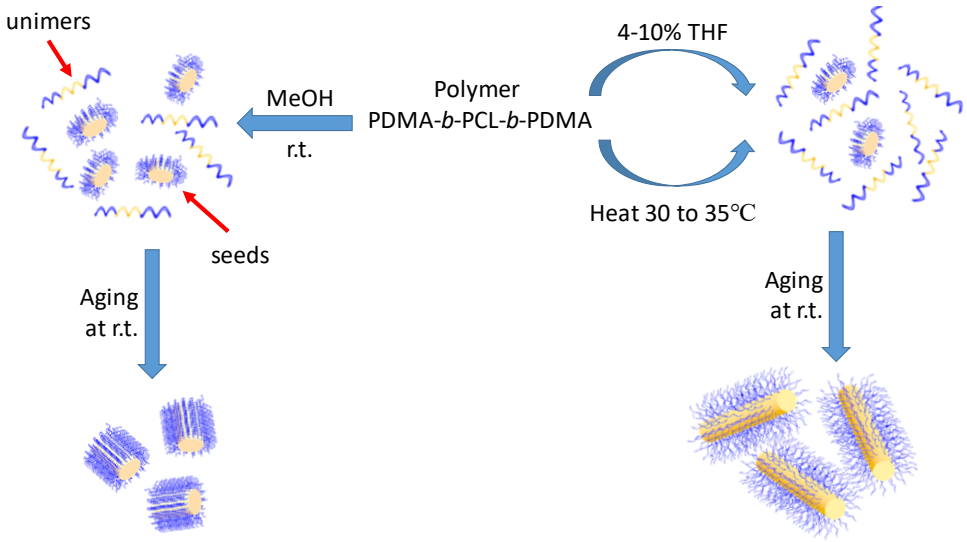

Figure 5.23 Schematic representation of the preparation of near monodisperse fibres by self-seeding method.

5.4 Conclusion

In summary, the systematic CDSA study of PDMA-*b*-PCL-*b*-PDMA triblock copolymers to prepare crystalline poly(ε-caprolactone) assemblies *via* a simple, single component solution-phase methodology at room temperature is reported, which greatly simplifies the access to well-defined 1D and 2D organic nanoparticles. It was further demonstrated that the solubility of the copolymers could be exploited to control the size and morphology of the nanoparticles, which was mainly affected by two factors i.e. the block ratio and solvent property. In accordance with the recent reports of poly(ester) crystalline nanoparticles, good solvent quality and large corona-core ratios facilitated the formation of crystalline micelles with fewer defect, such as 2D platelets or long cylindrical micelles, whereas the opposite part resulted in short fibres. Furthermore, it was proved that the cylinder length (84 nm to 1207 nm) of PCL based triblock copolymers can be manipulated by adjusting the amount of crystalline seeds through the variation of solvent composition and/or temperature. The ability to readily access and control the assembly of PCL-based triblock copolymers into spherical, cylindrical or lamellar micelles with uniform sizes through a simple assembly approach provides a platform to develop a series of new materials with more functionality and complexity such as ABC type terpolymers, which show great potential for future biorelevant applications.

5.5 Experimental section

5.5.1 Materials

Chemicals and solvents were purchased from Sigma-Aldrich, Acros, Fluka, TCI, Fisher Chemical, Alfa Aesar or VWR. ε-Caprolactone was distilled twice under vacuum over calcium hydride before being introduced into a glovebox and used. Diphenyl phosphate was recrystallized from dried $CHCl_3$/Hexane (3:1) and dried over P_2O_5. 2,2′-Azobis(isobutyronitrile) (AIBN) was received from Molekula. After recrystallisation from methanol it was stored at 4 °C. Deuterated solvents were used as received from Apollo Scientific. RAFT agent 2-(dodecylthiocarbonothioylthio)-2-methylpropionic acid (DDMAT) was synthesised as described in **Chapter 2**. All the monomers used for polymerisation were filtered through basic aluminium oxide to remove the inhibitor.

5.5.2 Instrument

Proton nuclear magnetic resonance (^{1}H NMR) spectroscopy measurements were conducted on a Bruker AV-400 spectrometer at 400 MHz. All spectra were recorded in $CDCl_3$ unless stated otherwise. The chemical shifts were reported as δ in parts per million and quoted downfield from the internal standard tetramethylsilane (δ = 0 ppm). Diffusion-ordered spectroscopy (DOSY) NMR spectroscopy was performed on a Bruker AV-500 AVANCE spectrometer equipped with a 5 mm broadband observe (BBO) z-axis gradient probe capable of generating nominal maximum field strengths of 53.5 G cm^{-1}. The measurement was performed using stimulated echo and LED pulse sequences incorporating bipolar-gradient pulses for diffusion, using a diffusion time of 100 ms and a LED delay of 5 ms. For each experiment, pulsed field gradients

with a duration of 2.5 ms followed by a recovery delay of 200 μs were applied with increases from 5% to 95% of the maximum strength in 32 equally spaced steps. Experiments were carried out on samples at a polymer concentration of 10 mg mL^{-1} in deuterated chloroform with active temperature regulation at 298 K. The DOSY spectrum was processed by the Bruker Topspin S3 software package (version 2.1).

Size exclusion chromatography (SEC) analyses were performed using an Agilent 1260 Infinity Multi-Detector GPC System fitted with a refractive index and UV detector, and equipped with a guard column (Varian PLGel) and two PLGel 5 μm mixed-D columns. The mobile phase was DMF with 5 mM NH_4BF_4, at a flow rate of 1 mL min^{-1} at 50 °C. All data was analysed using Cirrus v3.3 and Agilent GPC/SEC software v1 with calibration curves produced using Varian Polymer Laboratories linear PMMA standards.

Mass spectra were obtained using a Bruker Ultraflex II matrix-assisted laser desorption/ionization time-of-flight (MALDI-ToF) mass spectrometer. The MALDI-ToF samples were prepared using a trans-2-[3-(4-t-butyl-phenyl)-2-methyl-2-propenylidene] malononitrile (DCTB) matrix and sodium trifluoroacetate (NaTFA) as a cationization agent. Samples were prepared as follows: DCTB (2 μL, 10 mg mL^{-1} in tetrahydrofuran), sample (2 μL, 1 mg mL^{-1} in tetrahydrofuran) and NaTFA (2 μL, 0.1 mg mL^{-1} in tetrahydrofuran) were added to the MALDI-ToF plate successively. The samples were measured in reflection ion mode and calibrated using SpheriCal (1200–8000 g mol^{-1}) standards.

Transmission electron microscopy (TEM) was performed using a JEOL 2100FX at 200 kV. TEM samples were prepared on a formvar/carbon film TEM grid. In short, 2 μL of sample solution (1 mg mL^{-1}) was deposited on a grid and left to air dry. 5 μL of uranyl acetate (UA, 0.5 wt %) solution was then dropped on the grid and left for 60 seconds before blotting. The sample was kept in a desiccator overnight before characterisation. TEM images were analysed by Image J software, where at least 100 particles were counted for each sample to obtain the number-average length (L_n) and weight-average length (L_w). L_n and L_w were calculated by using the following equations:

$$L_n = \frac{\sum_{i=1}^{n} N_i L_i}{\sum_{i=1}^{n} N_i}$$

$$L_w = \frac{\sum_{i=1}^{n} N_i {L_i}^2}{\sum_{i=1}^{n} N_i L_i}$$

Where L_i is the length of each counted cylindrical micelle and N_i is the number of the cylindrical micelles with the length L_i.

Dynamic light scattering measurements were conducted using a Malvern Zetasizer Nano instrument equipped with a 4 mW He–Ne 633 nm laser module at 25 ℃, with data analysis using Malvern DTS 6.20 software. Measurements were carried out at a detection angle of 173° (backscattering). All determinations were made in triplicate unless otherwise stated (with 10 measurements recorded for each run).

5.5.3 Typical procedure for the homopolymerisation of ε-caprolactone (PCL_{30}, PCL_{40} and PCL_{60})

PCL_x were synthesized in a glove box under a nitrogen atmosphere. Typically, for PCL_{40}, ε-CL (1 mL, 9 mmol), 1, 3-propanediol (12.96 µL, 0.18 mmol) and diphenyl phosphate (DPP) (42.26 mg, 0.18 mmol) were added to an ampoule with 9 mL of solvent (chloroform or benzene). The solution was left stirring at room temperature for 24 h. the reaction mixture was precipitated in hexane before filtration and drying *in vacuo*. $M_{n,\,NMR}$ = 4.6 kDa, DP = 40. $M_{n,\,SEC}$ = 7.5 kDa, $Đ_M$ = 1.05. ^{1}H NMR (400 MHz, $CDCl_3$) δ (ppm) 4.06 (t, 2 H, CH_2OH), 3.65 (t, 2 H, CH_2OCO), 2.30 (t, 2 H, OCOCH_2), 1.73-1.33 (m, 10 H, OCO(CH_2)$_5$OH).

5.5.4 Typical procedure for Coupling RAFT agent to homopolymer PCL_x (PCL_{30}, PCL_{40} and PCL_{60})

PCL_{40} (0.80 g, 0.174 mmol), DDMAT (0.63 g, 1.739 mmol), DMAP (0.021 g, 0.174 mmol) and DCC (0.3588 g, 1.74 mmol) were mixed together in an ampoule with 9 mL of dichloromethane. The solution was left stirring at room temperature for 3 days. Then the reaction mixture was filtered off, the filtrate was precipitated in diethyl ether three times and further dried *in vacuo*. ^{1}H NMR (400 MHz, $CDCl_3$) δ (ppm) 4.06 (t, 2 H, CH_2OH), 3.65 (t, 2 H, CH_2OCO), 3.26 (t, 4 H, SCH_2CH$_2$), 2.30 (t, 2 H, OCOCH_2), 1.73-1.33 (m, 10 H, OCO(CH_2)$_5$OH).

5.5.5 Typical procedure for the chain-extension of the macro-CTA ($PDMA_{150}$-*b*-PCL_{30}-*b*-$PDMA_{150}$)

CTA-PCL_{30}-CTA (50 mg, 0.01 mmol), DMA (0.33 mL, 3.92 mmol) and AIBN

solution (16.42 µL, 10 mg mL^{-1} in 1, 4-dioxane 0.001 mmol) were mixed in dioxane (1 mL) in an ampoule. The solution was degassed *via* three freeze-pump-thaw cycles and refilled with argon. The solution was placed in an oil bath at 70 °C for 5 h. The reaction mixture (90% conversion, 0.18 g, 60% yield) was precipitated in diethyl ether and dried in *vacuo*. $M_{n,\,NMR}$ = 34.3 kDa, DP = 300. $M_{n,\,SEC}$ = 42.1 kDa, $Đ_M$ = 1.08. ^{1}H NMR (400 MHz, $CDCl_3$) δ (ppm) 4.06 (t, 2 H, CH_2OH), 3.65 (t, 2 H, CH_2OCO), 2.88 (s, 6 H, CON(CH_3)$_2$), 1.73-1.33 (m, 10 H, OCO(CH_2)$_5$OH), 1.24 (s, 21 H, $C_{10}H_{21}$), 0.87 (t, 3 H, CH_3CH_2).

5.5.6 Typical crystallisation-driven self-assembly method for PCL based block copolymers

A typical CDSA method is as follows: a solution of the triblock copolymer in methanol was prepared at a concentration of 5 mg mL^{-1} and then stirred at room temperature in a sealed vial for two days.

5.6 References

1. Qian, J.; Guerin, G.; Lu, Y.; Cambridge, G.; Manners, I.; Winnik, M. A. *Angewandte Chemie International Edition* **2011,** 50 (7), 1622-1625.
2. Qian, J.; Li, X.; Lunn, D. J.; Gwyther, J.; Hudson, Z. M.; Kynaston, E.; Rupar, P. A.; Winnik, M. A.; Manners, I. *Journal of the American Chemical Society* **2014,** 136 (11), 4121-4124.
3. Li, X.; Jin, B.; Gao, Y.; Hayward, D. W.; Winnik, M. A.; Luo, Y.; Manners, I. *Angewandte Chemie International Edition* **2016,** 55 (38), 11392-11396.
4. Hsiao, M.-S.; Zheng, J. X.; Van Horn, R. M.; Quirk, R. P.; Thomas, E. L.; Chen, H.-L.; Lotz, B.; Cheng, S. Z. D. *Macromolecules* **2009,** 42 (21), 8343-8352.
5. Inam, M.; Cambridge, G.; Pitto-Barry, A.; Laker, Z. P.; Wilson, N. R.; Mathers, R. T.; Dove, A. P.; O'Reilly, R. K. *Chemical Science* **2017,** 8 (6), 4223-4230.
6. Yu, W.; Inam, M.; Jones, J. R.; Dove, A. P.; O'Reilly, R. K. *Polymer Chemistry* **2017,** 8 (36), 5504-5512.
7. Rizis, G.; van de Ven, T. G.; Eisenberg, A. *Angewandte Chemie International Edition* **2014,** 53 (34), 9000-9003.
8. Ganda, S.; Dulle, M.; Drechsler, M.; Förster, B.; Förster, S.; Stenzel, M. H. *Macromolecules* **2017,** 50 (21), 8544-8553.
9. He, W.-N.; Zhou, B.; Xu, J.-T.; Du, B.-Y.; Fan, Z.-Q. *Macromolecules* **2012,** 45 (24), 9768-9778.
10. Arno, M. C.; Inam, M.; Coe, Z.; Cambridge, G.; Macdougall, L. J.; Keogh, R.; Dove, A. P.; O'Reilly, R. K. *Journal of the American Chemical Society* **2017,** 139 (46), 16980-16985.
11. Wang, J.; Zhu, W.; Peng, B.; Chen, Y. *Polymer* **2013,** 54 (25), 6760-6767.
12. Makiguchi, K.; Satoh, T.; Kakuchi, T. *Macromolecules* **2011,** 44 (7), 1999-2005.
13. Pitto-Barry, A.; Kirby, N.; Dove, A. P.; O'Reilly, R. K. *Polymer Chemistry* **2014,** 5 (4), 1427-1436.
14. Goldburg, W. *American Journal of Physics* **1999,** 67 (12), 1152-1160.
15. Vilgis, T.; Halperin, A. *Macromolecules* **1991,** 24 (8), 2090-2095.

General Conclusions and Outlook

In this thesis, we synthesised a series of well-defined coil-crystalline-coil triblock copolymers, whereas the crystalline core were mainly focused on biodegradable and semi-crystalline polyester i.e. polylactide and polycaprolactone. Through a facile CDSA methodology, dissolving polymers in single alcoholic solvent at room temperature, a variety of assembly morphologies could be obtained, which ranged from 1D cylinders to 2D platelets with respect to different block ratios. In contrast to corresponding diblock copolymers counterpart, triblock copolymers demonstrated their better solubility, which enable the self-assembly process feasible at mild conditions. Phase diagrams were fabricated accordingly to instruct the design of nanoparticles with different morphologies and an assumption was put forward based on this i.e. the solubility of the polymers plays a pivotal role in the crystallisation process whereas increased solubility facilitate the formation of intact crystals, platelet for instance. Besides, to our best knowledge, it was found for the first time that PLA based triblock copolymers could perform living CDSA and PCL based triblock copolymers were able to execute self-seeding process to achieve cylinders with uniform length.

As a consequence of the enhanced solubility, crystalline assemblies obtained from triblock copolymers demonstrated lower energy barrier for “unimer exchange” process in comparison to diblock counterparts. The morphological transition could be realised by mixing stereo-pure cylindrical micelles of PLA based triblock copolymers at body temperature in methanol. Although the transformation in aqueous solution is problematic, it is still a giant step closer to the goal i.e. to achieve the morphological transition in physiological conditions. To further optimise the system, polymer end

group should be partially ionized to boom the solubility to a greater extent and if the morphological transformation do occur, *in vivo* cell study could be followed in the future. This will be a breakthrough concept in the drug-delivery realm whereby enantiomer pure micelles themselves could be utilised as stimuli for specific drug release.